Molecular Engineering of Dipolar and Octupolar Non-Linear Optical Materials for Next-Generation Telecommunications

Christopher M. Ashcroft

Homerton College

The University of Cambridge

This thesis is submitted for the degree of Doctor of Philosophy

Department of Physics
September 2018

Declaration

This thesis is the result of my own work and includes nothing, which is the outcome of work done in collaboration except as declared in the Preface and specified in the text.

It is not substantially the same as any that I have submitted, or, is being concurrently submitted for a degree or diploma or other qualification at the University of Cambridge or any other University or similar institution except as declared in the Preface and specified in the text. I further state that no substantial part of my dissertation has already been submitted, or, is being concurrently submitted for any such degree, diploma or other qualification at the University of Cambridge or any other University or similar institution except as declared in the Preface and specified in the text

It does not exceed the prescribed word limit for the relevant Degree Committee.

Christopher M. Ashcroft

Molecular Engineering of Dipolar and Octupolar Non-Linear Optical Materials for Next-Generation Telecommunications

Christopher M. Ashcroft

Abstract

In an age where next-generation all-optical circuitry and optical data storage are at the forefront of the telecommunications industry, the molecular engineering and design of new organic materials continues apace. Such materials are particularly attractive on account of their fast optical response times, and superior non-linear optical susceptibilities, relative to their traditional inorganic counterparts. While dipolar molecules dominate the field of organic non-linear optical (NLO) materials, octupolar molecules have the potential to produce far greater NLO effects; moreover, they have the capacity to produce 3-D sensitive NLO phenomena.

This PhD explores new classes of dipolar organic and octupolar organometallic materials, where computations have predicted them to serve with superior NLO properties. To this end, concerted experimental and theoretical data are employed to characterise the electronic structure of these materials and elucidate their NLO properties. Data for electronic structures in this thesis were secured via in-house and synchrotron-based X-ray diffraction experiments (by proxy), which the author employed for charge density analyses. Multipolar modelling of experimental charge densities of the subject NLO materials forms an integral part of this thesis. Topological analysis is applied to these electronic structures, using the quantum theory of atoms in molecules (QTAIM), from which the structural and chemical origins of their NLO properties are assessed. Complementary theoretical methods were also used in this work, including calculations undertaken via density functional theory, as well as the relatively new technique of X-ray constrained wave-function refinement, which especially complements multipolar modelling methods, providing direct corroboratory topological analysis. An array of complementary experimental and computational methods is employed to evaluate the NLO properties of these materials in the gas-, solution-, and solid state-phase. The organometallic complexes presented in this thesis were also synthesised by the author.

Chapter 1 of this work begins by presenting some of the main principles behind NLO phenomena, before providing a review of some of the most salient organic and organometallic NLO materials investigated, to date. Chapter 2 provides details pertaining to the experimental and computational methods used within this work to evaluate the molecular origins of the NLO properties of the materials investigated herein. Chapter 3 explores the molecular origins of the NLO properties of a

new class of dipolar organic chromophores via structural analysis, experimental charge density analyses, hyper-Rayleigh scattering and density functional theory. Chapter 4 similarly investigates a new class of dipolar organic NLO chromophores via structural analysis, hyper-Rayleigh scattering and density functional theory. However, topological analysis herein was undertaken solely via the X-ray constrained wave-function fitting method, due to the absence of high-resolution X-ray diffraction data for experimental multipolar modelling. Chapter 5 investigates two ionic organic chromophores and the implications of their intermolecular interactions on their respective NLO responses by building up the ionic system using a ‘molecular lego’ approach. Chapters 6-7 detail investigations of newly identified octupolar NLO organometallic complexes, and feature several rare examples of charge-density studies of materials containing heavy elements, such as the transition metal, zinc, and bromine These heavy elements are particularly challenging even for state-of-the-art experimental and computational materials characterisation methods. Chapter 8 concludes this work, and identifies possible future directions for investigations of NLO materials for next-generation telecommunications.

Acknowledgements

Keeping this to one side of A4 proved challenging to say the least. The number of people I would like to acknowledge for making this PhD possible is extensive, varied and a testament to the amazing people I have the great privilege to know. Without a shadow of a doubt the first person to mention is my supervisor, Jacqui Cole, without whom this PhD would not have been possible. Her scientific guidance, endless academic and emotional support and, (sorry Jacqui) terrible puns have seen me through my time at Cambridge. With supervisors in mind, I'd also like to thank my MSci supervisor at QUB, Marty Gregg. If it hadn't been for Marty's encouragement I might not have even applied to Cambridge, and thus I may not have had the privilege of this amazing, enriching experience.

Encouragement. That word calls to mind friends. I'd especially like to thank Vaughan Connolly, Dr Pallawi Sinha, Dr Philip Moller, Alex Bennie, Dr Alisha Cramer, Alice Archer, Benjamin Clawson, Dudley Delderfield, Gina Youens, Jonathon Beagle, Henrietta Boyle, Anthony Drew, Dr Aaron Dsouza, Dr Oliver Melvill, and Shaun Kauffman, who have been there through the good and the bad times, the fun times and the stressful times…and of course the wine times! Then there are my non-Cambridge based friends, who have been just as integral to my PhD time. I'd especially like to thank Peter Mason, and indeed the Mason family in general for their support and friendship. Henry Adams, Ramon McHardy, Dr Sharn Bowen and Darren O'Brien have also been a great source of encouragement and laughter, and I wouldn't be without any of you.

However, despite all these amazing people, there is one group of people who are especially important to me; my family. I thank them all for their love, support and encouragement. Of course, there is a special subset of my family who require a dedicated mention: my parents. It's hard to put into words how much I owe to them, and how much I love them. Their never-ending support, encouragement, and most importantly, love has brought me to this day and I will be eternally grateful to them for being the amazing people they are.

I dedicate this thesis to my parents, and to everyone who has touched my life. Thank you! May our journey continue!

Deo Gratias!
Fiat Lux et Lux Fuit!

Table of Contents

Experimental and Computational Methods

Chapter 6 **175**

Molecular Origins of Octupolar Non-linear Optical Activity in dichlorobis(3-pyridinecarboxaldehyde-*κ-N*)Zn(II) Deduced by High-resolution X-ray Diffraction Analysis and *ab initio* Calculations

Revealing the Molecular Origins of the Non-linear Optical Activity of Octupolar dihalidebis(3-chloropyridine-κ-*N*)Zn(II) Complexes via the Concerted use of High-resolution X-ray Diffraction and *ab initio* Calculations

Conclusions and Future Outlook

List of Abbreviations

A	Acceptor
ADP	Anisotropic Thermal Parameter
BLA	Bond Length Alternation
CD	Charge Density
CT	Charge Transfer
D	Donor
DFT	Density Functional Theory
EDD	Electron Deformation Density
esd	estimated standard deviation
esu	electrostatic unit of charge
GC	Gram-Charlier
HAR	Hirshfeld Atom Refinement
HB	Hydrogen Bond
HF	Hartree-Fock
HRS	Hyper-Rayleigh Scattering
IAM	Independent Atom Model
ICT	Intramolecular Charge Transfer
MM	Multipolar Model
NPD	Non-Positive Definite
NLO	Non-Linear Optical
QTAIM	Quantum Theory of Atoms In Molecules
SCM	Su-Coppens-Macchi
SDS	Stewart-Davidson-Simpson
SHG	Second Harmonic Generation
XCW	X-ray Constrained Wave-function fitting
XWR	X-ray Wave-function Refinement

List of Publications

Chapter 1

Introduction to Molecular Engineering of Organic and Organometallic Second-Order Non-linear Optical Materials

Ashcroft, C. M.; Cole, J. M. Ch. 18 Molecular Engineering of Organic and Organometallic Second-Order Non-Linear Optical Materials. In *Handbook of Organic Materials for Electronic and Photonic Devices*; Elsevier.

Cole, J. M.; Ashcroft, C. M. Generic Classification Scheme for Second-Order Dipolar Nonlinear Optical Organometallic Complexes That Exhibit Second Harmonic Generation. *J. Phys. Chem. A* **2018**.

Chapter 3

Relating the Structure of Geminal Amido Esters to their Molecular Hyperpolarizability

Cole, J. M.; Lin, T.-C.; Ashcroft, C. M.; Perez-Moreno, J.; Tan, Y.; Venkatesan, P.; Higginbotham, A. P.; Pattison, P.; Edwards, A. J.; Piltz, R. O.; et al. Relating the Structure of Geminal Amido Esters to Their Molecular Hyperpolarizability. *J. Phys. Chem. C* **2016**, *120* (51), 29439–29448.

Chapter 4

Molecular Origins of the Nonlinear Optical Responses of a Series of α-(X-2-pyridylamino)-*o*-cresol Chromophores from Concerted X-ray Diffraction, Hyper-Rayleigh Scattering, and *ab initio* Calculations

Ashcroft, C. M.; Jacqueline M. Cole; Boardman, E. A.; Lin, T.-C.; Perez-Moreno, J.; Clays, K. Molecular Origins of the Nonlinear Optical Responses of a Series of α-(X-2-Pyridylamino)-o-Cresol Chromophores from Concerted X-Ray Diffraction, Hyper-Rayleigh Scattering, and Ab Initio Calculations. *J. Phys. Chem. C* **2019**, *123* (1), 665–676.

Chapter 5

Multi-phase Structural Models of Stilbazolium-ions Built Up Ion-by-Ion Correlate with Molecular Hyperpolarizability Calculations to Explain their Non-linear Optical Properties

Cole, J. M.; Ashcroft, C. M.; Lin, T.-C.; Malaspina, L. A.; Kwon, O.-P. Multi-Phase Structural Models of Stilbazolium-Ions Built Up Ion-by-Ion Correlate with Molecular Hyperpolarizability Calculations to Explain Their Non-Linear Optical Properties. (**in preparation**).

Chapter 6

Molecular Origins of Octupolar Non-linear Optical Activity in dichlorobis(3-pyridinecarboxaldehyde-*κ-N*)Zn(II) Deduced by High-resolution X-ray Diffraction Analysis and *ab initio* Calculations

Cole, J. M.; Merz, T. A.; Ashcroft, C. M.; de Coene, Y.; Clays, K. Investigation of New Metalorganic Non-Linear Optical Materials Predicted by Data-Mining. (**in preparation**).

Ashcroft, C. M.; Chen, Y.-S.; Cole, J. M. Molecular Origins of Octupolar Nonlinear Optical Activity in Dichlorobis(3-Pyridinecarboxaldehyde-κ-N)Zn(II) Deduced by High-Resolution X-Ray Diffraction Analysis and Ab Initio Calculations. (**in preparation**).

Chapter 7

Revealing the Molecular Origins of the Non-linear Optical Activity of Octupolar dihalidebis(3-chloropyridine-κ-*N*)Zn(II) Complexes via the Concerted use of High-resolution X-ray Diffraction and *ab initio* Calculations

Ashcroft, C. M.; Chen, Y.-S.; Cole, J. M. Revealing the Molecular Origins of the Nonlinear Optical Activity of Octupolar Dihalidebis(3-Chloropyridine-κ-N)Zn(II) Complexes via the Concerted Use of High-Resolution X-Ray Diffraction and Ab Initio Calculations. (**in preparation**).

Chapter 1

Introduction to Molecular Engineering of Organic and Organometallic Second-Order Non-linear Optical Materials

1.1 Introduction

This chapter forms part of a book chapter submission to the publisher Elsevier.

Research into the area of non-linear optical (NLO) materials and their applications has yielded a plethora of technological advancements in the last few decades. More specifically, the study and development of bespoke organic chromophores that are capable of second harmonic generation (SHG) have contributed significantly toward improvements in prospective materials that exhibit faster process speeds in data-transfer, telecommunications or optical switching, as well as other optoelectronic applications. Nevertheless, the ever-increasing demand for new improved materials, coupled with the rise of nanotechnology, requires the flexibility to scale down the physical size of such materials while retaining or improving their NLO responses as they are incorporated into nano-devices via nanofabrication techniques.

A review of the recent scientific literature reveals how far research on organic NLO materials for SHG applications has advanced over the last few decades. Indeed the axioms of structure-property relationships of dipolar organic chromophores are now well established[1]. Consequently, the molecular engineering of such chromophores has become a viable strategy to develop custom-tailored organic NLO materials for SHG applications. However, despite the huge interest in the field and its very rapid developments, some fundamental obstacles remain, particularly with respect to achieving faster optical response times and larger SHG responses.

Herein, we present a brief introduction to the phenomenon of non-linear optics, second harmonic generation (SHG), and the considerations required when designing chromophores on a molecular level for such applications, before presenting the state-of-the-art in the field and its future prospects.

1.1.1 Non-linear optics: A brief introduction

As a phenomenon in its own right, molecular electronic polarization of a material is widely understood and can be viewed from a classical perspective by applying Newtonian mechanics to the motion of the atoms within the material of interest. These atoms oscillate within the material according to Newton's laws of motion and the concept of simple harmonic motion according to:

$$F = m\frac{\partial^2 x}{\partial t^2} + \gamma\frac{\partial x}{\partial t} + kx = -qE \qquad (1.1)$$

where F is force,

m is the mass of the electron,

x is atomic displacement,

t is time,

γ and *k* are constants,

q is electronic charge,

E is the external electric field applied to the molecule to induce polarization.

The steady-state solution of Eq. 1.1 is given by:

$$x = \frac{-qmE}{(k-\omega^2-i\gamma\omega)}e^{-i\omega t} \tag{1.2}$$

where ω is the oscillation frequency.

The polarization of a material is defined as the sum of all dipole moments within the structure:

$$P = Nqx = \frac{-qNm\boldsymbol{E}}{(k-\omega^2-i\gamma\omega)}e^{-i\omega t} \tag{1.3}$$

where N is number of dipole moments in the material which leads to:

$$\frac{-qNm}{(k-\omega^2-i\gamma\omega)}e^{-i\omega t} = \varepsilon_0\chi_{\boldsymbol{ij}}^{(1)} \tag{1.4}$$

where ε_0 is the electrical permittivity of free space, and $\chi_{ij}^{(1)}$ is the second-rank electric susceptibility tensor of the material. This equation simplifies to:

$$\boldsymbol{P} = \varepsilon_0\chi_{\boldsymbol{ij}}^{(1)}\boldsymbol{E_j} \tag{1.5}$$

This is the so-called first-order (linear) polarization response of a material that is induced when the material interacts with an external electric field, $\boldsymbol{E_j}$.

However, Eq. 1.5 is only correct for electric field strengths of low intensity. The polarization response becomes increasingly non-linear as the electric field across a material is raised; the development of the laser has afforded the option to polarize media with high-electric fields, which has led to the observation of unprecedented non-linear effects in materials, In this scenario, Eq. 1.5 must be extended as a power series using a Taylor series expansion in order to account for higher-order (non-linear optical) effects. Additionally, a term can be added to account for any permanent electronic polarization that exists within the material:

$$\boldsymbol{P}_{\boldsymbol{i}}^{\boldsymbol{TOTAL}} = \boldsymbol{P}_{\boldsymbol{0}} + \varepsilon_0 \left(\chi_{\boldsymbol{ij}}^{(1)}\boldsymbol{E}_{\boldsymbol{j}} + \chi_{\boldsymbol{ijk}}^{(2)}\boldsymbol{E}_{\boldsymbol{j}}.\boldsymbol{E}_{\boldsymbol{k}} + \chi_{\boldsymbol{ijkl}}^{(3)}\boldsymbol{E}_{\boldsymbol{j}}.\boldsymbol{E}_{\boldsymbol{k}}.\boldsymbol{E}_{\boldsymbol{l}} + \cdots\right) \tag{1.6}$$

where $\boldsymbol{P_0}$ accounts for any permanent electronic polarization of the material,
$\chi_m^{(n)}$ has m subscripts that denote the rank of the n^{th} order susceptibility tensor of the material.

The susceptibility matrix $\chi_{ij}^{(1)}$ refers to the linear response of the material, while the $\chi_{ijk}^{(2)}$ and $\chi_{ijkl}^{(3)}$ terms describe the second- and third-order non-linear responses of the material, respectively. These macroscopic polarization characteristics can be equally described at the molecular scale, by simply exchanging the macroscopic coefficients, $\chi_m^{(n)}$ for their analogous microscopic (hyper)polarizability coefficients:

$$\boldsymbol{P}_{\boldsymbol{i}}^{\boldsymbol{TOTAL}} = N\left[\boldsymbol{\mu} \quad + \varepsilon_0\left(\alpha_{\boldsymbol{ij}}\boldsymbol{E}_{\boldsymbol{j}} + \beta_{\boldsymbol{ijk}}\boldsymbol{E}_{\boldsymbol{j}}.\boldsymbol{E}_{\boldsymbol{k}} + \gamma_{\boldsymbol{ijkl}}\boldsymbol{E}_{\boldsymbol{j}}.\boldsymbol{E}_{\boldsymbol{k}}.\boldsymbol{E}_{\boldsymbol{l}} + \cdots\right)\right] \tag{1.7}$$

where ε_0 is the electrical permittivity of free space,
$\boldsymbol{\mu}_i$ is the permanent molecular dipole moment vector,
$\boldsymbol{\alpha}_{ij}$ is the second-rank electric polarizability tensor of the molecule,
β_{ijk} is the first molecular hyperpolarizability, which takes the form of a third-rank tensor,
γ_{ijkl} is the second molecular hyperpolarizability, which takes the form of a fourth-rank tensor,
N is the number of molecules within the material.

Hence, when one considers a single molecule in isolation, Eq. 1.7 can be simplified to:

$$\boldsymbol{P}_{\boldsymbol{i}}^{\boldsymbol{Molecule}} = \boldsymbol{\mu} + \varepsilon_0\left(\alpha_{\boldsymbol{ij}}\boldsymbol{E}_{\boldsymbol{j}} + \beta_{\boldsymbol{ijk}}\boldsymbol{E}_{\boldsymbol{j}}.\boldsymbol{E}_{\boldsymbol{k}} + \gamma_{\boldsymbol{ijkl}}\boldsymbol{E}_{\boldsymbol{j}}.\boldsymbol{E}_{\boldsymbol{k}}.\boldsymbol{E}_{\boldsymbol{l}} + \cdots\right) \tag{1.8}$$

The terms in parenthesis therefore describe the induced polarization of the molecule, whereby the β_{ijk} and γ_{ijkl} terms afford a measure of the non-linear response of the molecule to external stimulation through intense electric fields. More specifically, the first hyperpolarizability, β_{ijk}, relates to the ability of the molecule to exhibit second-order nonlinearity such as second harmonic generation (SHG), while γ_{ijkl} relates to the analogous third-order NLO effects.

1.1.2 Second Harmonic Generation (SHG)

1.1.2.1 A definition of SHG

Second harmonic generation (SHG) is a non-linear response produced by a wide range of materials when stimulated by intense electric fields that can be rationalized in terms of photon-electron interactions. Before the invention of the laser, the controlled excitation of the electronic state was non-trivial, and only possible in special cases. However, once the invention of the laser enabled a means of intense coherent, monochromatic light, the possibility to observe non-linear interactions between materials and light became possible. SHG was first demonstrated by Franken *et al.* (1961)[2], who focused a ruby laser (λ = 694 nm) onto a quartz sample. The output light was fed into a spectrometer, and the results, recorded on photographic paper, indicated the generation of light with a wavelength of 347 nm, ie, the frequency of the incident light had been doubled, which is illustrated in Figure 1.1.

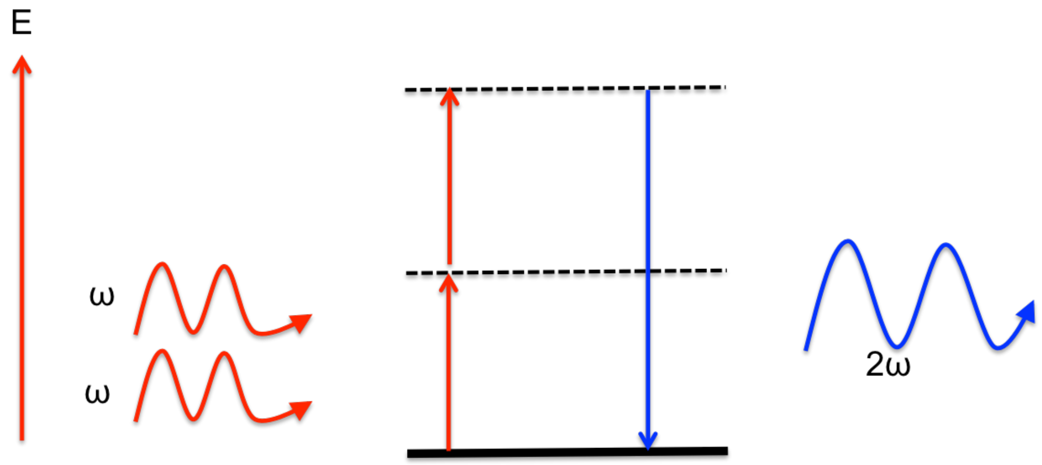

Figure 1.1: A schematic illustration of second harmonic generation (SHG); two waves of incident infrared light are converted into one wave of blue light with double the frequency.

Here, two photons of frequency ω are emitted from the laser with a time interval that is much smaller than that of electron de-excitation (the order of femtoseconds). Both photons coherently interact with one electron in the structure, causing an excitation from its lowest energy state to a virtual energy level characterized by $2\hbar\omega$. After a period typically of the order of femtoseconds, this electron relaxes back to its original energy state with concomitant emission of a single photon with energy of $2\hbar\omega$. By the conservation of energy, *two* photons of frequency ω have been converted into *one* photon of frequency 2ω.

1.1.2.2 Crystallographic symmetry considerations

SHG pertains to an even (second) order non-linear optical phenomenon; as such, it is affected by symmetry elements associated with the structure of a material that produces SHG effects. Owing to its even nature, it is impossible for SHG to occur in crystal structures that contain a centre of inversion, eg, crystalline materials can only exhibit SHG if they possess a non-centrosymmetric crystal structure.

This crystallographic symmetry constraint has sparked substantial interest in the design of SHG-active materials at the molecular level. Consequently, the concept of molecular hyperpolarizability and its relationship to molecular non-linear optical responses have been investigated intensively. Due to the development of many new nanofabrication methods, as well as advances in polymer science, the NLO response of individual molecules can now also be accessed in a way that circumvents the macroscopic material limitations exerted by crystal centrosymmetry.

As devices employing SHG move from the macroscopic to the molecular level, the symmetry considerations change so that the point group symmetries of individual molecules have to be considered instead of crystallographic inversion symmetry. Once again, centrosymmetry is to be avoided, albeit now at the local (molecular) rather than macroscopic level. This in turn provides access to a greater range of chemical structures that can be investigated for potential SHG applications in NLO nano-devices. Therefore, even molecules that are intrinsically centrosymmetric may potentially be used after judicious molecular engineering. For example, the incorporation of a chiral centre, or the addition of a simple hydrogen bond may break the point-group centrosymmetry of the molecule, and thus render it a viable prospect for NLO applications.

1.1.2.3 From ionic- to electronically-derived SHG responses

A variety of inorganic, organic and organometallic compounds exhibit SHG. Historically, inorganic SHG materials have featured primarily in technological applications, such as laser systems and telecommunication networks; two of the most common inorganic materials for SHG applications are potassium dihydrogen phosphate, KDP, and lithium niobate, $LiNbO_3$. The phenomenological origins of SHG in inorganic compounds arise from perturbations of key ions within the solid-state crystal structure of the material. The ionic displacement of certain ions in the crystal lattice induces an anisotropic net polarization effect. Given that the crystal structure possesses a permanent dipole moment, the material is able to afford an SHG response in accordance with electromagnetic and polarization theory, as previously discussed (*cf*. sections 1.1.1 and 1.1.2).

In contrast, SHG in organic materials owes its molecular origins to electronic charge transfer, a process that is much faster than ionic displacement. As such, organic materials afford faster NLO response times than their inorganic counterparts. Industry is increasingly demanding faster optical response times and higher data capacities than inorganic compounds can provide. Research that develops new organic SHG materials has therefore proliferated, since they could hold the key prospects to the future of next-generation SHG applications.

Zyss and Berthier[3] demonstrated the intrinsic link between large SHG responses of organic compounds and high levels of electronic charge transfer across a molecule that is facilitated by π-conjugation. Since then, much research has been carried out on a variety of organic materials in order to identify molecular design guidelines for the optimization of their molecular SHG response, as evaluated by β.

The majority of SHG reports on organic materials refer to dipolar SHG effects, as this is the predominant manifestation of SHG properties. Dipolar SHG materials will therefore be the focus of §1.3 in this chapter. However, a molecule can also exhibit octupolar SHG. Octupolar SHG-active molecules have an octupolar moment that contributes to its NLO properties, and thus they can exhibit NLO properties even when their point group symmetry precludes them from possessing dipole moments; this is discussed in more detail in §1.4.

1.2 Measuring the SHG Response of a Molecular Chromophore

The field of non-linear optics has, to date, focused primarily on the investigation of materials that exhibit SHG effects, despite the potential for materials to also exhibit third-, and fourth- harmonic generation effects (THG and QHG, respectively). This propensity to focus on SHG over THG and QTG is not without reason; with SHG exhibiting the strongest NLO response as a consequence of non-linear effects emanating from a power series (*cf* §1.1). The structure-function relationships that drive SHG are thus the focus of this chapter. Notwithstanding this fact, the THG phenomenon has gradually become more prevalent over time as the strength of NLO signals needed for certain applications has diminished[4]. Furthermore, with the absence of a non-centrosymmetry constraint in THG, its use is becoming increasingly popular. The structure-function relationships that govern THG effects are significantly different to those that dictate SHG and thus are outside the scope of this chapter. Materials for THG are discussed in a review by Long[4] to which readers are directed for more information on this area.

To investigate the potential second-order NLO response of a material, a range of experimental and computational techniques have been developed to probe the β value of a molecule; and thence relate this to its structure to develop structure-function relationships for SHG applications. That said, large errors (10-30%)[5] are typically associated with the determination of β values. As such, a variety of independent methods that evaluate β over the three main states of matter have been developed. These methods may be used in concert to compare and contrast β against the structural properties of a compound in different phases, which is especially important when translating research results to the phase of the device application.

Four well-established methods that are regularly used are:

i) Electric field induced second harmonic generation (EFISH) measurements.
ii) Hyper-Rayleigh scattering measurements.
iii) *Ab initio* calculations based on density functional theory (DFT).
iv) *Ab initio* calculations based on Sum-over-States (SOS) methods.

However, during the last few decades, two new methods have also emerged:

v) Deriving β from the formation of an *ab initio* ‘experimental’ wave function of the chemical molecule that has been obtained by *ab initio* DFT calculations of the structure, which are tempered via their refinement against experimental X-ray data.

vi) Deriving *β* empirically from multipolar moments of each atom in a molecule that emanate from the multipolar modelling of molecular electron densities obtained from high-resolution X-ray diffraction data.

These methods, which can be divided into empirical, semi-empirical, and *ab initio* techniques, are assessed below.

1.2.1 Experimental Determinations of *β*

1.2.1.1 Electric Field Induced Second Harmonic Generation (EFISH)

Electric Field Induced Second Harmonic Generation (EFISH) is a solution-based experimental method that allows the indirect measurement of the molecular hyperpolarizability of a material through the application of an external electric field, which triggers a non-linear response of the material. The response is quantified by comparing it to the known NLO signal of a reference sample such as quartz. The method actually measures the second molecular hyperpolarizability, *γ*, from which one derives *β* via:

$$\gamma^r \equiv \frac{\mu\beta}{5kT} \qquad (1.9)$$

where γ^r is the average dipolar rotational contribution of the vector part of the second molecular hyperpolarizability,
μ is the dipole moment of a material,
β is the first molecular hyperpolarizability,
k is the Boltzmann constant,
T is the temperature.

A detailed description of the EFISH technique has been reported[6]. A major drawback of EFISH is the indirect nature of the *β* evaluation, which makes its determination subject to significant error.

1.2.1.2 Hyper-Rayleigh Scattering (HRS)

Hyper-Rayleigh Scattering (HRS) is a solution-based experimental technique that allows the direct determination of *β* and, in principle, an evaluation of all 27 components of the hyperpolarizability tensor of a material[7]. HRS relies on the fact that the intensity of scattered second-harmonic light, which is measured, is proportional to the average macroscopic hyperpolarizability of the material. The macroscopic value can be transformed into a molecular-scale quantity under the assumption that the scattering centres are randomly oriented molecules within the material. Owing to their complex and sensitive experimental set ups, few HRS facilities are available worldwide. Nevertheless, pending availability, HRS is the preferred method for determining *β*.

1.2.2 Computationally-assisted Determinations of *β*

1.2.2.1 Density Functional Theory (DFT)

Ab initio computational methods such as density functional theory (DFT), introduced by Hohenbeg and Kohn (1964)[8], with further work undertaken by Kohn and Sham[9], can be used to determine the gas-phase value of *β* for a molecule. The atomic coordinates of a structure, determined by X-ray and/or neutron diffraction analysis, can be used as an input for the DFT calculations, or the approximate molecular geometry of the structure can be sketched. This initial approximate molecular geometry is then optimized, before using the optimized geometry to compute the minimum energy of the molecular system. A variety of basis sets and functionals are available to allow DFT to compute the molecular wavefunction of a molecule.

1.2.2.2 Sum-over-States (SOS) methods

Expressions for the polarization and NLO susceptibilities of small molecular systems, through the application of perturbation theory, were introduced by Ward[10], and further developed Orr and Ward[11], which resulted in the development of SOS expressions for the molecular hyperpolarizability. These expressions have also since been updated to exclude dipolar terms, unnecessary in the determination of hyperpolarizabilities of compounds with only octupolar components[12], such as 2,4,6-triaryloxy-1,3,5-triazine (TPOT)[13]. An assessment of the two different regimes[14] suggested that, at least for typical donor-π-acceptor (D-π-A) conjugated systems, it is best to calculate the static *β* value and error for the structure by averaging the results derived from the expressions derived by Kuzyk[12], and Orr and Ward[11].

1.2.2.3 X-ray Wavefunction Refinement (XWR)

The X-ray wavefunction refinement (XWR) method[15], devised by Jayatilaka and Grimwood, can be employed to determine the molecular hyperpolarizability of a compound. While still under development, the method has already yielded results that are in good agreement with DFT values[16,17].

XWR[15] is a sequential process, and begins by taking the atomic coordinates and atomic displacement parameters (ADPs) of a crystal structure, as determined from X-ray derived Bragg intensities (*cf.* § for more information on crystal structure determination), and refining them via Hirshfeld Atom Refinement (HAR)[18,19] Here one minimizes the energy of the molecule in the mean field created by the nearest neighbour, while keeping the difference between calculated and experimental structure factor amplitudes to a minimum. The structure that results from the converged HAR is then used as input to undertake an X-ray Constrained Wave-function (XWC) fitting[19,20] During XWC, a self-consistent field (SCF) calculation is applied to the non-interacting molecule. The structure factors generated from the experimentally derived Bragg intensities are then used to constrain the theoretical calculation by refining it iteratively against a fit of the calculated and (fixed) experimentally determined structure factor amplitudes, until the theoretical results converge to that of the experimental data. Upon convergence, the resulting wavefunction of a molecule can be employed to determine its properties, including the first molecular hyperpolarizability, β[17,21].

1.2.2.4 Calculations of β from multipolar refinement of X-ray diffraction data

Solid-state values of β can also be obtained using empirical calculations in concert with high-resolution X-ray diffraction data[22]. The high-resolution nature of such data allows a charge-density mapping of the molecular structure of a material by assigning the electron density around each atom to its respective atomic multipoles (representing shapes of orbitals) and refining these atomic multipoles as part of the crystal structure refinement; this contrasts with a conventional crystal structure determination where electron density is assigned to atoms modelled as spheres. Once a multipolar refinement has been completed, β can be determined by applying the multipolar moments modelled on each atom in the molecule to an empirical relation that exists between the quadrupolar and octupolar moments of an atom and β, based on the theory of Robinson[23]:

$$\boldsymbol{\beta}_{\boldsymbol{xyz},\mathbf{0}} = \left(\frac{2}{n}\right)^2 (Q_{xx}Q_{yy} + Q_{yy}Q_{zz} + Q_{xx}Q_{zz})O_{xyz} \tag{1.10}$$

where n is the number of electrons and
Q_{ij} and O_{ijk} refers to the second and third Cartesian[1] moment of the molecular charge distribution, respectively

β is being determined by this method for a growing number of compounds[16,24,25]. Owing to the crystal structure origins of this determination of β, this method provides a solid-state measure of the molecular hyperpolarizability. Moreover, its experimentally determined electron-density origins offer a solid-state β value, which incorporates implicitly the electronic intramolecular charge transfer (ICT) characteristics that underpin the molecular origins of the SHG phenomenon, as we shall now see in §1.3.

---

[1] Cartesian here refers to the Cartesian frame, a geometric co-ordinate system that specifies a unique point within three-dimensional Euclidean space, (x, y, z), with respect to a fixed reference point of origin.

1.3 Dipolar SHG Molecular Chromophores

1.3.1 Molecular Hyperpolarizability Metrics for Dipolar SHG Chromophores

There are numerous *β* metrics that can be utilized to express the first molecular hyperpolarizability of a dipolar SHG chromophore; for the purposes of following discussion two such metrics are used. The first is the static molecular hyperpolarizability, β_0 (*cf.* Eq 1.11), which refers to a frequency-independent *β* value evaluated by determining *β* at a given frequency (eg, from EFISH or HRS measurements) and extrapolating *β* to its zero-frequency value. The determination of a zero-frequency *β* value provides a normalized value of the first molecular hyperpolarizability of the chromophore, independent of the frequency at which the chromophore was excited, from which its static SHG properties can be assessed and compared.

$$\beta_0 = \frac{\beta_{2\omega}}{F(\omega_1 - \omega)} \tag{1.11}$$

where $\beta_{2\omega}$ is the dynamic hyperpolarizability at the second-harmonic frequency,
$F(\omega_1, \omega)$ is a dispersion away from resonance and is defined as:

$$F(\omega_1, \omega) = \frac{{\omega_1}^4}{({\omega_1}^2 - 4\omega^2)({\omega_1}^2 - \omega^2)} \tag{1.12}$$

where ω_1 and ω are the frequencies associated with the charge transfer, and ground state of the molecule, respectively.

The second metric is the intrinsic molecular hyperpolarizability, β_{Int}, developed by Zhou and Kuzyk[26]. This is β_0 normalized to a number of parameters, including the number of electrons in the molecule under study, *c.f.* the relationship:

$$\beta_{int} = \frac{\beta_0}{\beta_0^{max}} \tag{1.13}$$

where β_0 is the static hyperpolarizability, and β_0^{max} is defined as:

$$\beta_0^{max} = \sqrt[4]{3}\left(\frac{e\hbar}{\sqrt{m}}\right)^3 \frac{N^{3/2}}{E_{10}^{7/2}} \tag{1.14}$$

where *e* is the electron charge,
ħ is the reduced Plank's constant,

m is the mass of the electron,
N is the number of π-conjugated electrons in the molecule,
E_{10} is the energy difference between the systems ground state and first excited state.

Where the conjugation pathway of the molecule is broken or disrupted in some way, then each conjugated sub-section of the molecule i must be treated as possessing its own set of π-conjugated electrons N_i. In this instance, Eqs 1.13 and 1.14 still stand for the calculation of β_{Int}, however the number of π-conjugated electrons in the molecule is instead determined by Eq. 1.15:

$$N_i = \left(\sum_i N_i^{3/2}\right)^{2/3} \qquad (1.15)$$

where N_i is the number of π-conjugated electrons in the sub-section i.

This derivation of N should be undertaken with care however, as in the instance where one subunit is significantly larger than another, the value of N is overestimated.

This normalization affords an intrinsic measure of the SHG activity per unit length of a molecule. This is important since large molecules will naturally produce larger SHG responses than smaller ones, and yet they may be less efficient per unit length of the molecule. Systematic molecular design strategies work on the basis of building up a molecule from its constituent parts, or 'molecular lego', where each piece interacts with others so as to maximize the overall SHG activity of the designed molecule. β_{Int} is a valuable diagnostic in this regard, as it permits an assessment of the efficiency of the molecule towards SHG activity, at the individual electron level.

For example, *p*NA, molecule (**2**) in Figure 1.2(a), is an industry standard for SHG activity in organic chromophores. It exhibits a modest β_0, yet substantial β_{Int}, by virtue of its small molecular size yet high SHG response per unit molecular length. This demonstrates that *p*NA is a well designed molecule in terms of having an efficient set of molecular constituents for SHG, which interact well when pieced together, to afford an overall efficient SHG per unit molecular length.

One can compare the β_{Int} of *p*NA with that of MNA, molecule (**5**) in Figure 1.2(a). The presence of its methyl rather than hydrogen substituent in *p*NA more than halves its β_{Int} value. It transpires that the arene ring p-conjugation in MNA has been affected by this methyl substitution in a deleterious fashion towards SHG. Indeed, Oudar and Chemla[27] have shown that the substitution pattern of arene rings has a significant impact on the scale of the molecular SHG response, as will be discussed further in the next section.

1.3.2 Molecular Design of Dipolar Organic Compounds for SHG Applications

Research conducted over the last 50 years has helped to develop well-established structure-property relationships for organic NLO chromophores, which currently form the basis of the molecular design rules that enable the engineering of new NLO materials. What follows is a brief survey of these molecular design rules for SHG, while the reader is directed to a review by Cole[1] for a more comprehensive assessment of the literature on this topic.

Figure 1.2(a) and 1.2(b) presents some typical organic dipolar SHG-active compounds, together with their molecular hyperpolarizability values.

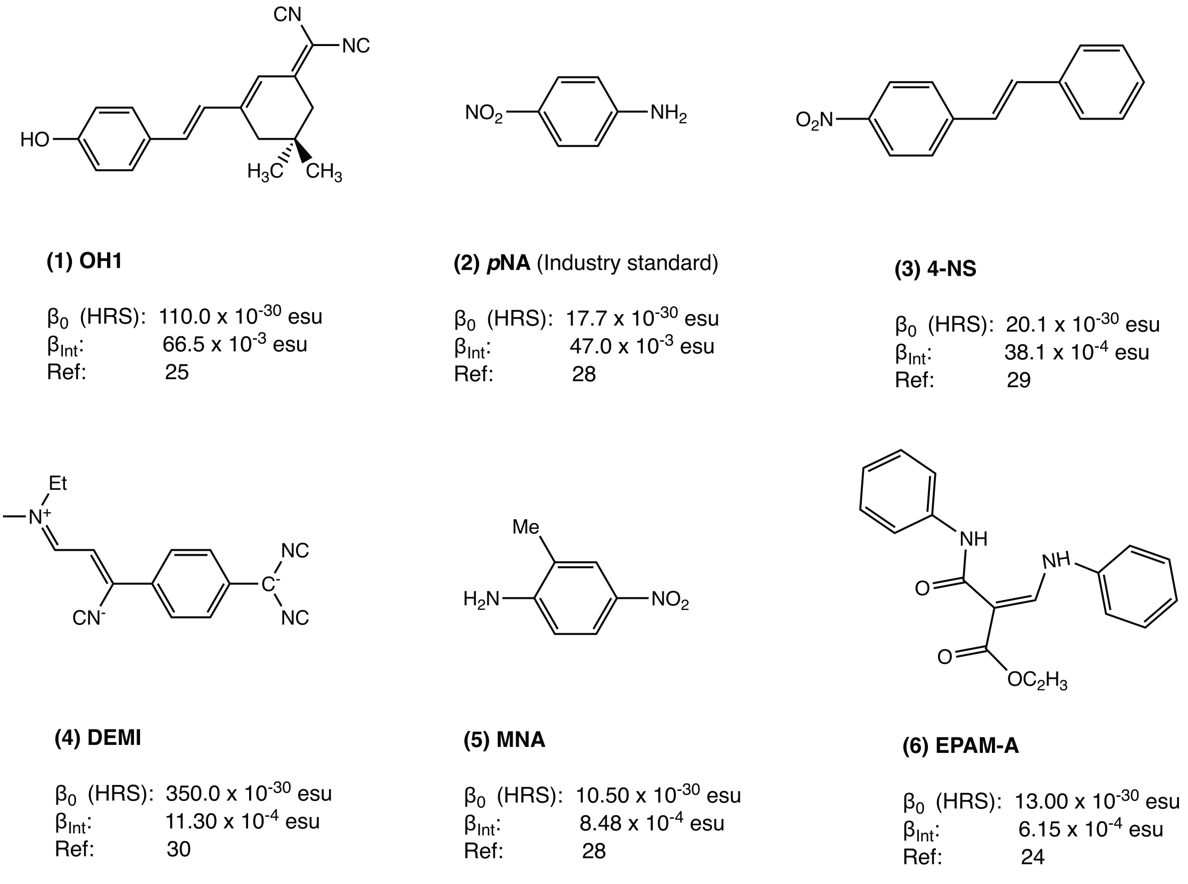

(1) OH1

β_0 (HRS): 110.0 x 10^{-30} esu
β_{Int}: 66.5 x 10^{-3} esu
Ref: 25

(2) *p*NA (Industry standard)

β_0 (HRS): 17.7 x 10^{-30} esu
β_{Int}: 47.0 x 10^{-3} esu
Ref: 28

(3) 4-NS

β_0 (HRS): 20.1 x 10^{-30} esu
β_{Int}: 38.1 x 10^{-4} esu
Ref: 29

(4) DEMI

β_0 (HRS): 350.0 x 10^{-30} esu
β_{Int}: 11.30 x 10^{-4} esu
Ref: 30

(5) MNA

β_0 (HRS): 10.50 x 10^{-30} esu
β_{Int}: 8.48 x 10^{-4} esu
Ref: 28

(6) EPAM-A

β_0 (HRS): 13.00 x 10^{-30} esu
β_{Int}: 6.15 x 10^{-4} esu
Ref: 24

(a)

Figure 1.2(a): A representative sample of previously reported organic chromophores together with their β_0 and β_{Int} values, which were determined by HRS experiments. References: 24, 25, 28–30

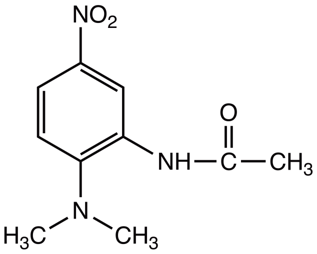

(7) DAN

β_0 (EFISH): 17.00 x 10^{-30} esu
β_{Int}: 8.44 x 10^{-4} esu
Ref: 31

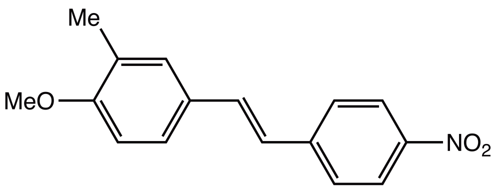

(8) MMONS

β_0 (EFISH): 21.00 x 10^{-30} esu
β_{Int}: 7.61 x 10^{-4} esu
Ref: 32

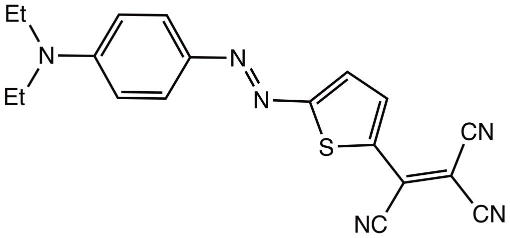

(9) TCDEA

β_0 (EFISH): 321.00 x 10^{-30} esu
β_{Int}: 7.04 x 10^{-4} esu
Ref: 33

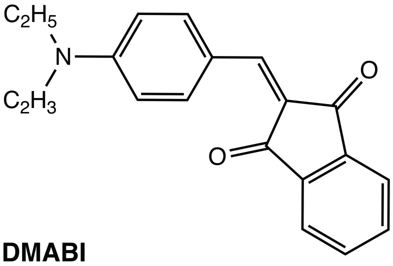

(10) DMABI

β_0 (EFISH): 37.90 x 10^{-30} esu
β_{Int}: 3.94 x 10^{-4} esu
Ref: 33

Figure 1.2(b): A representative sample of previously reported organic chromophores together with their β_0 and β_{Int} values, which were determined by EFISH experiments. References: 31–33

a) Donor-p-acceptor molecular motifs

Oudar[34] and Oudar and Zyss[35] demonstrated that molecules manifesting electron donor-π-acceptor (D-p-A) backbones with high levels of π-conjugation present a key molecular architecture for organic compounds, which exhibit good SHG properties (eg, see Figure 1.3, left). The electron-donating and electron-withdrawing moieties in this molecular motif afford the source and sink of intramolecular charge transfer (ICT), which are connected by a delocalized π–medium to channel the ICT. Additional substituents, R^1 and R^2 in Figure 1.3 (left), can be used to fine-tune the SHG response.

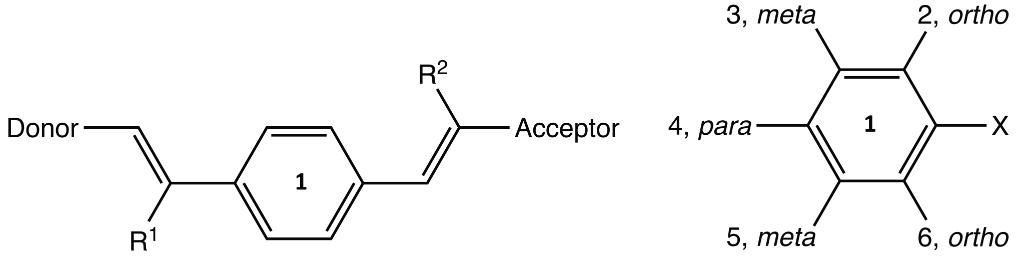

Figure 1.3: (left) Schematic illustration of a traditional donor-π-acceptor molecular motif of an organic compound with additional substituents R^1/R^2 for SHG fine-tuning. (right) Chemical substitution positions available on the central arene ring for the molecular design of organic SHG chromophores.

b) Bond-Length Alternation (BLA)

Marder *et al.*[36,37] established a link between the molecular hyperpolarizability, β, and the bond-length alternation (BLA) in organic SHG compounds. BLA is defined as the average of the difference in length between adjacent C–C bonds in a conjugated chain; in the context of D-p-A organic chromophores, it is a measure of the level of delocalization in the π-bridge between the donor and acceptor. Marder *et al.* showed that β increases with decreasing BLA values, ie, the more delocalized the p-medium of a molecule with a D-p-A motif, the higher its β value, all other things being equal. The attractiveness of BLA as a diagnostic for SHG potential in organic molecules is its simplicity in determination, given it derives from bond lengths that can be easily determined via *ab initio* electronic structure calculations, or via the crystal structure of an organic compound obtained using diffraction techniques. BLA values derived from crystallography data, where available, are generally regarded as superior to calculated values, given that a crystal structure provides solid-state bond-lengths, this phase being perhaps more device relevant, and affects experimental errors to quantify their level of accuracy. It is worth noting, however, that while BLA tends towards zero for a high prospective β value, the optimum β value never corresponds to a zero BLA value owing to Peierls' distortion[2]. Moreover, the introduction of certain molecular fragments, such as aromatic rings, can disrupt the local p-delocalization within a certain part of a D-p-A molecular motif and yet still have a beneficial effect on SHG, as described in the next section.

c) Inclusion of Aromatic Groups

The inclusion of aromatic rings within the π-conjugated pathway of an organic D-p-A compound is generally considered to improve its SHG prospects. This is despite the fact that arene rings have their own well-defined delocalization energy and this tends to have a slightly disruptive local effect on the p-conjugation path that immediately passes through it[38,39].

---

[2] Peierls' distortion, also known as Peierls' transition, is a distortion of the periodic crystal lattice that occurs because atom positions in the lattice oscillate such that its perfect order is broken.

Nonetheless, the presence of an aromatic ring has been shown to stabilize the p-medium in organic D-p-A compound while providing a ready availability of p-p* electronic transitions[32] which are often responsible for the SHG effect used in an application.

d) Aromatic Substitution Position Effects

The substitution sites that are used to embed aromatic rings within a p-conjugated medium of a D-p-A compound have an important bearing on the SHG effect. A well-documented example of the effects that different aromatic substitution patterns have on an SHG-active organic molecule concerns the chemical family of nitroanilines (NAs). Oudar and Chemla[27] correlated the different aromatic substitution patterns of *ortho-, meta-*, and *para*-nitroaniline with their SHG response. Substantial differences in β were found for *ortho-, meta-*, and *para*-substitution (Fig 1.3, (right)). Since this report, others have investigated this series of nitroanilines using HRS experiments[28,29] and have observed this same trend: a nearly 715% reduction in β_0 is observed when shifting from *p*-nitroaniline (**11**) to *m*-nitroaniline (**13**) (Fig. 1.4).

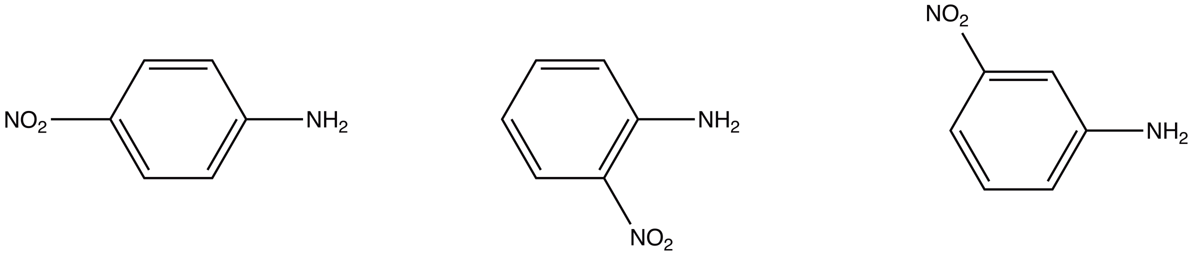

(11) *p*NA (Industry standard)

β_0 (HRS): 10.60×10^{-30} esu
β_{Int}: 31.60×10^{-3} esu

(12) *o*NA

β_0 (HRS): 2.59×10^{-30} esu
β_{Int}: 6.62×10^{-3} esu

(13) *m*NA

β_0 (HRS): 1.30×10^{-30} esu
β_{Int}: 2.59×10^{-3} esu

Figure 1.4: Molecular structures of *ortho-, meta-*, and *para*-nitroaniline and the substantially different hyperpolarizability values measured using the HRS method in a 1-dioxane solvent solution. Reference: 28

e) Aromatic Substitution Type Effects

The nature of the chemical substituents on an aromatic ring, more generally, will affect the SHG activity of the organic material, and will depend on whether the functionalizing group is an electron donating, or an electron accepting (withdrawing); this in turn will influence the format of the molecule's D-π-A framework. Furthermore, the extent to which a substituent donates or accepts (withdraws) electronic charge from the aromatic ring to which it is bonded varies, and can be classified broadly into strong, moderate and weak in strength. Table 1.1 below outlines a non-exhaustive selection of common substituents and their respective classification.

Electron Donor / Acceptor	Effect Strength	Substituent
Donor	Strong	Amino groups, -NH_2, -NR_2
		Hydroxy groups, -OH
	Moderate	Esters, -OCOR
	Weak	Phenyl groups, -C_6H_5
		Alkyl groups, eg, -CH_3
Acceptor	Strong	Nitro groups, eg, -NO_2
		Sulfonic groups, -SO_2R
	Moderate	Carboxyl groups, -CO_2R
	Weak	Nitroso groups, -N=O
		Halo groups, - Cl, Br, I

Table 1.1: A non-exhaustive selection of arene substitution groups and their respective electron donating / withdrawing characteristic and strength

f) Effects of p-Conjugation Length

The extension of the delocalized p-conjugation pathway between the donor and acceptor of an organic compound is known to be capable of increasing the hyperpolarizability of the compound; although, this rule is not applicable in all instances as was investigated by Cheng *et al.*[38]. Through their study on oligomeric polyphenyl and α,ω-diphenylpolyyne derivatives, Cheng *et al.* demonstrated that β and p-conjugation length are correlated by a power law such that:

$$\beta \propto L^{\eta} \qquad (1.16)$$

where L is the conjugation length,

η is an exponent whose value is dependent on a variety of factors such as the number of orbitals involved in the p-conjugation, and the effects emanating from third order hyperpolarizability (Y_{ijkl}) components.

g) Effects of the oscillation strength of SHG-relevant electronic transitions

Assuming a two-level model for SHG applications[40], the oscillation strength describes the probability of electronic excitations between the highest-occupied molecular orbital (HOMO) and lowest unoccupied molecular orbital (LUMO). To this end, Oudar and Chemla[27] demonstrated that there exists a relationship between molecular hyperpolarizability and the oscillation strength of the electronic transition that is responsible for the SHG effect, whereby:

$$\beta_{et} = \frac{3e^2\hbar^2}{2m}\frac{W}{(W^2-(2\hbar\omega)^2)(W^2-(\hbar\omega)^2)} f\Delta\mu_{eg} \qquad (1.17)$$

where β_{et} is the molecular hyperpolarizability arising from the D-p-A charge transfer,
e is the electronic charge,
m is the mass of an electron,
$\hbar\omega$ is the energy of the photon absorbed by the molecule for excitation,
W is the energy of the UV/vis absorption band owing to the electronic transition that is associated with the intramolecular charge transfer (and thus, the SHG effect),
f is the oscillation strength,
$\Delta\mu_{eg}$ is the dipole transition, defined as the change in the dipole moment of the molecule between its excited and ground state, ie, $\Delta\mu_{eg} = \mu_e - \mu_g$.

Hence, molecular hyperpolarizability (and thus ICT) is linearly proportional to the oscillator strength of an SHG-relevant electronic transition.

h) The dipole transition of the molecule

Equation 1.17 also shows that β_{et} is directly proportional to the dipole transition. The dipole transition is the change in the dipole moment of the molecule between its excited and ground state, and occurs during an NLO electronic transition, as outlined in *g)* above, and is dependent on interactions between the molecule's electron donor and acceptor. This stands to reason since the SHG phenomenon is actualized through ICT upon absorption of light. Given this direct bearing on ICT, it follows that the molecular design of SHG-active organic materials should involve the tailoring of electron donor and acceptor groups in a way that maximizes the dipole transition.

i) Thermal stability

One practical shortcoming of organic chromophores is their relatively low thermal stability, which hampers their applications in regimes where they heat up, eg, sustained laser irradiation on an SHG material. This limitation can be deterred through the incorporation of aromatic rings into the SHG chromophore. However, the resultant improved thermal stability comes at the expense of diminishing ICT, which in turn depletes the SHG response. This so-called 'thermal-stability trade off' problem has been well documented. However, the development of new organometallic structures, where the metal species acts as a thermal stabilizer for its organic components, is becoming increasingly popular for overcoming this problem *cf*. Long[4].

j) Concluding Assessment

Over the last 50 years, the understanding of the structure-property relationships for organic SHG compounds has greatly improved. These relationships provide the necessary knowledge to design bespoke molecular chromophores, which can be fine-tuned to provide the desired level of SHG response. In summary, the following molecular design features should be considered, and, where possible implemented for the molecular engineering of SHG-active materials:

- A donor-π-acceptor backbone
- Maximization of electron delocalization in the π-bridge between the donor and acceptor.
- Maximization of the π-conjugation length of the molecule.
- Maximization of the dipole transition of the molecule.
- Maximization of the oscillation strength of the molecule.
- The presence of aromatic rings to ensure thermal stability.
- The selection of *para*- or *ortho*-substitution over *meta*-substitution patterns.

So far, much work has been carried out in an attempt to design and synthesize structures that meet these criteria. As highlighted in *i)*, one potential solution to this problem consists of the incorporation of metal species in organic structures to form organometallic complexes. This is because such materials usually exhibit at least a similar level of molecular hyperpolarizability, while affording much higher melting points, and thus greater thermal stability than their organic counterparts.

Organometallic complexes have a further practical advantage over organic compounds in that they offer much greater versatility in molecular design given the mix of ligands and metals in their structural construct. Therein, the nature of the SHG-active ligand, that bears a D-p-A ICT motif, can be tuned just like an organic molecule as has been discussed in this section. The surrounding ligands can also be engineered such that they cooperate with the SHG-active ligand in a way that augments its D-p-A ICT strength. The manifold selection choices for the metal species afford further versatility in molecular design. There are a wide range of stable organometallic complexes that host a diverse set of transition metals, whose electronic configurations have varying levels of d-orbital availability and a multitude of possible oxidation states; thus, the metal offers a variety of coordination geometries and ICT contributions for the molecular engineering of SHG-active organometallic complexes. The next section discusses this in further detail.

1.4 Dipolar Organometallic SHG Molecular Chromophores

The development of systematic design rules for organic SHG chromophores, as highlighted in §1.3, are now well known and provide the ability to build bespoke molecules for specific SHG applications. However, as the demand for both greater SHG responses and greater molecular design flexibility increases, coupled with the need to ameliorate thermal stability restrictions, the design of new organometallic SHG complexes is becoming more prevalent. Since the 1980s, many studies of dipolar organometallic complexes and their NLO activity have been undertaken, with ruthenium- and iron-based complexes being the most investigated thus far. Extensive reviews on such complexes and their second- and third-order NLO responses have been presented by Long[4] and Nalwa[41], with a more recent review of the second-order NLO responses of co-ordination metal complexes presented by Lacroix *et al.*[42]

Despite the extensive nature of such reviews, they provide more of a catalogue of compounds, sectioned by a chemical means such as the metal element or group, rather than an ordering according to their SHG structure-property relationships. A classification scheme which helped identify the D-p-A motif within a given organometallic complex that is responsible for its SHG effect, and rationalized the presentation of organometallic complexes accordingly, would help forge better molecular design rules for SHG-active organometallic complexes. Such classification is not trivial, however, as the literature evidences via its detailed discussions that lead to the identification of the D-p-A unit for each complex determined. The complicated nature of this classification process is a consequence of the presence of multiple competing ligands, and the implications of metal atom characteristics: from considering ligand- and crystal-field theory to help identify whether the metal participates in Metal-to-Ligand or Ligand-to-Metal charge transfer (MLCT/LMCT), to determining resonance structures, relative electron donor and acceptor strengths, metal oxidation states, the extent of metal coordination (saturation level), and the SHG-relevant D-π-A component in the complex if there are multiple options. Nevertheless, a generic classification scheme that characterizes the molecular origins of SHG in organometallic complexes has recently been formulated by Cole & Ashcroft (2018)[43]. This scheme offers a simple workflow to navigate through the SHG-relevant molecular design rules for organometallic complexes (Fig 1.5), from which the D-p-A structural motifs, which pertain to the SHG-relevant ICT phenomena, can be identified. Having pinpointed the main structural origins of this NLO activity within a complex, a supplementary process is performed to assess the augmenting or deleterious effects of the ligands that surround the metal, which will inevitably be part of the D-p-A constituent and will thus be naturally influenced by the ICT characteristics of its coordination environment.

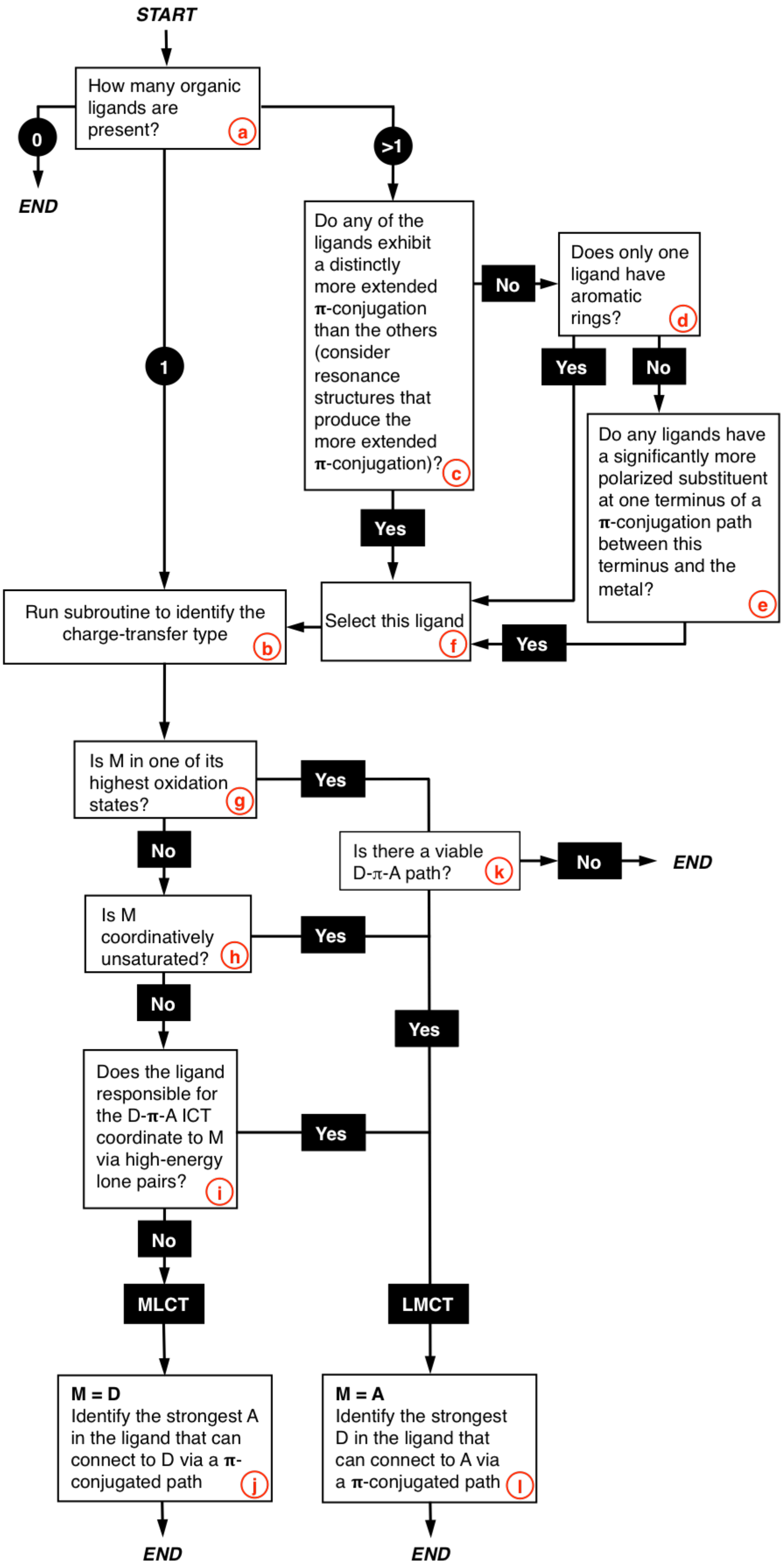

Figure 1.5: Workflow for the classification of the origins of dipolar SHG activity in organometallic complexes. MLCT = Metal-to-Ligand Charge Transfer, LMCT = Ligand-to-Metal Charge Transfer. Reference: 43

1.4.1 Application of the new classification workflow

An example application of this classification workflow is demonstrated herein for a series of four $Ru(II)(NH_3)_4X,Y$ complexes investigated by Coe *et al.*[44] These four SHG chromophores (**14**-**17** in Fig. 1.6) consist of a Ru(II) metal centre with ammine ligands in the equatorial plane and two axial ligands which vary in their molecular design and p-conjugation length, where X = NH_3 (**14**, **15**) or X = 1-methylimidazole (**16**, **17**); Y = 1′-methyl-2-2′-bipyridinium (**14**, **16**) or Y = 1′-phenyl-2-2′-bipyridinium (**15**, **17**).

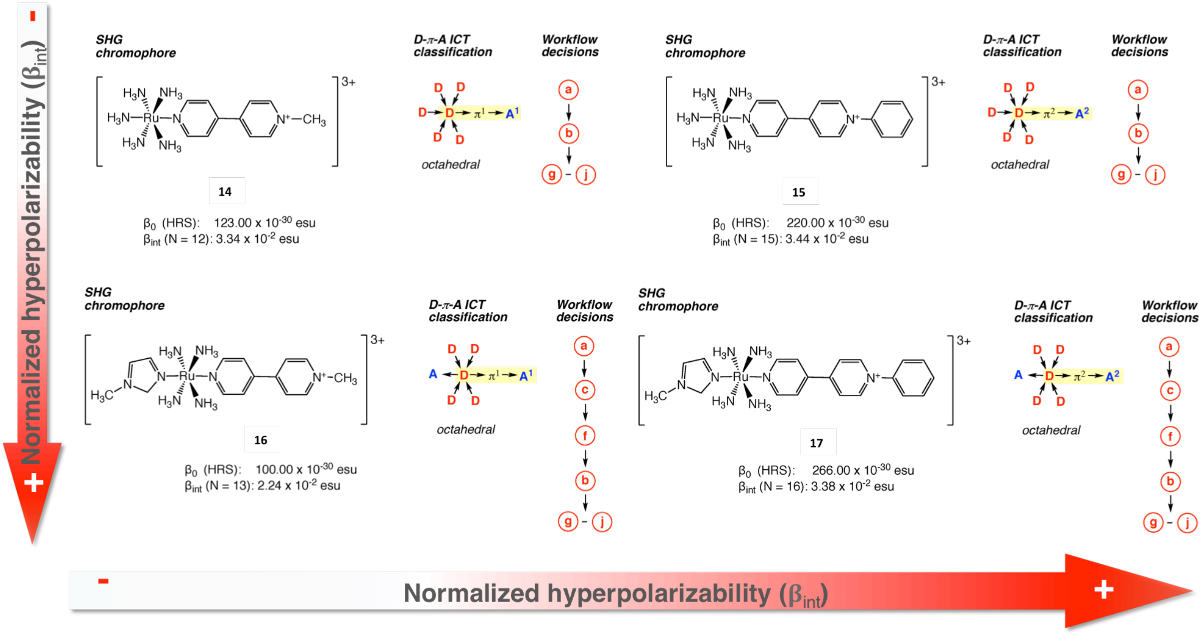

Figure 1.6: Four $Ru(II)(NH)_X$-4,4'-bipyridine complexes with their respective β_0 and β_{Int} values. Reference: 43, 44

Consider first the pair of complexes, **14** and **15**, which have X = NH_3 in common, but differ in Y which is either the π-conjugated organic ligand, 1′-methyl-2-2′-bipyridinium (**14**) or 1′-phenyl-2-2′-bipyridinium (**15**). By applying the workflow (*cf* Fig 1.6) to each complex, the π-conjugated organic ligand is instantly identified, by workflow decision (a), as the SHG-relevant D-p-A ICT motif since it is the only organic ligand present. It then falls to a subroutine, beginning in workflow decision (b), to determine if the directionality of ICT is metal-to-ligand or ligand-to-metal in nature. Given that ruthenium is in its low-spin 2^+ oxidation state, it is coordinatively saturated in this complex, and the D-p-A motif does not involve metal-ligand coordination via high-energy lone pairs, the workflow decision-making steps (g)-(j) determine that the metal must act as the electron donor of the framework, with the terminal *N*-methyl (**14**) and *N*-phenyl (**15**) thus performing the role of electron acceptor, i.e. the D-p-A motif employs metal-to-ligand charge transfer (MLCT).

Having used this workflow to identify the D-π-A fragment of the complex that is responsible for its SHG activity, and the directionality of the ICT therein, the secondary charge-transfer effects of its surrounding ligands are considered. Using the auxiliary chart in Figure 1.7, the NH_3 ligands in **14** and **15** are classified as donors, and so 'push' electrons to ruthenium and thus augment the donating capabilities of the metal. This will naturally improve the inherent strength of ICT across the D-p-A motif, and thus enhance the SHG response of the complex. The SHG response for **14** and **15** will be similarly affected by the surrounding ligands since they are the same in both complexes.

Indeed, **14** and **15** only differ by the nature of their organic ligand, which is naturally part of the D-p-A motif. So the differences in SHG response between **14** and **15** are a result of the different nature of the acceptor group in the organic ligand: the N atom of the pyridyl ring possesses a positive charge, so it will be stabilized to a greater extent by a phenyl ring (**15**) than a methyl group (**14**); consequently, the 'push-pull' ICT effects will be more pronounced in **15** than in **14**, resulting in **15** exhibiting a larger SHG response as observed by the increase in both β_0 and β_{int}.

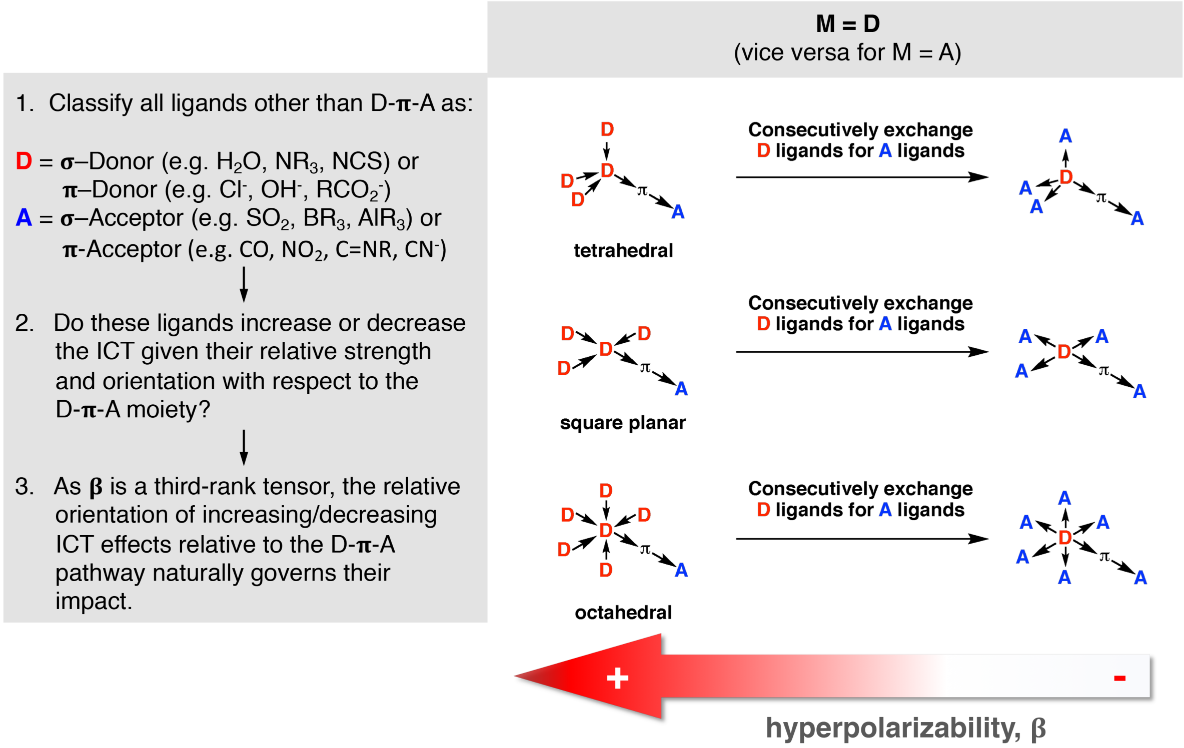

1. Classify all ligands other than D-**π**-A as:

D = **σ**–Donor (e.g. H_2O, NR_3, NCS) or **π**–Donor (e.g. Cl^-, OH^-, RCO_2^-)
A = **σ**–Acceptor (e.g. SO_2, BR_3, AlR_3) or **π**-Acceptor (e.g. CO, NO_2, C=NR, CN^-)

2. Do these ligands increase or decrease the ICT given their relative strength and orientation with respect to the D-**π**-A moiety?

3. As **β** is a third-rank tensor, the relative orientation of increasing/decreasing ICT effects relative to the D-**π**-A pathway naturally governs their impact.

Figure 1.7: Assessing competing constituent factors that contribute to the ICT in the D-π-A motif that is responsible for the second-order NLO response.

Turning to complexes **16** and **17,** they once again consist of a Ru(II) metal centre, but unlike **14** and **15**, the metal coordinates to only four NH_3 ligands, while the other two ligands comprise different π-conjugated organic moieties, 1-methylimidazole (**16**-**17**) and, 1'-methyl-2-2'-bipyridinium (**16**), 1'-phenyl-2-2'-bipyridinium (**17**). As with **14** and **15**, the ligand that represents the SHG-relevant D-π-A motif for these complexes is the 2-2'-bipyridinium moiety. The workflow requires a few more steps to make this decision compared to the case of **14** and **15**, as shown in the decision trees of Fig. 1.6.

This is because **16** and **17** have two organic ligands to choose from, in terms of identifying, which one participates in the SHG-relevant D-p-A ICT motif. In this case, the greater extent of p-conjugation in the 2-2′-bipyridinium moiety dictates its selection in workflow decision (c) as being the organic constituent of this D-p-A motif. For similar reasons to those discussed for **14** and **15**, its ICT directionality is determined to be MLCT in nature.

Regarding their D-p-A ICT strength, **16** and **17** possess one less (four) NH_3 ligand than **14** and **15**, and so there is less augmentation of the electron donating capabilities of the Ru(II) metal in **16** and **17** from these types of ligands. Regarding the organic ligand that is not involved in the D-p-A motif, the process shown in Figure 1.7 classifies the 1-methylimidazole ligand as an acceptor. It will thus have a deleterious effect upon the SHG response in **16** and **17**, especially since it is diametrically opposed to the D-p-A unit geometrically and, as such, the two organic ligands will generate an electronic ‘pull’ directly against each other; this direct competition will naturally diminish the overall ‘push-pull’ induced ICT, and SHG response. This SHG diminution is clearly observed by comparing β_{Int} of **14** and **16** versus **15** and **17**. Considering the relative SHG-response of **16** and **17**, the same argument presented for comparing **14** and **15** prevails, ie, the β_{Int} value of **17** is naturally larger than that of **16** owing to the greater acceptor strength of the methyl (**16**) and phenyl groups (**17**).

This classification workflow can, in principle, be applied to all known SHG-active organometallic complexes. Moreover, its decision-tree logic makes it attractive for encoding into an algorithm, by which D-p-A ICT motifs in SHG-active dipolar organometallic complexes could become identified automatically. This would stand to benefit the emerging materials-by-design strategies to predict new SHG materials. This workflow is nonetheless specific to dipolar SHG effects in organometallic complexes; it does not translate to octupolar SHG-active media that will be described in the next section.

1.5 Octupolar SHG Chromophores

1.5.1 From Dipolar to Octupolar Materials

Until the early 1990s, almost all work on the molecular design of organic and organometallic materials for SHG applications was conducted on dipolar SHG effects in materials. Despite the fact that the nonlinear responses of octupolar structures have revealed that they have good potential, octupolar compounds remain underrepresented in the literature. The initial work of Zyss and co-workers[45,46] subdivided octupolar materials into two classes: i) materials that exhibit a dipolar and an octupolar contribution, and ii) materials that exhibit solely an octupolar contribution. Zyss and Ledoux[46] showed that the third-rank tensor of a material, which describes the first molecular hyperpolarizability, could only have two components of order 1 and 3, such that the irreducible components can be written as:

$$\beta = \beta_{J=1} \oplus \beta_{J=3} \qquad (1.18)$$

Consequently, even in the absence of a dipolar contribution ($\beta_{J=1}$), a material may not have an overall β value of zero, if its molecular symmetry permits an octupolar contribution ($\beta_{J=3}$).

In principle, structures that have both dipolar and octupolar components may exhibit an augmented nonlinear response. Yet, in practice, the dipolar or octupolar SHG effects of a material have contrasting molecular symmetry requirements, and this generally results in these two forms of SHG contributions compromising each other in terms of their prospective performance. The non-centrosymmetry requirements of the dipolar component of SHG effects have already been discussed (*cf.* §1.1.2.2).

Given the three-fold symmetry of an octupolar moment, octupolar SHG activity is naturally restricted to materials whose molecular structures feature three-fold molecular symmetry, as classified by the point groups illustrated in Fig 1.8. Such structures can be formed from a cubic structure (the octupole shown in Fig 1.8) via two different methods: i) projections of the cubic structure along a C_3 axis, which gives rise to D_{3h} and thence D_3 symmetry, or ii) fusion of charge in the centre of the cubic structure giving rise to T_d, or D_{2d} symmetry. Octupolar SHG-active molecules can therefore be either 2- or 3-dimensional in their structural form.

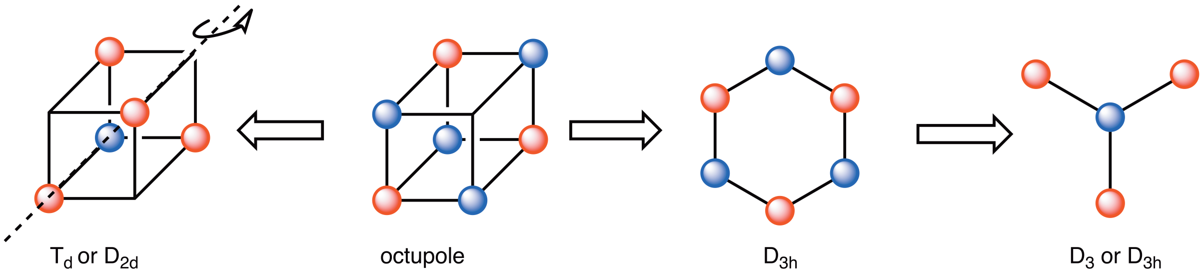

Figure 1.8: A depiction of the symmetry options for purely octupolar structures.

2-D octupolar SHG-active molecules are the most studied to date, especially within the field of organic compounds. To this end, substantial efforts have been devoted to remove the typically compromising dipolar component of β for prospective second-order NLO materials, thus inducing a purely octupolar SHG response. Efficient SHG from a material with a vanishing dipole moment was first shown by Zyss *et al.*[47]. While the lack of a dipole in a molecular structure is not essential to achieve large first molecular hyperpolarizability, it is considered preferable. We now highlight a range of octupolar compounds, the vast majority of which are 2-D and organic in form, as per the current literature representation.

1.5.2 Examples of Octupolar Molecules

1.5.2.1 Historical Introduction

One of the earliest demonstrations of an octupolar molecule exhibiting SHG effects was performed on the material triaminotrinitrobenzene, TATB (**18**) using powder SHG experiments[48]. This study was shortly followed up by a complementary computational study of TATB by Bredas *et al.*[49]

TATB consists of an arene ring that is substituted with NH_2 groups in the 1-, 3-, and 5-positions, and NO_2 groups in the 2-, 4-, and 6-positions (Fig. 1.9). This alternating donor-acceptor substitution pattern around a π-conjugated (planar) phenyl ring that exhibits six-fold symmetry presents a molecule with D_{3h} point group symmetry. Even though TATB does not exhibit a dipole moment, owing to the cancelling effects of the three opposing NH_2-p_{ring}-NO_2 dipoles on symmetry grounds, it still exhibits a significant β value on account of an octupolar contribution. Indeed, the computationally derived β value of TATB is by a factor of 1.60 higher than that of the industry standard dipolar SHG material, *p*NA (~ 60% increase).

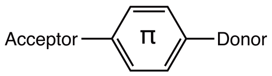

Dipolar contributions

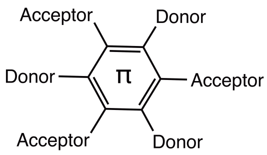

Octupolar contributions

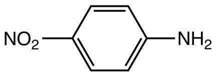

***p*NA** (Industry standard)

β_0 (DFT): 9.97 x 10^{-30} esu
Ref: Bredas *et al* (1992)

β_{zzz} (HRS): 16.9 x 10^{-30} esu
Ref: Verbiest *et al* (1994)

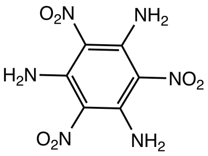

(18) TATB

β_0 (DFT): 16.02 x 10^{-30} esu
Ref: Bredas *et al* (1992)

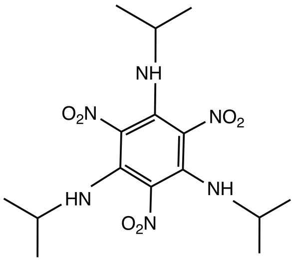

(19) TIATB

β_{zzz} (HRS): 16.00 x 10^{-30} esu
Ref: Verbiest *et al* (1994)

Figure 1.9: (top) A comparison of the NLO response of the organic dipolar industry standard *p*NA with that of the organic octupolar TATB. These β values were as determined by *ab initio* DFT calculations at the CHPF/3-21G level of theory[49]. (bottom) TAITB compound investigated using HRS techniques by Verbiest *et al.*[50]

Due to the volatility of TATB and its solubility in organic solvents, HRS measurements of its hyperpolarizability have not been pursued. However, Verbiest *et al.*[50], investigated a slightly modified form of TATB, triisopropylaminotrinitrobenzene, TIATB (**19**). TIATB has D_{3h} octupolar symmetry and has four nonzero β tensorial components, all equal to the β_{ZZZ} component. Verbiest *et al.* undertook HRS measurements to investigate its octupolar behaviour, and noted that a direct comparison of the HRS-derived β_{ZZZ} values of TIATB and *p*NA are difficult given the large solvent-dependence associated with the *p*NA measurements. However, as dipole interactions between *p*NA and the solvent are lowest for *p*-dioxane, comparison of this value with TIATB was undertaken. Here, Verbiest *et al.* show that the hyperpolarizability value of TIATB is almost equal to that of *p*NA, which, given that *p*NA only has one significant tensorial β component, means that the total β value of TIATB is approximately two times the size of *p*NA.

A year later, Stadler *et al.*[51] reported a study on three similar octupolar (**20, 22, 24**) structures and their cognate dipolar (**21, 23, 25**) methyl-terminated analogues (Fig. 1.10). They determined the dynamic hyperpolarizability, β_{HRS} (ie, frequency-dependent) of these compounds at λ = 1064nm, and were able to compare the dipolar and octupolar SHG responses. $\beta_{1064\text{nm}}$(HRS) for these three octupolar molecules was found to be 2.5 to 4 times higher than those of their dipolar counterparts. They also discovered that the replacement of cyano substituents for aldehyde groups afforded similar HRS results.

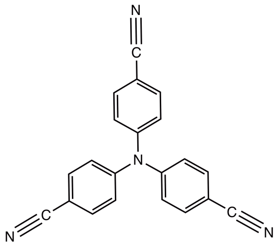

(20) 4,4',4''-nitrilotribenzonitrile
β_{1064nm} (HRS): 48.0 x 10^{-30} esu

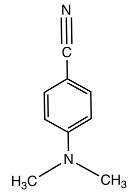

(21) 4-(dimethylamino)benzonitrile
β_{1064nm} (HRS): 12.0 x 10^{-30} esu

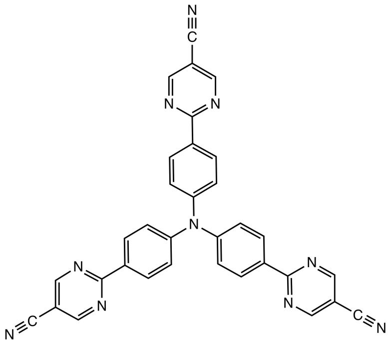

(22) 2,2',2''-(nitrilotris(benzene-4,1-diyl))tris(pyrimidine-5-carbonitrile)
β_{1064nm} (HRS): 97.0 x 10^{-30} esu

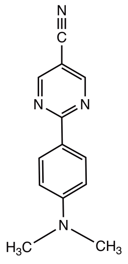

(23) 2-(4-(dimethylamino)phenyl)pyrimidine-5-carbonitrile
β_{1064nm} (HRS): 39.0 x 10^{-30} esu

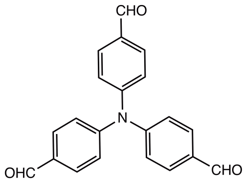

(24) 4,4',4''-nitrilotribenzaldehyde
β_{1064nm} (HRS): 45.0 x 10^{-30} esu

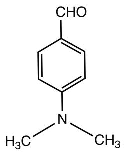

(25) 4-(dimethylamino)benzaldehyde
β_{1064nm} (HRS): 12.0 x 10^{-30} esu

Figure 1.10: A comparison of the molecular hyperpolarizability of a range of cyano, pyrimidine-5-carbonitrile, and aldehyde-substituted octupolar D_{3h} structures investigated by Stadler *et al.*[42]

These seminal studies stimulated substantial interest in octupolar structures, and a variety of studies into the molecular design of two-dimensional octupolar structures with 1, 3, 5-phenyl backbone architectures with either D_3 or D_{3h} symmetry soon followed.

1.5.2.2 Other D_{3h} octupolar molecules

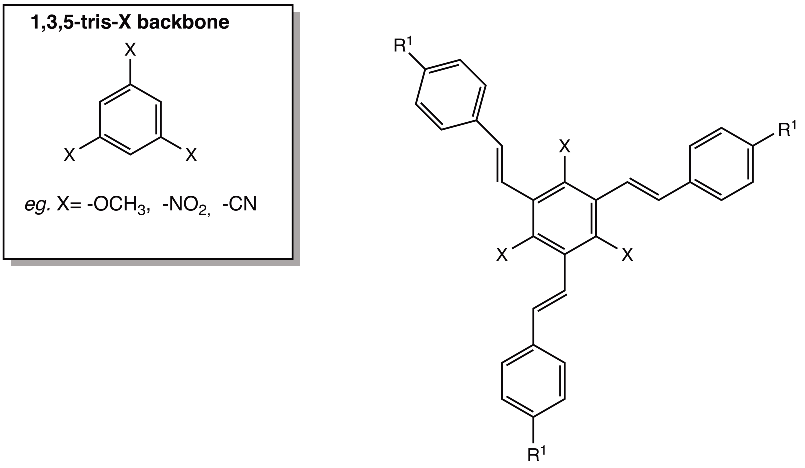

1,3,5-TrisX derivatives

(26)
X = OMe; R^1 = NO_2
β_0 (HRS): 11.0 x 10^{-30} esu

(27)
X = NO_2; R^1 = NEt_2
β_0 (HRS): 63.0 x 10^{-30} esu

(28)
X = CN; R^1 = NEt_2
β_0 (HRS): 65.0 x 10^{-30} esu

Figure 1.11 Three 1,3,5-tris-X-2,4,6-tris-Z-type octupolar structures with methoxy, nitro, and cyano substituents at the 1-, 3-, and 5-positions studied by Cho *et al.*[52,53]

Three of the most extensively investigated 1,3,5-tris-X-2,4,6-tris-Z-type backbones are shown in Fig. 1.11. β_0 for **27** was found to be substantially larger than that of **26**, whereupon the R^1 group in **26** changes from an electron withdrawing (A = NO_2) to donating group (D = NEt_2) in **27**, while X simultaneously changes from an electron donating (D = OMe) to withdrawing group (A = NO_2). This pairwise switch in D, A substitution patterns suggests that X and R^1 need to be of a type, A and D, respectively, to afford a good SHG response. This indication is corroborated by the finding that changing X from NO_2 to CN groups (**27** and **28**) affords comparable β_0 values, ie, changing X for another electron withdrawing group will have little effect on the molecular hyperpolarizability. That said, the UV/vis absorption band of **28** exhibits a significant bathochromic shift ($\Delta\lambda$ = 64 nm) relative to that of **27,** indicating that the energy of the electronic transition associated with the SHG response is affected.

The molecular design of D_{3h} octupolar molecules can also employ heteroatoms to induce the required point-group symmetry. One example is the series of derivatives shown in Fig 1.12 (**29**-**31**), which consist of a boroxine ring[54], in which the oxygen atoms alternate with all boron atoms that are substituted with *para*-substituted phenyl rings, leading to D_{3h} symmetry. **29**-**31** all exhibit good β_0 values, whose magnitude follows the chemical substitution pattern, R^1 = NMe_2 > OMe > SMe_2, which tracks their decreasing electron donating strength, as one would expect.

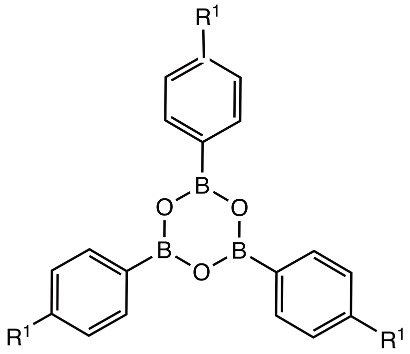

Trioxatriborinane derivatives

(29) R^1= OMe; β_0 (HRS): 35.0 x 10^{-30} esu
(30) R^1= NMe_2; β_0 (HRS): 56.0 x 10^{-30} esu
(31) R^1= SMe; β_0 (HRS): 31.0 x 10^{-30} esu

Figure 1.12 Molecular structures of three boroxine derivatives, revealing the effects of different *para*-substituents on the molecular hyperpolarizability. Reference: 54

1.5.2.3 A D_3 octupolar molecule: Case Study

A study by Zyss *et al.*[55] on the chiral ion, Ruthenium(II)-tris[2,2'-bipyridyl] (RuTB) (**32**), is a classic example of an octupolar molecule with D_3 symmetry. The complexation of three 2,2'-bipyridyl ligands to a central Ru(II) ion results in the formation of a chiral D_3 propeller-type geometry (Fig 1.13). The molecular hyperpolarizability of this compound emanates from metal-to-ligand charge transfer (MLCT) from the donating metal centre to the electron accepting tris[2,2'-bipyridyl] ligands. This study provided the first evidence of substantial β values in trigonal organometallic chiral cations. There was nonetheless contention about the value of β_0 for RuTB. While Zyss *et al.* reported β_0 = (210 ± 60) x 10^{-30} esu, Morrison *et al.*[56] demonstrated that its β_0 value was in fact (25 ± 5) x10^{-30} esu, once the HRS signal had been corrected for multiphoton fluorescence contributions[3]. Despite this initial overestimation of β_0, the corrected value for RuTB continues to point towards the beneficial contribution that octupolar molecules can play in producing large hyperpolarizability responses.

---

[3] Multiphoton fluorescence de-convolution in HRS experiments has since been reported by Olbrechts *et al.*[57] and Wostyn *et al.*[58]

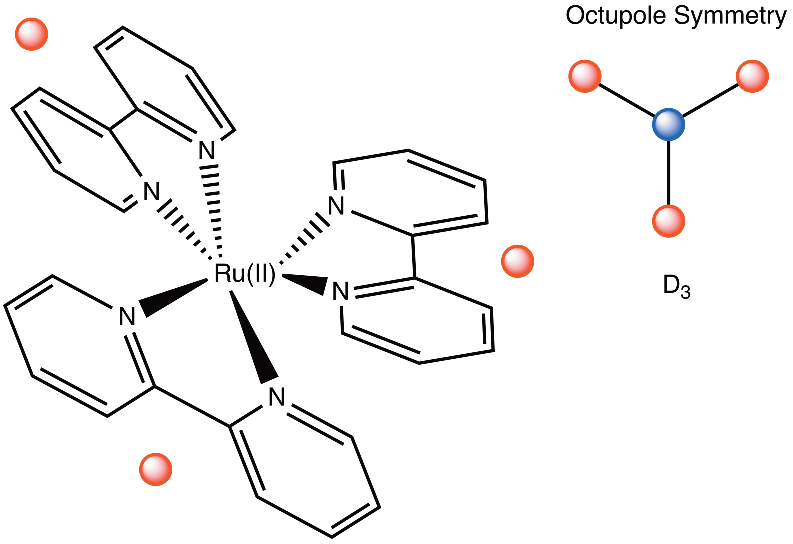

(32) RuTB

β_0 (HRS): $(25.0 \pm 5) \times 10^{-30}$ esu

Ref: 55

Figure 1.13 Molecular structure of RuTB (left) and its octupolar framework (right)

1.5.2.4 A D_{2d} octupolar molecule: Case Study

A metalorganic octupolar molecule with tetrahedral D_{2d} symmetry was reported by Sénéchal *et al.*[59] and consists of the complexation of a Zn(II) central metal ion coordinated to two bipyridyl ligands, wherein the *para-* position of each pyridyl ring is substituted by a p-conjugated chain that is terminated by an electron donating -NBu_2 group (Fig 1.14, **33**).

The very large reported molecular hyperpolarizability of **33** (β_0 = 157 x10^{-30} esu), was justified by considering that the harmonic wavelength (955 nm) in the HRS measurement was sufficiently far from the optical absorption cut-off of the complex that any multiphoton fluorescence contributions could be regarded as negligible. The result was compared against an analogous Cu(I) structure[60] whose molecular hyperpolarizability was reported as being 50% smaller (β_0 = 78 x10^{-30} esu). The superior molecular hyperpolarizability of the subject complex was attributed to the Zn(II) being a better electron acceptor that Cu(I).

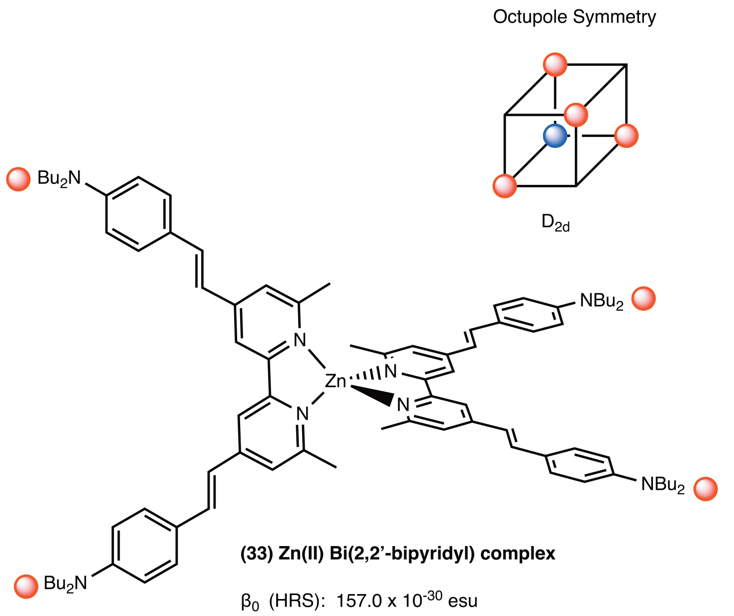

(33) Zn(II) Bi(2,2'-bipyridyl) complex

β_0 (HRS): 157.0 x 10^{-30} esu

Figure 1.14 Molecular structure of Zn(II) D_{2d} structure of Sénéchal *et al.*[59] (left) and its octupolar framework (right).

1.5.2.5 A T_d octupolar molecule: Case Study

The T_d symmetry of octupolar structures is the least studied to date. Such structures possess three-dimensional charge-transfer effects and thus transition moments in all three spatial dimensions. Such structures are also non-polar and hence are primed for the development of non-centrosymmetric SHG materials. A series of organo-tin complexes with T_d symmetry were reported by Lequan *et al.*[61]; the one with the largest molecular hyperpolarizability value (β_0 = 42 x 10^{-30} esu) is shown in Fig 1.15, (**34**). This complex consists of a Sn metal bonded to four (*E*)-*N*,*N*-dibutyl-4-(*p*-tolyldiazenyl)aniline ligands in a tetrahedral arrangement. Each ligand possesses an extended level of π-conjugation, which includes two arene rings.

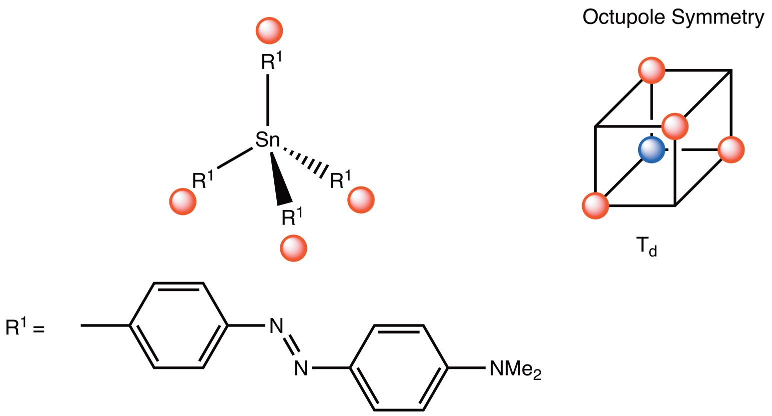

(34) Sn Complex

β_0 (HRS): 47.0 x 10^{-30} esu

Figure 1.15 Molecular structure of Sn T_d structure of Lequan *et al.*[61] (left) and its octupolar framework (right)

1.6 Conclusion

Herein we present studies on a range of new novel organic and organometallic materials that have been predicted to exhibit promising levels of nonlinear optical activity. These materials will be assessed based on their molecular architectures and first order hyperpolarizability, which has been enumerated via a range of experimental and computational methods that extend the three main states of matter; gas, solution, and solid-state. These enumerations thus present a rare example of a multi-phase assessment of material hyperpolarizabilities.

Our selection of materials includes both neutral and ionic species, as well as dipolar and octupolar materials. While, the studies on the organic materials augment pre-existing structure-property relationships, the organometallic complexes studied herein present rare examples of NLO assessments of materials containing heavy elements. These are particularly challenging even for state-of-the-art experimental and computational materials characterisation methods

1.7 References

(1) Cole, J. M. Organic Materials for Second-Harmonic Generation: Advances in Relating Structure to Function. *Philos. Trans. R. Soc. Lond. Ser. Math. Phys. Eng. Sci.* **2003**, *361* (1813), 2751–2770.

(2) Franken, P. A.; Hill, A. E.; Peters, C. W.; Weinreich, G. Generation of Optical Harmonics. *Phys. Rev. Lett.* **1961**, *7* (4), 118–119.

(3) Zyss, J.; Berthier, G. Nonlinear Optical Properties of Organic Crystals with Hydrogen-bonded Molecular Units: The Case of Urea. *J. Chem. Phys.* **1982**, *77* (7), 3635–3653.

(4) Long, N. J. Organometallic Compounds for Nonlinear Optics—The Search for En-Light-Enment! *Angew. Chem. Int. Ed. Engl.* **1995**, *34* (1), 21–38.

(5) *Characterization Techniques and Tabulations for Organic Nonlinear Optical Materials*; Kuzyk, M. G., Dirk, C. W., Eds.; Optical engineering; Marcel Dekker: New York, 1998.

(6) Levine, B. F.; Bethea, C. G. Second and Third Order Hyperpolarizabilities of Organic Molecules. *J. Chem. Phys.* **1975**, *63* (6), 2666–2682.

(7) Clays, K.; Persoons, A. Hyper-Rayleigh Scattering in Solution. *Phys. Rev. Lett.* **1991**, *66* (23), 2980–2983. https://doi.org/10.1103/PhysRevLett.66.2980.

(8) Hohenberg, P.; Kohn, W. Inhomogeneous Electron Gas. *Phys. Rev.* **1964**, *136* (3B), B864–B871. https://doi.org/10.1103/PhysRev.136.B864.

(9) Kohn, W.; Sham, L. J. Self-Consistent Equations Including Exchange and Correlation Effects. *Phys. Rev.* **1965**, *140* (4A), A1133–A1138.

(10) Ward, J. F. Calculation of Nonlinear Optical Susceptibilities Using Diagrammatic Perturbation Theory. *Rev. Mod. Phys.* **1965**, *37* (1), 1–18.

(11) Orr, B. J.; Ward, J. F. Perturbation Theory of the Non-Linear Optical Polarization of an Isolated System. *Mol. Phys.* **1971**, *20* (3), 513–526.

(12) Kuzyk, M. G. Compact Sum-over-States Expression without Dipolar Terms for Calculating Nonlinear Susceptibilities. *Phys. Rev. A* **2005**, *72* (5), 053819.

(13) Zyss, J.; Brasselet, S.; Thalladi, V. R.; Desiraju, G. R. Octupolar versus Dipolar Crystalline Structures for Nonlinear Optics: A Dual Crystal and Propagative Engineering Approach. *J. Chem. Phys.* **1998**, *109* (2), 658–669.

(14) Champagne, B.; Kirtman, B. Evaluation of Alternative Sum-over-States Expressions for the First Hyperpolarizability of Push-Pull π-Conjugated Systems. *J. Chem. Phys.* **2006**, *125* (2), 024101.

(15) Woińska, M.; Jayatilaka, D.; Dittrich, B.; Flaig, R.; Luger, P.; Woźniak, K.; Dominiak, P. M.; Grabowsky, S. Validation of X-Ray Wavefunction Refinement. *ChemPhysChem* **2017**, *18* (23), 3334–3351.

(16) Cole, J. M.; D. D Hickstein. Molecular Origins of Nonlinear Optical Activity in Zinc Tris(Thiourea)Sulfate Revealed by High-Resolution x-Ray Diffraction Data and Ab Initio Calculations. *Phys. Rev. B* **2013**, *88* (18), 184105.

(17) Hickstein, D. D.; Cole, J. M.; Turner, M. J.; Jayatilaka, D. Modeling Electron Density Distributions from X-Ray Diffraction to Derive Optical Properties: Constrained Wavefunction versus Multipole Refinement. *J. Chem. Phys.* **2013**, *139* (6), 064108.

(18) Capelli, S. C.; Bürgi, H.-B.; Dittrich, B.; Grabowsky, S.; Jayatilaka, D. Hirshfeld Atom Refinement. *IUCrJ* **2014**, *1* (5), 361–379. https://doi.org/10.1107/S2052252514014845.

(19) Jayatilaka, D. Wave Function for Beryllium from X-Ray Diffraction Data. *Phys. Rev. Lett.* **1998**, *80* (4), 798–801.

(20) Jayatilaka, D.; Grimwood, D. J. Wavefunctions Derived from Experiment. I. Motivation and Theory. *Acta Crystallogr. A* **2001**, *57* (1), 76–86.

(21) Jayatilaka, D.; Munshi, P.; J. Turner, M.; K. Howard, J. A.; A. Spackman, M. Refractive Indices for Molecular Crystals from the Response of X-Ray Constrained Hartree–Fock Wavefunctions. *Phys. Chem. Chem. Phys.* **2009**, *11* (33), 7209–7218.

(22) Higginbotham, A. P.; Cole, J. M.; Blood-Forsythe, M. A.; Hickstein, D. D. Identifying and Evaluating Organic Nonlinear Optical Materials via Molecular Moments. *J. Appl. Phys.* **2012**, *111* (3), 033512.

(23) Robinson, F. N. H. Nonlinear Optical Coefficients. *Bell Syst. Tech. J.* **1967**, *46* (5), 913–956.

(24) Cole, J. M.; Lin, T.-C.; Ashcroft, C. M.; Perez-Moreno, J.; Tan, Y.; Venkatesan, P.; Higginbotham, A. P.; Pattison, P.; Edwards, A. J.; Piltz, R. O.; et al. Relating the Structure of Geminal Amido Esters to Their Molecular Hyperpolarizability. *J. Phys. Chem. C* **2016**, *120* (51), 29439–29448.

(25) Lin, T.-C.; Cole, J. M.; Higginbotham, A. P.; Edwards, A. J.; Piltz, R. O.; Pérez-Moreno, J.; Seo, J.-Y.; Lee, S.-C.; Clays, K.; Kwon, O.-P. Molecular Origins of the High-Performance Nonlinear Optical Susceptibility in a Phenolic Polyene Chromophore: Electron Density Distributions, Hydrogen Bonding, and Ab Initio Calculations. *J. Phys. Chem. C* **2013**, *117* (18), 9416–9430.

(26) Zhou, J.; Kuzyk, M. G. Intrinsic Hyperpolarizabilities as a Figure of Merit for Electro-Optic Molecules. *J. Phys. Chem. C* **2008**, *112* (21), 7978–7982. https://doi.org/10.1021/jp7120824.

(27) Oudar, J. L.; Chemla, D. S. Hyperpolarizabilities of the Nitroanilines and Their Relations to the Excited State Dipole Moment. *J. Chem. Phys.* **1977**, *66* (6), 2664–2668.

(28) Kaatz, P.; Shelton, D. P. Polarized Hyper-Rayleigh Light Scattering Measurements of Nonlinear Optical Chromophores. *J. Chem. Phys.* **1996**, *105* (10), 3918–3929.

(29) Kodaira, T.; Watanabe, A.; Ito, O.; Matsuda, M.; Clays, K.; Persoons, A. Evaluation of Hyperpolarizability of Nonlinear Optical Organic Molecules by Hyper-Rayleigh Scattering. *Jpn. J. Appl. Phys.* **1996**, *35* (12R), 6074.

(30) Szablewski, M.; Thomas, P. R.; Thornton, A.; Bloor, D.; Cross, G. H.; Cole, J. M.; Howard, J. A. K.; Malagoli, M.; Meyers, F.; Brédas, J.-L.; et al. Highly Dipolar, Optically Nonlinear Adducts of Tetracyano-p-Quinodimethane: Synthesis, Physical Characterization, and Theoretical Aspects. *J. Am. Chem. Soc.* **1997**, *119* (13), 3144–3154.

(31) Paley, M. S.; Harris, J. M.; Looser, H.; Baumert, J. C.; Bjorklund, G. C.; Jundt, D.; Twieg, R. J. A Solvatochromic Method for Determining Second-Order Polarizabilities of Organic Molecules. *J. Org. Chem.* **1989**, *54* (16), 3774–3778.

(32) Cheng, L. T.; Tam, W.; Stevenson, S. H.; Meredith, G. R.; Rikken, G.; Marder, S. R. Experimental Investigations of Organic Molecular Nonlinear Optical Polarizabilities. 1. Methods and Results on Benzene and Stilbene Derivatives. *J. Phys. Chem.* **1991**, *95* (26), 10631–10643. https://doi.org/10.1021/j100179a026.

(33) Moylan, C. R.; McNelis, B. J.; Nathan, L. C.; Marques, M. A.; Hermstad, E. L.; Brichler, B. A. Challenging the Auxiliary Donor Effect on Molecular Hyperpolarizability in Thiophene-Containing Nonlinear Chromophores: X-Ray Crystallographic and Optical Measurements on Two New Isomeric Chromophores. *J. Org. Chem.* **2004**, *69* (24), 8239–8243.

(34) Oudar, J. L. Optical Nonlinearities of Conjugated Molecules. Stilbene Derivatives and Highly Polar Aromatic Compounds. *J. Chem. Phys.* **1977**, *67* (2), 446–457.

(35) Oudar, J. L.; Zyss, J. Structural Dependence of Nonlinear-Optical Properties of Methyl-(2,4-Dinitrophenyl)-Aminopropanoate Crystals. *Phys. Rev. A* **1982**, *26* (4), 2016–2027.

(36) Marder, S. R.; Gorman, C. B.; Tiemann, B. G.; Perry, J. W.; Bourhill, G.; Mansour, K. Relation Between Bond-Length Alternation and Second Electronic Hyperpolarizability of Conjugated Organic Molecules. *Science* **1993**, *261* (5118), 186–189.

(37) Marder, S. R.; Perry, J. W. Molecular Materials for Second-order Nonlinear Optical Applications. *Adv. Mater.* **1993**, *5* (11), 804–815.

(38) Cheng, L. T.; Tam, W.; Marder, S. R.; Stiegman, A. E.; Rikken, G.; Spangler, C. W. Experimental Investigations of Organic Molecular Nonlinear Optical Polarizabilities. 2. A Study of Conjugation Dependences. *J. Phys. Chem.* **1991**, *95* (26), 10643–10652.

(39) Morley, J. O.; Docherty, V. J.; Pugh, D. Non-Linear Optical Properties of Organic Molecules. Part 2. Effect of Conjugation Length and Molecular Volume on the Calculated Hyperpolarisabilities of Polyphenyls and Polyenes. *J. Chem. Soc. Perkin Trans. 2* **1987**, *0* (9), 1351–1355.

(40) Levine, B. F. Donor—Acceptor Charge Transfer Contributions to the Second Order Hyperpolarizability. *Chem. Phys. Lett.* **1976**, *37* (3), 516–520.

(41) Nalwa, H. S. Organometallic Materials for Nonlinear Optics. *Appl. Organomet. Chem.* **1991**, *5* (5), 349–377.

(42) Lacroix, P. G.; Malfant, I.; Lepetit, C. Second-Order Nonlinear Optics in Coordination Chemistry: An Open Door towards Multi-Functional Materials and Molecular Switches. *Coord. Chem. Rev.* **2016**, *308*, 381–394.

(43) Cole, J. M.; Ashcroft, C. M. Generic Classification Scheme for Second-Order Dipolar Nonlinear Optical Organometallic Complexes That Exhibit Second Harmonic Generation. *J. Phys. Chem. A* **2018**.

(44) Coe, B. J.; Chamberlain, M. C.; Essex-Lopresti, J. P.; Gaines, S.; Jeffery, J. C.; Houbrechts, S.; Persoons, A. Large Molecular Quadratic Hyperpolarizabilities in Donor/Acceptor-Substituted Trans-Tetraammineruthenium(II) Complexes. *Inorg. Chem.* **1997**, *36* (15), 3284–3292.

(45) Zyss, J. Molecular Engineering Implications of Rotational Invariance in Quadratic Nonlinear Optics: From Dipolar to Octupolar Molecules and Materials. *J. Chem. Phys.* **1993**, *98* (9), 6583–6599.

(46) Zyss, J.; Ledoux, I. Nonlinear Optics in Multipolar Media: Theory and Experiments. *Chem. Rev.* **1994**, *94* (1), 77–105.

(47) Zyss, J.; Chemla, D. S.; Nicoud, J. F. Demonstration of Efficient Nonlinear Optical Crystals with Vanishing Molecular Dipole Moment: Second-harmonic Generation in 3-methyl-4-nitropyridine-1-oxide. *J. Chem. Phys.* **1981**, *74* (9), 4800–4811.

(48) Ledoux, I.; Zyss, J.; Siegel, J. S.; Brienne, J.; Lehn, J.-M. Second-Harmonic Generation from Non-Dipolar Non-Centrosymmetric Aromatic Charge-Transfer Molecules. *Chem. Phys. Lett.* **1990**, *172* (6), 440–444.

(49) Bredas, J. L.; Meyers, F.; Pierce, B. M.; Zyss, J. On the Second-Order Polarizability of Conjugated .Pi.-Electron Molecules with Octupolar Symmetry: The Case of Triaminotrinitrobenzene. *J. Am. Chem. Soc.* **1992**, *114* (12), 4928–4929.

(50) Verbiest, T.; Clays, K.; Samyn, C.; Wolff, J.; Reinhoudt, D.; Persoons, A. Investigations of the Hyperpolarizability in Organic Molecules from Dipolar to Octopolar Systems. *J. Am. Chem. Soc.* **1994**, *116* (20), 9320–9323.

(51) Stadler, S.; Feiner, F.; Bräuchle, Ch.; Brandl, S.; Gompper, R. Determination of the First Hyperpolarizability of Four Octupolar Molecules and Their Dipolar Subunits via Hyper-Rayleigh Scattering in Solution. *Chem. Phys. Lett.* **1995**, *245* (2–3), 292–296.

(52) Cho, B. R.; Lee, S. J.; Lee, S. H.; Son, K. H.; Kim, Y. H.; Doo, J.-Y.; Lee, G. J.; Kang, T. I.; Lee, Y. K.; Cho, M.; et al. Octupolar Crystals for Nonlinear Optics: 1,3,5-Trinitro-2,4,6-Tris(Styryl)Benzene Derivatives. *Chem. Mater.* **2001**, *13* (5), 1438–1440.

(53) Cho, B. R.; Chajara, K.; Oh, H. J.; Son, K. H.; Jeon, S.-J. Synthesis and Nonlinear Optical Properties of 1,3,5-Methoxy-2,4,6-Tris(Styryl)Benzene Derivatives. *Org. Lett.* **2002**, *4* (10), 1703–1706.

(54) Alcaraz, G.; Euzenat, L.; Mongin, O.; Katan, C.; Ledoux, I.; Zyss, J.; Blanchard-Desce, M.; Vaultier, M. Improved Transparency–Nonlinearity Trade-off with Boroxine-Based Octupolar Molecules. *Chem. Commun.* **2003**, *0* (22), 2766–2767.

(55) Zyss, J.; Dhenaut, C.; Chauvan, T.; Ledoux, I. Quadratic Nonlinear Susceptibility of Octupolar Chiral Ions. *Chem. Phys. Lett.* **1993**, *206* (1–4), 409–414.

(56) Morrison, I. D.; Denning, R. G.; Laidlaw, W. M.; Stammers, M. A. Measurement of First Hyperpolarizabilities by Hyper-Rayleigh Scattering. *Rev. Sci. Instrum.* **1996**, *67* (4), 1445–1453.

(57) Olbrechts, G.; Strobbe, R.; Clays, K.; Persoons, A. High-Frequency Demodulation of Multi-Photon Fluorescence in Hyper-Rayleigh Scattering. *Rev. Sci. Instrum.* **1998**, *69* (6), 2233–2241.

(58) Wostyn, K.; Binnemans, K.; Clays, K.; Persoons, A. Hyper-Rayleigh Scattering in the Fourier Domain for Higher Precision: Correcting for Multiphoton Fluorescence with Demodulation and Phase Data. *Rev. Sci. Instrum.* **2001**, *72* (8), 3215–3220.

(59) Sénéchal, K.; Maury, O.; Le Bozec, H.; Ledoux, I.; Zyss, J. Zinc(II) as a Versatile Template for the Design of Dipolar and Octupolar NLO-Phores. *J. Am. Chem. Soc.* **2002**, *124* (17), 4560–4561.

(60) Renouard, T.; Bozec, H. L.; Brasselet, S.; Ledoux, I.; Zyss, J. Tetrahedral Bipyridyl Copper(I) Complexes: A New Class of Non-Dipolar Chromophore for Nonlinear Optics. *Chem. Commun.* **1999**, *0* (10), 871–872.

(61) Lequan, M.; Branger, C.; Simon, J.; Thami, T.; Chauchard, E.; Persoons, A. First Hyperpolarizability of Organotin Compounds with Td Symmetry. *Adv. Mater.* **1994**, *6* (11), 851–853.

Chapter 2

Experimental and Computational Methods

2.1 X-Ray Diffraction

Throughout this thesis, X-ray diffraction (XRD) is a central experimental method used to i) determine molecular crystal structures and ii) to undertake molecular charge density analyses. The theory of XRD is well documented[1,2] and hence a detailed discussion of the theory is not presented in this thesis. However, a brief overview is given herein in the interest of completeness.

In any XRD setup, a source of X-rays is directed towards a mounted crystal of the compound under investigation, which is rotated in three dimensions. As the X-rays strike the crystal, they are scattered off the electron clouds of its constituent atoms. Consequently, different elements result in different levels of scattering, which are described by atomic scattering factors.

Once scattered, a CCD camera detects the Bragg intensities of the scattered X-rays. The Bragg intensities, $I(hkl)$, which describe the intensity of each diffracted X-ray beam as a function of position in reciprocal space and atomic scattering factor are the square of the modulus of the structure factor $|F(hkl|^2$ (*cf.* Eq. 2.1) and thus the phase information associated with the scattered X-rays is not measured. This is known as the 'Phase Problem' and must be resolved during the reverse Fourier transformation of the Bragg intensities into electronic charge distributions.

$$F(hkl) = \sum_{j=1}^{N} f_j exp\left[2\pi i\left(hx_j + ky_j + lz_j\right)\right] \qquad (2.1)$$

where f_j is the atomic form factor,

h, k, l are the Miller indices, and

x_j, y_j z_j are basis vectors

After processing using XRD software, the Bragg intensities ($|F(hkl|^2$) and Miller indices (*h*, *k*, and *l*) can be used to determine an initial list of atoms to be included in the crystal structure refinement by applying said reverse Fourier transformations to the data. This is usually undertaken using specialised crystal structure determination software that applies Direct

Methods, or Maximum Likelihood Optimization techniques, which reveal the charge density of the compound (*cf.* Eq 2.2). The modulus of the structure factors are related to the charge density of the material via the following reverse Fourier transformation:

$$\rho(hkl) = \frac{1}{V}\sum_{hkl}^{N}|F(hkl)|.exp\left[-2\pi i\left(hx_j + ky_j + lz_j - \phi(hkl)\right)\right] \qquad (2.2)$$

where V is the volume of the crystal structure,

$F(hkl)$ is the structure factor (*cf.* Eq 2.1),

h, k, l are the Miller indices, and

x_j, y_j z_j are basis vectors

$\phi(hkl)$ are the phases associated with the structure factor data

2.2 Standard Crystal Structure Determination

All standard determinations of crystal structures from low-angle XRD experiments discussed within this thesis were undertaken at The Cavendish Laboratory (University of Cambridge) using a Rigaku Saturn724+ CCD X-ray diffractometer equipped with a Mo-Kα X-ray tube (λ = 0.71073 Å). The diffractometer was equipped with an Oxford Cryosystems Cryostream, which allowed carrying out the XRD experiments in the temperature range of 80-300 K.

2.2.1 Sample Preparation

All crystalline samples used for XRD experiments were initially assessed for their viability using an optical microscope. Ideally samples for XRD should be small (dimensions: 0.05~0.5 x 0.05~0.5 x 0.05~0.5 mm^3) in order to reduce deleterious absorption and extinction phenomena. Where necessary, samples were carefully separated from parent crystals using a scalpel blade or solvent cutting. While under the microscope, samples were also assessed with respect to their uniformity and the absence of faults such as striations. Cross polarisers were used to check for potential twinning of the crystals.

Once selected, the crystals were attached to a loop that protrudes from a small pin using an epoxy resin that is fast setting once cooled (using e.g. liquid nitrogen) in order to ensure that the sample remains stationary on the loop throughout the duration of data collection. The pin was then mounted onto the goniometer head of the X-ray diffractometer and centred in order to ensure that the sample is in the centre of the pathway of the X-ray beam, and that the crystal samples centre of mass remains in the same position throughout the data collection process. The translation of the goniometer head in three dimensions is achieved using a grub screw.

2.2.2 Data Collection

Prior to collecting a full data set, it is important to ascertain the viability of any crystal for XRD by initially collecting a small number of images. The images should cover a variety of sections of reciprocal space to ensure that the crystal diffracts with the same efficacy in all regions. These images also help to determine the optimum exposure time for the crystal, which is a delicate balance between maximising intensity, while minimizing overexposure, which may damage the sample, and cause issues when attempting to determine appropriate absorption and extinction corrections.

Once a good set of initial images has been obtained, these can be used to index the observed reflections and hence refine the orientation matrix of the crystal, which is essentially a 3 x 3 matrix that describes the relationship between the fixed Cartesian co-ordinates of the diffractometer axes and the reciprocal lattice axes of the crystal as determined by the position of the diffraction spots.

Once indexed, the XRD software will determine a data collection strategy. However, this can be altered manually if necessary in order to achieve the particular aims of any given study. For example, in the case of charge density studies, special consideration of the redundancy of the data collection as well as the angle of the detector, and thus the range of scattered X-rays to be collected has to be taken into account in the data collection strategy.

For a standard determination of a crystal structure, data redundancy is useful to ensure that the correct space group is assigned and that the appropriate absorption corrections are applied, especially when multi-scan methods or transition surfaces are used. However, the redundancies achieved when using a data collection strategy of lower symmetry than the crystal being investigated are usually more than sufficient for the determination of standard crystal structures. For charge density analyses on the other hand, this is usually not the case and the data redundancy may need to be significantly increased.

Finally, the value of the detector position, 2ϑ, also needs to be decided as the resolution of the reflections measured will depend on where they hit the detector: near the primary beam there will be low resolution, strong reflections, while at the opposite edge, higher resolution and weaker reflections will be detected. For a standard determination of a single-crystal structure a low-angle value of ~25 ^{o} is typical as at this position the detector is able to catch reflections in a wide resolution range.

Linked to the detector angle is the exposure time necessary to produce images from which data can be extracted. As one moves the detector further out, the intensity of scattered X-rays decreases sharply, which results in the need for the X-ray exposure time to be increased. However, an increase in exposure time is commensurate with an undesirable increase in the amount of background radiation collected. Colloquially known as 'zingers' this background radiation manifests in the diffraction images as one-off spots. Many XRD software packages now have options that attempt to ameliorate this problem using correlated frames, where two images are taken per scan, compared, and adjusted accordingly. However, this correction method in itself presents problems, given the doubling of the data collection period. This not only means that data collection may become prohibitively time-consuming and costly, but it also increases the potential for failures in the experimental setup such as the formation of ice, crystal movement, crystal damage, and/or hardware failure. All of these must therefore be taken into consideration when developing a strategy.

For the purposes of the compounds studied in this thesis, a $2\vartheta/\omega$ scan was adopted such that $2\vartheta = 25\ ^{o}$ for standard structure determinations. The duration of each image collection was chosen so as to increase its precision, while preventing overexposure phenomena.

2.2.3 Data Reduction

Data reduction and integration of the in-house collected data was carried out using d*TRECK in CrystalClear 2.0[3]. The d*TRECK integration is a two-step process. Initially the program scans each image searching for strong reflections. It subsequently uses these scans to build three-dimensional pictures of each strong reflection while attempting to block as much of the background noise as possible.[4] The integrated volume of the three-dimensional spots then determines the intensity of each reflection. A library of the profiles of the strong reflections is then created to assist with the integration of weaker reflections.

When integrating the weaker reflections, the software may have difficulty separating the reflection from the background noise. To improve upon this, the software will use the library of the strong reflections. More specifically, profiles of the strong reflections that are close in ϑ to the weak reflection are used to model the profiles of those weak reflections enabling clearer distinction from the background noise.

---

[4] A dark image is usually taken before data collection to measure the background noise. This can then be subtracted from the data during processing. Background noise is also ameliorated using the de-zinger method as highlighted above.

Lorentz and polarization correction are applied to diffracted intensities automatically by the data-reduction software of the diffractometer, therefore they will not be discussed here.

2.2.4 Data Correction & Merging

2.2.4.1 Absorption Corrections

Before entering the structure determination process, the experimental data must to be corrected for the effects of absorption and multiple scattering. To correct for absorption phenomena, which occurs due to either i) the composition of the compound being measured, or ii) the occurrence of multiple-reflection of the diffracted beam within the crystal, the program SORTAV[4,5] implemented in the WinGX suite[6] was used. SORTAV performs an empirical absorption correction on the data by modeling a transmission surface for the crystal using real spherical harmonics. However, in order to accurately model the surface, multiple reflections are necessary and thus high data redundancy is beneficial. By using spherical harmonics, the anisotropic nature of the crystal can also be taken into account, thus achieving more accurate absorption corrections for crystals with ill-defined shapes.

For all data sets described in this thesis, the SORTAV empirical absorption correction method was used.

2.2.4.2 Data Merging

Unless stated otherwise, data merging prior to structure refinement was also carried out in SORTAV[5,7], which allows corrected data to be merged on the basis of its Laue class. Additionally, the program also allows for the suppression or removal of outliers. For more information on the schemes available in SORTAV, the reader is directed to the literature cited.

2.2.5 Solving the Crystal Structure

After data collection, reduction and correction, the crystal structure determination begins. Here, the experimental Bragg intensities collected by the detector ($|F(hkl|^2$) are used to solve the 'Phase Problem' through the application of reverse Fourier transformations to the data. During this processes phases are determined and assigned to the data based on the following two mathematical assumptions: i) electron density is always positive and, ii) the electron density is composed of discrete atoms.

These two assumptions are used to compare moduli of the structure factors, and thus determine which phases to assign to the data (either 0 ^{o} or 180 ^{o}). Once a sufficient number of phases are reached they are used to calculate the electron density distribution, from which an approximate position of the atoms in the structure is derived. At this point, with a starting list of atoms, one can refine the structure by calculating theoretical structure factors of the atoms and comparing them with the observed structure factors; this procedure is usually undertaken via a least-squares approach.

Many methods have been developed to overcome the problem of the lack of phase information, whereby the two main methods are:

- Patterson Synthesis
- Direct Methods

All organic compounds mentioned in this thesis were solved using Direct Methods, while the organometallic structures were solved using the Patterson Synthesis as implemented in SHELX-2013[8].

These crystal structure solutions are Independent Atom Models (IAM) of the crystal structures. An IAM is a model in which the electron density distribution of the atoms in the structure is assumed to be spherical, and thus isotropically distributed around the nucleus of the atom, dependent only on the distance from the said nucleus. An IAM therefore is a simplified model of the crystal structure that does not take account of aspherical charge density.

The space group of most compounds presented in this thesis was preliminarily determined by the XPREP program[9], which uses the raw unmerged data set from the X-ray diffraction experiment and the lattice parameters of the crystal to determine systematic absences in the data. Based on these absences, the program attempts to determine the Laue class, Bravais lattice, and ultimately the space group of the structure. Thereafter, initial refinement files can be generated for the structural refinement.

2.3 Charge Density Data

Initial attempts to collect high-quality, high-angle X-ray diffraction data using the in-house Rigaku machine were unsuccessful, which was attributed predominantly to the two factors outlined below.

Bimodal Scattering: The presence of a heavy metal and halides (eg, Zn, Br, I) in combination with light organic elements (eg, C, N, O, H) resulted in bimodal scattering, whereby the intensities of the measured reflections were either very strong or weak. This phenomenon was particularly prominent when comparing low- vs. high-angle data sets. Consequently, merging and scaling low- and high-angle data sets proved difficult, and resulted in merged data sets that yielded poor refinements.

Collection Speed: Due to the need to maximise data redundancy at both low and high angles, time-consuming data collection strategies (up to a month per sample) were necessary, which poses the increased risk of malfunctions of the experimental setup, eg, fluctuations in sample temperature, cryostream failure, electrical power cuts, and radiation damage to the sample.

A comparison of the in-house and synchrotron data of the complex dichlorobis(3-pyridinecarboxaldehyde-κ-N)Zn(II) is presented in §2.3.1 and highlights how these conclusions were drawn.

After some consideration, it was decided that an application for beam time at a synchrotron facility was the next logical step. To this end, time at The Advanced Photon Source (APS) at The Argonne National Laboratory (Chicago, USA) was obtained, where all data were collected by J. M. Cole and Y. S. Chen on my behalf.

2.3.1 In-house vs. synchrotron data: An assessment

The first organometallic complex to be investigated using the in-house diffractometer was dichlorobis(3-pyridinecarboxaldehyde-*κ*-N)Zn(II) (Fig 2.1). The low- ($2\vartheta = 25\,^{\mathrm{O}}$) and high-angle data ($2\vartheta = 60\,^{\mathrm{O}}$) were collected using the in-house Rigaku X-ray diffractometer as outlined in §2.2.2-§2.2.3. These two different data sets were then corrected for absorption and merged in SORTAV. Below, a comparison of the two SHELX and multipole model fitting statistics is presented, which is based on the in-house and the synchrotron data, respectively.

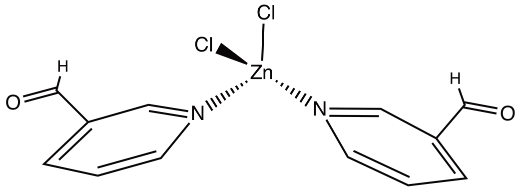

Figure 2.1 Chemical structure of dichlorobis(3-pyridinecarboxaldehyde-κ-N)Zn(II).

Table 2.1 Summary of the IAM model refinement statistics of dichlorobis(3-pyridinecarboxaldehyde-κ-N)Zn(II) based on data collected in-house and at the APS synchrotron.

Parameter	**In-house structure** **$\lambda = 0.71073$ Å**	**Synchrotron structure** **$\lambda = 0.41328$ Å**
a (Å)	5.7696(13)	5.7509(3)
b (Å)	12.2080(30)	12.1999(7)
c (Å)	19.1190(40)	19.0906(11)
α (^{O})	90.0	90.0
β (^{O})	90.0	90.0
γ (^{O})	90.0	90.0
V (Å^3)	1345.65	1339.40
Z	4	4
Space Group	Pnam	Pnam
μ (mm^{-1})	2.22	0.46
Unique Reflections	5872	6259
F(000)	704.0	704.0
Resolution / ($\sin\vartheta/\lambda$) (Å^{-1})	1.09	1.04
R_1 (I > 2sigI)	0.0463	0.0249
wR_2	0.1121	0.0711
ρ_{max} / ρ_{min} (eÅ^{-3})	1.25 / -1.06	0.73 / -0.56

Table 2.1 provides a preliminary assessment of the in-house and synchrotron data sets of dichlorobis(3-pyridinecarboxaldehyde-κ-N)Zn(II) based on their respective IAM refinements in SHELX. Despite the synchrotron data set being at a slightly lower resolution, it appears to yield a much better refinement solution. The fitting residual factor R1 sees an improvement of 54%, while the ρ_{max}/ρ_{min} values are also substantially improved suggesting that the absorption corrections applied to the data are better. This is hardly surprising given that:

a) The lower wavelength of the synchrotron source results in lower levels of absorption and extinction phenomena.

b) The higher data redundancy afforded by synchrotron collection means that the empirical absorption correction applied in SORTAV will be more accurate.

These two data sets were also compared using their respective fitting plots and analysis of variance for the reflections employed in each SHELX refinement.

2.3.1.1 Fitting Plots

Plots 2.2(a)-(b)

Plots 2.2(*a*) and 2.2(*b*) are normal probability plots, also known as Q-Q plots, and can be used to asses how well standard uncertainties (s.u.) associated with the data are modelled. Where the errors of the data are heavily under-, or overestimated, the data is not well defined and could lead to modelling inaccuracies. Here the plots 2.2(*a*) and 2.2(*b*) show the theoretical (expected) and experimental residuals of the in-house and synchrotron data sets of dichlorobis(3-pyridinecarboxaldehyde-κ-N)Zn(II) respectively. An ideal form for the plot, consistent with accurate modelling of data errors, would consist of points lying along the line $y = x$. In the case of 2.2(*a*), the residuals diverge heavily at the tail ends of the normal distribution, and also appear to underestimate those residuals that lie parallel to the line $y = x$. According to the work of Henn & Meindl[10] this tail divergence from a Gaussian distribution likely arises from underestimations of the errors associated with strong reflections or, from other forms of systematic errors. The errors of the residuals therefore appear to be estimated better in the case of the synchrotron data set (*b*).

Plots 2.2(c)-(d)

Plots (*c*) and (*d*) reveal the summation of the ratio of the experimental structure factors (F_O) against the theoretical structure factors (F_C) for each resolution bin for the data set of the in-house and synchrotron data sets of dichlorobis(3-pyridinecarboxaldehyde-κ-N)Zn(II), respectively. Ideally, the model should calculate F_C sufficiently well that F_O / F_c equals unity for all reflections across all resolution bins. This trend is observed in 2.2(*d*) except for one point in the low-resolution range, which is not unreasonable, especially when low, but very intense reflections such as 100, 101, or 001 are not omitted from the data set. In the case of 2.2(*c*) however, the data points oscillate around the line *y = 1.0*, suggesting that the structure factors calculated from the available model do not match well with the experimental data; this is particularly true for high-resolution bins. This was investigated further through a careful assessment of the data set's respective analysis of variance for the reflections employed in each SHELX refinement (*cf.* Table 2.2 - 2.3)

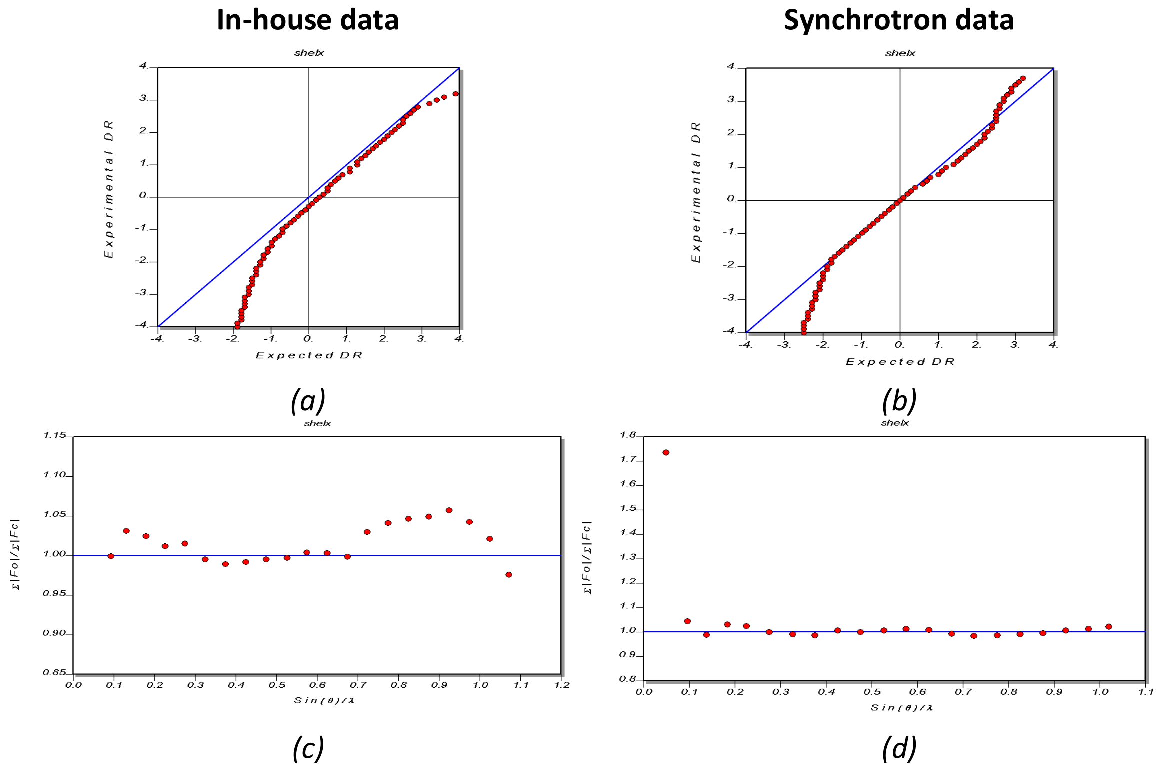

(a) *(b)*

(c) *(d)*

Figure 2.2 Scatter plots of the in-house and synchrotron data sets for dichlorobis(3-pyridinecarboxaldehyde-κ-N)Zn(II). (*a, b*) Q-Q scatter plots of the theoretical (expected) and experimentally observed residuals of the in-house and synchrotron data sets, respectively. (*c, d*) Scatter plots of the summation of the experimental structure factors (F_O) divided by the theoretical structure factors (F_C) for each resolution bin for the data set of the in-house and synchrotron data sets, respectively.

2.3.1.2 Analysis of variance

A comparison of the in-house and synchrotron data via the analysis of variance (Table 2.2) revealed that the in-house data have serious fitting problems in the high-resolution bins, with R1 values between 8.9-20.6% for the resolution bins 0.54-0.46 Å ($\sin\vartheta/\lambda$ = 0.94-1.08 Å^{-1}). Furthermore, the comparison revealed problems with the high-intensity reflections ($F_C/F_{C(MAX)}$ = 0.00-0.007), which also manifests in a high K value (5.136) that implies that the model is not particularly suitable to accurately calculate the theoretical structure factors associated with these reflections.

A comparison of the in-house high-resolution data set (Table 2.2, bottom) with an in-house low-resolution data set collected for the same crystal (Table 2.3) revealed that the problems associated with the high-intensity reflections are significantly more prominent when the low- and high-resolution data sets are merged. It is thus feasible to assume that most of these problems are associated with the high-resolution data sets.

2.3.1.3 Concluding assessment

After an assessment of the in-house data, it was concluded that dichlorobis(3-pyridinecarboxaldehyde-κ-N)Zn(II), due to the presence of both light organic elements such as C, N, and H, as well as heavy elements such as Zn affords bimodal scattering effects.

As the molecules under investigation contain mainly light organic elements, with only one to three heavy elements, the range of scattering intensities, which are proportional the elements' atomic number, is small, and of two extremes. Consequently, during processing the application of weighting algorithms when merging data sets proved challenging.

Furthermore, these effects should become more pronounced upon incorporating heavier halides in the Zn complex, which would have a significantly negative impact on the research aims of this thesis.

2.4 Neutron diffraction

When it was possible to grow large crystals, these were sent to The Bragg Institute of The Australian Nuclear Science and Technology Organisation (ANSTO, Sydney) for the collection of complementary neutron diffraction data. This form of diffraction technique allows the collection of data, which as with X-ray diffraction data, can be used to undertake a crystal structure determination via the application of reverse Fourier transformations to the data to solve the 'Phase Problem' and provide an initial list of atoms. Similarly to X-ray methods, with a starting list of atoms, one can refine the structure; usually undertaken via a least-squares approach.

However, unlike in X-ray diffraction techniques, neutron diffraction, results from neutrons interacting with, and scattering off, the nucleus of atoms, rather than their electron cloud as in X-ray diffraction. Consequently, the scattering length *b* of a diffracted neutron beam is independent of the scattering angle, resulting in neutron diffraction experiments being able to yield well-defined diffraction peaks even at high angles. Given their interaction with the nucleus, neutron diffraction experiments are also able to distinguish between isotopes of the same element type.

Importantly in the case of the studies presented herein, neutron diffraction experiments, given their interaction with the nucleus and independence on scattering angle, are able to provide information on the position and anisotropic thermal parameters (ADPs) of the hydrogen atoms within molecules; something not accurately achievable with X-ray diffraction due to the presence of only one electron from which X-rays can scatter off.

The neutron data utilized in the studies herein was collected using the KOALA neutron diffractometer after successful applications for beam time. KOALA has a cylindrical image-plate detector and a white neutron beam (whole spectrum; Laue diffraction).

J. M. Cole, G. McIntyre and A. Edwards carried out all neutron diffraction experiments and the corresponding image processing.

2.5 Charge Density Analysis

The field of Charge Density Analysis has, over the last decade, become a powerful tool for the investigation of materials, with many excellent reviews and books on the field now beginning to emerge[11–13]. We herein present the salient history, theory and general aspects of charge density analysis most relevant to the work undertaken in this thesis.

Once a structure has been solved and refined using an IAM, a charge density analysis of the structure can be undertaken through the use of a multipole formalism, provided that the data resolution is sufficiently high. By using multipole models (MM), the atomic and molecular orbitals of a structure can be taken into account by assigning charge density to them. To that end, a plethora of information about the structure at a microscopic level can be determined, such as intramolecular charge transfer and bonding character, which affords a better understanding of the origins of a compound's properties.

2.5.1 Spherical Kappa Formalism

Initial attempts to improve upon the IAM led to the spherical kappa formalism, which was developed by Coppens *et al.*[14] This formalism attempted to modify the IAM in order to account for the effects of charge transfer between atoms. To achieve this, scattering from valence electrons is separated from that of core electrons. By introducing two different groupings of electrons additional parameters can be applied to the structural refinement in order to adjust the populations and radial dependencies of only the valence shells, i.e. those shells that participate in molecular bonding.

In the case of the Coppens Kappa Formalism, two additional parameters are introduced, P_v, a valence shell population parameter and κ, which models the expansion-contraction of the valence shell of each atom. By the introduction of these two new parameters, the charge density of each individual atom in a molecular structure can be determined by:

$$\rho_{ATOM} = \rho_{CORE} + P_v \kappa^3 \rho_{VALENCE}(\kappa r) \qquad (2.4)$$

where ρ_{CORE} is the charge density associated with the core electrons of the atom

P_v the charge population of the valence electronic shell

κ the expansion-contraction of the valence electronic shell, and

$\rho_{VALENCE}(\kappa r)$ the charge density associated with the valence electrons of the atom.

The value of the expansion-contraction parameter, κ, scales with the radial coordinate, r, such that $\kappa > 1$ signifies a contraction of the valence shell, while $\kappa < 1$ refers to an expansion. Moreover, κ is normalized to the valence electron density:

$$N4\pi \int \rho_{VALENCE}(\kappa r) r^2 dr = 1 \qquad (2.5)$$

where N is the total number of valence electrons in the atom (under the assumption that the core electrons are not perturbed[15], and

$\rho_{VALENCE}(\kappa r)$ is the charge density associated with the valence electrons of the atom.

As the unperturbed density is also normalized to 1, κ has to be proportional to the number of respective valence electrons, thus providing a useful measure of the reliability of its value during refinements. This inherent relationship between κ and the number of valence electrons further implies a relationship between κ and the scattering factor, f, of each respective atom, enabling κ-modified scattering factors to be acquired directly from IAM–based values.

Promising results arise from the implementation of this formalism. For example, the use of the spherical κ-formalism yields net charges that are in good agreement with accepted electronegativity notions.

However, the spherical κ-formalism also has limitations. It does not, for example, include terms that consider aspherical density associated with non-*s*-type orbitals. Such a model is therefore unable to explain concepts such as lone-pair electrons. Therefore, the incorporation of molecular orbital theory[16] is required to to account for the deformation of the electron density around atoms due to bonding interactions[17].

2.5.2 Aspherical Kappa Formalism

The aspherical kappa formalism, developed by Hansen and Coppens[18], hereafter referred to as the multipole model (MM), uses atomic density functions to model the electron density around atoms. The density functions adopted by Hansen and Coppens are described in terms of three polar co-ordinates (*r*, *ϑ*, and *Φ*), which express radial and angular information, respectively. In the MM, the density is expressed as the product of radial and angular functions, whereby the angular function is taken from the series of spherical harmonics, $Y_{lm\pm}(\theta, \phi)$. These functions are well-known solutions to the Laplace equation and describe the hydrogenic orbitals. The spherical harmonics, once chosen, must be normalised to give a density function, $d_{lm\pm}(\theta, \phi)$.

As molecular orbitals are formed through the combination of atomic orbitals, the radial functions used in the MM are also based on spherical harmonics. However, they must be carefully chosen so as to maintain the shell structure of the spherical elements of the density, while also being able to model the accumulation of charge in molecular bonds. Slater-type radial functions yield promising results, particularly for atoms from the first and second row elements of the periodic table:

$$R_l(r) = \kappa'^3 \frac{\xi^{n_l+3}}{(n_l+2)!} (\kappa' r)^{n(l)} \exp{(-\kappa' \xi_l r)} \qquad (2.6)$$

where κ' is an aspherical expansion-contraction parameter

ξ the energy-optimised single-Slater value for electron subshells of isolated atoms[19], and

$n_l \geq l$, as required by the Poisson electrostatic law[20].

Moreover:

$$\xi = \frac{Z-\sigma}{n} \qquad (2.7)$$

where *Z* is the charge

σ a screening constant, and

n the principle quantum number.

By combining the normalized angular-dependent spherical harmonics and the radial functions, the spherical kappa formalism (Eq. 2.4) can be modified thus:

$$\rho_{ATOM}(r) = P_C\rho_{CORE}(r) + P_v\kappa^3\rho_{VALENCE}(\kappa r) + \sum_{l=0}^{l_{max}} \kappa'^3 R_l(\kappa' r) \sum_{m=0}^{l} P_{lm\pm} d_{lm\pm}(\theta,\phi) \quad (2.8)$$

where P_c, P_v and $P_{lm\pm}$ are population coefficients of the core and valence shells, and the harmonic function, respectively;

ρ_{CORE} and $\rho_{VALENCE}$ have the same meaning as in the spherical formalism;

κ is the spherical expansion-contraction parameter;

κ' is the aspherical expansion-contraction parameter;

R_l is the radial function described in Eq 2.6;

$d_{lm\pm}$ is a normalized spherical harmonic function;

l refers to the multipolar terms (monopole: l = 0; dipole: l = 1; etc.)

This is the aspherical kappa formalism of Hansen and Coppens[18] and is used throughout this thesis. To date, a variety of charge density programs and software packages have been developed. All charge density studies in this thesis were undertaken using XD2006[21].

2.5.3 The Modeling of Hydrogen

Due to a lack of electrons, the modeling of hydrogen atoms using the spherical and aspherical kappa formalisms is difficult. These difficulties arise, as it is very challenging to accurately determine the expansion-contraction parameter, κ, of the hydrogen atom from X-ray data. Erroneous values of κ arise during multipole refinements on account of its strong correlation with temperature parameters.

In a seminal study, Stewart *et al.*[22] attempted to address the correlation problems of hydrogen refinement by fitting a flexible, spherical hydrogen atom form factor to the molecular scattering of high-quality, theoretical charge density data of the hydrogen molecule. They found that the bonded atoms' shells are contracted relative to an isolated hydrogen atom; $\kappa \approx 1.16$. Their modeled density fitted within an error of 0.11% compared to 7.12% for the isolated 1s proton centred density. Their form factor, known as the SDS form factor, and the related κ value has since become the standard for charge density analysis involving hydrogen atoms. Neutron data, when available, can also be used to improve the SDS κ value for X-H type bonds[14]. Madsen[23] discusses the modelling of hydrogen atoms, including the use of the SDS value, in detail.

The lack of core density in hydrogen atoms also leads to other parameter errors during structural and multipole refinement, specifically with respect to their position and anisotropic thermal parameters (ADPs). However, this data can be extracted from neutron diffraction studies and incorporated in the X-ray-based multipole models where appropriate. Combined X-ray- and neutron-based data analysis is an optimal approach to charge density studies and should be undertaken when possible. However, the incorporation of neutron data must be carried out with care in order to ensure that the anisotropic thermal parameters are scaled to reflect any temperature difference between the X-ray- and neutron-based studies. Corresponding formalisms for scaling ADPs have been developed by Blessing[24], with more recent formalisms developed by Madsen and Hoser[25] and, Lübben, Bourhis and Dittrich[26].

In reality, access to neutron beams can prove logistically and/or financially difficult and hence alternative methods of correction have been developed. It is now widely accepted that the positional parameters of hydrogen atoms can be corrected by fixing the X-H bond lengths to accepted neutron-derived values listed in the *International Tables of Crystallography*. The values contained therein have been obtained from a series of neutron diffraction studies by Allen *et al.*[27]. The ADPs of hydrogen atoms can be predicted based on an X-ray structure refinement using the SHADE 2.1 server[28]. This server uses a translation–libration–screw model[29] to analyze the ADPs of the non-hydrogen atoms, which are then used to estimate the mean square displacements of the hydrogen atoms. A comparative study, in which neutron-derived hydrogen ADPs were compared to those generated using the SHADE server, revealed excellent agreement between experimentally observed and calculated hydrogen ADPs[30]; accordingly, the SHADE server is recommended as a routine method to obtain such information. A study by Madsen *et al.* further validated the use of SHADE-generated hydrogen ADPs in charge density studies[31].

However, SHADE-generated hydrogen ADPs may struggle to accurately depict ADPs of hydrogen atoms that partake in hydrogen bonding[30]. In such instances, the results of SHADE-generated hydrogen ADPs must be examined with particular care to ensure they have a reasonable size and shape. Madsen has discussed the issues associated with the correct modelling of hydrogen atoms partaking in strong hydrogen bonds[23].

2.5.4 Undertaking Charge Density Studies

Having outlined the theory of charge density analysis, a standardized method for carrying out a charge density study from an initial IAM to a finalized MM using XD2006 is described below.

Before beginning a charge density study, it is paramount to consider in detail the level of data to be collected. Failure to collect enough data at sufficient quality may render multipolar refinement difficult and, under certain circumstances, impossible. In such cases, the results obtained may either be unrealistic and/or chemically unreasonable.

2.5.4.1 Selecting the Databank

When undertaking a study of organic compounds, the Clementi-Roetti databank, which contains Clementi and Roetti wavefunctions for all neutral atoms and principal ions up to Kr, is usually used as a standard[32]. Single-ξ functions[5] are obtained from Clementi and Raimondi[19], while analytical spherical scattering factors are obtained from the *International Tables of Crystallography*. In the case of the electronic configuration of transition metals, the databank is set up so that 4*s* electrons are part of the valence orbitals (except for Cr and Cu).

However, when modeling organometallic compounds and complexes, the choice of databank should be taken with care, especially when using synchrotron sources for data collection. Although the Clementi-Roetti databank can be used for the modelling of transition metals, the wavefunctions are not corrected for relativistic effects, which may become important, especially for heavy elements. Additionally, given the diffuse nature of the 4*s* valence electrons of transition metals, the ability to model their density correctly can prove challenging. Accordingly, information pertaining to the 4*s* is strongly affected by absorption and extinction. Consequently, databanks that treat the 4*s* electrons as part of the core density, while using the 3*d* electrons as the valence electrons have been developed, with the most common example being the Su-Coppens-Macchi (SCM) databank[33,34]. Further information regarding databanks available in XD2006 can be found in the XD2006 manual.

---

[5] Single-ξ functions are single-Slater wavefunctions stored in the databank and are used to describe atomic orbitals of atoms in their ground state.

2.5.4.2 Setting of Initial Parameters

Once a suitable databank has been identified, and systematic absences searched and removed from the reflection file, chemical constraints and symmetry conditions should be introduced so that chemically equivalent atoms are initially treated identically. Such constraints are particularly important for hydrogen atoms that take part in H-bonding as initial monopole populations tend to be modelled incorrectly in these instances due to the ensuing electrostatic interaction if not controlled. Furthermore, atoms that sit on special positions should be treated with care to ensure that ADPs and multipoles that are physically meaningless are not refined. The programs LSDB[35–37] and MoleCoolQT[38] can be used to determine such constraints.

Once chemical constraints have been introduced, an initial refinement of the atomic positions and thermal parameters should be carried out. Where possible, this should be accomplished together with complementary, neutron-derived positional and thermal parameters of hydrogen atoms, which can be incorporated into the model manually. However, where such data are not available, hydrogen atoms can be modeled using the standard bond lengths as found in the *International Tables of Crystallography* and thermal parameters obtained through use of the SHADE 2.1 server (*cf.* §2.6.4).

2.5.4.3 Gram-Charlier Anharmonic Refinement

When a compound contains heavy atoms (e.g. transition metals), a careful examination should be carried out to determine if anharmonic nuclear libration of these atoms persists. This may prove vital for the validity of the final charge density model, given that residuals pertaining to anharmonic librations look similar to residuals resulting from electron deformation density, especially in the case of transition metals[39].

Anharmonic libration usually presents itself in residual density maps, as what is known as 'shashlick' residual density features. Shashlik residual density features are characterized by the presence of alternating regions of positive (peaks) and negative (holes) residual density surrounding the librating atom. When present, such features can be modeled through the refinement of Gram-Charlier (GC) coefficients[40]. GC coefficients up to the 3rd order (ten additional parameters) and/or 4th order (15 additional parameters) can be included in programs such as XD2006. However, a GC refinement should be undertaken with caution, and the obtained coefficients should be evaluated through an assessment of their standard uncertainties and their probability density functions (PDFs) to determine if their values are realistic.

Furthermore, GC refinement should only be undertaken when the data resolution is sufficiently high[6]; the minimum resolution required can be calculated[41] via:

$$K_n = 2\left(\frac{n\,ln2}{\pi}\right)^{1/2}\frac{1}{\langle u^2\rangle^{1/2}} \qquad (2.9)$$

where n is the order of the GC refinement (3rd / 4th), and

u^2 the atomic mean-squared displacement.

The treatment of anharmonic libration through GC refinement in charge densities studies and its effects on the model has previously been investigated by Herbst-Irmer *et al.*, while the implications of neglecting such libration in the model has also been discussed in the literature[42,43].

2.5.4.4 Introducing Multipoles

Subsequently, multipole parameters can be introduced sequentially to the model, starting with the introduction of one monopole for each atom[7]. Once converged, dipole, quadrupole, and octupole parameters are refined sequentially for all non-hydrogen atoms (refinement of hydrogen should be truncated after the introduction of bond-directed dipoles unless their population values suggest otherwise). Additional hexadecapoles should be included for transition metals and can also be used for atoms that exhibit hexadecapolar populations[8] much greater than 2σ.

---

[6] It should be noted that Herbst-Irmer *et al.* suggest that Kuhs criteria may be too strict, especially for heavier elements.

[7] An additional monopole can be included in the model for transition metals if the 4s population is to be modelled as part of the atoms valence electronic configuration. Any introduction of a second monopole must be carried out with great care and should be monitored throughout the refinement to ensure realistic population values.

[8] As a rule of thumb, hexadecapoles are not included for first-row atoms, unless their populations are significant. This is due to the fact that hexadecapoles correspond to *f*-orbitals that are physically meaningless for first-row atoms, and would normally gravitate toward zero.

When introducing monopoles, the spherical contraction-expansion parameter κ is also simultaneously refined for all non-hydrogen atoms[9]. For hydrogen atoms, the κ value should be set to the SDS value of 1.16, as is now standard practice in charge density studies[22]. Once multipole parameters have been introduced, κ' parameters for each atom (except H) can be refined and tested for reasonable values. Where unreasonable values reveal themselves, the κ' value should not be refined.

The chemical constraints can then be released, and the model can be refined one last time if this is deemed beneficial, before the viability of the model is assessed.

2.5.4.5 Testing the feasibility of an MM

There are numerous ways of determining the accuracy and feasibility of an MM. The principal options include:

- Model statistics
- Reasonable valence charge assignment
- Reasonable κ and κ' values
- Residual charge density maps
- Hirshfeld rigid-bond test
- Parameter correlation

Here we look at each of these in turn highlighting the importance of each.

Model statistics: Initially, the validity of a model should be determined via its model statistics. Similar to structure determination, MMs figures of merit such as a residual R factor, a weighted residual R factor, a data-parameter ratio, and a model convergence value should be assessed. As a crude measure of improvement, one should always work to reduce the residual R factor. However, focusing exclusively on the statistics can be misleading. For example, the R-value of a model will always decrease upon introduction of more parameters to be refined. This is the case even when their inclusion is physically meaningless. The data-parameter ratio should also be regularly checked throughout the refinement. If its value decreases below 20, the model may struggle to accurately determine the charge density, and properties derived from the resultant model may be incorrect and/or physically

---

[9] Where groups of atoms have been constrained to be chemically equivalent, it can prove beneficial for the model to provide them with their own κ parameter for refinement, e.g. sp^2 and sp^3 carbons should ideally have separate κ parameter.

meaningless[10]. Even when the data-parameter ratio is good, and the R-value decreases, the iterative refinement of the model may not converge due to problems with the data or model parameters. Consequently, the model statistics should always be considered holistically in order to determine whether the model is reasonable at a rudimentary level.

Valence charges: The valence population, P_v, assigned by the model should conform to chemically reasonable values. For example, carbon atoms with the electron configuration $1s^2 2s^2 2p^2$ should be assigned a valence close to four electrons.

κ and κ′ values: The values of κ and κ' should also be chemically reasonable, i.e. a negative value for either parameter is physically meaningless. The κ value for hydrogen atoms should be fixed at the SDS value or similar unless high-quality neutron data is being used in conjunction with the X-ray data. Even in this case, it is standard practice to fix the κ value for hydrogen. For organic elements, $\kappa \gg 1$ should be considered suspect and examined. κ' values should also be examined carefully and replaced with standard values where unreasonable (usually automatically assigned by the refinement software).

Residual electron density maps: Residual electron density maps are a visual representation of the difference between the actual charge density (determined by X-ray diffraction) and the modelled density ($F_{obs} - F_{model}$), in other words, it affords a depiction of the size and regions of unmodeled charge density. As multipoles are introduced into the model, the amount of charge density being unaccounted for should decrease until the contour map becomes flat and featureless. A map that is featureless at a resolution of 0.1 eÅ^{-3} is considered to be indicative of a 'good' model. Features as large as 0. 6 eÅ^{-3} or greater, particularly around organic elements, should be a cause for concern.

This is less of a concern around heavy elements where problems modelling the density are expected. Such large residual density may be indicative of issues elsewhere in the model that should be addressed before finalizing a model.

Hirshfeld rigid-bond test: The Hirshfeld rigid-bond test[44] provides a measure of how well the MM is modeling the anisotropic thermal parameters of the atoms. The test assumes that all

---

[10] A data-parameter ratio of 20 or above is a generally accepted value in the field. Models with values below 20 should be used with caution and care.

bonds vibrate homogenously and hence predicts that, on average, the ADPs of mutually bonded atoms should be displaced by the same amount. The Hirshfeld tolerance level is set to ≤ 0.001 Å for organic elements, and any substantial deviation from this value should be investigated further. Large values, particularly for heavy atoms such as metals, can also be indicative of unmodeled nuclear anharmonic libration, which can be corrected via the inclusion of Gram-Charlier coefficients (*cf.*§2.5.4.3).

Parameter correlation: The correlation between parameters should be carefully examined, and where possible minimized. Correlations greater than 80% should be considered problematic for the accuracy of the model and taken into further consideration. Yet, high correlations between similar parameters on the same atom may be considered acceptable and even permissible. Still, correlation between unrelated parameters and/or between different atoms should be corrected. If high levels of parameter correlation are found across the model, block refinement methods should be adopted in an attempt to reduce them.

Once a satisfactory final model has been achieved, it can be used to afford a range of information regarding the specific molecular structure being studied e.g. bonding character, molecular dipoles, bond polarisation, and the (hyper)polarizability of the structure, which are fundamental to the ability of a material to exhibit NLO responses.

2.6 Analysis of the MM Results

2.6.1 Deformation Density Maps

Deformation density maps can be generated once a model has been finalised in order to generate a visualisation of the bonding and polarisation phenomena in a molecular structure. These maps compare the difference between the electron densities of the MM to that of the IAM. Traditionally this was achieved using:

$$\delta\rho(r) = \rho_{MM} - \sum_k \rho_k(r - r_k) \qquad (2.10)$$

where ρ_{MM} is the charge density associated with the multipolar model, and

ρ_k is the charge density associated with an IAM i.e. the pro-molecular density.

The pro-molecular density term is a summation of the spherical atomic densities $\rho_k(r)$, which have been centred at the nuclear positions in the molecule. However, this method is problematic, as it does not always reveal the true character of a molecular bond as a result of the equal weight it applies to all molecular orbitals. As such, a Fourier transform method has since been adopted:

$$\delta\rho(r) = \sum_k [F_O(k) - F_C(k)] e^{-2\pi i k r} \qquad (2.11)$$

where $F_0(k)$ are the observed structure factors, and

$F_C(k)$ are the calculated structure factors.

This function compares the difference between the observed and calculated structure factors, before converting the result into the charge density for mapping.

These maps are able to reveal the nature of the molecular bonds as well as their relative strength through the comparison of contour levels. The maps also assist in ascertaining the orbitals that are partaking in bonding activity when studied in conjunction with the multipoles being used. Furthermore, the maps are usually able to clearly reveal the presence and relative strength of polarisation behaviour in bonds. Additionally, lone pairs can be identified visually. All of these features demonstrate that deformation electron density maps are a highly versatile and, useful tool in the analysis of charge density, and hence, they have been used throughout this thesis.

2.6.2 Bader Topological Analysis & Laplacian Maps

Although electron deformation density maps are of great value, their functionality is limited. For example, the maps are not very useful when attempting to identify the actual character of chemical bonds, ie, although bonds are apparent in deformation maps it is not always obvious if the bonds are covalent or ionic, and in case of the former, if they are σ- or π-bonds. Furthermore, although deformation maps can provide a crude measure of relative strength between bonds, they do not directly measure these strengths. This can however be achieved through a topological analysis of the final multipolar model. The theory used in a topological analysis is outlined in Bader's Quantum Theory of Atoms in Molecules (QTAIM)[45,46], wherein the plethora of property information affordable through the calculation of the first and second-order derivatives of a compound's molecular charge density is highlighted.

2.6.2.1 Bond Critical Points & Ellipticities

In QTAIM, the first-order derivative of the molecular charge density in three dimensions can be used to identify bond critical points (BCPs) in the molecular density, i.e. points where the derivative equals zero:

$$\nabla\rho(r_C) = \hat{\imath}\frac{\partial\rho}{\partial x} + \hat{\jmath}\frac{\partial\rho}{\partial y} + \hat{k}\frac{\partial\rho}{\partial z} = 0 \qquad (2.12)$$

wherein r_C represents the position vector of the critical point.

By identifying BCPs in the charge density of the molecule, the nature of the bonds can be ascertained via a determination of the second derivative of the charge density (Laplacian function) at these BCPs. The BCPs are thus characterized as minima, maxima, or saddle points according to[11]:

$$\nabla^2\rho(r_C) = \hat{\imath}\frac{\partial^2\rho}{\partial x^2} + \hat{\jmath}\frac{\partial^2\rho}{\partial y^2} + \hat{k}\frac{\partial^2\rho}{\partial z^2} \qquad \begin{matrix} < 0 \rightarrow Maximum \\ = 0 \rightarrow Saddle \\ > 0 \rightarrow Minimum \end{matrix} \qquad (2.13)$$

---

[11] The off-diagonal terms of the second-order derivative are all zero due to orthogonality considerations and are hence omitted.

The solution of the second derivative thus yields a matrix of eigenvalues, known as the Hessian Matrix. Conventionally the eigenvalues are denoted λ_1, λ_2, and λ_3 respectively.

Through these eigenvalues, the nature of the BCP can be determined and classified via a nomenclature consisting of a rank and signature value (ω, σ). The rank, ω, represents the number of nontrivial eigenvalues, while the signature value is the sum of all three senses of diagonal eigenvalues. As such, there are four key classifications:

(3, -3) These are peaks in the charge density, and correspond to points were the curvatures are negative in all three dimensions. Therefore, the charge density is maxima at r_C, and thus indicate nuclear positions.

(3, -1) These are saddle points in the charge density that correspond to two curvatures being negative and one positive. At r_C, the density is thus a maxima in the plane defined by the axes of the two negative curvatures, while the density is a minima perpendicular to the plane. These peaks occur at BCPs.

(3, +1) These are known as pales and consist of two positive curvatures and one negative. In contrast to (3, -1) types, the density is at a minimum at r_C in the plane defined by the axes of the two positive curvatures and maxima in the direction perpendicular to the plane. These occur at the centre of ring structures.

(3, +3) These are pits consisting of three positive curvatures with a minimal charge density at r_C. These can be found in cage structures.

The use of this classification allows one to identify the position of nuclei, BCPs, as well as ring and cage structures in molecules.

As well as classifying the BCPs, the eigenvalues of the Hessian matrix can also be used to determine the nature of the bonds. To this end, a measure known as the bond ellipticity is of particular interest, and provides a measure of the extent of the σ- and π-bonding in a molecular bond.

The ellipticity of a bond is calculated using the eigenvalues of the Hessian matrix according to:

$$\varepsilon = \frac{\lambda_1 - \lambda_2}{\lambda_2} \qquad (2.14)$$

where λ_1 and λ_2 are the eigenvalues perpendicular to the bond vector.

Where ε = 0, the bond will be spherical i.e. no elliptical character, and indicates a σ-bond. Conversely, when $\varepsilon > 0.1$, the bond possesses distinct π-bonding character.

2.6.2.2 Covalent, Ionic, and Hydrogen Bonds

As well as allowing the determination of the σ- and π-bonding character of a bond, the Laplacian function can also be used to determine whether a bond is covalent, covalent polar shared, or ionic.

Table 2.3 Summary of Bader bond-type classifications according to energy density descriptors[45].

Bader classification	Bond type	$\rho(r_{BCP})$	$\nabla^2\rho(r_{BCP})$	$G(r_{BCP})/\rho(r_{BCP})$	$H(r_{BCP})$
Closed shell	Ionic	Small	> 0	≥ 1	> 0
Open shell	Polar shared	Large	Arbitrary	≥ 1	< 0
	Covalent	Large	< 0	< 1	< 0

Table 2.3 presents the criteria for each bond type, which are obtained from the QTAIM topological analysis. $\rho(r_{BCP})$ is the electron density at the BCP along the bond, while $\nabla^2\rho(r_{BCP})$ is the Laplacian, $G(r_{BCP})/\rho(r_{BCP})$ and $H(r_{BCP})$ are the kinetic energy density and the total energy at the BCP, respectively:

$$H(r_{BCP}) = G(r_{BCP}) + V(r_{BCP}) \qquad (2.15)$$

where

$$G(r_{BCP}) = \frac{3}{10}(3\pi^2)^{\frac{2}{3}}\rho^{\frac{5}{3}}(r_{BCP}) + \frac{1}{6}\nabla^2\rho(r_{BCP}) \qquad (2.16)$$

where $\rho(r_{BCP})$ is the charge density at the BCP, and

$\nabla^2\rho(r_{BCP})$ the Laplacian at the BCP.

$$V(r_{BCP}) = \frac{1}{4}\nabla^2\rho(r_{BCP}) - 2G(r_{BCP}) \qquad (2.17)$$

BCPs found along the trajectory of suspected hydrogen bonds can also be verified through these parameters and generally take the form of a closed shell (ionic) interaction (*cf.* Table 2.3). However, work by Flensburg *et al.*[47] have revealed that hydrogen bonds can also adopt the form of an open shell interaction. Espinosa *et al.*[48] have therefore suggested that the determination of hydrogen bonding is better achieved via the assessment of the bond's λ_3 eigenvalue. A positive λ_3 eigenvalue at the BCP of a suspected hydrogen bond is consistent with the presence of a real hydrogen bond.

2.7 MMs and Semi-Empirical *β*

MMs provide a unique expression of a material's (hyper)polarizability, as charge density analyses provide a solid-state value. Meanwhile, experimental techniques such as hyper-Rayleigh scattering (HRS) only yield solution-phase values, and quantum-chemical calculations provide gas-phase values. A multipole-derived β value therefore affords information regarding the potential effects of solvation and intermolecular forces, when compared to HRS and theoretical values. This unique feature of MMs points to their invaluable efficacy in the study of structure-property relationships.

Until recently, the determination of the hyperpolarizabilities through charge density studies was nontrivial. However, thanks to the work of Higginbotham *et al.*[49], a static β_0 value[12] is accessible through the use of the Cartesian moments of the molecular charge density (*cf.* §1.2.2.4, & Eq. 1.10)

The extraction of the Cartesian moments of the molecular charge density can be carried out using a variety of different spatial partitioning methods, whereby the values of β vary with the choice of method. In this thesis, the Stockholder and the Bader partitioning have been employed, and the results have been compared. The basics of these partitioning schemes are outlined below.

2.7.1 Stockholder Partitioning

Stockholder spatial partitioning was devised by Hirshfeld[50] and assigns charge density to the constituent atoms of a molecular structure through the application of a continuous sampling function. The charge density assigned to an atom *i* is given by:

$$\rho_i = w_i(r)\rho_{TOTAL} \tag{2.18}$$

with

$$w_i(r) = \frac{\rho_{spherical\,atom}(r)}{\rho_{promolecule}(r)} \tag{2.19}$$

where $\rho_{spherical\,atom}$ is the spherical charge density of the individual atom, and

---

[12] A static β_0 value describes the hyperpolarisability of a material in the absence of dispersion phenomena.

$\rho_{promolecule}$ the spherical charge density of the pro-molecule.

The Stockholder regime is completely general, requires no arbitrary placing of boundary surfaces, and produces well-defined atomic fragments that differ from the free atoms only in as far as the molecule itself differs from a superposition of free-atom densities.

After the charge density has been partitioned and assigned to specific atoms based on the weighting function (Eq. 2.18), properties inherently linked to the molecular charge density can be determined through use of an expectation value:

$$\langle A\rangle = \int_V \hat{A}\,\rho(r)dr \tag{2.20}$$

where $\hat{A}$ is the operator associated with the property being extracted, and

V the volume of integration.

The electronic charge of each atom within the structure is thus given by:

$$\langle Q\rangle = -\int_V \rho(r)dr \tag{2.21}$$

The net atomic charge is then obtained from adding this value to the nuclear charge of the atom, Z.

2.7.2 Bader Partitioning

Bader partitioning[45,46] separates the charge based on the topology of the total electron density of the molecule. This method uses atomic basins of nuclei, which are defined as discrete regions of space formed by interatomic surfaces. The interatomic spaces are defined by the zero-flux boundary condition:

$$\nabla\rho(r).n(r) = 0 \tag{2.22}$$

where $\nabla\rho(r)$ is the first derivative of the charge density, and

$n(r)$ the surface normal.

Using Eq 2.21 the total electronic charge of each atom can be calculated by exchanging the volume of integration, V for the atomic basin, Ω, the space enclosed by a zero-flux surface (*cf.* Eq 2.22), including the nucleus.

2.8 Hyper-Rayleigh Scattering (HRS)

HRS was discovered in 1977, in an experiment that attempted to optimise a hyper-Raman set up for CCl_4[51]. Since then, many research groups have endeavoured to build an operational HRS setup due to its potential to directly provide solution-based measures of the hyperpolarizability tensor of a material.

All HRS experiments reported within this thesis were carried out by K. Clays, Y. de Coene or J. Perez-Moreno at the University of Leuven (Belgium). Even though the HRS setup used there has already been reported[52], a brief outline is given herein for completeness.

All compounds studied were initially dissolved in solutions of varying concentrations and deposited into quartz cuvettes. The prepared samples were subsequently subjected to incident light radiation of 800 nm, supplied in 130 fs pulses via the fundamental frequency of a mode-locked femtosecond Ti:Sapphire laser (Tsunami, Spectra Physics), which was pumped by an Ar+ laser at a repetition frequency of 80 MHz with an average power of ~1.8 W. The scattered second-harmonic (SH) light was collected via a condenser lens system, positioned at 90° scattering geometry in the X-Y plane, and passed through an interference filter. This filtered SH signal was detected via a photomultiplier tube (PMT). For polarization-resolved measurements, the vertical (V) and horizontal (H) polarized states of the scattered SH radiation were selected by inserting an analyzer between the interference filter and the PMT. The results were derived from sample measurements at five successively diluted concentrations, c/5 (c = 1-5). Data were analyzed using the external reference sample, tris(4-(dimethylamino)phenyl)methylium chloride ($C_{25}N_3H_{30}Cl$), more commonly called Crystal Violet ($\beta_{zzz} = 338 \pm 60 \times 10^{-30}$ esu in methanol at 800 nm), using a parent concentration of $c = 1.31 \times 10^{-3}$ M. The demodulation technique was used to discriminate multi-photon fluorescence contributions from the signal, so that the dynamic first hyperpolarizability, β_{HRS}, could be determined[53], which refers to the total β value, averaged over all orientations.

2.9 X-Ray Wave-function Refinement (XWR)

The X-ray wave-function refinement (XWR) method[54] was employed in this thesis via the program TONTO[55]. The XWR method is a two-stage refinement process that consists of a Hirshfeld Atom Refinement (HAR)[56,57] of the atomic coordinates and ADPs of the compound being studied, followed by the X-ray constrained wave-function fitting (XCW)[57,58].

A validation of this method has recently been undertaken by Woińska *et al.*[54] on a broad range of high-resolution amino acid data sets, and revealed that the XWR method yields better fit and, better results than traditional MMs.

2.9.1 Hirshfeld Atom Refinement (HAR)

The HAR process[56,57] applies a self-consistent field (SCF) calculation to a non-interacting molecule, using the atomic coordinates and ADPs from the IAM refinement of the compound under investigation. Initial attempts to refine the ADPs of any hydrogen atoms in the compound under investigation is usually undertaken and assessed for their viability. Where the ADPs are found to be highly flat and/or non-positive definite (NDP), they can be refined isotropically, or set to values generated by the SHADE 2.1 server[28] and fixed throughout subsequent refinements.

2.9.2 X-ray Constrained Wave-function fitting (XCW)

The refined atomic coordinates and ADPs are subsequently used as a starting point for the construction of an 'experimental' wave-function[57,58]. The resulting wave-function of the molecule enables the generation of theoretical X-ray structure factors, which are subsequently subjected to a correction for thermal motion. These calculated structure factors are then compared with the experimentally derived X-ray structure factors, whereupon the wave-function is optimised, and is constrained by the experimental data. This refinement procedure employs the Lagrange multiplier, λ_L (*cf.* Eq. 2.23), to minimize the wave-function energy *E*, subject to a penalty function that incorporates a test statistic (χ^2). The associated Lagrange equation is given as:

$$L(\boldsymbol{c}, \varepsilon_L, \lambda_L) = E(\boldsymbol{c}, \varepsilon_L) - \lambda_L[\chi^2(\boldsymbol{c}) - \Delta] \qquad (2.23)$$

where ***c*** are the molecular-orbital coefficients,

ε_L the Lagrange multipliers related to the orthogonality of the orbitals,

Δ the desired error in χ^2, whereby

χ^2 is defined as:

$$\chi^2 = \frac{1}{N_r - N_p} \sum_{\boldsymbol{h}}^{N_r} \frac{[F(h) - F^*(h)]^2}{\sigma^2(h)} \tag{2.24}$$

where N_r and N_p are the number of h reflections and parameters, respectively,

F and F^* the calculated and experimental structure factors, respectively, and

σ^2 is the error in the structure factor.

The χ^2 test statistic was chosen by the system developers due to its sensitivity to small differences in a fit compared to the R-factor[59], and its ability to incorporate the experimentally measured error in each structure factor.

2.9.3 Analysis of XWR Results

Once complete, the resulting X-ray wave-function can be used to extract a plethora of information on the compound under investigation e.g. full QTAIM topological analysis via programs that can read wave-function files such as AIM2000[60] or Multiwfn[61]. Throughout this thesis, the program Multiwfn was used for the QTAIM topological analysis of the materials studied.

Meanwhile, the molecular dipole moments, refractive indices, and (hyper)polarizability tenors can be calculated using TONTO by applying coupled perturbed Hartree–Fock (CPHF) routines to an XWR-derived wave-function[62,63]. This method to determine molecular properties from the XWR wave-function has been tested on a variety of organic and organometallic chromophores[63], and have obtained results in good agreement with DFT-derived values.

2.10 Quantum Chemical Calculations

Quantum chemical calculations can be carried out using a variety of different methods, Density Functional Theory (DFT) being the most common. DFT is a computational method of modeling the electronic structure of atoms and molecules, from which salient information can then be extracted. The method is described in two seminal publications by Hohenberg and Kohn[64] and, Kohn and Sham[65].

The work of Hohenberg and Kohn deals with an interacting, inhomogeneous electron gas in an external potential. Their results show that a universal functional of the electron density of the gas exists, which is independent of the external potential acting upon it. The existence of the functional permits the formation of an energy functional, whose minimum value corresponds to the ground state electronic configuration of the gas.

Kohn and Sham built upon the work of Hohnenberg and Kohn through the use of approximation methods that treat the electrons as non-interacting. This is achieved through the construction of an 'effective' potential. Simplification to a non-interacting electron system allows for the wave-function of the system to be described via a single Slater determinant and results in a set of self-consistent equations, analogous to the Hartree-Fock equations. For further information on the Hartree-Fock method and Slater determinants the reader is directed to the literature[66].

All DFT calculations outlined in this thesis were carried out using the Kohn-Sham formalism as applied in either the Gaussian09 suite[67] or GAMESS[68,69]. Where possible, X-ray diffraction-determined structures were used as the initial starting point for the molecular geometry. When diffraction data were not available, the structure was assembled, using *a priori* knowledge based on chemical intuition via either GaussView[70] for Gaussian09 or, MacMolPlt[71] for GAMESS.

Throughout this thesis, previous literature was consulted when choosing basis sets and functionals. Initially, the energy of the compound under investigation are optimized so that the structure is in its ground state configuration. Once optimised, properties of the compound such as full (hyper)polarizability tensors can be extracted. DFT methods also allow the generation of molecular orbitals eg, HOMO, LUMO, LUMO+1, etc., and the corresponding orbital diagrams to study the molecular charge transfer within a structure upon excitation to higher energy states can be used.

2.11 References

(1) Blake, A. J.; Cole, J. M.; Evans, J. S. O.; Main, P.; Parsons, S.; Watkin, D. J.; Clegg, W. *Crystal Structure Analysis: Principles and Practice*, 2 edition.; OUP Oxford: Oxford ; New York, 2009.

(2) Clegg, W. *Crystal Structure Determination*; OUP Oxford: Oxford ; New York, 1998.

(3) Rigaku. *CrystalClearTM 2.0*; Rigaku (Europe), Sevenoaks, Kent TN15 6QY, England.

(4) Blessing, R. H. An Empirical Correction for Absorption Anisotropy. *Acta Crystallogr. A* **1995**, *51* (1), 33–38.

(5) Blessing, R. H. Outlier Treatment in Data Merging. *J. Appl. Crystallogr.* **1997**, *30* (4), 421–426.

(6) Farrugia, L. J. *WinGX* and *ORTEP for Windows* : An Update. *J. Appl. Crystallogr.* **2012**, *45* (4), 849–854.

(7) Blessing, R. H. Data Reduction and Error Analysis for Accurate Single Crystal Diffraction Intensities. *Crystallogr. Rev.* **1987**, *1* (1), 3–58. https://doi.org/10.1080/08893118708081678.

(8) Sheldrick, G. M. A Short History of *SHELX*. *Acta Crystallogr. A* **2008**, *64* (1), 112–122.

(9) Sheldrick, G. M. *XPREP in SHELXTL*; Siemens Analytical X-ray Instruments, Inc.: Madison, Wisconsin, U.S.A., 1995.

(10) Henn, J.; Meindl, K. Two Common Sources of Systematic Errors in Charge Density Studies. *Int. J. Mater. Chem. Phys.* **2016**, *1* (3), 417–430.

(11) Coppens, P. Charge Densities Come of Age. *Angew. Chem. Int. Ed.* **2005**, *44* (42), 6810–6811.

(12) Coppens, P.; Iversen, B.; Larsen, F. K. The Use of Synchrotron Radiation in X-Ray Charge Density Analysis of Coordination Complexes. *Coord. Chem. Rev.* **2005**, *249* (1–2), 179–195.

(13) Gatti, C.; Macchi, P. *Modern Charge-Density Analysis*; Springer Science & Business Media, 2012.

(14) Coppens, P.; Guru Row, T. N.; Leung, P.; Stevens, E. D.; Becker, P. J.; Yang, Y. W. Net Atomic Charges and Molecular Dipole Moments from Spherical-Atom X-Ray Refinements, and the Relation between Atomic Charge and Shape. *Acta Crystallogr. Sect. A* **1979**, *35* (1), 63–72.

(15) Bentley, J.; Stewart, R. F. Core Deformation Studies by Coherent X-Ray Scattering. *Acta Crystallogr. Sect. A* **1974**, *30* (1), 60–67.

(16) Lennard-Jones, J. E. The Electronic Structure of Some Diatomic Molecules. *Trans. Faraday Soc.* **1929**, *25* (0), 668–686.

(17) Coppens, P. *X-Ray Charge Densities and Chemical Bonding*; Oxford University Press: Chester, England : Oxford ; New York, 1997.

(18) Hansen, N. K.; Coppens, P. Testing Aspherical Atom Refinements on Small-Molecule Data Sets. *Acta Crystallogr. A* **1978**, *34* (6), 909–921.

(19) Clementi, E.; Raimondi, D. L. Atomic Screening Constants from SCF Functions. *J. Chem. Phys.* **1963**, *38* (11), 2686–2689.

(20) Stewart, R. F. V. One-Electron Density Functions and Many-Centered Finite Multipole Expansions. *Isr. J. Chem.* **1977**, *16* (2–3), 124–131.

(21) Volkov, A; Macchi, P; Farrugia, L. J; Gatti, C; Mallinson, C; Richter, T; Koritsanszky, T. *XD2006 - a Computer Program for Multipole Refinement, Topological Analysis of Charge Densities and Evaluation of Intermolecular Energies from Experimental or Theoretical Structure Factors.*; 2006.

(22) Stewart, R. F.; Davidson, E. R.; Simpson, W. T. Coherent X-Ray Scattering for the Hydrogen Atom in the Hydrogen Molecule. *J. Chem. Phys.* **1965**, *42* (9), 3175–3187.

(23) Madsen, A. Ø. Modeling and Analysis of Hydrogen Atoms. In *Electron Density and Chemical Bonding I: Experimental Charge Density Studies*; Stalke, D., Ed.; Structure and Bonding; Springer Berlin Heidelberg: Berlin, Heidelberg, 2012; pp 21–52.

(24) Blessing, R. H. On the Differences between X-Ray and Neutron Thermal Vibration Parameters. *Acta Crystallogr. B* **1995**, *51* (5), 816–823.

(25) Madsen, A. Ø.; Hoser, A. A. SHADE3 Server: A Streamlined Approach to Estimate H-Atom Anisotropic Displacement Parameters Using Periodic Ab Initio Calculations or Experimental Information. *J. Appl. Crystallogr.* **2014**, *47* (6), 2100–2104.

(26) Lübben, J.; Bourhis, L. J.; Dittrich, B. Estimating Temperature-Dependent Anisotropic Hydrogen Displacements with the Invariom Database and a New Segmented Rigid-Body Analysis Program. *J. Appl. Crystallogr.* **2015**, *48* (6), 1785–1793.

(27) Allen, F. H.; Kennard, O.; Watson, D. C.; Brammer, L.; Orpen, A. G.; Taylor, R. Tables of Bond Lengths Determined by X-Ray and Neutron Diffraction. Part 1. Bond Lengths in Organic Compounds. *J. Chem. Soc. Perkin Trans. 2* **1987**, No. 12, S1–S19.

(28) Madsen, A. Ø. *SHADE* Web Server for Estimation of Hydrogen Anisotropic Displacement Parameters. *J. Appl. Crystallogr.* **2006**, *39* (5), 757–758.

(29) Schomaker, V.; Trueblood, K. N. On the Rigid-Body Motion of Molecules in Crystals. *Acta Crystallogr. B* **1968**, *24* (1), 63–76.

(30) Munshi, P.; Madsen, A. Ø.; Spackman, M. A.; Larsen, S.; Destro, R. Estimated H-Atom Anisotropic Displacement Parameters: A Comparison between Different Methods and with Neutron Diffraction Results. *Acta Crystallogr. A* **2008**, *64* (4), 465–475.

(31) Madsen, A. Ø.; Sørensen, H. O.; Flensburg, C.; Stewart, R. F.; Larsen, S. Modeling of the Nuclear Parameters for H Atoms in X-Ray Charge-Density Studies. *Acta Crystallogr. A* **2004**, *60* (6), 550–561.

(32) Clementi, E.; Roetti, C. Roothaan-Hartree-Fock Atomic Wavefunctions: Basis Functions and Their Coefficients for Ground and Certain Excited States of Neutral and Ionized Atoms, Z≤54. *At. Data Nucl. Data Tables* **1974**, *14* (3–4), 177–478.

(33) Macchi, P.; Coppens, P. Relativistic Analytical Wave Functions and Scattering Factors for Neutral Atoms beyond Kr and for All Chemically Important Ions up to I−. *Acta Crystallogr. A* **2001**, *57* (6), 656–662.

(34) Su, Z.; Coppens, P. Nonlinear Least-Squares Fitting of Numerical Relativistic Atomic Wave Functions by a Linear Combination of Slater-Type Functions for Atoms with Z = 1–36. *Acta Crystallogr. A* **1998**, *54* (5), 646–652.

(35) Volkov, A.; Li, X.; Koritsanszky, T.; Coppens, P. Ab Initio Quality Electrostatic Atomic and Molecular Properties Including Intermolecular Energies from a Transferable Theoretical Pseudoatom Databank. *J. Phys. Chem. A* **2004**, *108* (19), 4283–4300.

(36) Dominiak, P. M.; Volkov, A.; Li, X.; Messerschmidt, M.; Coppens, P. A Theoretical Databank of Transferable Aspherical Atoms and Its Application to Electrostatic Interaction Energy Calculations of Macromolecules. *J. Chem. Theory Comput.* **2007**, *3* (1), 232–247.

(37) Volkov, A.; Messerschmidt, M.; Coppens, P. Improving the Scattering-Factor Formalism in Protein Refinement: Application of the University at Buffalo Aspherical-Atom Databank to Polypeptide Structures. *Acta Crystallogr. D Biol. Crystallogr.* **2007**, *63* (2), 160–170.

(38) Hübschle, C. B.; Dittrich, B. MoleCoolQt – a Molecule Viewer for Charge-Density Research. *J. Appl. Crystallogr.* **2011**, *44* (1), 238–240.

(39) Mallinson, P. R.; Koritsanszky, T.; Elkaim, E.; Li, N.; Coppens, P. The Gram–Charlier and Multipole Expansions in Accurate X-Ray Diffraction Studies: Can They Be Distinguished? *Acta Crystallogr. A* **1988**, *44* (3), 336–343.

(40) Trueblood, K. N.; Bürgi, H.-B.; Burzlaff, H.; Dunitz, J. D.; Gramaccioli, C. M.; Schulz, H. H.; Shmueli, U.; Abrahams, S. C. Atomic Dispacement Parameter Nomenclature. Report of a Subcommittee on Atomic Displacement Parameter Nomenclature. *Acta Crystallogr. A* **1996**, *52* (5), 770–781.

(41) Kuhs, W. F. Generalized Atomic Displacements in Crystallographic Structure Analysis. *Acta Crystallogr. A* **1992**, *48* (2), 80–98.

(42) Herbst-Irmer, R.; Henn, J.; Holstein, J. J.; Hübschle, C. B.; Dittrich, B.; Stern, D.; Kratzert, D.; Stalke, D. Anharmonic Motion in Experimental Charge Density Investigations. *J. Phys. Chem. A* **2013**, *117* (3), 633–641.

(43) Meindl, K.; Herbst-Irmer, R.; Henn, J. On the Effect of Neglecting Anharmonic Nuclear Motion in Charge Density Studies. *Acta Crystallogr. A* **2010**, *66* (3), 362–371.

(44) Hirshfeld, F. L. Can X-Ray Data Distinguish Bonding Effects from Vibrational Smearing? *Acta Crystallogr. Sect. A* **1976**, *32* (2), 239–244.

(45) Bader, R. F. W. Atoms in Molecules. *Acc. Chem. Res.* **1985**, *18* (1), 9–15.

(46) Bader, R. F. W. *Atoms in Molecules: A Quantum Theory*; Clarendon Press, 1994.

(47) Flensburg, C.; Larsen, S.; Stewart, R. F. Experimental Charge Density Study of Methylammonium Hydrogen Succinate Monohydrate. A Salt with a Very Short O-H-O Hydrogen Bond. *J. Phys. Chem.* **1995**, *99* (25), 10130–10141.

(48) Espinosa, E.; Souhassou, M.; Lachekar, H.; Lecomte, C. Topological Analysis of the Electron Density in Hydrogen Bonds. *Acta Crystallogr. B* **1999**, *55* (4), 563–572.

(49) Higginbotham, A. P.; Cole, J. M.; Blood-Forsythe, M. A.; Hickstein, D. D. Identifying and Evaluating Organic Nonlinear Optical Materials via Molecular Moments. *J. Appl. Phys.* **2012**, *111* (3), 033512.

(50) Hirshfeld, F. L. Bonded-Atom Fragments for Describing Molecular Charge Densities. *Theor. Chim. Acta* **1977**, *44* (2), 129–138.

(51) Schmid, W. J.; Schrötter, H. W. Direct Observation of the Twisting Vibration in Tetrachloroethylene through the Hyper-Raman Effect. *Chem. Phys. Lett.* **1977**, *45* (3), 502–503.

(52) Clays, K.; Persoons, A. Hyper-Rayleigh Scattering in Solution. *Phys. Rev. Lett.* **1991**, *66* (23), 2980–2983.

(53) Olbrechts, G.; Strobbe, R.; Clays, K.; Persoons, A. High-Frequency Demodulation of Multi-Photon Fluorescence in Hyper-Rayleigh Scattering. *Rev. Sci. Instrum.* **1998**, *69* (6), 2233–2241.

(54) Woińska, M.; Jayatilaka, D.; Dittrich, B.; Flaig, R.; Luger, P.; Woźniak, K.; Dominiak, P. M.; Grabowsky, S. Validation of X-Ray Wavefunction Refinement. *ChemPhysChem* **2017**, *18* (23), 3334–3351.

(55) Jayatilaka, D.; Grimwood, D. J. Tonto: A Fortran Based Object-Oriented System for Quantum Chemistry and Crystallography. In *Computational Science — ICCS 2003*; Sloot, P. M. A., Abramson, D., Bogdanov, A. V., Gorbachev, Y. E., Dongarra, J. J., Zomaya, A. Y., Eds.; Lecture Notes in Computer Science; Springer Berlin Heidelberg, 2003; pp 142–151.

(56) Capelli, S. C.; Bürgi, H.-B.; Dittrich, B.; Grabowsky, S.; Jayatilaka, D. Hirshfeld Atom Refinement. *IUCrJ* **2014**, *1* (5), 361–379.

(57) Jayatilaka, D. Wave Function for Beryllium from X-Ray Diffraction Data. *Phys. Rev. Lett.* **1998**, *80* (4), 798–801.

(58) Jayatilaka, D.; Grimwood, D. J. Wavefunctions Derived from Experiment. I. Motivation and Theory. *Acta Crystallogr. A* **2001**, *57* (1), 76–86.

(59) Jayatilaka, D.; Dittrich, B. X-Ray Structure Refinement Using Aspherical Atomic Density Functions Obtained from Quantum-Mechanical Calculations. *Acta Crystallogr. A* **2008**, *64* (3), 383–393.

(60) Biegler-König, F.; Schönbohm, J.; Bayles, D. AIM2000 - A Program to Analyze and Visualize Atoms in Molecules. *J. Comput. Chem.* **2001**, *22* (5), 545–559.

(61) Lu, T.; Chen, F. Multiwfn: A Multifunctional Wavefunction Analyzer. *J. Comput. Chem.* **2012**, *33* (5), 580–592.

(62) Jayatilaka, D.; Munshi, P.; J. Turner, M.; K. Howard, J. A.; A. Spackman, M. Refractive Indices for Molecular Crystals from the Response of X-Ray Constrained Hartree–Fock Wavefunctions. *Phys. Chem. Chem. Phys.* **2009**, *11* (33), 7209–7218.

(63) Hickstein, D. D.; Cole, J. M.; Turner, M. J.; Jayatilaka, D. Modeling Electron Density Distributions from X-Ray Diffraction to Derive Optical Properties: Constrained Wavefunction versus Multipole Refinement. *J. Chem. Phys.* **2013**, *139* (6), 064108.

(64) Hohenberg, P.; Kohn, W. Inhomogeneous Electron Gas. *Phys. Rev.* **1964**, *136* (3B), B864–B871.

(65) Kohn, W.; Sham, L. J. Self-Consistent Equations Including Exchange and Correlation Effects. *Phys. Rev.* **1965**, *140* (4A), A1133–A1138.

(66) Slater, J. C. A Simplification of the Hartree-Fock Method. *Phys. Rev.* **1951**, *81* (3), 385–390.

(67) Frisch, M. J; Trucks, G. W; Schlegel, H. B.; Scuseria, G. E; Robb, M. A; Cheeseman, J. R; Scalmani, G; Barone, V; Mennucci, B; Petersson, G. A; et al. *Gaussian09*; Gaussian, Inc.: Wallingford CT, 2009.

(68) Gordon, M. S.; Schmidt, M. W. Advances in Electronic Structure Theory: GAMESS a Decade Later. In *Theory and Applications of Computational Chemistry: the first forty years*; Dykstra, C. E., Frenking, G., Kim, K. S., Scuseria, G. E., Eds.; Elsevier: Amsterdam, 2005; pp 1167–1189.

(69) Schmidt, M. W.; Baldridge, K. K.; Boatz, J. A.; Elbert, S. T.; Gordon, M. S.; Jensen, J. H.; Koseki, S.; Matsunaga, N.; Nguyen, K. A.; Su, S.; et al. General Atomic and Molecular Electronic Structure System. *J. Comput. Chem.* **1993**, *14* (11), 1347–1363.

(70) Dennington, R; Todd, K; Millam, J. *GaussView*; Semichem Inc: Shawnee Mission, KS, 2009.

(71) Bode, B. M.; Gordon, M. S. MacMolPlt: A Graphical User Interface for GAMESS. *J. Mol. Graph. Model.* **1998**, *16* (3), 133–138, 164.

Chapter 3

Relating the Structure of Geminal Amido Esters to their Molecular Hyperpolarizability

3.1 Introduction

Organic non-linear optical (NLO) materials are receiving increasing attention on account of their desirably fast, purely electronic, optical response times, which are particularly attractive for telecommunication applications, and the ease by which they can be manipulated for thin film technology. This contrasts with their inorganic counterparts, which exhibit NLO activity as a result of the much slower ionic displacement (*cf.* electronic charge-transfer in organic materials), and are largely insoluble. Moreover, recent advancements in thin-film fabrication methods have circumvented major historical limitations associated with organic NLO materials, especially thermal stability requirements. They have also voided the need for crystallographic non-centrosymmetry in second-order NLO materials. Consequently, the NLO potential of a material is now determined predominantly by examining the molecular first hyperpolarizability, β, rather than the traditionally-used analogous macroscopic parameter, the second-order optical susceptibility, χ^2.

Therefore, molecular factors that influence NLO phenomena are becoming the key consideration. To this end, various structure-function relationships have been established for organic NLO materials from studies over the last decade or so[1] which have become the basis for the rational and systematic design of new organic NLO chromophores at the molecular and supramolecular level. Within the realm of non-centrosymmetric molecular topologies for second-order nonlinear optics, one such relationship requires organic NLO materials to bear donor-π-acceptor type molecular architectures within which lies high intramolecular charge transfer facilitated through highly delocalized π-bond conjugation paths. At the slightly larger nanoscale, it is important to consider crystal field effects that exist between organic molecules, in order to anticipate any adverse molecular aggregation phenomena that may occur in the liquid or solid state.

Molecular design rules are becoming ever more accurate in their prediction of material properties of target compounds, given that these predictions are based on a growing number of case studies. This work extends the chemical diversity of such case studies via a report on a new series of five potential organic NLO chromophores that belong to the chemical family of geminal amido esters: (E)-ethyl 3-(phenylamino)-2-

(phenylcarbamoyl)acrylate (**35**); (E)-ethyl 3-(4-methylphenylamino)-2-(4-methylphenylcarbamoyl)acrylate (**36**); (E)-ethyl 3-(4-nitrophenylamino)-2-(2,5-methoxyphenylcarbamoyl)acrylate (**37**); (E)-ethyl 3-(2-chlorophenylamino)-2-(2-chloropheny lcarbamoyl)acrylate (**38**); and (E)-ethyl 3-(4-chlorophenylamino)-2-(4-chlorophenylcarbamoyl)acrylate (**39**). The chemical structures of **35-39** are shown in Fig. 3.1. The molecular structures and optical properties of **35-39** are herein determined, especially with respect to the NLO effect and the molecular first hyperpolarizability, *β*.

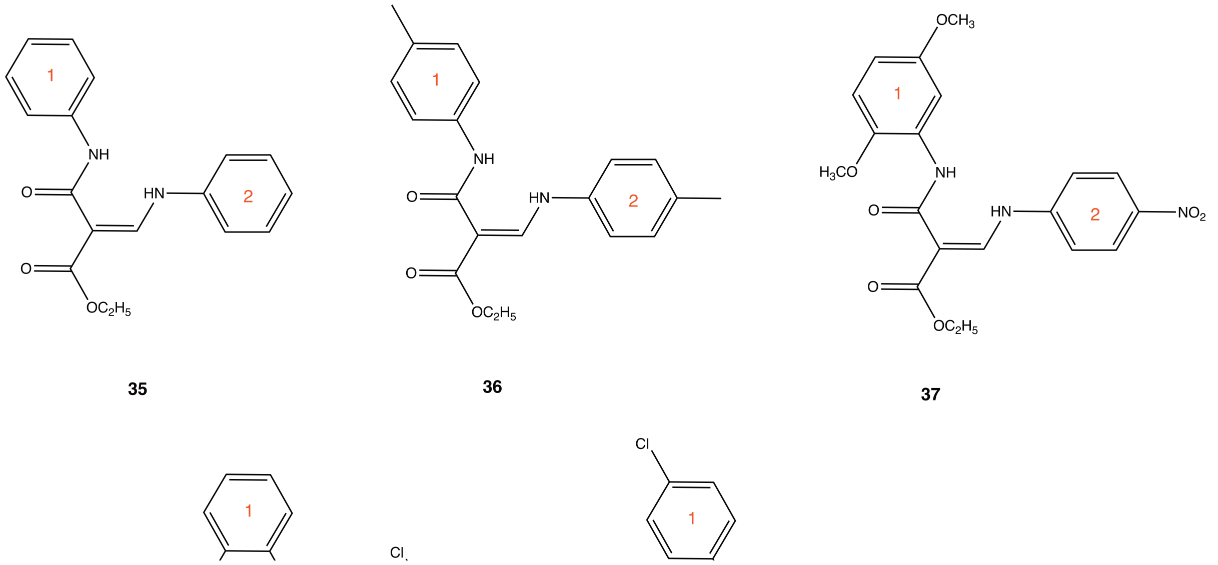

35 **36** **37**

Figure 3.1 A schematic diagram of the 5 NLO Chromophores under investigation.

The molecular hyperpolarizability, *β*, for these five subject chromophores is evaluated by three independent methods, which is important given the typically large errors (10-30%) that are associated with any given determination of *β* coefficients[2]. Two of these methods are already well established: i) calculations based on density functional theory (DFT)[3] and ii) hyper Rayleigh scattering measurements[4]. The third method (iii) derives *β* empirically from multipolar moments of each atom in a molecule that emanate from the multipolar modeling of molecular electron densities obtained by high-resolution X-ray diffraction data. This employs an empirical relation between multipolar moments of an atom and *β* which is based on the original theory of Robinson[5]. So far, this empirical method has been little exercised, since a sufficiently accurate correlation model between atomic multipolar moments and β was developed only recently[6]. That report demonstrated its successful application to three distinct types of NLO materials: two organic chromophores that exist in zwitterionic[7] or neutral[8] forms and a metal-organic compound[9]. Since that demonstration, one other study has used this method to successfully determine the molecular hyperpolarizability of an organic NLO chromophore[9]. Nevertheless, more case studies are needed to test the boundaries of this empirical approach.

This paper begins by assessing the molecular architecture of **35-39** by conventional single-crystal X-ray diffraction and complementary neutron diffraction techniques; with a particular focus on identifying the p-conjugated intramolecular charge transfer pathways. Subsequently, the linear and non-linear optical properties of **35-39** are assessed using a variety of materials characterization techniques such as UV-Vis spectroscopy, charge-density analysis, DFT calculations and hyper-Rayleigh scattering measurements. The study then considers crystal field effects associated with these molecules and an overall understanding of their NLO capabilities in different phase states. In this regard, β is rather informative since its enumeration via methods (i), (ii) and (ii) is undertaken in the gas, solution and solid state, respectively. This comparison of β values between methods is not only performed for this reason, but it is also discussed within the scope of augmenting the emerging evidence base of β evaluations via method (iii); while discussions that seek some level of consistency of β determined by independent methods are also presented, for assurance against the well-known accuracy issues associated with β evaluations. With this assurance in hand, the study concludes with an assessment of the potential of **35-39** to act as NLO chromophores, especially with a view to bespoke NLO device applications.

3.2. Experimental & Computational Methods

3.2.1 Synthesis and crystallization of 35-39

Compounds **35-39** were obtained from colleagues in India (P. Venkatesan and A. Ilangovan of Bharathidasan University) via a chemical synthesis route previously outlined[10] and presented in Fig 3.2. High yields (89-94 %) were achieved for all compounds except **37** (64 %).

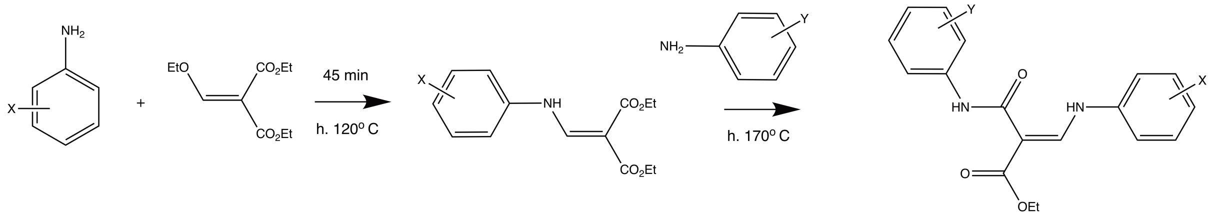

Figure 3.2 Outline of the chemical synthesis route for **35-39**.

High-quality single crystals of these compounds were obtained by slow evaporation methods using ethyl acetate as solvent for all samples except for **37**, which crystallized in dimethylsulfoxide.

3.2.2 Conventional single-crystal X-ray diffraction

The collection of conventional single-crystal X-ray diffraction data on these compounds was undertaken by T.-C. Lin & Dr P. Waddell. T.-C. Lin undertook initial processing and data reduction.

A single crystal of **35** (0.2 x 0.2 x 0.1 mm), **36** (0.3 x 0.2 x 0.1 mm), **37** (0.266 x 0.100 x 0.077 mm), **38** (0.100 x 0.312 x 0.299 mm), or **39** (0.4 x 0.3 x 0.3 mm) was mounted onto the in-house Rigaku Saturn 724+ CCD single-crystal X-ray diffractometer as per §2.2.1. Crystals were cooled to 120 K via a liquid N_2 cryostream, and subsequently maintained at this temperature for the duration of the data collection. Data were collected at ϑ = 25 ° with full-sphere reciprocal space coverage, using ω-scans with a scan width of 0.3 °. Data acquisition, collection and processing, including cell indexing, cell refinement, and data reduction was undertaken as per §2.2.2 and §2.2.3. Reduced data were corrected for X-ray absorption using an empirical model as per §2.2.4.

A conventional IAM crystal structure refinement was undertaken using SHELXL[11] (*cf* §2.2.5) and afforded the following statistics (*cf.* Table 3.1):

Table 3.1 A summary of the IAM structural refinement statistics of **35-39** using conventional X-ray diffraction techniques

	35	36	37	38	39
Chemical Formula	$C_{18}H_{18}N_2O_3$	$C_{20}H_{22}N_2O_3$	$C_{20}H_{21}N_3O_7$	$C_{18}H_{16}N_2O_3Cl_2$	$C_{18}H_{16}N_2O_3Cl_2$
a	7.0737(14)	18.7330(37)	9.3109(19)	14.6554(29)	18.6150(37)
b (Å)	13.4194(27)	11.9894(24)	30.3487(61)	7.6519(15)	11.9660(24)
c	16.9353(34)	15.4386(31)	6.9539(14)	15.5346(31)	15.4805(31)
α	90.00	90.00	90.00	90.00	90.00
β (°)	93.35(3)	91.62(3)	100.09(3)	91.77(3)	91.28(3)
γ	90.00	90.00	90.00	90.00	90.00
Z	4	8	4	4	8
Crystal System	Monoclinic	Monoclinic	Monoclinic	Monoclinic	Monoclinic
Space Group	$P2_1/c$	C_2/c	$P2_1/c$	$P2_1/n$	C_2/c
Sin(θ)/λ (Å^{-1})	0.68	0.86	0.62	0.89	0.72
R1 [I > 2σ(I)]	0.0597	0.0752	0.0840	0.0795	0.0721
wR2 [(I > 2σ(I)]	0.1545	0.2107	0.2327	0.3141	0.2073
GoF	1.171	1.115	1.418	1.339	1.307
Max / Min Residuals (Å^{-3})	0.36 / -0,18	0.48 / -0.45	0.68 / -0.43	0.99 / -1.00	0.33 / -0.38

3.2.3 High-resolution single-crystal X-ray diffraction for charge-density studies

3.2.3.1 Laboratory-based data collection for 38

The collection of charge-density quality X-ray diffraction data for compound **38** was undertaken by T.C. Lin & Dr P. Waddell. T.-C. Lin undertook initial processing and data reduction.

A single crystal of **38** (0.515 x 0.248 x 0.331 mm) was mounted onto the in-house Rigaku Saturn 724+ CCD single-crystal X-ray diffractometer as per §2.2.1. Crystals were cooled to 120 K and subsequently maintained at this temperature for the duration of the data collection. Data were collected at ϑ = 25°, 50°, and 65° detector positions with full-sphere reciprocal space coverage, using ω-scans with a scan width of 0.3°. The Rigaku CrystalClearTM 2.0 software package was employed for data acquisition, collection and processing with d*TREK (interfaced with CrystalClearTM 2.0) being used for cell indexing, cell refinement, and data reduction. Data acquisition, collection and processing, including cell indexing, cell refinement, and data reduction was undertaken as per §2.2.2 and §2.2.3. Reduced data were corrected for X-ray absorption using an empirical model as per §2.2.4. The three datasets (ϑ = 25°, 50°, and 65°) were then merged and scaled using a least-squares fit of the common reflections in XPREP[12].

3.2.3.2 Synchrotron-based data collection for 39

The collection of charge-density quality X-ray diffraction data for compound **39** was undertaken by Philip Pattison and T.-C. Lin. T.-C. Lin undertook initial processing and data reduction.

Charge-density quality data for **39** were collected using synchrotron-based single-crystal X-ray diffraction, at the Swiss-Norwegian beam line, BM01A, at the European Synchrotron Radiation Facility, Grenoble, France. A 0.030 x 0.052 x 0.055 mm^3 sized crystal was mounted onto a 6-circle KUMA kappa diffractometer, equipped with an ONYX detector from Oxford Diffraction and an Oxford Cryosystems CryostreamPlus. Data were collected and integrated using CrysAlisPro software, version 171.35.11a [13].

3.2.3.3 Structure solution and refinement of 38 and 39 from high-resolution X-ray diffraction data

A conventional IAM crystal structure refinement was undertaken by full matrix least square on F^2 using SHELXL[11] (*cf* §2.2.5) and afforded the following statistics (*cf.* Table 3.2):

Table 3.2 A summary of the IAM structural refinement statistics of **38-39** using high-resolution X-ray diffraction techniques

	38	39
Chemical Formula	$C_{18}H_{16}N_2O_3Cl_2$	$C_{18}H_{16}N_2O_3Cl_2$
a	14.5520(29)	18.5768(3)
b / Å	7.5870(15)	11.9368(1)
c	15.6000(31)	15.3607(1)
α	90.00	90.00
β / °	91.99(3)	92.03(1)
γ	90.00	90.00
Z	4	8
Crystal System	Monoclinic	Monoclinic
Space Group	$P2_1/n$	C_2/c
Sin(θ)/λ (Å^{-1})	0.98	1.08
R1 [I > 2σ(I)]	0.0477	0.0434
wR2 [(I > 2σ(I)]	0.1505	0.1306
GoF	1.109	1.076
Max / Min Residuals (Å^{-3})	0.50 / -0.65	1.06 / -0.43

3.2.4 Modeling hydrogen atoms by single-crystal Laue-based neutron diffraction

A. J. Edwards undertook the collection of neutron diffraction data. T. C. Lin undertook initial processing and data reduction.

Single crystals of **35** (0.5 x 0.6 x 0.4 mm) or **39** (0.6 x 0.6 x 0.75 mm), were mounted onto the ф axis of the KOALA Laue diffractometer at the Bragg Institute, ANSTO, Australia as per §2.4. Each sample was cooled to 120 K using a helium closed-cycle refrigerator and maintained at this temperature during the acquisition of 19 Laue images per sample. Each image was separated by 17° rotational increments in φ (perpendicular to the neutron beam), and neutron beam exposure times of 3 hours (**35**) or 2 hours 25 minutes (**39**) were applied. Integrated intensities were corrected for detector efficiency, wavelength-dependent incident intensity normalization, secondary extinction, and time-dependent effects ie, sample decay. Data with a $(\sin\vartheta/\lambda)_{max}$ cut-off of 0.99 Å^{-1} (**35**) or 0.80 Å^{-1} (**39**) were retained, which were then refined against a structural model via full-matrix least-squares procedures using SHELXL-97[11]. The final structural models, with R1 (I >2s(I)) of 0.0252 (**35**) or 0.0310 (**39**), comprised refined positional and ADPs for all atoms, following the location of all hydrogen atoms directly from Fourier difference maps.

3.2.5 Multipolar refinement of molecular charge densities

C. M. Ashcroft undertook all multipolar refinements.

Initially chemical equivalences were introduced into the model to constrain the charge assigned to certain atoms. Hydrogen atoms belonging to methyl and methylene groups respectively were constrained to be chemically equivalent. Additionally in the case of **38** the hydrogen atom partaking in hydrogen bonding was chemically constrained to have the same charge as another hydrogen atom in the structure related by symmetry. Once the refinement of the initial parameters had converged, multipolar terms were introduced starting with the refinement of monopoles and dipoles (only bond-directed dipoles for hydrogen atoms) on all atoms.

Once converged, quadrupolar and octupolar terms were refined for all non-hydrogen atoms except for Cl, O and N for which hexadecapolar terms are refined additionally. Normally the primary *s* and *p* character of N and O atoms would lead to questions about the appropriateness of such modelling however; some of the hexadecapolar populations for these atoms were found to be between 3-4 times greater than their standard error and so were included in the models. Refinement at the hexadecapolar level for carbon atoms was also attempted and a few significant populations were found to exist in the non-phenyl based carbon atoms. However; no major improvement was seen in the residual density plots or the deformation density maps. Additionally changes to structural properties were minimal. As such it was decided that refinement of carbon to the hexadecapolar level was not appropriate.

A κ parameter for each atom-type was employed. All κ values relating to non-hydrogen atoms were initially set at 1.0 and refined whereas the κ value for hydrogen atoms was fixed to the Stewart-Davidson-Simpson (SDS) value of 1.16[14]. An attempt to refine κ′ parameters was made, however they did not yield reasonable values and so were fixed at 1.0 for all non-hydrogen atoms and 1.2 for hydrogens (these are the standard values assigned by XD2006). At the final stages of refinement all chemical constraints were lifted except in **38** where the chemical constraints associated with the hydrogen atom partaking in hydrogen bonding was kept.

When modelling **39**, difficulties were encountered resulting in the presence of double peaks in some of the bonds as seen in the charge density maps. This was ameliorated to some extent through the removal of some of the high-angle data by setting the data set sin(θ)/λ threshold to 1.0 $Å^{-1}$. It was found that setting a threshold lower than 1.0 $Å^{-1}$ resulted in unreasonable values of (hyper)polarizability. On the other hand the charge density maps of **39** show promising features such as lone-pair phenomenon around the oxygen and chlorine atoms as would be expected. Similar lone-pair features are observed in the charge density maps of **38**.

Residual electron-density maps (*cf.* Appendix A, §A.1) of the final charge-density model of **38** were essentially featureless at the 0.1 $eÅ^{-3}$ level, with the exception of the areas around the chlorine atoms where 0.40 $eÅ^{-3}$ residual density was observed around the Cl(1) and Cl(2) atoms after being modeled up to the hexadecapolar level. The refinement of the structure of **39** proved to be more problematic, leading to residual maps that still show some large features in the region connecting the two aryl rings. In this region, electron density up to 0.43 $eÅ^{-3}$ was observed close to C(7), while electron density up to 0.45 $eÅ^{-3}$ was found around the chlorine atoms. Close inspection of the monopole populations and net atomic charges of the atoms in both models reveal a transfer of charge away from the Cl atoms in the *ortho-* substituted compound **38**, while in the case of **39** charge transfers toward the Cl atoms which are found in the *para*- position. This is further substantiated when one considers the critical points where it is observed that there is a change of bond type for the Cl-C bonds from covalent (**38**) to polar shared (**39**) *cf.* Appendix B, §B.1.

The final models were assessed via the Hirshfeld rigid bond test [15], which calculates the difference of mean-square displacement amplitudes (DMSDAs) in the bond directions. DMSDA values for **38** and **39** beyond 0.0010 Å^2 existed for O(2)-C(10) (**38**) and O(3)-C(11), C(14)-C(15), C(15)-C(16) (**39**). However, the associated correlations were monitored and deemed sufficiently small in order to ascertain an appropriate deconvolution of all bonding and thermal motion effects.

Least-squares refinement statistics on F for the final multipolar model yielded the following (*cf.* Table 3.3):

Table 3.3 A summary of the multipolar modelling (MM) refinement statistics of **38-39** using high-resolution X-ray diffraction techniques

	38	39
Sin(θ)/λ (Å^{-1})	0.98	1.00
R1 [F]	0.0389	0.0274
R$_w$ [F]	0.0295	0.0220
Data-parameter	18.04	17.17
Max / Min Residuals (Å^{-3})	0.40 / -0.29	0.43 / -0.11

3.2.6 Hyper-Rayleigh scattering measurements

Koen Clays and Javier Perez-Moreno at The University of Leuven, Belgium undertook HRS measurements.

A generic experimental set-up and operational procedures were used for the hyper-Rayleigh scattering[4] as per §2.8. Acetonitrile solutions of **35, 36** and **38** were prepared. The results were derived from sample measurements at five successively diluted concentrations, c/5 (c =1-5) where parent concentrations were c = 3.84 x 10^{-3} M (**35**); 3.84 x 10^{-3} M (**36**); 2.66 x 10^{-3} M (**38**). HRS measurements on **37** and **39** were also attempted, but no results were tractable owing to a lack of sufficient HRS signal. In this regard, the small quantities of sample available were a contributory factor, as were the relatively modest *β* values that this series of compounds are shown to exhibit, a deficit that is effectively magnified when considering that the measurements were conducted off-resonance.

3.2.7 Density functional theory calculations

Electrostatic moments and (hyper)polarizability values of **35-39** were calculated by DFT using Gaussian09[16] as per §2.10. For **35** and **39**, neutron-derived structures were directly imported into Gaussian09 and used as the starting point for DFT calculations. All other structures were imported into Gaussian from initial XRD structures. DFT calculations were carried out at the B3YLP/6-31+(d, p) level of theory. Initially, IAM-derived atomic position parameters were used to perform a ground-state geometry optimization that comprised finding the minimum on the potential energy surface of the ground state. All default settings for Gaussian09 were maintained. Subsequently, the components of the (hyper)polarizability tensor of the structure were calculated at the same level of theory.

3.3 Results & Discussion

3.3.1 Molecular Architectures and Intramolecular Charge Transfer

The molecular structures of **35-39** in the crystalline state, determined by conventional single-crystal X-ray diffraction analysis, are shown in Fig. 3.3(a-c), and they reveal some clear implications regarding their potential utility as NLO chromophores. All these structures are dipolar, which is pertinent since their propensity to exhibit NLO features is based on intramolecular charge transfer (ICT), which arises from π-conjugation across typical donor-π-acceptor (D-π-A) architectures.

The molecular structures of **35** and **36** feature a planar central backbone based on a 2-methylene-1,3-dione motif, connected to two aminophenyl substituents that adopt, relative to the backbone plane, dihedral angles of 18.5(2)° and 22.6(2)° for (**35**) and 10.5(2)° and 33.9(2)° for (**36**), respectively (Fig. 3.3(a)). The substantial deviation from co-planarity observed between this backbone and these aminophenyl rings will constrain **35-36** from reaching an optimum level of π-bonding between these fragments and consequently limit their ICT prospects.

Conversely, the structures of **37**-**39** reveal (Fig 3.3(b-c)) that one of the aminophenyl rings (henceforth defined as ring 1) adopt a coplanar arrangement with the backbone (dihedral angles ≤ 5°), indicating that in these structures the aminophenyl rings may participate in ICT more readily than those of **35** and **36**, as a result of more efficient π-conjugation in **37**-**39**. Among these three structures, **37** is particularly promising, as it contains ring 1 within a 2,5-dimethoxyphenylcarbamoyl moiety, to which is adjoined a 3-nitrophenyl moiety (featuring ring 2), thus producing an overall asymmetric architecture. Such asymmetry is attractive since it promotes dipolar D-p-A tendencies across a molecule, thereby enhancing ICT.

In the case of **38** and **39**, each aryl ring bears a donating Cl atom bound at the *ortho*- and *para*- position, respectively. Although usually an acceptor of charge owing to its inductive electron withdrawing effect, when bound to an aromatic ring, Cl is seen to behave differently with there being some movement of electrons away from the Cl into the delocalized region of the aryl ring; this mesomeric donating effect dominates, resulting in a reduction of polarization across the chloro-substituted aromatic unit.

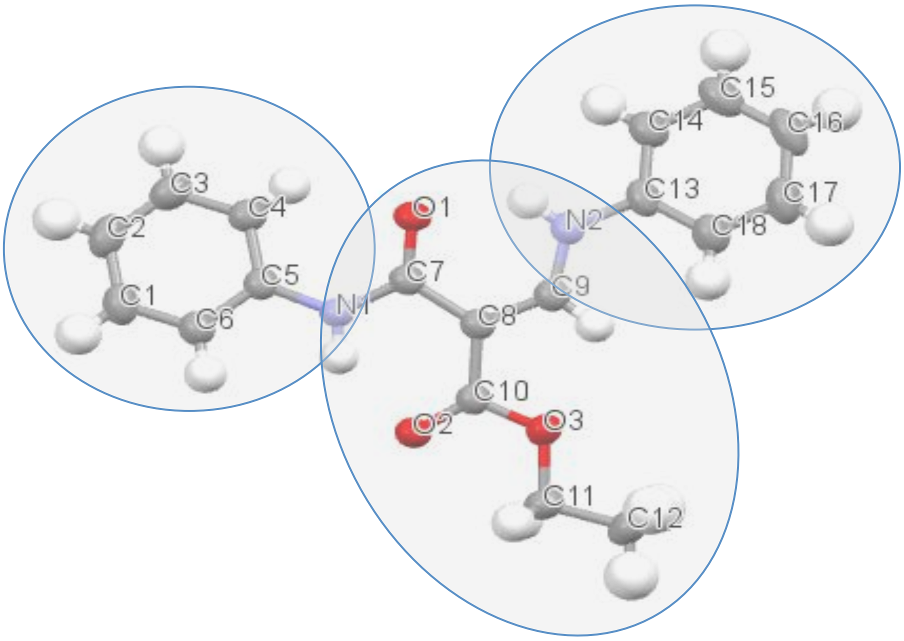

35

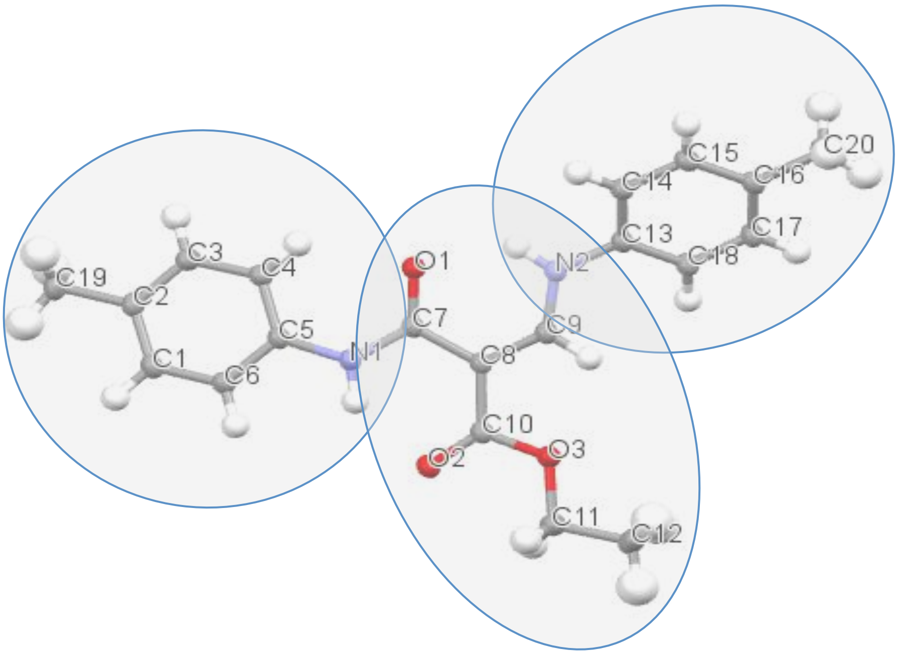

36

Figure 3.3(a). 50% atomic displacement parameter (ADP) plots (T = 120K) and D-π-A motif of **35-36**. Shaded regions enclose co-planar atoms.

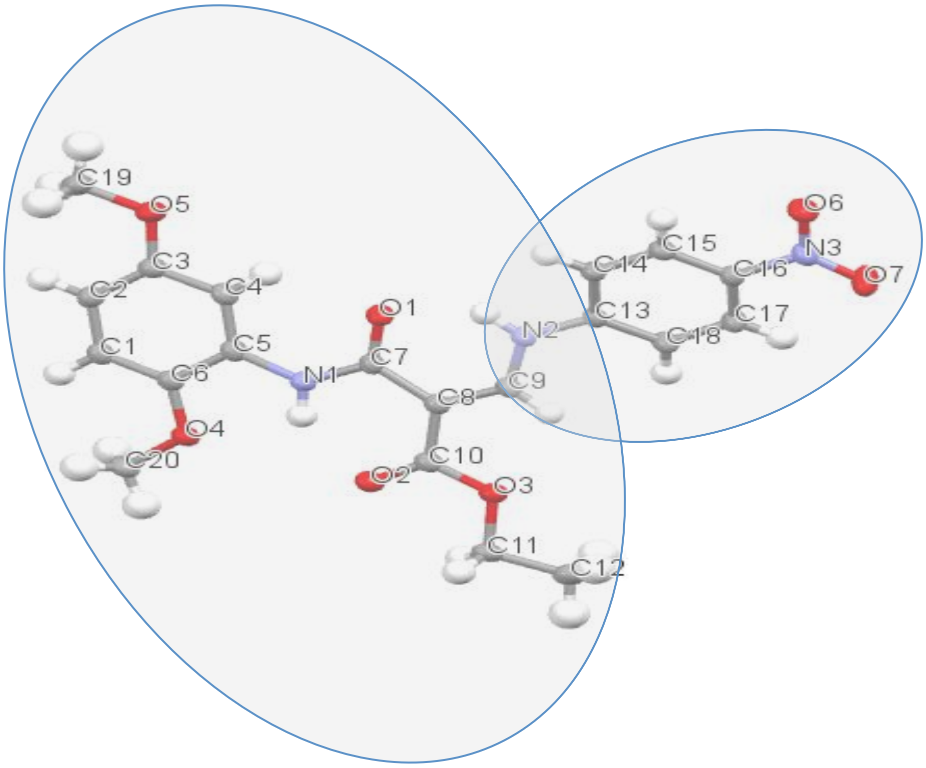

37

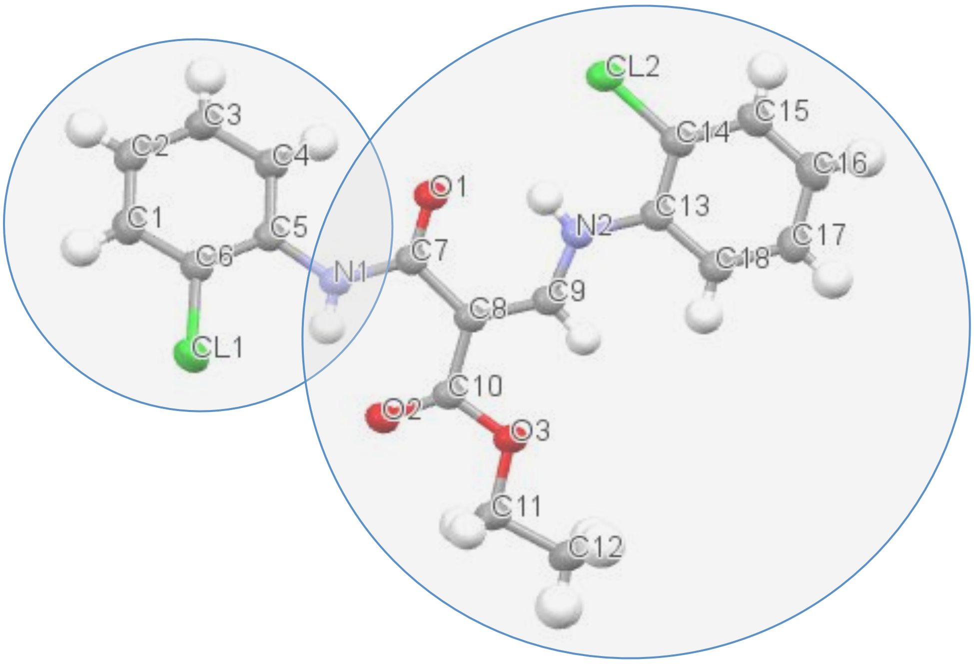

38

Figure 3.3(b). 50% atomic displacement parameter (ADP) plots (T = 120K) and D-p-A motif of **37-38**. Shaded regions enclose co-planar atoms.

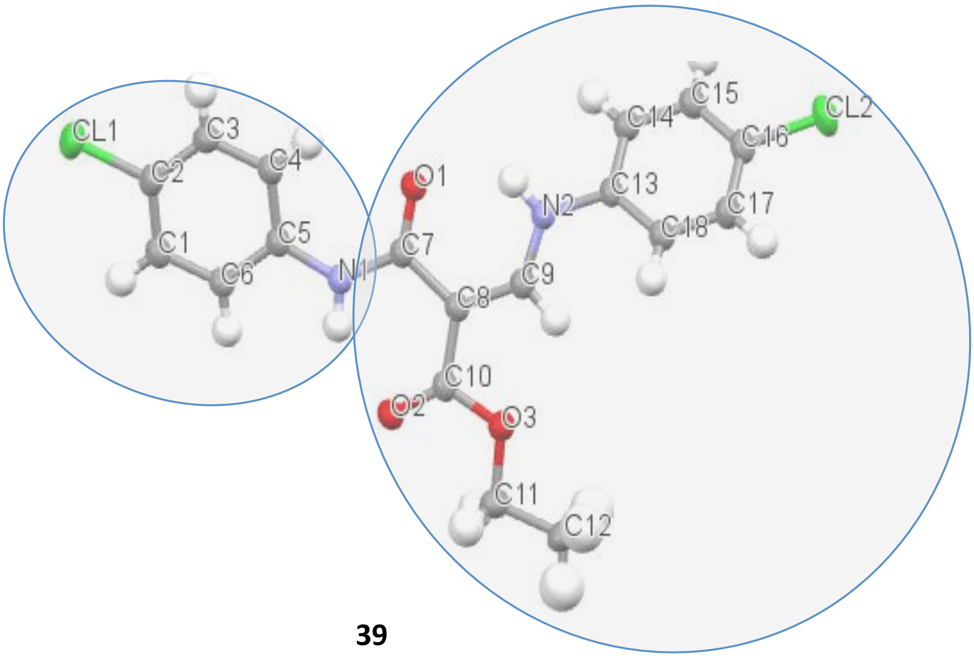

39

Figure 3.3(c). 50% atomic displacement parameter (ADP) plots (T = 120K) and D-p-A motif of **39**. Shaded regions enclose co-planar atoms**.**

DFT models of the aforementioned structures all show similar geometrical configurations to their X-ray determined counterparts, albeit the dihedral angles between the central backbone of the structure and its aryl rings in the calculated gas-phase structures are reduced, thus providing a greater potential for π-conjugation and thus ICT in this state. This reduction in dihedral angles is particularly evident for compounds **35** and **36** where angles reduce to approximately 1.0° and 12.3°, a reduction of 17.5° and 10.3°, respectively, relative to that of the crystal structures. Such a reduction will result in hypothetically better intramolecular charge transfer across the calculated structures, with charge likely to transfer from ring 1 to ring 2 in the case of both compounds.

A similar situation was observed for the DFT-generated structures of **37**, **38**, and **39** with the most marked change observed for **37** where the dihedral angles between the aryl rings and the backbone of the structure are less than 1.0°, confirming that this particular structure is likely to be the most promising in the series for NLO applications. It should be remembered here that such a marked change in dihedral angle stands to be a result of the absence of crystal packing forces in the gas-phase. Indeed, the extent by which the dihedral angles differ between the crystal structures and the DFT-generated structures are significantly larger for **37**, compared to those of **35**, **36**, **38** or **39**, indicating that the substituent groups of

37 have a larger impact on crystal field effects and unit cell packing than the hydrogen, methyl and 2-Cl and 4-Cl substituent groups of **35**, **36**, **38** and **39**, respectively.

Analysis of hydrogen-bonding via X-ray diffraction (**36-38**) and complementary neutron diffraction studies (**35, 39)** reveal the presence of two intramolecular O···H bonds in all structures (Figure 3.4). In the case of **35** the neutron-derived N(1)-H···O(2) and N(2)-H···O(1) bonds have distances and angles of 1.790(6) Å, 142.0(5)^{O} and 1.852(6) Å, 135.4(5)° respectively, while the analogous bonds in **39** have distances and angles of 1.844(8) Å, 130.8(5)° and 1.781(8) Å, 143.8(5)° respectively, suggesting that these intramolecular hydrogen bonds impart real electrostatic interactions as opposed to being a result of steric constraints. These hydrogen bonds are also shown by the presence of bond critical points in the Laplacian map between the O···H bond paths for **38** and **39** using XD2006; these manifest as saddle points of minimum electron density in the plane containing the O···H vector, as are nicely illustrated by the Laplacian maps in these regions (Fig 3.5). Furthermore, these bond critical points have low ρ(r) values and positive ∇^2(r) values, indicative of an electrostatic interaction that is consistent with hydrogen bonding (*c.f.* Tables 3.4 & 3.5). Since these intramolecular O···H interactions form true bonds, pseudo-rings also form in each case, given the 'pincer'-shaped geometry of the adjoining carbon atoms. An associated ring critical point is present in each case (Fig 3.5).

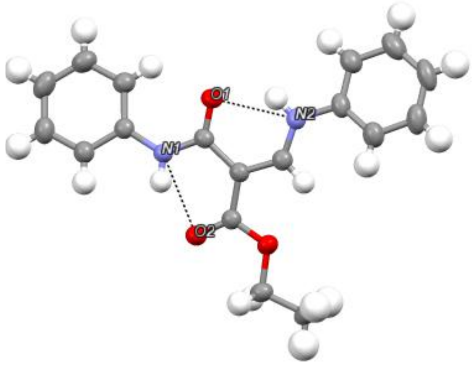

Figure 3.4 Example diagram of the two intramolecular hydrogen bonds present in all five compounds (Compound **35**)

In the case of **36-38**, the N(1)-H···O(2) and N(2)-H···O(1) bonds have distances and angles of 1.96(1) Å, 140.8(5)^{O} and 1.93(1) Å, 131.0(5)^{O} (**36**), 1.97(1) Å, 140.4(5)^{O} and 1.91(1) Å, 134.2(5)^{O} (**37**) 1.93(1) Å, 140.6(5)^{O} and 1.97(1) Å, 132.3(5)^{O} (**38**), respectively. Compound **37** also has an additional hydrogen-bond at N(1)-H···O(4) with a distance and angle of 2.18(1) Å, 110.0(5)^{O}. As with compounds **35** and **39**, such angle measurements are suggestive of the presence of real intramolecular hydrogen bonds. However, in the case of **36-38**, care should be taken with such an assessment as these measurements were taken from X-ray diffraction studies, where the position of the H atoms are modeled as riding upon their parent N atom such that the hydrogen atoms were positioned with idealized geometries and their ADPs constrained according to the riding model, U_{eq} (H)= 1.2U_{eq} (C).

The formation of two such intramolecular O···H bonds in the crystalline state is believed to release energy and thus bring the molecules to a thermodynamically more favourable state[17]. More importantly, from an NLO perspective, the presence of such hydrogen-bonding will constrain rotational degrees-of-freedom in the 2-methylene-1,3-dione motif, thus causing its dihedral angles with the phenyl groups to be lower than they might be otherwise, i.e. a higher level of planarity will result.

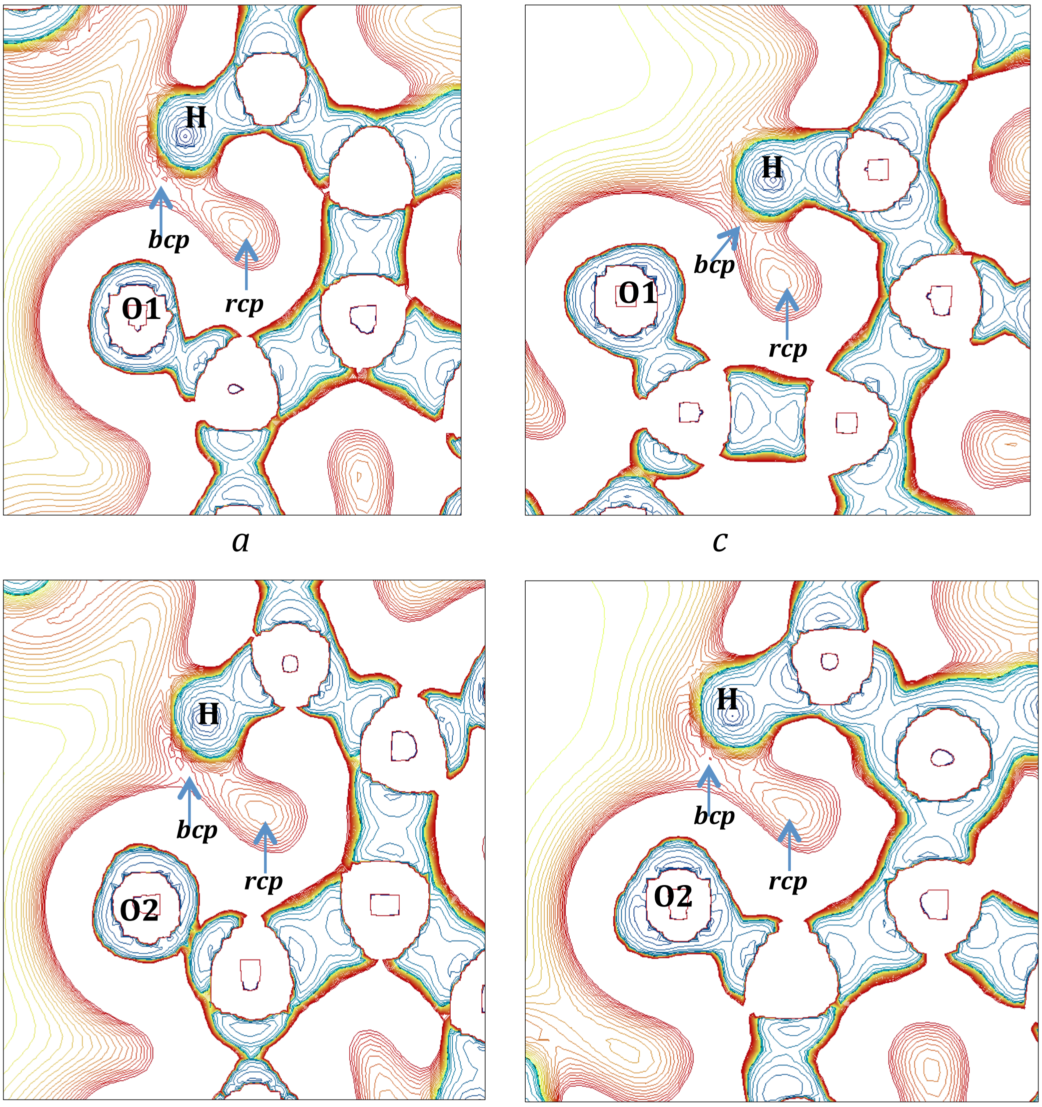

a *c*

b *d*

Figure 3.5 Laplacian maps in the plane of the O1···H and O2···H interactions in **38** *(a-b)* and **39** *(c-d)*. The positions of bond and ring critical points on the plots are labelled bcp and rcp, respectively.

Table 3.4 A summary of the critical point analysis on the O···H interactions in compound **38**

Bond	ρ(r)	$\nabla^2(r)$	Rij	d1	d2	Hessian Eigenvalues			ε[13]
O(1)-H	0.234	3.548	1.8469	1.1530	0.6939	-1.26	-1.00	5.81	0.26
O(2)-H	0.232	3.820	1.8114	1.1388	0.6726	-1.20	-1.00	6.03	0.21
Pseudo-Ring 1	0.127	2.200	N/A	N/A	N/A	-0.32	0.97	1.56	N/A
Pseudo-Ring 2	0.121	2.100	N/A	N/A	N/A	-0.27	0.94	1.47	N/A

---

[13] The large ellipticities are suggestive of the presence of some non-sigma bonding contributions. After investigation, it was found that the biggest multipole contributions for both O(1) and O(2) are quadrupolar in nature.

Table 3.5 A summary of the critical point analysis on the O···H interactions in compound **39**

Bond	$\rho(r)$	$\nabla^2(r)$	Rij	d1	d2	Hessian Eigenvalues			ε
O(1)-H	0.219	3.280	1.8610	1.1721	0.6889	-1.11	-1.05	5.44	0.06
O(2)-H	0.269	3.831	1.7907	1.1565	0.6342	-1.49	-1.41	6.73	0.05
Pseudo-Ring 1	0.135	2.200	N/A	N/A	N/A	-0.42	0.71	1.94	N/A
Pseudo-Ring 2	0.120	2.300	N/A	N/A	N/A	-0.36	1.04	1.63	N/A

3.3.2. Crystal packing effects

Determination of crystal packing effects can be important when considering NLO properties of molecular structures; as such effects will influence the Lorentz forces that control the macroscopic NLO effect, which is defined by χ^2 rather than β. However, major developments in thin-film fabrication methods for optical device technology are circumventing the traditional need to consider bulk NLO characteristics; indeed, since χ^2 is a second-order optical susceptibility, non-centrosymmetric crystal structures would be required for crystal applications of these NLO materials, while all of the subject compounds are in fact centrosymmetric. Nevertheless, it is helpful to discern the primary nature of these crystal packing effects in case molecules risk some form of molecular aggregation during an eventual optical device fabrication process.

The X-ray structure of **35** reveals that its closest intermolecular short contacts relate to C(7)···C(9′) and C(9)···(7′) separations [18], with a separation of 3.8 Å leading to a centrosymmetric crystal packing of the molecular structure which in turn will act to render zero χ^2 values for the solid-state compound. The same phenomenon is seen in the neutron-derived structure **39** where the shortest intermolecular contact bond lies between C(8)···C(8′) with a separation of 3.4 Å. Similarly, analysis of the X-ray structures of **36-38** reveal that their shortest intermolecular interactions occur between C(7)···C(8′) and C(8)···C(7′) with a separation of 3.4 Å (**36**); C(9)···C(15′) with a separation of 3.3 Å (**37**); and C(7)···C(8′) and C(7)···C(9′) with separations of 3.4 Å and 3.3 Å, respectively (**38**); which duplicates for analogous bonds involving C(8), C(9) and C(7′). The molecular structures of **36-38** all pack in a centrosymmetric fashion, which renders them zero χ^2 values in their solid-state form.

Such large distances indicate that the intermolecular forces in **35-39** are likely to be weak and non-directional for the most part; as such, one can assume that van der Waals forces will likely dominate. The associated Lorentz forces will therefore have little impact on the NLO responses of the solid-state materials. Such an assessment is further substantiated by the fact that the gas-phase values of β, where such intermolecular interactions do not exist, are comparable to their analogous solid-state values.

3.3.3 Linear Optical Properties of 35-39

Solution-based UV/vis absorption spectra for all five compounds were obtained and their maximum peak absorption wavelengths, $\lambda_{\mathrm{max}}^{\mathrm{peak}}$, were determined. Compounds **35-39** exhibit absorption bands, which are relatively close to one another with the largest $\lambda_{\mathrm{max}}^{\mathrm{peak}}$ being observed for **37**. The $\lambda_{\mathrm{max}}^{\mathrm{peak}}$ values for the all compounds were: 317 nm (**35**), 345 nm (**36**), 379 nm (**37**), 361nm (**38**), 363nm (**39**); these values are approximate given that the peaks are not clearly defined. Nonetheless, the $\lambda_{\mathrm{max}}^{\mathrm{peak}}$ value for **35** provides a good benchmark value from which to assess the other $\lambda_{\mathrm{max}}^{\mathrm{peak}}$ values. Indeed, the fact that it possesses the smallest value of all five compounds is natural, considering that it forms the basic structural motif of the other molecules within the series. An assessment of the other UV-Vis spectra demonstrate that **38** and **39** have very similar $\lambda_{\mathrm{max}}^{\mathrm{peak}}$ values which is unsurprising, given that both compounds are chemically similar, differing only in the position of the Cl atoms on the ring (i.e. a move from *ortho-* to *para-*). Once again, **37** reveals itself as the most promising for NLO application, with its absorption spectrum extending into the visible region of the electromagnetic spectrum by the greatest extent of all five compounds. This suggests that **37** has the smallest HOMO-LUMO energy gap of the five compounds under consideration and thus has the greatest propensity for ICT.

Complementary DFT calculations enabled the associated optical transitions in **35-39** to be related to perturbations in their electronic structure. To this end, the electron-density distribution of the highest-occupied molecular orbital (HOMO), lowest-unoccupied molecular orbital (LUMO) and orbital of the next highest energy, LUMO+1, is given in Fig. 3.6. The presence of these three levels allows for the possibility of intramolecular charge-transfer (ICT) effects needing up to a three-level model to provide a representative description of the optical properties of **35-39**, as is common in highly polarizable materials such as NLO chromophores[19]. A comparison of the HOMO and LUMO distributions shown in Figure 3.6 reveals that the optical absorption of **35-39** is accompanied with distinct and consistent shifts in electron-density from ring 1 to ring 2. Notwithstanding the exception of **38**, this shift propagates further when moving up in energy to LUMO+1, given orbital distributions at this level lie wholly within ring 2 of **35**-**37** and **39**. These trends reflect that ICT spreads across the full length of the molecule, and is directed from ring 1 to ring 2 along an essentially single p-conjugation path. This determination of ICT directionality further suggests that the 'push-pull' character of these chromophores arises from one or more chemical substituent in ring 1 acting as the electron donor moiety, to provide the 'push'; and a chemical substituent in ring 2 manifesting as the electron withdrawing group, to afford the 'pull'.

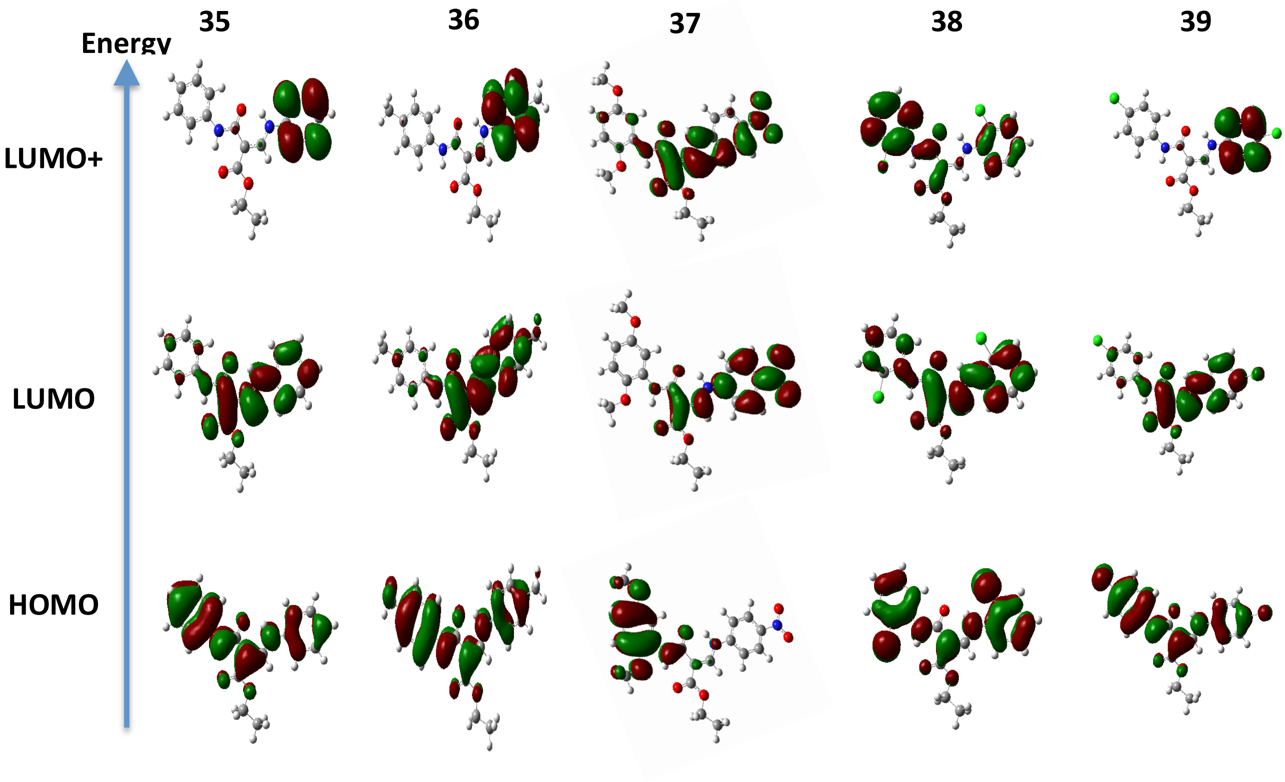

Figure 3.6. HOMO, LUMO and LUMO+1 for all five compounds. Generated using GaussView[20]. Calculated using B3LYP 6-31G+(d, p)

This 'push-pull' effect appears greatest for **37**, judging from the essentially bipartite orbital density contributions from atoms in its HOMO and LUMO. This stands to reason since the aryl rings of **37** bear different chemical substituents, in contrast to all other subject compounds. This chemical asymmetry in **37** naturally enhances the 'push-pull' capability of this chromophore, relative to its symmetric counterparts. Moreover, its nitro group is a strong electron withdrawing group, especially when located in a para-position of an aryl ring, as in **37** (*c.f.* its Hammett constant[14], s_{para} (NO_2) = 0.78)[21]. This contrasts with the relatively weak inductive and resonance effects that will be displayed by the methoxy groups in the opposing ring in **37**.

The HOMO, LUMO and LUMO+1 distributions of **35**, **36** and **39** are very similar. This makes sense when considering the symmetric nature of the chemical substituents on these molecules: the rings in **35** contain no terminal substituents, while the methyl and chloro substituents in the rings of **36** and **39**, respectively, all lie in the para position, i.e. they symmetrically oppose each other. So they will essentially exhibit cancelling ICT contributions towards each other in terms of 'push' and 'pull' effects. Accordingly, the origins of the ICT in **35**, **36** and **39**, which enable their linear optical absorption properties, presumably arise mostly from the asymmetric 2-methylene-1,3-dione backbone between the aryl rings that they all have in common. The fact that the HOMO, LUMO and LUMO+1 for **35**, **36** and **39** appear so similar would seem to substantiate this presumption.

As stated in the discussion above, **38** presents a distinct exception to the other subject compounds, in terms of its LUMO+1 distribution. In fact, its HOMO and LUMO distributions are also somewhat different, whereby the ICT from ring 1 to ring 2 in the HOMO-to-LUMO transition of **38** is much diminished relative to that observed for **35-37** and **39**. The ortho-positioning of the terminal substituents of **38** would seem to offer the most likely rationale for this exception. Ortho-substitution of any type of chemical group to each ring in this family of geminal amido esters will result in some level of chemical asymmetry between the two rings. As illustrated by its crystal structure in Fig. 3.3, the ortho-substituted chloro groups orient in a trans configuration, thereby generating greater molecular asymmetry than would be afforded by a *cis-* configuration. The cancelling ICT effects described for **35**, **36** and **39** therefore do not apply for **38**, even though both rings bear a common chemical substituent in all four cases. Indeed, the charge density analysis of **38** reveals a difference in the direction of molecular charge transfer direction in **38** compared to **39**. Nonetheless, this molecular asymmetry in **38** is nowhere near as prominent as those observed in **37** because the chemical substituents are the same for **37**, and are chloro groups that have moderate Hammett values[21]. Moreover, *para-* substituents such as the strongly electron withdrawing

---

[14] The Hammett constant is a measure of the total polar effect exerted by a substituent on a reaction centre, eg, a arene ring

nitro group in **37**, are usually better at facilitating charge transfer than *ortho*-substituents that feature in **38**[15].

Overall, these findings would seem to suggest that **37** exhibits the greatest ICT, and will therefore deliver the most promising optical absorption properties of the series studied herein. Meanwhile, the optical properties of **35**, **36**, and **39** would likely be similar to each other, and those of **38** would perhaps be slightly elevated relative to **35**, **36** or **39**, but distinctly less than those of **37**.

Finally, it is worth remembering that ICT in this series of compounds appears to involve contributions from the LUMO+1 level as well as the HOMO and LUMO levels, i.e. it is helpful to use a three-level model to describe the optical properties of **35-39**. Indeed, the need for such a model is typical of organic NLO chromophores. To that end, the NLO properties of **35-39** are now considered.

3.3.4. NLO properties of 35-39

The NLO properties of **35-39** were assessed by the examination of the hyperpolarizability of each compound, which acts as a molecular measure of the ability of a material to exhibit second-harmonic generation. Three independent methods were used for the determination of β and the results are summarized in Table 3.6. Where possible, β values were determined for each material in the solid state, liquid state, and gas phase, using a charge-density analysis, hyper-Rayleigh scattering measurements, or DFT calculations, respectively. The evaluation and comparison of these independently obtained β values must be done with caution, given the large errors (typically 10-30%) that are associated with the determination of β coefficients[2]. Additionally, the use of several different methods should allow an assessment of the β values of a compound in different phases, and help to reveal salient crystal packing effects, which may become important for device applications. Furthermore, the practical versatility of employing each method is an important consideration since in this instance β was not obtainable using all methods. Indeed, this is the case for the subject study where β could only be determined for **39** using all methods; practical limitations associated with the absence of high-quality single crystals (required for charge-density analysis) or the limited availability of powdered samples (for optical measurements) prohibited the use of certain methods for the other subject compounds. The complementary nature of these methodological practicalities is another reason to ensure that there are several accessible routes to derive β for a given material.

With the exception of the HRS results, Table 3.6 shows the static hyperpolarizability values, β_0, for **35-39** where the static hyperpolarizability, β_0, is free from dispersion. β_0 values are often the most useful form of β to report, since they offer dispersion-free comparatives against cognate β_0 values obtained by other methods, at other energies, or under different experimental conditions. In principle, the HRS measurements report dynamic values, although they were conducted at a non-resonant wavelength; as such, the reported value is so heavily damped, when taking into account the width of the transition that it effectively affords a static hyperpolarizability.

Table 3.6. Molecular hyperpolarizability values for **35-39** derived in their gas, solution and solid-states via DFT, HRS and charge-density studies, respectively.

β / 10^{-30} esu	**3.5**	**36**	**37**	**38**	**39**
Charge density (β_0) (Stockholder)	Not obtained	Not obtained	Not obtained	13.8	13.0
Charge density (β_0) (QTAIM)	Not obtained	Not obtained	Not obtained	14.6	13.0
HRS (β_{800}) #	13 ± 3	14 ± 3	Not obtained	18 ± 4	Not obtained
DFT gas phase, (β_0)	13.6	16.3	116.9	14.9	16.5

The errors in β_{HRS} were predicated by the 20% statistical error on the evaluation of β for the Crystal Violet HRS reference sample, since this error propagates through to the uncertainty in β for **35**, **36** and **38**.

In the case of the solid-state determination of β, two different charge density based derivations of β are given in Table 3.6. These distinct values arise because there are several ways to assign electron density contributions to a given atom in a molecule, and the chosen atomic partitioning method influences the corresponding value of the multipolar moment that is derived for a given atom in a charge-density study; these moments are then used in the empirical calculation for β (*cf.* Eq. 1.10)[6]. See §1.2.2.4 for more on the partition methods and the empirical calculation of β .

3.3.4.1 Comparison of β values determined from the three independent methods

35 presents the unsubstituted aryl form of **36-39**, and so its β value provides a good benchmark for assessing the effects of aryl substitution on the molecular hyperpolarizability in this series of compounds. A corresponding survey of Table 3.6 reveals that the addition of chemical substituents to the aryl rings in these compounds increases *β*, with DFT-calculated values of molecular hyperpolarizability for each compound following the order: **37** >> **39** > **36** > **38** > **35**. DFT is the only method by which *β* values could be obtained for all of the subject compounds. However, the trends observed between DFT calculations on a cognate set of compounds are generally deemed to be accurate, even if the absolute values cannot always be assured[22]. Indeed, Table 3.6 shows that *β* values determined for each compound from the different methods are very similar, where multiple data are available. This is certainly encouraging, especially in light of the fact that evaluations of *β* by experimental methods are notoriously fraught with large errors (10-30%).

Moreover, these DFT results offer gas-phase *β* values, which provide a valuable benchmark for comparing the contribution of *β* from the isolated molecule, against that of supramolecular effects that will be contained within *β* values derived from methods that assess a subject material in its solution or solid-state. This comparison of gas-phase results against those of the solution-phase (HRS) and solid-state (charge-density) findings is enabled by a survey of Table 3.6, which shows that *β* values for each compound are very similar irrespective of the method used for *β* determination. The most compelling case to illustrate this trend is given by **38**, for which *β* values are available across all three states of matter and are essentially identical.

Considering *β* for **35-39** in the solution phase, their similarity with the gas-phase results suggest that solvent environment has minimal polarization effects on the subject NLO molecules, at least for the solvent used in the HRS measurements (acetone). This also indicates that molecular aggregation phenomena are likely absent for **35-39** within this solution medium. Such aggregation is a common feature in NLO chromophores since their electronic 'push-pull' nature generally affords them high molecular dipole moments that can, in turn, invite dimerization or the clustering of molecules. The resulting aggregates can prove beneficial[8,9,23–28] or have deleterious effects on the NLO performance of a material[29–31], depending on the precise nature by which the aggregation affects its electronic structure, and therefore the molecular polarization. In cases where molecular aggregation produces deleterious effects, NLO device processing problems are commonly encountered[32], so it is important to discern that aggregates are absent in these molecules in order to help diagnose their innate NLO prospects from a molecular engineering perspective.

Considering the solid-state phase, their similarity with the gas-phase *β* evaluations suggests that any crystal packing effects, and therefore Lorentz forces[33,34], in the subject compounds will likewise have a negligible impact on the NLO prospects of the molecule. Taking together these NLO implications on all three states of matter, one therefore might anticipate that the NLO effects of these molecules would be minimally affected by NLO device processing conditions, irrespective of the eventual form of the NLO materials, eg, embedded within thin-film technology or applied as a bulk crystal using alternating domain stacking.

The solution-phase *β* determinations are also striking from another perspective: they are identical to the other *β* values reported for a given compound in Table 3.6 within experimental error. This result is remarkable given that experimental methods, which enumerate *β* typically, differ by an order of 10-30%[2]. This excellent match of *β* values between methods also confirms our notion that the non-resonant nature of the HRS experiments leads to negligible dispersion effects for this series of compounds. Furthermore, it is helpful to remember that HRS measurements make no assumption about the symmetry of the molecule, in terms of any *a priori* interpretation of non-zero tensorial components, eg, there is no assumption of a dipolar or octupolar molecule, affording certain dominant or negligible β_{xyz} components. The finding that these HRS *β* values are identical to the results from the other two methods, which employ the explicit partitioning of multipolar moments of each atom, is therefore all the more impressive.

The solid-state charge density results for **38** and **39** are also worthy for further commentary, with regards to the two atomic partitioning methods used to generate the multipolar moments that are required for the empirical calculation of *β*; indeed, this method comparison is of particular interest, in light of the fact that there are so few examples of using this empirical method to determine *β* as of yet. It transpires that the use of multipolar moments, enumerated from either stockholder or QTAIM atomic partitioning methods, produce very similar *β* values from the empirical calculation derived by Higginbotham *et al.*[6]; *c.f.* Table 3.6 shows that the two charge-density results for **39** are identical, while those for **38** differ by only 0.8×10^{-30} esu. So it would appear that these two atomic partitioning methods are equally suited to provide multipolar moments for the evaluation of *β* from charge-density data. These two *β* evaluations for **38** are also essentially identical to those derived by HRS and DFT methods, while those for **39** differ from the DFT evaluation by 21% which compares closely to the 20% experimental error in β_{HRS} values given in Table 3.6, this being a typical metric of uncertainty for HRS data. These results therefore demonstrate the efficacy of charge density modeling of multipolar moments for the evaluation of *β*, using either the stockholder or QTAIM atomic partitioning methods.

3.3.4.2 Relating *β* to the molecular structures of 35-39

Table 3.6 reveals that **37** bears a substantially higher *β* value than the other compounds. While the absence of HRS and charge density *β* values for **37** prevents direct comparison, this result is substantiated by the fact that it is entirely in line with the ICT and molecular planarity findings discussed in §3.3.1 and §3.3.3. Those results depicted **37** with a classical D-p-A molecular architecture, whereby strongly donating and accepting methoxy and nitro groups are connected via a highly delocalized π-conjugated pathway that is afforded by an essentially planar molecular configuration.

It is hard to judge if there are real differences between *β* values from the other subject compounds with any surety, owing to the substantial uncertainties associated with the different methods that determine *β*. However, **38** presents the second largest value of *β* in Table 3.6, on average, notwithstanding the statistical uncertainty imposed by error propagation from the NLO reference sample (see footnote in Table 3.6); and it is the largest HRS value recorded in this Table which is compared against that of **35** and **36**. Averaging over all four determinations of *β* for **38** would temper *β* down to a value of 15.5 x 10^{-30} esu, which is larger than the corresponding average of **39** (14.2 x 10^{-30} esu). This relay of comparisons might suggest that **38** is slightly elevated with respect to **35**, **36** and **39** which would be in line with the ICT analysis in §3.3.3 which argued for slightly augmented ICT in **38**, relative to **35**, **36** and **39**, owing to its greater molecular asymmetry caused by ortho-positioned chloro-substituents in the rings of **37**. However, further corroboratory evidence would be needed to place this proposal on a sure footing. This is particularly pertinent given that the benefits of *para*- over *ortho*- substitution of arene rings are well documented for the general case[35], although these arguments are difficult to apply here since **39**, the *para*-

substituted counterpart of **38**, exhibits cancelling effects with the same chloro-substituent residing on the opposing ring (*cf.* §3.3.3).

In broader terms, it is believed that **35-39** will all respond as NLO chromophores when in a solution or gas-phase state, given that they all crystallize in centrosymmetric space groups; but that **37** will display a significantly larger response than the others four chromophores. Such a result is nevertheless promising when one considers the simplicity of the substituents in this series; and that such a range of β values goes some way to validating the idea that even simple molecular engineering design can achieve varying levels of NLO responses, thus affording the ability to design compounds for bespoke application.

3.4. Conclusion

A series of five geminal amido esters with generic formula, (E)-ethyl 3-(X-phenylamino)-2-(Y phenylcarbamoyl)acrylate (where X,Y = 4-H,4-H (**35**); 4-CH_3, 4-CH_3 (**36**); 4-NO_2, 2,5-OCH_3 (**37**); 2-Cl, 2-Cl (**38**); 4-Cl, 4-Cl (**39**)), has been synthesized and characterized in terms of their structural and optical properties. In particular, their non-linear optical (NLO) prospects are assessed. To that end, the molecular architectures and intramolecular charge transfer aspects of the electronic structures of **35-39** are related to their optical properties, especially the molecular hyperpolarizability, β, which provides a molecular measure of the NLO response in a chromophore. Given the notorious difficulties in obtaining reliable values of β, the molecular hyperpolarizability is evaluated by up to four independent methods (in one of three states of matter): density functional theory (gas phase), hyper-Rayleigh scattering (solution-phase), and charge-density analysis (solid-state) which yields two possible values of β. The two options of β offered by charge-density analysis arise because there are several types of atomic partitioning methods that are available to determine the multipolar moments which are needed for the empirical calculation of β. Accordingly, β values were enumerated from multipolar moments derived from stockholder and QTAIM partitioning methods. A comparison of the results revealed that these two atomic partitioning methods produced equally reliable β values. The empirical calculation used to determine β is based on a theory reported by Robinson in 1967, but its application to charge-density analysis to deliver reliable β values was only successfully demonstrated recently. It is therefore important to test this method on a number of case studies and this chapter provides the fifth and sixth exemplification of this method to enumerate β, via the two charge-density data sets reported herein. Results are very encouraging since they compare well with those from HRS measurements and DFT calculations, where these are available for **35-39**. The concerted use of theory and experiment, especially where experimental data may not be available, is worth mentioning in its own right since this relates to one of the core principles of the Materials Genome Initiative[36], i.e. that the concerted use of theory and computation in materials discovery efforts is imperative if one is to achieve the transformative reduction in ‘molecule-to-market’ innovation timescales that is considered necessary to remain globally competitive. In terms of a materials-centered perspective, the structure-property relationships established through this work revealed that supramolecular effects in **35-39** were not significant in either the solution phase or the solid-state. Furthermore, the findings indicated that **37** stood out from the other subject materials in holding the most promise as an organic NLO chromophore, when suitably poled in a media that circumvents its macroscopic centrosymmetry. It would seem possible to accommodate this caveat readily, given the rapid and continuing rise in thin-film technology and the emerging embodiment of NLO phenomena in nanotechnology[37–39].

3.5 References

(1) Cole, J. M. Organic Materials for Second-Harmonic Generation: Advances in Relating Structure to Function. *Philos. Trans. R. Soc. Lond. Ser. Math. Phys. Eng. Sci.* **2003**, *361* (1813), 2751–2770.

(2) *Characterization Techniques and Tabulations for Organic Nonlinear Optical Materials*; Kuzyk, M. G., Dirk, C. W., Eds.; Optical engineering; Marcel Dekker: New York, 1998.

(3) Hohenberg, P.; Kohn, W. Inhomogeneous Electron Gas. *Phys. Rev.* **1964**, *136* (3B), B864–B871.

(4) Clays, K.; Persoons, A. Hyper-Rayleigh Scattering in Solution. *Phys. Rev. Lett.* **1991**, *66* (23), 2980–2983.

(5) Robinson, F. N. H. Nonlinear Optical Coefficients. *Bell Syst. Tech. J.* **1967**, *46* (5), 913–956.

(6) Higginbotham, A. P.; Cole, J. M.; Blood-Forsythe, M. A.; Hickstein, D. D. Identifying and Evaluating Organic Nonlinear Optical Materials via Molecular Moments. *J. Appl. Phys.* **2012**, *111* (3), 033512.

(7) Cole, J. M.; Copley, R. C. B.; McIntyre, G. J.; Howard, J. A. K.; Szablewski, M.; Cross, G. H. Charge-Density Study of the Nonlinear Optical Precursor DED-TCNQ at 20 K. *Phys. Rev. B* **2002**, *65* (12), 125107.

(8) Cole, J. M.; Goeta, A. E.; Howard, J. A. K.; McIntyre, G. J. X-Ray and Neutron Diffraction Studies of the Non-Linear Optical Compounds MBANP and MBADNP at 20 K: Charge-Density and Hydrogen-Bonding Analyses. *Acta Crystallogr. B* **2002**, *58* (4), 690–700.

(9) Lin, T.-C.; Cole, J. M.; Higginbotham, A. P.; Edwards, A. J.; Piltz, R. O.; Pérez-Moreno, J.; Seo, J.-Y.; Lee, S.-C.; Clays, K.; Kwon, O.-P. Molecular Origins of the High-Performance Nonlinear Optical Susceptibility in a Phenolic Polyene Chromophore: Electron Density Distributions, Hydrogen Bonding, and Ab Initio Calculations. *J. Phys. Chem. C* **2013**, *117* (18), 9416–9430.

(10) Venkatesan, P.; Thamotharan, S.; Ilangovan, A.; Liang, H.; Sundius, T. Crystal Structure, Hirshfeld Surfaces and DFT Computation of NLO Active (2E)-2-(Ethoxycarbonyl)-3-[(1-Methoxy-1-Oxo-3-Phenylpropan-2-Yl)Amino] Prop-2-Enoic Acid. *Spectrochim. Acta. A. Mol. Biomol. Spectrosc.* **2016**, *153*, 625–636.

(11) Sheldrick, G. M. A Short History of *SHELX*. *Acta Crystallogr. A* **2008**, *64* (1), 112–122.

(12) Sheldrick, G. M. *XPREP in SHELXTL*; Siemens Analytical X-ray Instruments, Inc.: Madison, Wisconsin, U.S.A., 1995.

(13) Agilent. *CrysAlis PRO*; Agilent Technologies Ltd,Yarnton, Oxfordshire, UK, 2014.

(14) Stewart, R. F.; Davidson, E. R.; Simpson, W. T. Coherent X-Ray Scattering for the Hydrogen Atom in the Hydrogen Molecule. *J. Chem. Phys.* **1965**, *42* (9), 3175–3187.

(15) Hirshfeld, F. L. Bonded-Atom Fragments for Describing Molecular Charge Densities. *Theor. Chim. Acta* **1977**, *44* (2), 129–138.

(16) Frisch, M. J; Trucks, G. W; Schlegel, H. B.; Scuseria, G. E; Robb, M. A; Cheeseman, J. R; Scalmani, G; Barone, V; Mennucci, B; Petersson, G. A; et al. *Gaussian09*; Gaussian, Inc.: Wallingford CT, 2009.

(17) Steiner, T. The Hydrogen Bond in the Solid State. *Angew. Chem. Int. Ed.* **2002**, *41* (1), 48–76.

(18) Macrae, C. F.; Edgington, P. R.; McCabe, P.; Pidcock, E.; Shields, G. P.; Taylor, R.; Towler, M.; van de Streek, J. *Mercury* : Visualization and Analysis of Crystal Structures. *J. Appl. Crystallogr.* **2006**, *39* (3), 453–457.

(19) Kanis, D. R.; Ratner, M. A.; Marks, T. J. Design and Construction of Molecular Assemblies with Large Second-Order Optical Nonlinearities. Quantum Chemical Aspects. *Chem. Rev.* **1994**, *94* (1), 195–242.

(20) Dennington, R; Todd, K; Millam, J. *GaussView*; Semichem Inc: Shawnee Mission, KS, 2009.

(21) Hansch, C.; Leo, A.; Taft, R. W. A Survey of Hammett Substituent Constants and Resonance and Field Parameters. *Chem. Rev.* **1991**, *91* (2), 165–195.

(22) Sholl, D.; Steckel, J. A. *Density Functional Theory: A Practical Introduction*; John Wiley & Sons, 2011.

(23) Cole, J. M.; Howard, J. A. K.; McIntyre, G. J. Influence of Hydrogen Bonding on the Second Harmonic Generation Effect: Neutron Diffraction Study of 4-Nitro-4′-Methylbenzylidene Aniline. *Acta Crystallogr. B* **2001**, *57* (3), 410–414.

(24) Coradin, T.; Clément, R.; Lacroix, P. G.; Nakatani, K. From Intercalation to Aggregation: Nonlinear Optical Properties of Stilbazolium Chromophores−MPS3 Layered Hybrid Materials. *Chem. Mater.* **1996**, *8* (8), 2153–2158.

(25) Datta, A.; Pati, S. K. Dipole Orientation Effects on Nonlinear Optical Properties of Organic Molecular Aggregates. *J. Chem. Phys.* **2003**, *118* (18), 8420–8427.

(26) Duan, Y.; Ju, C.; Yang, G.; Fron, E.; Coutino-Gonzalez, E.; Semin, S.; Fan, C.; Balok, R. S.; Cremers, J.; Tinnemans, P.; et al. Aggregation Induced Enhancement of Linear and

Nonlinear Optical Emission from a Hexaphenylene Derivative. *Adv. Funct. Mater.* **2016**, n/a-n/a.

(27) Kwon, O.-P.; Kwon, S.-J.; Jazbinsek, M.; Seo, J.-Y.; Kim, J.-T.; Seo, J.-I.; Lee, Y. S.; Yun, H.; Günter, P. Phenolic Polyene Crystals with Tailored Physical Properties and Very Large Nonlinear Optical Response. *Chem. Mater.* **2011**, *23* (2), 239–246.

(28) Thalladi, V. R.; Boese, R.; Brasselet, S.; Ledoux, I.; Zyss, J.; Jetti, R. K. R.; Desiraju, G. R. Steering Non-Centrosymmetry into the Third Dimension: Crystal Engineering of an Octupolar Nonlinear Optical Crystal. *Chem. Commun.* **1999**, No. 17, 1639–1640.

(29) Cole, J. M.; Lin, T.-C.; Edwards, A. J.; Piltz, R. O.; Depotter, G.; Clays, K.; Lee, S.-C.; Kwon, O.-P. Concerted Mitigation of O···H and C(π)···H Interactions Prospects Sixfold Gain in Optical Nonlinearity of Ionic Stilbazolium Derivatives. *ACS Appl. Mater. Interfaces* **2015**, *7* (8), 4693–4698.

(30) Tekin, S.; Yaglioglu, H. G.; Elmali, A.; Kürüm, U.; Yanık, H.; Tekdaş, D. A.; Durmuş, M.; Ahsen, V. The Effect of Aggregation on the Nonlinear Optical Absorption Performance of Indium and Gallium Phthalocyanines in a Solution and Co-Polymer Host. *Mater. Chem. Phys.* **2013**, *138* (1), 270–276.

(31) Würthner, F.; Yao, S.; Debaerdemaeker, T.; Wortmann, R. Dimerization of Merocyanine Dyes. Structural and Energetic Characterization of Dipolar Dye Aggregates and Implications for Nonlinear Optical Materials. *J. Am. Chem. Soc.* **2002**, *124* (32), 9431–9447.

(32) Hales, J. M.; Kim, H.; Barlow, S.; Getmanenko, Y.; Zhang, Y.; Giesking, R.; Risko, C.; Shahin, S.; Kieu, K.; Norwood, R. A.; et al. Polymethines with Macroscopic Optical Nonlinearities Suitable for All-Optical Signal Processing; OSA, 2014; p STu3H.4.

(33) Seidler, T.; Stadnicka, K.; Champagne, B. Second-Order Nonlinear Optical Susceptibilities and Refractive Indices of Organic Crystals from a Multiscale Numerical Simulation Approach. *Adv. Opt. Mater.* **2014**, *2* (10), 1000–1006.

(34) Seidler, T.; Stadnicka, K.; Champagne, B. Investigation of the Linear and Second-Order Nonlinear Optical Properties of Molecular Crystals within the Local Field Theory. *J. Chem. Phys.* **2013**, *139* (11), 114105.

(35) Cheng, L. T.; Tam, W.; Stevenson, S. H.; Meredith, G. R.; Rikken, G.; Marder, S. R. Experimental Investigations of Organic Molecular Nonlinear Optical Polarizabilities. 1. Methods and Results on Benzene and Stilbene Derivatives. *J. Phys. Chem.* **1991**, *95* (26), 10631–10643.

(36) *"Materials Genome Initiative for Global Competitiveness", U.S. Government White Paper; National Science and Technology Council, Executive Office of the President of the United States (2011)*.

(37) Deng, H.-D.; Li, G.-C.; Dai, Q.-F.; Ouyang, M.; Lan, S.; Trofimov, V. A.; Lysak, T. M. Size Dependent Competition between Second Harmonic Generation and Two-Photon Luminescence Observed in Gold Nanoparticles. *Nanotechnology* **2013**, *24* (7), 075201.

(38) Ray, P. C. Size and Shape Dependent Second Order Nonlinear Optical Properties of Nanomaterials and Their Application in Biological and Chemical Sensing. *Chem. Rev.* **2010**, *110* (9), 5332–5365.

(39) Ronchi, M.; Pizzotti, M.; Orbelli Biroli, A.; Righetto, S.; Ugo, R.; Mussini, P.; Cavazzini, M.; Lucenti, E.; Salsa, M.; Fantucci, P. Second-Order Nonlinear Optical (NLO) Properties of a Multichromophoric System Based on an Ensemble of Four Organic NLO Chromophores Nanoorganized on a Cyclotetrasiloxane Architecture. *J. Phys. Chem. C* **2009**, *113* (7), 2745–2760.

Chapter 4

Molecular Origins of the Nonlinear Optical Responses of a Series of α-(X-2-pyridylamino)-*o*-cresol Chromophores from Concerted X-ray Diffraction, Hyper-Rayleigh Scattering, and *ab initio* Calculations

4.1 Introduction

Having studied a cognate series of organic chromophores that exhibit favorable, and somewhat similar NLO responses in the gas, solution and solid-state phase, we now present a smaller series of organic chromophores that exhibit marked differences in their NLO activity between phase states. Furthermore, the series presented herein, differs from the previous series of Chapter 3 in that α-(X-2-pyridylamino)-*o*-cresol chromophores experience intramolecular hydrogen interactions which, are critical to their respective NLO responses. To this end, this study contributes to the identification of structure-property relationships pertaining to the effects of intramolecular bonding and specifically how these interactions result in advantageous and/or deleterious effects upon the NLO responses of chromophores. These insights also contribute to the canon of structure-property relationships that have already been established for organic NLO materials to-date[1].

Within the realm of molecular topologies for second-order nonlinear optics, one such relationship requires organic NLO materials to bear donor-π-acceptor-type molecular architectures, which facilitate strong intramolecular charge transfer through highly delocalized π-bond conjugation paths[2,3]. At a slightly larger nano-scale, it is important to consider crystal field effects that exist between organic molecules, in order to anticipate any adverse molecular aggregation phenomena that may occur in the liquid or solid state.

Molecular design rules are becoming ever more accurate in their prediction of material properties of target compounds, given that these predictions are based on a growing number of detailed high-level case studies. This paper furthers the chemical diversity of such case studies via a report on a new series of three potential organic NLO chromophores that belong to the family of α-(X-2-pyridylamino)-o-cresol chromophores: α-(4-methyl-2-pyridylamino)-o-cresol (**40**), α-(5-chloro-2-pyridylamino)-o-cresol (**41**), and α-(3,5-dichloro-2-pyridylamino)-o-cresol (**42**) (Fig. 4.1). Herein, the structure-property relationships of **40-42** are determined and discussed, especially with respect to their second-order NLO effects as determined through their molecular hyperpolarizability, β.

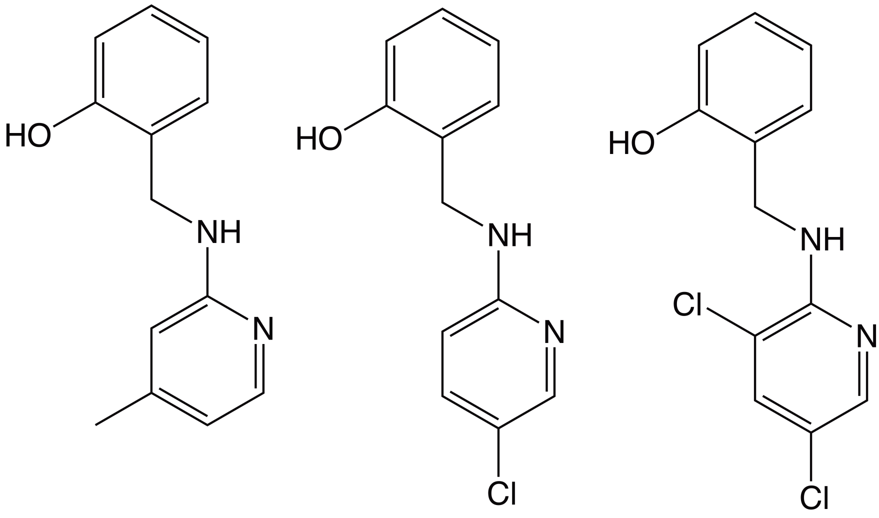
40 **41** **42**

Figure 4.1. Chemical structures of **40**-**42**.

The β values for **40-42** were evaluated with respect to their molecular structure using three independent methods: i) hyper-Rayleigh scattering (HRS) measurements,[4] ii) *ab initio* gas-phase density functional theory (DFT) calculations and iii) X-ray wavefunction refinement (XWR)[5], a semi empirical technique that constructs a theoretical molecular wavefunction constrained to reproduce X-ray experimental diffraction data. This is a relatively new technique in the field of quantum chemistry, and allows the building of a wavefunction which is representative of the molecule under investigation, from which molecular properties can be extracted[6,7]; as well as a full Bader Quantum Theory of Atoms in Molecules (QTAIM)[8,9] topological analysis, similar to those afforded by multipolar model (MM) methods[10,11]. Indeed, a recent validation study of the XWR method[5] revealed that the use of high-resolution data sets in the XWR of four amino acids achieved statistical agreement and molecular topological properties that were in closer agreement with both DFT and experimental diffraction patterns, than those obtained from using analogous MMs derived using the Hansen-Coppens formalism[12]. Furthermore, Woińska *et al.* also suggested in their study that using the XWR method significantly reduces problems associated with the description of polar bonds in MMs. Similarly, the modeling of electron density in the vicinity of hydrogen atoms with the XWR method is visibly better than in a MM[5]. An earlier study by

Hickstein *et al.* on three organic NLO chromophores (DED-TCNQ[13], MBADNP[14], OH1[15]) and one Zn-based organometallic compound (ZTS[16]), demonstrated the efficacy of the XWR method and its good results compared to those obtained from using MMs.[17] Given these promising results, we herein also attempted to test and use the XWR method with good-quality, low-resolution, data sets in an effort to further assess the robustness of the XWR method.

This chapter begins by assessing the molecular architecture of **40-42** using conventional single-crystal X-ray diffraction analysis with a particular focus on identifying the π-conjugated intramolecular charge-transfer (ICT) pathways. Subsequently, the nature of these ICT pathways is corroborated via an XWR-derived topological analysis (deformation density, Laplacian maps, and QTAIM analysis), before the XWR results are used to determine the gas-phase β values of **40-42**, which are assessed considering the observed ICT phenomena. The NLO properties of **1**-**3** are also examined using HRS measurements and theoretical DFT modeling, thereby allowing a comparison of the NLO capabilities of **40-42** in solution (HRS) and the gas-phase (DFT & XWR). This, in turn, affords the opportunity to assess the implications of molecular aggregation on the NLO capabilities of **40-42**. The study concludes with an assessment of the potential of **40-42** to act as NLO chromophores, especially with a view to develop bespoke NLO devices.

4.2 Experimental and Computational Methods

4.2.1 Conventional Independent Atom Model (IAM) Refinement

X-ray diffraction data were collected by Edward A. Boardman and T.-C. Lin.

A single crystal of **40** (0.46 x 0.19 x 0.09 mm), **41** (0.30 x 0.20 x 0.20 mm), **42** (0.23 x 0.20 x 0.19 mm), was mounted onto the in-house Rigaku Saturn 724+ CCD single-crystal X-ray diffractometer as per §2.2.1. Crystals were cooled to 150 K via a liquid N_2 cryostream, and subsequently maintained at this temperature for the duration of the data collection. Data were collected at ϑ = 25° with full-sphere reciprocal space coverage, using ω-scans with a scan width of 0.3°. Data acquisition, collection and processing, including cell indexing, cell refinement, and data reduction was undertaken as per §2.2.2 and §2.2.3. Reduced data were corrected for X-ray absorption using an empirical model as per §2.2.4.

A conventional IAM crystal structure refinement was undertaken by full matrix least square on F^2 using SHELXL[18] (*cf* §2.2.5) and afforded the following statistics (*cf.* Table 4.1):

Table 4.1 A summary of the IAM structural refinement statistics of **40-42** using conventional X-ray diffraction techniques

	40	41	42
Chemical Formula	$C_{13}H_{14}N_2O$	$C_{12}H_{11}N_2O_1Cl$	$C_{12}H_{10}N_2O_1Cl_2$
a	6.3693(13)	6.3999(13)	7.1642(12)
b (Å)	11.3819(23)	7.8507(16)	8.6294(14)
c	15.2915(31)	12.0418(24)	10.9154(17)
α	90.00	100.61(3)	102.65(1)
β (°)	90.00	102.31(3)	102.35(1)
γ	90.00	101.19(3)	112.00(1)
Z	4	2	2
Crystal System	Orthorhombic	Triclinic	Triclinic
Space Group	$P2_12_12_1$	$P\bar{1}$	$P\bar{1}$
Sin(θ)/λ (Å^{-1})	0.70	0.64	0.70
R1 [I > 2σ(I)]	0.0458	0.0578	0.0444
wR2 [(I > 2σ(I)]	0.1346	0.1080	0.1234
GoF	1.082	0.897	0.789
Max / Min Residuals (Å^{-3})	0.36 / -0.38	0.24 / -0.22	0.41 / -0.42

4.2.2 Hyper-Rayleigh Scattering (HRS)

Koen Clays and Javier Perez-Moreno at The University of Leuven, Belgium undertook HRS measurements.

A generic experimental set-up and operational procedures were used for the hyper-Rayleigh scattering[4] as per §2.8. Acetonitrile solutions of **40, 41** and **42** were prepared. Concentrations were low enough to avoid self-absorption of the HRS signal at the second-harmonic wavelength.

4.2.3 *Ab initio* Quantum Chemical Calculations

Electrostatic moments and (hyper)polarizability values of **40-42** were calculated by DFT using GAMESS[19,20] as per §2.10. All calculations were carried out at the Cam-B3YLP/6-31G(d,p) level of theory. Initially, IAM-derived atomic position parameters were used as input to perform a ground-state geometry optimization that comprised finding the minimum on the potential energy surface of the ground state. All default settings for GAMESS were maintained. Subsequently, the components of the (hyper)polarizability tensor of the structure were calculated at the same level of theory. Molecular orbitals were viewed using the program MacMolPlt[21].

4.2.4 X-ray Wave-Function Refinement (XWR)

The XWR method[5] was employed via the program TONTO[22] as outlined in §2.9 on **40-42**. Initial attempts to refine the ADPs of the hydrogen atoms for **40-42** using HAR lead so some hydrogen ADPs being highly oblate or non-positive definite (NDP); possibly due to data resolution issues. Consequently, the ADPs of all hydrogen atoms were generated using SHADE2.1[23] and fixed throughout the refinements for all three structures. Convergence of the XWR was assured by testing the refinement test statistical parameter, χ^2, against a range of λ_L values. The XWR was allowed to run in λ_L steps of 0.1 increments until was achieved, and afforded the following statistics (*cf.* Table 4.2):

Table 4.2 A summary of the XWR statistics of **40-42**.

	40	**41**	**42**
λ_L	0.4	1.5	1.0
R	0.0239	0.0458	0.0354
R_w	0.0253	0.0360	0.0365
GoF ($\sqrt{\chi^2}$)	1.08	0.99	1.37
Max / Min Residuals (Å^{-3})	0.04 eÅ^{-3} [C12] -0.02 eÅ^{-3} [H10]	0.18 eÅ^{-3} [N2] -0.12 eÅ^{-3} [H3]	0.24 eÅ^{-3} [C12] -0.07 eÅ^{-3} [Cl2]

The resultant min/max residuals represent a reduction in the min/max residuals of the SHELX models. The residual density maps were either essentially featureless (**40**) or at the very least revealed a random distribution of residuals that could not be attributed to specific bonding features (**41**, **42**); they were thus deemed adequate for the given quality of data (*cf.* Appendix C, §C.1). The respective fitted wave functions were subsequently used to undertake a topological analysis of **40**-**42** via the program Multiiwfn[24] as per §2.9.3.

4.3 Results and Discussion

4.3.1 Molecular Architectures and Intramolecular Charge Transfer

The molecular structures of **40-42** in the crystalline state, determined by conventional single-crystal X-ray diffraction analysis, are shown in Fig. 4.2.

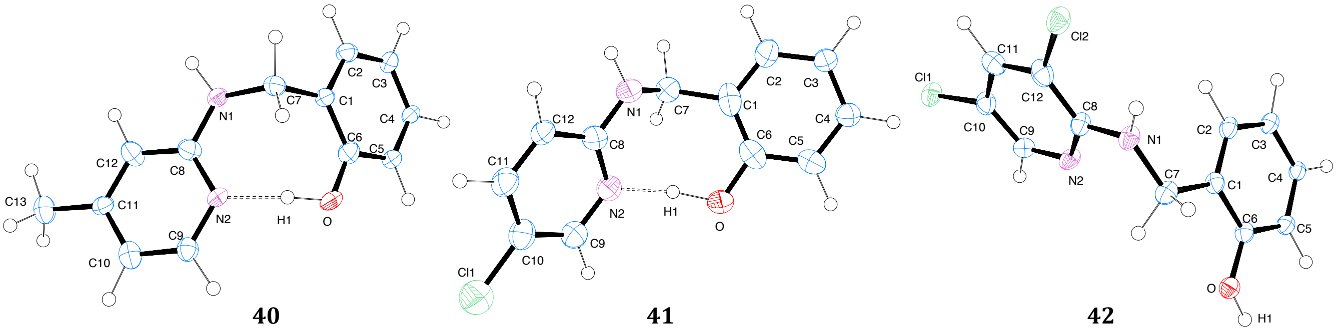

Figure 4.2. Molecular structures of **40-42** revealing the intramolecular OH···N bonds in **40-41** (not in **42**) that result in dihedral angles between the *o*-cresol and the *X*-2-pyridylamino moieties. Structures are generated via ORTEP[25]; ellipsoids are shown at the 50% probability level for non-H atoms.

These results expose some clear structural implications regarding their potential efficacy as NLO chromophores. All three molecular structures are dipolar, which is appropriate since their propensity to exhibit NLO features is based on ICT, which arises from π-conjugation across their donor-π-acceptor (D-π-A) molecular architectures. All of these structures are also asymmetric, which will act to foster dipolar D-π-A tendencies across the molecules, thereby enhancing their ICT.

The structures of **40-42** feature an overall non-planar molecular architecture but, with local regions of highly planar moieties: a planar *o*-cresol motif, connected to planar 4-methyl-2-pyridylamino (**40**), 5-chloro-2-pyridylamino (**41**), or 3,5-dichloro-2-pyridylamino (**42**) motifs, via dihedral angles [C(8)-N(1)-C(7)-C(1)] of 93.45(3) ° **40**), 79.14(3) ° (**41**), and 87.15(1) ° (**42**). Fig. 4.2 also reveals that the direction of this dihedral twist in **40** and **41** is in a different direction to that of **42**, resulting in the absence of an intramolecular OH···N bond in **3**. This difference results in a greater distortion of the bridge in **42** and thus further inhibits ICT between its aromatic units. The extent of deviation from co-planarity observed for the two constituent parts of **40-42** will constrain them from reaching an optimum level of π-bonding between the fragments and consequently limit their ICT abilities. Indeed, measurement of the bond lengths in the C(8)-N(1)-C(7)-C(1) bridging chain (Table 4.3) for **40-42**, revealed the presence of N(1)-C(7) and C(7)-C(1) single bonds, while the C(8)-N(1) bonds[26] appears to experience some conjugation effects. This break in π-conjugation suggests that no delocalized π-conjugation exists between the two rings; rather π-conjugation will reside in an isolated fashion within the two ring motifs. Consequently, since the *o*-cresol motif is common to all three chromophores, any variation in NLO activity among these compounds would be expected to arise primarily from the functionalized 2-pyridylamino moieties.

Table 4.3. Experimentally-determined bond lengths for the C(8)-N(1)-C(7)-C(1) chain bridging the pyridyl and *o*-cresol moieties in **40-41**.

Compound	Bond	Bond length (Å)
40	C(8) - N(1)	1.3616(3)
	N(1) - C(7)	1.4619(3)
	C(7) - C(1)	1.5192(3)
41	C(8) - N(1)	1.3602(3)
	N(1) - C(7)	1.4606(3)
	C(7) - C(1)	1.5081(3)
42	C(8) - N(1)	1.3514(2)
	N(1) - C(7)	1.4544(2)
	C(7) - C(1)	1.5132(3)

Of these structures, **42** is particularly promising, as it contains a 3,5-dichloropyridyl moiety. In terms of electrophilic substitution, halides usually behave as *para*- or *ortho*- directors; although, unlike most other *para*- or *ortho*- directors, halides tend to deactivate aromatic rings by withdrawal of electron density, which manifests as significant polarization across chloro-substituted aromatic moieties. The *para*-director effect should be observed in both **41** and **42**; while the presence of two chloro substituents (*para*- and *ortho*-) in **42** will increase the electron-withdrawing 'pull' effect from its aromatic ring, and thus increase the polarization across **42** relative to that of **41**. Meanwhile, the *meta*-methyl group in **40** should activate the pyridyl ring and thus reduce the net polarization across the 4-methylpyridyl moiety.

Analyses of **40-42** revealed the presence of intramolecular OH···N interactions in **40** and **41** with their hydrogen-bond lengths [H···N] of 1.582(3) Å (**40**) and 1.548(3) Å (**41**), [O···N] of 2.614(3) Å (**40**) and 2.619(3) Å (**41**) and, angles of 164.96(5)^{O} (**40**) and 170.37(5)^{O} (**41**). These near-linear angles suggest that these intramolecular hydrogen bonds impart strong real electrostatic interactions as opposed to simply being a result of steric constraints. Meanwhile, the analogous hydrogen atom of the *o*-cresol moiety in **42** points away from the nitrogen atom of the pyridyl ring as a result of the *o*-cresol being rotating around the C(3)-C(5) bond, which prevents effective hydrogen bonding. In all three cases, however, care should be taken with any further detailed assessment of hydrogen bonds as these measurements were taken from conventional X-ray diffraction studies, where the positions of the H atoms are modeled as riding upon their parent atom such that the hydrogen atoms are positioned with idealized geometries and their ADPs constrained according to the riding model, U_{eq} (H)= 1.2U_{eq} (C).

4.3.2 Initial Assessment of the Presence of ICT from DFT

The charge transfer characteristics of **40-42** were initially assessed via the DFT analysis of molecular orbitals (MOs) that relate to the optical absorption band gap. These are defined by the frontier orbitals, namely the highest occupied and lowest unoccupied molecular orbitals (HOMO and LUMO) and, other noteworthy MOs where relevant, such as the LUMO+1 in this case study. Given the energy levels associated with HOMOs and LUMOs, molecular orbital analysis permits the inference of the direction, as well as the extent, of ICT ensuing in a compound upon optical excitation.

A comparison of the frontier orbitals of **40-42** (Fig 4.3) reveals that optical absorption in compound **40** and **41** results in the stark shifting of the electron density from the *o*-cresol moieties to that of the functionalized pyridine ring; in contrast, no such shift is observed for **42**. One might therefore presuppose that the pyridyl moiety in **42** is wholly responsible for its NLO response; this would render the *o*-cresol moiety affording only a steric effect. Moreover, the optimized geometries of **40-42** reveal that the bond lengths in the C(8)-N(1)-C(7)-C(1) bridging chain remain consistent with those determined by experiment (Table 4.3) ie. suggesting single-bond character for N(1)-C(7)-C(1) and a double-bond character for C(8)-N(1). It may therefore seem surprising on first assessment, to see that shifts in the electron density for **40** and **41** extend across the molecules as a whole, given the lack of π-conjugation in the bridge between the *o*-cresol and functionalized pyridyl groups (*cf.* §4.3.1).

Interestingly, the chromophores where DFT indicates that ICT is ensues across the molecule (**40** and **41**) both appear to contain an intramolecular hydrogen bond, in contrast to **42** where no such ICT occurs. It therefore may be the case that these hydrogen bonds play a key role in the ICT and thus NLO activity of **40** and **41**. Hence, we employed XWR on the structures of these three chromophores in order to undertake a topological analysis of the bonds in the chromophores to: a) further validate the presence of the hydrogen bonds in **40** and **41** and, b) identify the ICT pathways in these chromophores.

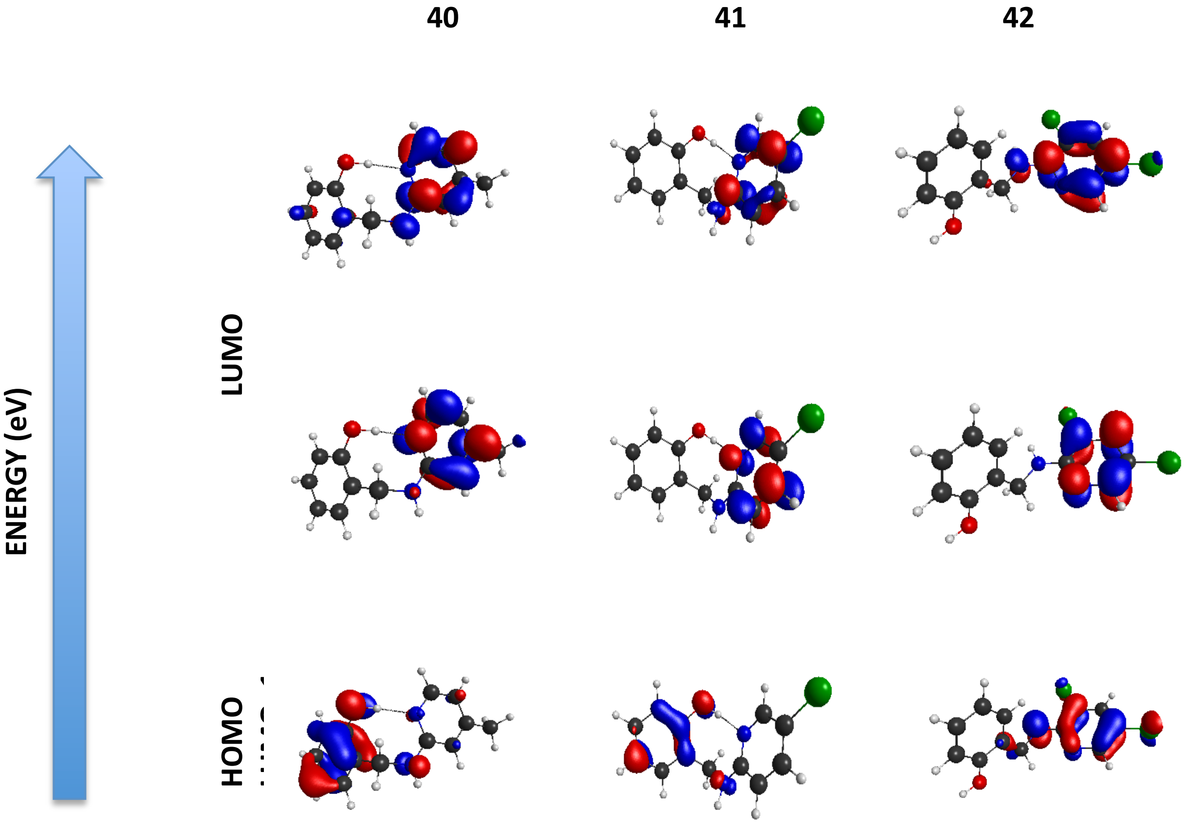

Figure 4.3. HOMOs, LUMOs, and LUMO+1s of **40-42**, calculated at the Cam-B3LYP/6-31G(d, p) level of theory.

4.3.3 Topological Analysis of the XWR models of 40-42

4.3.3.1 The Presence of Intramolecular Hydrogen Bonds in 40 and 41

Conformational assessments in §4.3.1 already established that no intramolecular hydrogen bond persists in **42**. Confirmation of the presence or absence of hydrogen bonds in **40** and **41** was sought via a QTAIM[9] analysis as implemented in Multiwfn using the XWR-derived wave-function for **40** and **41**. The XWR method is particularly useful in the absence of neutron diffraction studies, as it provides the assessment of a gas-phase electronic structure, which is nonetheless tempered by experimental X-ray data; i.e. structure factor amplitudes. XWR has been found to realize hydrogen-bond length values in good agreement with neutron diffraction derived lengths.[26] QTAIM analysis revealed bond critical points (BCPs) for the OH···N interaction in **40** and **41**. A BCP is defined as the point along a bond path where the electron density is at a minimum along the trajectory of the bond path and, where the rate of change in the electron density reaches zero i.e. $\nabla\rho(r) = 0$; while, the electron density is at a maximum in each of the two trajectories perpendicular to the bond path. The presence of BCPs between two atoms is a strong indicator of the likely presence of a bond; moreover, low $\rho(r)$ values and positive $\nabla^2\rho(r)$ values for **40** [ρ(r): 0.460 eÅ^{-3}; $\nabla^2\rho(r)$: 3.371 eÅ^{-5}] and **41** [ρ(r): 0.479 eÅ^{-3}; $\nabla^2\rho(r)$: 2.378 eÅ^{-5}] are consistent with a closed shell type electrostatic interaction (*cf.* Table 2.3 in §2.7.2.2).[8,27] This corroborates the notion of the presence of intramolecular hydrogen-bonds in **40** and **41**.

It should be noted that previous studies have shown that hydrogen bonds can also take the form of an open-shell interaction[28] and thus the use of such energy descriptors should be assessed with care. Espinosa *et al.* have suggested that a positive curvature at the BCP of a hydrogen bond (λ_3) is the most meaningful parameter for their characterization and classification[29] i.e., a positive λ_3 value is consistent with the presence of a hydrogen bond; this measure of hydrogen bonds has been used with earlier XWR work; for example, oxalic acid dehydrate.[6] In our study, λ_3 values of 9.81 eÅ^{-5} (**40**) and 9.46 eÅ^{-5} (**41**) for the hydrogen bonds in **40** and **41** are consistent with the presence of hydrogen bonds in accordance with the classification of Espinosa and co-authors.[29]

The formation of these intramolecular OH···N bonds should release energy and thus bring the molecules to a thermodynamically more favourable state. From an NLO perspective, the presence of such intramolecular hydrogen bonding will constrain the rotational degrees-of-freedom in the *o*-cresol motif, thus causing its dihedral angles with the pyridyl group to be lower than they might be otherwise, as for example, in the case of **42** where no such hydrogen-bond manifests.

4.3.3.2. Elucidation and Assessment of the ICT in 40-42

Having confirmed the presence of real intramolecular hydrogen bonds in **40** and **41,** the XWR-derived wave-functions of **40-42** were used to undertake a full QTAIM topological analysis of the molecular charge-density phenomena of **40-42** via QTAIM parameters. Parameters of particular interest when assessing bonding character, and can be obtained via QTAIM methods, include the ellipticity of the bond, ε, kinetic energy density per electron, $G(r)/\rho(r)$, and total energy density, $H(r)$. The definitions of these topological energy descriptors and their use in identifying bond character have been discussed in §2.6.2.2. The QTAIM parameters for **40** are presented in Table 4.4; as the bonds of **41** and **42** are very similar to those of **40**, the QTAIM parameters of **41** and **42** are shown in the Appendix C. §C.2. Selected parameters for bonds of interest, such as those linked to the functionalized substituents of **41** and **42**, are shown in Table 4.5.

The BCPs of **40-42** and their respective energy descriptors were evaluated in conjunction with the electron the Laplacian maps, and corroborated by corresponding electron deformation density (EDD) mappings (Appendix C. §C.3.), of each segment of **40-42**, thus affording a comprehensive assessment of the ICT across the chromophores. EDD maps represent the difference between the XWR fitted model, and the spherical atom model, thereby effectively showing the nature of the bonding density and electronic polarization arising in a given cross-section of the molecule. Meanwhile, Laplacian maps display the second derivative of the electron density at its stationary points, i.e., for $\nabla\rho(r) = 0$, and thus reveal the extent of local concentrations/depletions of electronic charge around atoms.

Table 4.4. Parameters of the (3, -1) BCPs and intramolecular hydrogen bond BCP of **40**. ρ(r) is the electron density, $\nabla^2\rho$(r) the Laplacian of the electron density; ε the bond ellipticity, G(r)/ρ(r) the kinetic energy density per electron, and H(r) the total energy density [in atomic units, a.u.].

Bond	**ρ(r) [eÅ^{-3}]**	**$\nabla^2\rho$(r) [eÅ^{-5}]**	**ε**	**G(r)/ρ(r) [a.u.]**	**H(r) [a.u.]**	**Bond type *cf.* Table 2.3**
C1-C2	2.112	-21.047	0.19	0.297	-0.311	Covalent (π)
C2-C3	2.141	-23.695	0.06	0.234	-0.320	Covalent (σ)
C3-C4	2.179	-25.667	0.03	0.214	-0.335	Covalent (σ)
C4-C5	2.185	-22.896	0.27	0.299	-0.334	Covalent (π)
C5-C6	2.139	-24.446	0.07	0.214	-0.322	Covalent (σ/π)
C6-C1	2.132	-24.823	0.03	0.204	-0.322	Covalent (σ)
C6-O	2.017	-9.252	0.15	1.287	-0.481	Polar shared (π)
C1-C7	1.774	-17.569	0.03	0.179	-0.229	Covalent (σ)
C7-N1	1.736	-17.082	0.03	0.700	-0.357	Covalent (σ)
N1-C8	2.270	-24.259	0.07	0.972	-0.579	Covalent (σ/π)
C8-N2	2.384	-26.953	0.09	0.951	-0.616	Covalent (π)
N2-C9	2.265	-18.284	0.02	1.169	-0.582	Polar shared (σ)
C9-C10	2.236	-23.902	0.24	0.305	-0.349	Covalent (π)
C10-C11	2.107	-22.249	0.15	0.270	-0.315	Covalent (π)
C11-C12	2.196	-22.337	0.28	0.322	-0.336	Covalent (π)
C12-C8	2.089	-21.954	0.17	0.273	-0.312	Covalent (π)
C11-C13	1.793	-18.151	0.03	0.209	-0.244	Covalent (σ)
H Bond (OH···N1)	0.460	3.371	0.05	0.778	-0.018	Mixed

Table 4.5. Parameters of the (3, -1) BCPs of the bonds associated with the functionalising substituents of **40-42**; ρ(r) is the electron density , $\nabla^2\rho$(r) the Laplacian of the electron density, ε the bond ellipticity, G(r)/ρ(r) the kinetic energy density per electron, and H(r) the total energy density [in atomic units, a.u.].

Structure	Bond	ρ(r) [eÅ^{-3}]	$\nabla^2\rho$(r) [eÅ^{-5}]	ε	G(r)/ρ(r) [a.u.]	H(r) [a.u.]	Bond type *cf.* Table 2.3
40	**C11-C13**	1.793	-18.151	0.03	0.209	-0.244	Covalent (σ)
41	**C10-Cl1**	1.397	-9.947	0.05	0.327	-0.171	Covalent (σ)
42	**C10-Cl1**	1.431	-10.187	0.06	0.297	-0.169	Covalent (σ)
	C12-Cl2	1.419	-9.815	0.06	0.314	-0.168	Covalent (σ)

The most striking observation is seen in the Laplacian maps of the XWR in the OH···N region of **40** and **41**, which corroborate the existence of intramolecular hydrogen bonds. These manifest in the form of concentrations of electron density in the plane containing the OH···N vector (*cf.* highlighted areas in Figs 4.4a,b) and these findings are further confirmed by the QTAIM parameters (*cf.* Table 4.4 and Appendix C; §C.2). Electron density and energy descriptors for the intramolecular hydrogen bonds in **40** and **41** are suggestive of a mixed bonding character with both ionic and covalent components (*cf.* Table 4.4). One therefore may assume that, rather than the ensuing ICT being contained within the *o*-cresol moiety of **40** and **41**, it in fact extends into the functionalized pyridyl group via the intramolecular OH···N bond. Meanwhile, the lack of a similar hydrogen bond in **42** explains the preclusion of ICT between the two aromatic units in this molecule, as observed by the absence of an electron density shifting in the frontier orbitals of **42** (Fig 4.3). A previous example of such ICT phenomena being influenced via intramolecular interactions in NLO organic chromophores has been reported by Cole *et al.*[30]; here they reported an augmentation of ICT across an thiophenylcyanoacrylate based dye via a S···C≡N bond, identified by QTAIM parameters.

In terms of **40** and **41**, it is expected that the electron donation of the *o*-cresol moiety, via the OH···N bond, opposes the deactivating effect of the methyl group (**40**), reducing the net polarization across this molecule as a whole. Similarly, the competing negative inductive and positive mesomeric properties of the chloro group (**41**) will also likely result in a 'push' effect that will oppose the donating *o*-cresol moiety as confirmed by the electron deformation maps *cf.* Appendix C. §C.3. Additionally, given the greater 'push' effect of chloro compared to that of methyl groups, it is expected that **41** will experience a greater reduction in net polarization as a consequence of opposing ICT pathways, compared to **40**. Consequently, the

OH···N bond in **40** and **41** appears to affect their ICT and thus, molecular hyperpolarizabilities in a deleterious manner, with the strength of the NLO activity of the three chromophores studied herein expected to present as **42** > **40** > **41**.

A polarization of the electron density in all three chromophores toward the two N atoms in both the pyridyl ring and the amino moiety of the connecting bridge, is confirmed by the polar-shared nature of the N-X bonds in **40** and **41** (*cf.* Table 4.4) as is further corroborated by the EDD maps of **40-42** (Appendix C. §C.3.). In the case of **42**, some of the N-X bonds appear to be more classically covalent, as opposed to polar-shared, especially those associated with N(2) of the pyridyl ring (*cf.* Table 4.4; Appendix C; §C.2); this is likely a consequence of the absence of an intramolecular hydrogen bond in **42**, which should result in a lower accumulation of charge on the N atom. The topological parameters of the N(1)-C(8) bond indicated it is covalent polar-shared (Table 4.3 and Appendix C; §C.2), while the QTAIM parameters, the N(1)-C(7) bond ,especially the low ellipticity, suggest that this bond has a covalent nature, with a distinct σ character. This implies that π-delocalization does not extend through this bond, thus preventing ICT from the pyridyl to the *o*-cresol moiety; this result is consistent with the initial assessment that changes in the NLO response of **40-42** should emanate from ICT phenomena in the functionalized pyridylamino moiety. The bonds in the *o*-cresol moieties appear to exhibit low degrees of polarization, except for the O atom, which is polar shared.

The bonds in the functional groups of **40-42**, e.g. the C-C_{methyl} bond, C(11)-C(13), in **40**, exhibit σ-bonding character, which corroborates our findings that π-conjugation does not carry through to these formally single bonds. Thus, the methyl group can only donate σ-bonded electron density to the pyridylamino moiety, i.e., the ICT effects in **40** should emanate predominantly from the ICT between the amino to the pyridyl ring. Consequently, initial comparison of **40** and **41** may lead to the conclusion that **41** will exhibit a stronger NLO response than **40** as a result of the presence of a) the deleterious activating methyl group in **40**, coupled with b) the strong electron-withdrawing chloro substituent. However, the competing negative inductive and positive mesomeric properties of the chloro substituent will likely result in an overall reduction of the net polarization across the chloro-substituted aromatic unit. Close inspection of the EDD maps (Appendix C; §C.3); confirm this, and reveal that the Cl(1)-C(10) bond in both **41** and **42** experience a polarization of electron density *toward* the pyridyl ring, which creates an opposing ‘push-pull’ effect of charge on the chloro-substituted site. Consequently, the ICT in **41** will be lower than that experienced in **40** as the mesomeric effects, and thus electron donation of the chloro group, will be greater than that of methyl group.

Moving on to compound **42**, it is reasonable to assume that the ICT, and thus the NLO response should be higher in **42** than in **40** and **41**, given the additional 3-chloro substituent on the pyridyl ring of **42**. However, the reasons for this are more involved, and require appreciation of the tensorial nature of molecular hyperpolarizability. In the case of **41** and **42**, the 5-chloro substituent will experience competing inductive and mesomeric effects, reducing the net polarization across the 3,5-dichloro-2-pyridylamino unit due to an opposing ‘push-pull’ effect as a result of the 5-chloro being diametrically opposite the donating amino group. However, the additional 3-chloro group in **42**, being *ortho*-substituted, does not diametrically oppose the donation of the amino group, thus affording an overall increase of ICT compared to **41** and thus an amelioration of its NLO response.

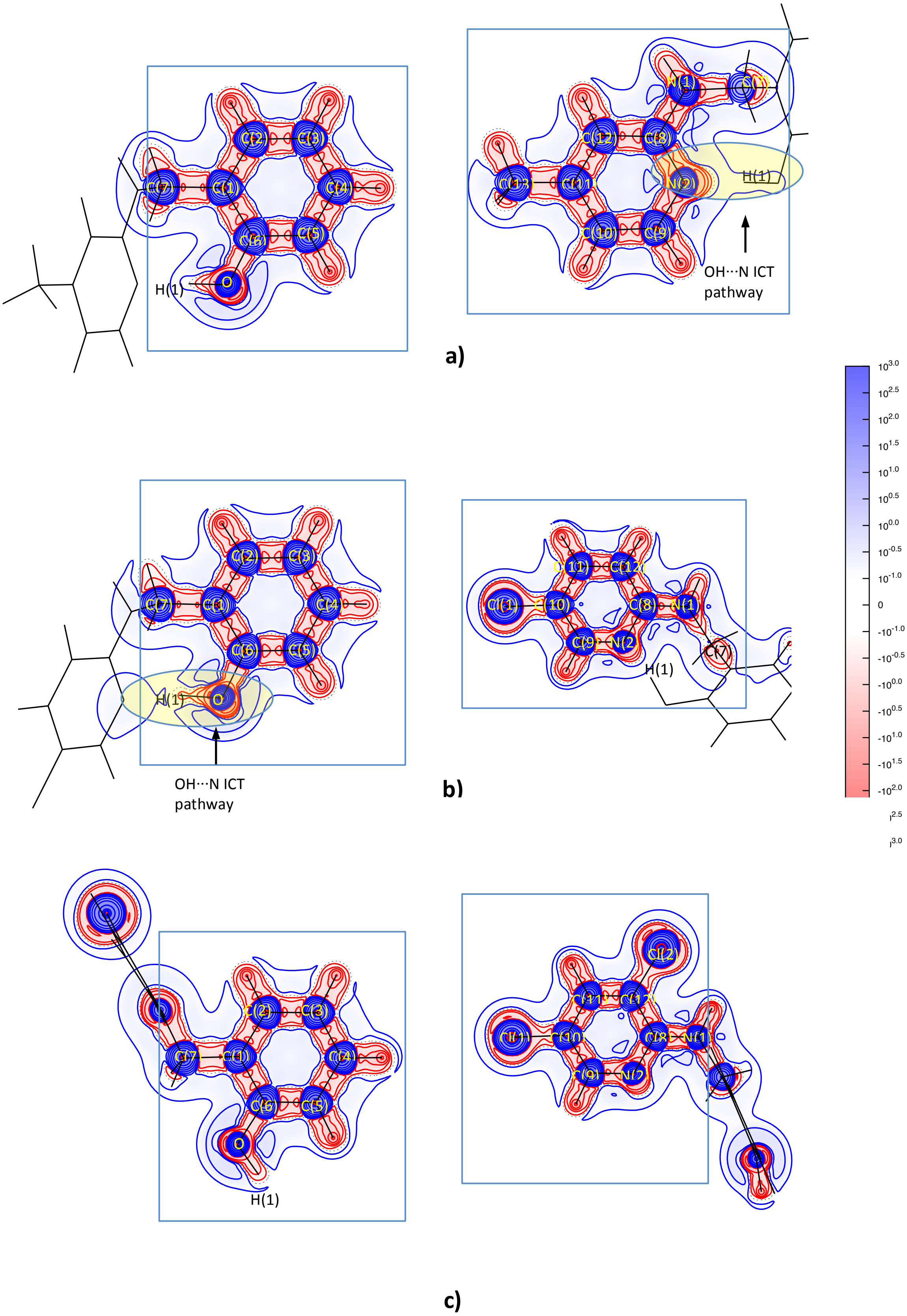

Figure 4.4. Laplacian maps of **40** (a), **41** (b) and **42** (c). Boxed segments are in the plane of the page. The color scale in the Laplacian maps refers to local concentrations (blue) and depletions (red) of electronic charge. Contour levels are shown at 0.1 eÅ^{-5} gradient scaling. The yellow regions of the selected maps highlight the Laplacian feature associated with the OH¨N intramolecular hydrogen bond of **40** and **41**.

4.3.4. NLO Properties of 40-42: Determination of Molecular Hyperpolarizabilities, β

The linear optical properties of **40-42** were assessed and characterized using UV-Vis absorption spectroscopy. This confirmed that there was no light absorption at 400 nm for all three chromophores; thus the molecular hyperpolarizability, β, could be determined via HRS using a standard 800 nm laser setup (given 400 nm is its SHG wavelength)[4].

Three independent methods were used to determine β for all three chromophores, which are presented in Table 4.6. The XWR- and DFT-derived values presented represent the static hyperpolarizability (β_0) i.e. the measurement is free from dispersion (frequency-independent). In principle, HRS measurements report dynamic values (frequency dependent); however, since they were conducted at a non-resonant wavelength, the reported values are so heavily damped, when taking into account the width of the transition, that it effectively affords a static hyperpolarizability value.

The enumeration and comparison of these independently obtained β values is prudent, given large errors (typically 10-30%) are associated with the determination of β coefficients[31]. Moreover, the use of these three methods allows an assessment of the β values of each compound in different phases (HRS: solution; DFT: gas, XWR: gas within the pseudo-solid state environment of crystal field forces, given XWR is tempered by experimental X-ray diffraction data). This multi-phase comparison should help to uncover the presence or absence of molecular aggregation effects, which may become important for future device applications.

Compound	Molecular hyperpolarizability (β_0) / esu 10^{-30}			
	DFT	XWR	HRS#	Normalized HRS*
40	1.48	1.57	27.0 ± 1.0	1.72
41	1.25	1.47	15.7 ± 0.1	1.00
42	2.77	2.95	35.0 ± 1.0	2.23

Table 4.6. Molecular hyperpolarizability (β_0) values for **40-42** derived in their gas, {gas + crystal field forces}, and solution phases via DFT, XWR and HRS, respectively.

#The errors in β_{HRS} were predicated by the 20% statistical error on the evaluation of β for the Crystal Violet HRS reference sample.

*HRS values normalized to the smallest β_{HRS}; Compound **41**.

An initial survey of Table 4.6 shows that the molecular hyperpolarizabilities in this family follow the order **42 > 40 > 41**, in agreement with the aforementioned property predictions made about these chromophores via their molecular architecture information (§4.3.1) and their consequential ICT behavior (§4.3.2.2 & §4.3.3). Reassuringly, the observation that the **42 > 40 > 41** trend holds for both the gas- and solution-phase, suggests that the trends in these results are accurate. It is accepted that trends, rather than absolute values, observed between DFT calculations on a cognate set of compounds are generally accurate[26]. Moreover, there is good agreement between the DFT values and those determined through the relatively new XWR method, which is reassuring and provides further confirmation of the robustness of the XWR method. Once the HRS values are normalized against the smallest HRS value (**41**), the normalized HRS hyperpolarizabilities are found to be close to those of DFT and XWR. The absolute HRS values are an order of magnitude larger than those derived from DFT and XWR. This is presumably a result of Lorentz forces[32,33], that are beyond crystal field forces (that XWR factors in) such as geometric constraints of the chromophores caused by molecular aggregation. It is therefore reasonable to assume that the NLO effects of these molecules might be noticeably affected by NLO device processing conditions, and thus their eventual form should be considered carefully eg, embedded within thin-film technology or applied as a bulk crystal.

Considering the normalized β for **40-42** in the solution phase, their similarity with the gas-phase results suggest that solvent environment has minimal polarization effects on the subject NLO molecules, at least for the solvent used in the HRS measurements (acetonitrile). This also indicates that molecular aggregation phenomena are likely absent for **40-42** within this solution medium.

The tensorial components of the molecular hyperpolarizability of each structure were additionally determined by XWR (Fig 4.5). These enable the assessment of structure-function relationships of **40-42** in the crystalline state; *cf.* a comparison of β for **40-42** in terms of their unit cell axes (Fig 6). The largest components of **40** is the *yyy* followed by the *xxx* component, in line with the corresponding ICT in **40** that occurs along the Y-axis of the molecular unit (Fig 4.6, **40**) from the methyl group of the pyridylamino moiety, through to the *o*-cresol moiety via the OH···N intramolecular hydrogen bond. Similarly, the largest coefficients for **41** and **42** are assigned to the *zzz* component of the hyperpolarizability tensor. This corresponds to the ICT from the chloro groups to the pyridylamino moiety for **42**; and from the chloro group through to the *o*-cresol moiety for **41**, as influenced by the OH···N intramolecular hydrogen bond (Fig 4.6, **41-42**). These findings are crystal packing specific in agreement with the molecular assessments of the ICT for these chromophores (§4.3.3.3).

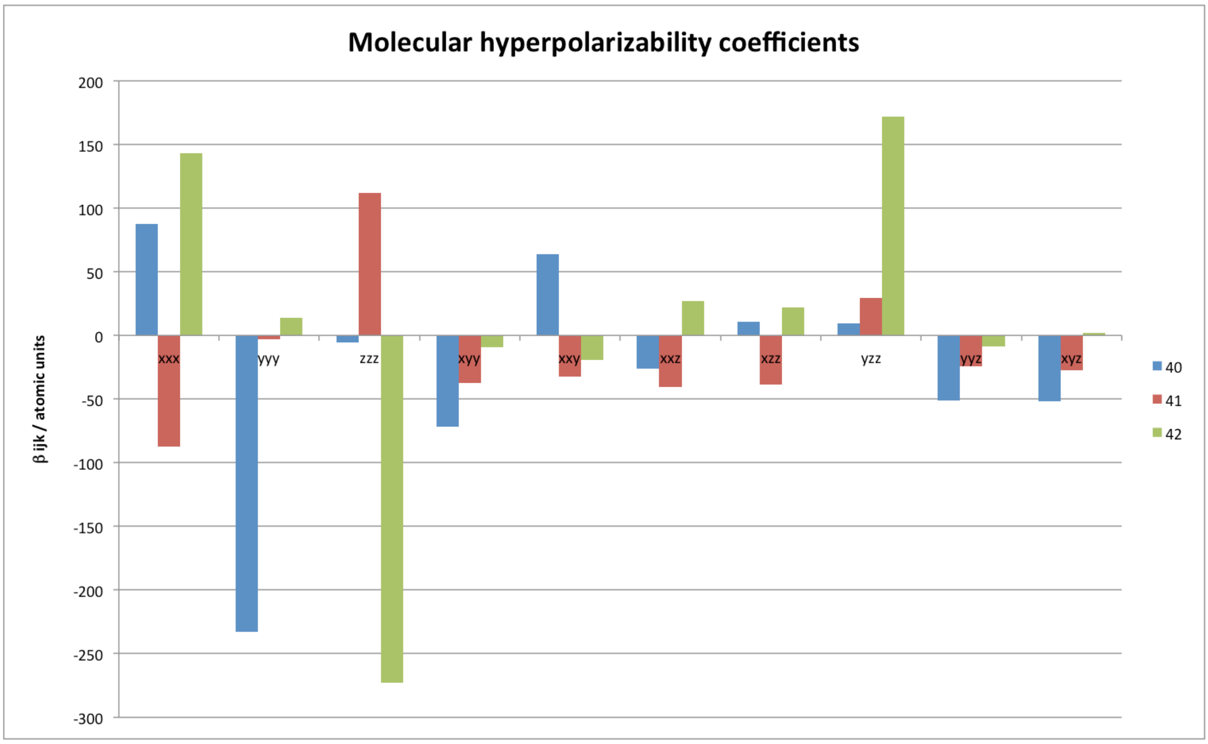

Figure 4.5. Molecular hyperpolarizability coefficients for **40-42**.

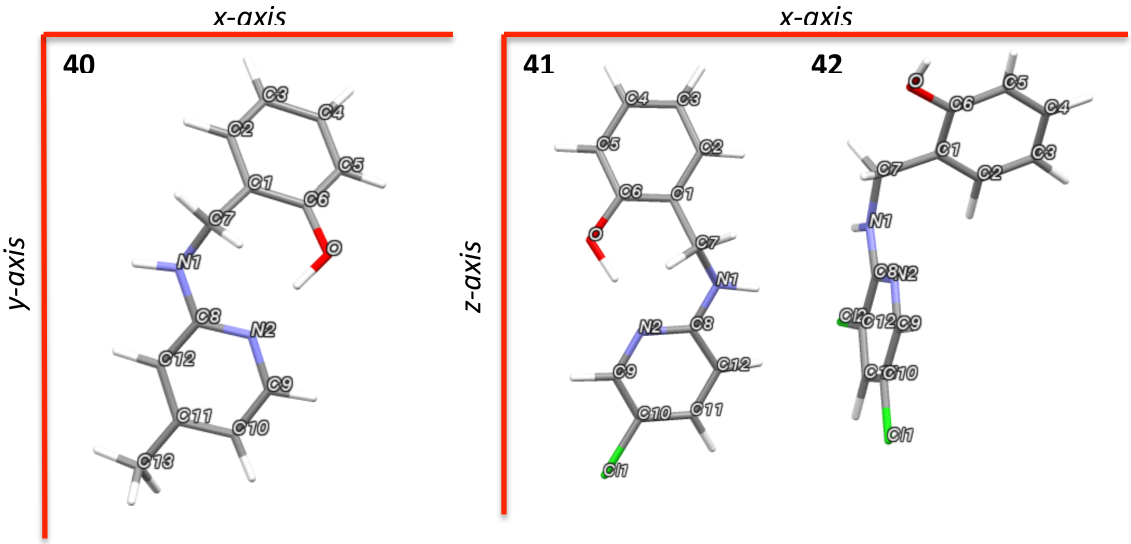

Figure 4.6. Compounds **40-42** oriented with respect to the X, Y, Z-axes of the crystallographic unit cell of the respective compound.

4.4. Conclusions

A series of three pyridylamino-*o*-cresols with generic formula, α-(X-2-pyridylamino)-o-cresol (where X = 4-methyl (**40**); 5-chloro (**41**); 3,5-dichloro (**42**)), have been characterized in terms of the structural and NLO properties. To that end, the molecular architectures and intramolecular charge transfer aspects of the electronic structures of **40-42** are related to their NLO activity, especially their molecular hyperpolarizability, β, which provides a molecular measure of the second-order NLO response in a chromophore. Given the notorious difficulties in obtaining reliable values of β, the molecular hyperpolarizability is evaluated by three independent methods that span the gas, {gas + crystal field forces}, and solution states. These results are promising since all three methods yield NLO measures for **40-42** that follow the same trend (**42 > 40 > 41**) that has been herein rationalized in terms of the respective molecular architectures, chemical composition and resultant ICT phenomena of each chromophore. The XWR method has given β values comparable to the DFT values. The XWR afforded a full topological analysis of these structures through Bader's Quantum Theory of Atoms in Molecules (QTAIM) formalism, yielding electron deformation density maps and Laplacian maps. It is noteworthy that QTAIM analysis is possible, despite the usual requirement for high-resolution X-ray diffraction data; this highlights the value, and robustness, of the XWR method.[5]

The ability to undertake QTAIM analysis in the case of these three chromophores has proven to be essential to the understanding of the structure-function relations that contribute to their subsequent NLO activity. This includes the salient identification of an OH···N bond in **40** and **41**, which provides an ICT pathway between the rings in these two molecules, acting to diminish their overall NLO responses. It is significant that this secondary ICT pathway causes a negative effect on such chromophores. This highlights the importance of considering the effects of hydrogen-bonding interactions in organic chromophores for NLO applications. This adds to the already well-established catalogue of structure-property relationships and design rules for organic NLO chromophores to date.

The evaluation of the molecular hyperpolarizability of these three chromophores together with a full topological assessment of the origins of their respective NLO responses demonstrates that **40-42** will all respond as NLO chromophores but, that **42** will display a significantly larger response than the other two chromophores. Given that **41** and **42** crystallize in centrosymmetric space groups, their prospective application would benefit from being embedded in a thin-film device environment. Thin film device environments would also suit **40**, although its non-centrosymmetric crystal structure means that a crystal phase of application might additionally be possible in this case. This result is promising when one considers the simplicity of both the molecular architecture and chemical substituents in this series. A significant range of β values across **40-42**, and between phase states, is also promising given the simplicity of these chromophores and further validates the idea that even simple molecular engineering design can achieve varying levels of NLO responses, thus affording the ability to design compounds for bespoke application.

4.5. References

(1) Cole, J. M. Organic Materials for Second-Harmonic Generation: Advances in Relating Structure to Function. *Philos. Trans. R. Soc. Lond. Ser. Math. Phys. Eng. Sci.* **2003**, *361* (1813), 2751–2770.

(2) Prasad, P. N.; Williams, D. J. *Introduction to Nonlinear Optical Effects in Molecules and Polymers*; Wiley, 1991.

(3) Cheng, L. T.; Tam, W.; Marder, S. R.; Stiegman, A. E.; Rikken, G.; Spangler, C. W. Experimental Investigations of Organic Molecular Nonlinear Optical Polarizabilities. 2. A Study of Conjugation Dependences. *J. Phys. Chem.* **1991**, *95* (26), 10643–10652.

(4) Clays, K.; Persoons, A. Hyper-Rayleigh Scattering in Solution. *Phys. Rev. Lett.* **1991**, *66* (23), 2980–2983.

(5) Woińska, M.; Jayatilaka, D.; Dittrich, B.; Flaig, R.; Luger, P.; Woźniak, K.; Dominiak, P. M.; Grabowsky, S. Validation of X-Ray Wavefunction Refinement. *ChemPhysChem* **2017**, *18* (23), 3334–3351.

(6) Bytheway, I.; Grimwood, D. J.; Jayatilaka, D. Wavefunctions Derived from Experiment. II. A Wavefunction for Oxalic Acid Dihydrate. *Acta Crystallogr. A* **2001**, *57* (Pt 1), 87–100.

(7) Bytheway, I.; Grimwood, D. J.; Jayatilaka, D. Wavefunctions Derived from Experiment. III. Topological Analysis of Crystal Fragments. *Acta Crystallogr. A* **2002**, *58* (Pt 3), 232–243.

(8) Bader, R. F. W. *Atoms in Molecules: A Quantum Theory*; Clarendon Press, 1994.

(9) Bader, R. F. W. Atoms in Molecules. *Acc. Chem. Res.* **1985**, *18* (1), 9–15.

(10) Coppens, P. *X-Ray Charge Densities and Chemical Bonding*; Oxford University Press: Chester, England : Oxford ; New York, 1997.

(11) Coppens, P. Charge-Density Analysis at the Turn of the Century. *Acta Crystallogr. A* **1998**, *54* (6), 779–788.

(12) Hansen, N. K.; Coppens, P. Testing Aspherical Atom Refinements on Small-Molecule Data Sets. *Acta Crystallogr. A* **1978**, *34* (6), 909–921.

(13) Cole, J. M.; Copley, R. C. B.; McIntyre, G. J.; Howard, J. A. K.; Szablewski, M.; Cross, G. H. Charge-Density Study of the Nonlinear Optical Precursor DED-TCNQ at 20 K. *Phys. Rev. B* **2002**, *65* (12), 125107.

(14) Cole, J. M.; Goeta, A. E.; Howard, J. A. K.; McIntyre, G. J. X-Ray and Neutron Diffraction Studies of the Non-Linear Optical Compounds MBANP and MBADNP at 20 K: Charge-Density and Hydrogen-Bonding Analyses. *Acta Crystallogr. B* **2002**, *58* (4), 690–700.

(15) Lin, T.-C.; Cole, J. M.; Higginbotham, A. P.; Edwards, A. J.; Piltz, R. O.; Pérez-Moreno, J.; Seo, J.-Y.; Lee, S.-C.; Clays, K.; Kwon, O.-P. Molecular Origins of the High-Performance Nonlinear Optical Susceptibility in a Phenolic Polyene Chromophore: Electron Density Distributions, Hydrogen Bonding, and Ab Initio Calculations. *J. Phys. Chem. C* **2013**, *117* (18), 9416–9430.

(16) Cole, J. M.; D. D Hickstein. Molecular Origins of Nonlinear Optical Activity in Zinc Tris(Thiourea)Sulfate Revealed by High-Resolution x-Ray Diffraction Data and Ab Initio Calculations. *Phys. Rev. B* **2013**, *88* (18), 184105.

(17) Hickstein, D. D.; Cole, J. M.; Turner, M. J.; Jayatilaka, D. Modeling Electron Density Distributions from X-Ray Diffraction to Derive Optical Properties: Constrained Wavefunction versus Multipole Refinement. *J. Chem. Phys.* **2013**, *139* (6), 064108.

(18) Sheldrick, G. M. A Short History of *SHELX*. *Acta Crystallogr. A* **2008**, *64* (1), 112–122.

(19) Schmidt, M. W.; Baldridge, K. K.; Boatz, J. A.; Elbert, S. T.; Gordon, M. S.; Jensen, J. H.; Koseki, S.; Matsunaga, N.; Nguyen, K. A.; Su, S.; et al. General Atomic and Molecular Electronic Structure System. *J. Comput. Chem.* **1993**, *14* (11), 1347–1363.

(20) Gordon, M. S.; Schmidt, M. W. Advances in Electronic Structure Theory: GAMESS a Decade Later. In *Theory and Applications of Computational Chemistry: the first forty years*; Dykstra, C. E., Frenking, G., Kim, K. S., Scuseria, G. E., Eds.; Elsevier: Amsterdam, 2005; pp 1167–1189.

(21) Bode, B. M.; Gordon, M. S. MacMolPlt: A Graphical User Interface for GAMESS. *J. Mol. Graph. Model.* **1998**, *16* (3), 133–138, 164.

(22) Jayatilaka, D.; Grimwood, D. J. Tonto: A Fortran Based Object-Oriented System for Quantum Chemistry and Crystallography. In *Computational Science — ICCS 2003*; Sloot, P. M. A., Abramson, D., Bogdanov, A. V., Gorbachev, Y. E., Dongarra, J. J., Zomaya, A. Y., Eds.; Lecture Notes in Computer Science; Springer Berlin Heidelberg, 2003; pp 142–151.

(23) Madsen, A. Ø. *SHADE* Web Server for Estimation of Hydrogen Anisotropic Displacement Parameters. *J. Appl. Crystallogr.* **2006**, *39* (5), 757–758.

(24) Lu, T.; Chen, F. Multiwfn: A Multifunctional Wavefunction Analyzer. *J. Comput. Chem.* **2012**, *33* (5), 580–592.

(25) Farrugia, L. J. *WinGX* and *ORTEP for Windows* : An Update. *J. Appl. Crystallogr.* **2012**, *45* (4), 849–854.

(26) Allen, F. H.; Kennard, O.; Watson, D. C.; Brammer, L.; Orpen, A. G.; Taylor, R. Tables of Bond Lengths Determined by X-Ray and Neutron Diffraction. Part 1. Bond Lengths in Organic Compounds. *J. Chem. Soc. Perkin Trans. 2* **1987**, No. 12, S1–S19.

(27) Macchi, P.; Proserpio, D. M.; Sironi, A. Experimental Electron Density in a Transition Metal Dimer: Metal−Metal and Metal−Ligand Bonds. *J. Am. Chem. Soc.* **1998**, *120* (51), 13429–13435.

(28) Flensburg, C.; Larsen, S.; Stewart, R. F. Experimental Charge Density Study of Methylammonium Hydrogen Succinate Monohydrate. A Salt with a Very Short O-H-O Hydrogen Bond. *J. Phys. Chem.* **1995**, *99* (25), 10130–10141.

(29) Espinosa, E.; Souhassou, M.; Lachekar, H.; Lecomte, C. Topological Analysis of the Electron Density in Hydrogen Bonds. *Acta Crystallogr. B* **1999**, *55* (4), 563–572.

(30) Cole, J. M.; Blood-Forsythe, M. A.; Lin, T.-C.; Pattison, P.; Gong, Y.; Vázquez-Mayagoitia, Á.; Waddell, P. G.; Zhang, L.; Koumura, N.; Mori, S. Discovery of S···C≡N Intramolecular Bonding in a Thiophenylcyanoacrylate-Based Dye: Realizing Charge Transfer Pathways and Dye···TiO2 Anchoring Characteristics for Dye-Sensitized Solar Cells. *ACS Appl. Mater. Interfaces* **2017**, *9* (31), 25952–25961.

(31) *Characterization Techniques and Tabulations for Organic Nonlinear Optical Materials*; Kuzyk, M. G., Dirk, C. W., Eds.; Optical engineering; Marcel Dekker: New York, 1998.

(32) Seidler, T.; Stadnicka, K.; Champagne, B. Second-Order Nonlinear Optical Susceptibilities and Refractive Indices of Organic Crystals from a Multiscale Numerical Simulation Approach. *Adv. Opt. Mater.* **2014**, *2* (10), 1000–1006.

(33) Seidler, T.; Stadnicka, K.; Champagne, B. Investigation of the Linear and Second-Order Nonlinear Optical Properties of Molecular Crystals within the Local Field Theory. *J. Chem. Phys.* **2013**, *139* (11), 114105.

Chapter 5

Multi-phase structural models of stilbazolium-ions built up ion-by-ion correlate with molecular hyperpolarizability calculations to explain their non-linear optical properties

5.1 Introduction

Chapter 3 & 4 focused on neutral organic nonlinear optical (NLO) chromophores, and investigated the affects of crystal field effects, aromatic substitution and intramolecular interactions on the SHG response of optically active chromophores. Yet, some of the most promising organic chromophores for SHG to-date are in fact ionic; the most prominent example in industry being the material 4-N,N′ -dimethylamino-N-methyl-4-stilbazolium toyslate (**DAST**), which has been shown to exhibit significant SHG effects.[1] Unfortunately, recent studies reveal that the SHG response of **DAST** can not reach its full potential in the solid-state phase due to deleterious interionic interaction between its cation and anion[2], and thus efforts have been made to attempt to counter the negative impact of these interactions through the investigation of **DAST**-based derivatives.[2] This is particularly salient given the preponderance for SHG materials to be incorporated into devices when in the solid-state phase. The work of this chapter attempts to identify and characterise the nature of these deleterious interionic interactions in **DAST** and a promising DAST-derivative, N,N-dimethylamino-N'-2,5-dimethylbenzyl-stilbazolium p-toluenesulfonate (**BP3**), in an effort to establish new structure-function relationships that describe the impact of interionic interactions in ionic SHG chromophores.

For non-ionic organic chromophores, it can be generally assumed that their intermolecular interactions are weak, and therefore, the macroscopic second-order optical susceptibilities (χ^2) can be estimated by the orientational superposition of the molecular-scale second-order optical susceptibilities, i.e. β, which is known as the first-order molecular hyperpolarizability. However, this assumption, which is based on the *oriented-gas* model[3], cannot be used for ionic organic chromophores, such as stilbazolium-based compounds. Yet, such organic salts are particularly important in the NLO field. For instance, the stilbazolium-based chromophore, 4-N,N′ -dimethylamino-N-methyl-4-stilbazolium toyslate, (**43,** hereafter labelled **DAST)** (Fig. 5.1, left) is one of few organic molecules to have demonstrated longstanding commercial prospects for NLO applications. Ranges of chemical derivatives of **DAST** have thus been developed with the prospect that they might afford even better NLO properties. Structure-property relationships that help decode the molecular and supramolecular origins of the structure and properties of such derivatives stand to offer materials-by-design strategies, which could be used to systematically tackle this materials discovery goal.

In ionic organic chromophores, van der Waals forces, electrostatic (Coulombic) forces, and hydrogen-bonding need to be considered carefully, as these types of weak interactions are responsible for supramolecular arrangements that can influence the molecular origins of the ionic organic chromophores' NLO activity. Moreover, since there are positive and negative ions co-existing in organic salts, that will exhibit different ionic forces upon each other, all combinations of cation···anion, cation···cation and anion···anion inter-ionic interactions need to be assessed. Furthermore, the relative structural arrangement of each type of ion, with respect to each other, within the crystal lattice of an organic salt will influence its NLO output.

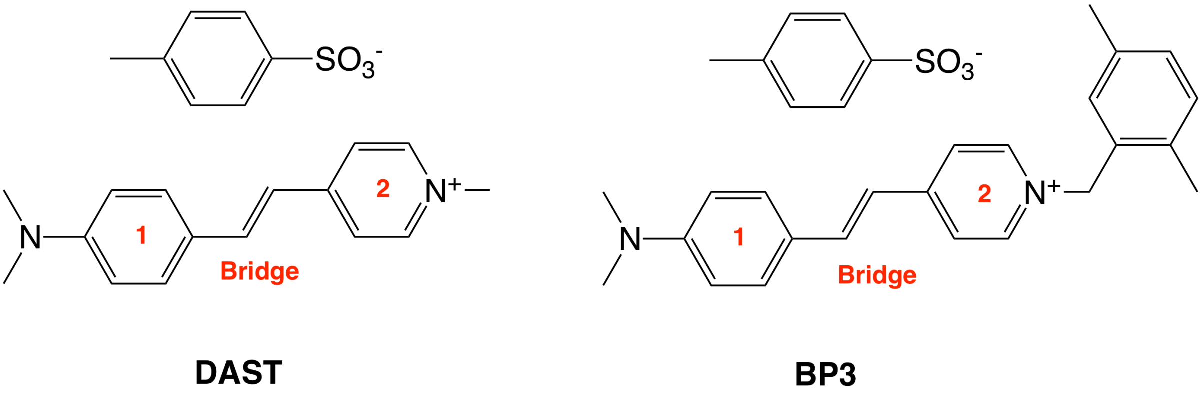

Fig 5.1. Chemical structures of **DAST** and **BP3** drawn in their default canonical representations

To this end, Cole *et al.*[2] showed that **DAST** exhibits a range of significant inter-ionic interactions. They further demonstrated that the presence of certain combinations of cation···anion interactions in **DAST** derivatives could diminish their molecular hyperpolarizability, β. In particular, the co-existence of C-H···O and C-H···C(π) hydrogen-bonds between cations and anions in **DAST** derivatives were shown to have a particularly deleterious effect on their β values. This led Cole *et al.*[2] to the advocacy that **DAST** derivatives, which are void of such cation anion interactions, could herald better NLO prospects than **DAST**. N,N-dimethylamino-N’-2,5-dimethylbenzyl-stilbazolium p-toluenesulfonate, (**44**, hereafter labelled **BP3)** (Fig. 5.1, right) is one such chemical derivative, since it is void of cationic···anionic C-H···C(π) hydrogen-bonds. The absence of these hydrogen-bonds in **BP3** appears to be due to its 2,5-dimethylbenzyl moiety which is responsible for an overall bent-shaped cation; as a result, larger cation···anion separations manifest in **BP3** than observed in **DAST**[2,4]. **DAST** and **BP3** also crystallize in different space groups (Cc and $P2_1$, respectively). Nevertheless, cation···anion interactions in both **DAST** and **BP3** essentially lie in crystallographic planes that are perpendicular to interleaving sheets of anion···anion and cation···cation interactions.[5]

The extent by which cation···anion Coulombic interactions in **DAST** derivatives affect β has also been studied via several computational efforts. Duan *et al.*[6] used semi-empirical calculations to show how β of a **DAST** cation (DAS+) was affected by its relative position to a negative point charge that was used to represent an anion. They found that the magnitude of β increased as the point charge became more in line with the ICT axis of DAS+, which can be regarded as essentially synonymous to its D-π-A axis. This is as expected since ICT and β are directly correlated[2]. Kim *et al.*[4] expanded this model for a similar **DAST**-derivative using point charges or isotropic representations of anions around a similar, N,N-dimethylamino-N′-phenyl-4-stilbazolium, cation. They discovered that the magnitude of β for this cation showed only modest change (< 15 %) as a function of variation in the relative position of the anionic species; moreover, the direction of β was unaffected by such variation. This means that Coulombic forces have insignificant effect on the DAS+ cation such that it can be modelled in isolation from this type of electrostatic interaction.

The main cation···cation interactions in **DAST** and **BP3** are expected to arise from weak van der Waals (vdW) forces, given that J-aggregation[15] has been characterized in the crystalline form of **DAST** by Follonier *et al;*[5] in that study, the absorption spectrum of **DAST** was compared in methanol and in the crystalline form. Results showed that cations organize themselves with respect to each other in head-to-tail or slipped co-facial configurations. Head-to-tail structural arrangements lead to supramolecular enhancements in NLO activity for highly planar organic chromophores such as **DAST** owing to the linear chain of D-π-A motifs incurred; thus, the observed J-type of aggregation. To this end, Follonier *et al* showed that cation-to-cation charge-hopping was possible in **DAST**, with a low activation energy of 0.34 ± 0.03 eV. J-aggregation has also been predicted in solid-state forms of **DAST** derivatives.[7,8] Thus, it is presumed that cation···cation interactions in **BP3** show similar traits, given that **DAST** and **BP3** cations pack in a similar fashion, as sheets within a crystal lattice. In the context of anion···anion interactions, it has already been established that the *p*-toluenesulfonate (pTS^-) anions, which comprise the anionic component of both **DAST** and **BP3**, are very inefficient NLO chromophores compared to the stilbazolium cations[9]. Their electronic contribution to the overall macroscopic nonlinearity of **DAST** or **BP3** should thus be negligible.

Overall, it would seem that cation···cation interactions in **DAST** and **BP3** stand to enhance β while certain types of cation···anion interactions will deplete β. A more detailed characterization of the various types of inter-ionic interactions that appear in **DAST** and **BP3** could thus prove valuable in order to facilitate the molecular engineering of **DAST** derivatives that exhibit superior NLO properties. To this end, it is equally important to establish the molecular-level contributions to their NLO activity in a detailed fashion since the nature of inter-ionic interactions are naturally dependent on the innate electronic characteristics of their molecular core.

The molecular and intermolecular origins of NLO activity in a range of neutral[10,11], zwitterionic[12] and ionic[13] organic chromophores have been elucidated previously via high-resolution electron-density mappings, as captured within their crystalline environment, from X-ray diffraction studies that employed multipolar refinements. These previous studies were all aided by the direct determination

---

[15] J-aggregation is a form of molecular stacking arrangement whereby the molecules arrange themselves head-to-tail (also known as edge-to-edge).

of β from their experimentally-determined electron-density mappings, using their multipolar moments in calculations based on an empirical method by Robinson[14,15]. The determination of β in a crystalline environment (eg, indirectly through charge density studies) is both rare and industrially pertinent, given that this is the phase in which a range of key practical applications for **DAST** have been considered[16]. Solid-state β values derived from single-crystal X-ray diffraction data are also important since they intrinsically incorporate the influence of crystal forces. As such, they can be compared with β values determined in other phases to distinguish the effect of holding an NLO chromophore within a crystal lattice. Furthermore, the ability to generate optical properties from crystal structure information presents an opportunity to develop structure-property relationships on materials with a valuable internal consistency. This last point is especially pertinent when considering that there are significant practical issues with the accuracy of optical experiments that evaluate β.

On a practical level, experimentally determined values of β are renowned for their large errors in quantification (10-30% error is quite typical)[17] Hyper Rayleigh scattering (HRS) is considered to produce the most reliable experimental values of β,[18] and so our calculations of β presented herein are compared against HRS values for **DAST**[1] and **BP3**.[2] That said, β values from HRS are determined on samples in solution. It is therefore prudent to calculate β in a number of phases, both by calculation and experiment, and place considerable importance on comparative trends in β across various states of matter: in gas-phase, solution, *and* solid-state if possible. Multi-phase evaluations of both electron-density mappings and β also allow the effects of intermolecular interactions to be distinguished, especially those pertaining to crystal-field effects.

We therefore present a study that explores the electronic structures of **DAST** and **BP3**, with a focus on determining the nature of their inter-ionic interactions and assessing how their intra-ionic charge transfer (ICT), and thus NLO response, is affected by them. We achieve this by building up the crystal lattice environment piece-by-piece, while studying modulations in their cation···anion interactions as a consequence of the piece-meal changes. Our starting point is a negative point-charge model that is similar to that employed by Kim *et al*.[4] except that it uses atomic coordinates from experimental diffraction data as its basis. This indicates that cation···anion interactions need to be considered in greater detail. Three models involving such interactions are then built up. The first comprises an isolated cation created by *ab initio* calculations using density functional theory (DFT) to which is added its nearest-neighbour anion (Fig. 5.3a); this model realizes the impact of this specific cation···anion interaction on the ICT of each organic salt. Models of their electronic structures that represent an isolated cation and anion but which are subjected to crystal forces are then developed, using X-ray wave function refinements (XWRs). Bond-length-alternation (BLA) analysis[19,20] performed on these XWR models is compared with cognate BLA results on the ion-pair in vacuum, revealing the influence of crystal forces upon the ICT of each ionic salt. A multipolar structural analysis of X-ray diffraction data on **DAST** and **BP3** is then carried out, to model these organic salts within their crystal lattice environment. BLA analysis is first applied to these multipolar structural models to distinguish the effect of *both* crystal forces and inter-ionic interactions on their ICT and thus NLO response. Electronic moments from these multipolar structural models are then used to derive solid-state values of β, using the approach of Robinson.[14,15] These β values are compared with those from gas-phase calculations using DFT, and with reference solution-state β values of **DAST** and **BP3** obtained from HRS experiments.[18] This multi-phase determination of β reveals a stark diminution of molecular-scale NLO response in **DAST** and **BP3** upon the formation of their crystalline states; these results also show that β in **DAST** deteriorates progressively from the gas to solid-state phase. These observations are thence rationalized, thus elucidating intra-ionic and inter-ionic structure-property relationships in **DAST** and **BP3** that control their NLO function.

5.2 Experimental & Computational Methods

5.2.1 X-ray diffraction studies

The collection of conventional single-crystal X-ray diffraction data on these compounds was undertaken by T.-C. Lin & Dr P. Waddell. T.-C. Lin undertook initial processing and data reduction.

A single crystal of **DAST** (0.30 x 0.35 x 0.50 mm), or **BP3** (0.50 x 0.55 x 0.70 mm) was mounted onto the in-house Rigaku Saturn 724+ CCD single-crystal X-ray diffractometer as per §2.2.1. Crystals were cooled to 120 K and subsequently maintained at this temperature for the duration of the data collection. Data were collected at θ = 25° (**DAST** & **BP3**), 50°, and 65° (**BP3** only) with full-sphere reciprocal space coverage, using ω-scans with a scan width of 0.3 °. Data acquisition, collection and processing, including cell indexing, cell refinement, and data reduction was undertaken as per §2.2.2 and §2.2.3. Reduced data were corrected for X-ray absorption using an empirical model and merged where necessary as per §2.2.4.

A conventional IAM crystal structure refinement of the X-ray data was undertaken using SHELXL[21] (*cf* §2.2.5) and afforded the following statistics (*cf.* Table 5.1):

Table 5.1 A summary of the IAM structural refinement statistics of **DAST** and **BP3** using conventional X-ray diffraction techniques

	DAST	BP3
Chemical Formula	$C_{23}H_{26}N_2O_3S$	$C_{31}H_{34}N_2O_3S$
a	10.3527(21)	7.6045(15)
b (Å)	11.1358(22)	14.9924(30)
c	17.7265(35)	11.7404(23)
α	90.00	90.00
β (°)	92.62(3)	101.04(3)
γ	90.00	90.00
Z	4	2
Crystal System	Monoclinic	Monoclinic
Space Group	Cc	$P2_1$
Sin(θ)/λ (Å^{-1})	0.77	1.04
R1 [I > 2σ(I)]	0.0353	0.0462
wR2 [(I > 2σ(I)]	0.0949	0.1307
GoF	1.06	1.15
Max / Min Residuals (Å^{-3})	0.39 / -0.31	0.63 / -0.85

Neutron data for **DAST** and **BP3** were also collected, and has been reported previously.[2]

5.2.2 Experimental charge density multipolar model refinement

T.-C. Lin undertook multipolar model refinement of **DAST** and **BP3** which were used by C.M. Ashcroft for analysis.

Initial atomic coordinates and anisotropic displacement parameters (ADPs) for all non-hydrogen atoms of **DAST** and **BP3** were obtained from the IAM refinement of the X-ray diffraction data (*cf.* §5.2.1) and used as a starting point for a multipolar refinement. Initial atomic coordinates for hydrogen atoms were determined via the neutron structures of **DAST** and **BP3**, while their ADPs were either calculated using SHADE2.1[22] (**DAST**) or taken from a neutron-derived structure and scaled to the X-ray data using UIJXN[23] (**BP3**). The ADPs were kept constant throughout subsequent refinements. In the case of **DAST**, its more limited data resolution precluded a traditional multipolar refinement. However, a transferable aspherical atom modeling (TAAM) refinement using the University of Buffalo Aspherical Atom Databank (UBDB)[24–26] was carried out to facilitate a comparison between **DAST** and **BP3**. In the TAAM regime, only the atomic coordinates and ADPs for the non-hydrogen atoms were refined, whereas their multipolar terms were directly imported from the UBDB databank using the LSDB code.[24–26] Multipolar models (MMs) for **DAST** and **BP3** were then implemented and refined, using the XD2006 program suite.[27] The least-squares refinement statistics on F for the final MM yielded the following (*cf.* Table 5.2):

Table 5.2 A summary of the multipolar modelling (MM) refinement statistics of **DAST** and **BP3** using TAAM (**DAST**) and high-resolution X-ray diffraction (**BP3**) techniques

	DAST	BP3
Sin(θ)/λ (Å^{-1})	0.77	1.04
R1 [F]	0.0278	0.0366
R_w [F]	0.0352	0.0257
Data-parameter	28.8	25.11
Max / Min Residuals (Å^{-3})	0.24 / -0.21	0.32 / -0.44

5.2.3 *Ab initio* density functional theory calculations

T.-C. Lin undertook DFT calculations of **DAST** and **BP3** which were used by C.M. Ashcroft for analysis.

DAST and **BP3** ions were modeled as clusters of various sizes to enable investigations on the cation-only and cation-plus-anion interactions. Those of the former are detailed in Appendix D, §D.1. Those of the latter employ cation-plus-negative-background-charges where such charges are a virtual entity to represent the counter-anions in order to study the contributions purely with respect to the intermolecular Coulomb interactions. Electrostatic moments and (hyper)polarizability values of these clusters of ions have been determined by DFT[28,29] using a coupled-perturbed method at the B3LYP/6-31+G(d) level of theory via Gaussian09.[30] Initially, neutron-derived atomic position parameters were optimized to ensure that their structures were in their electronic ground state. Subsequently, the components of the hyperpolarizability tensor of each structure were calculated at the same level of theory and β was determined.

5.2.4 Theoretical charge-density multipolar model refinement

T.-C. Lin undertook theoretical multipolar model refinement of **DAST** and **BP3** which were used by C.M. Ashcroft for analysis.

Several sets of theoretical X-ray structure factors for **DAST** and **BP3** were generated using the program DenProp.[31] This code applies an analytical quadrature-based Fourier-transformation on the molecular electron-density of the compounds, determined from their respective DFT-generated wave-functions. The DFT-derived wave-functions for these studies were determined at the B3LYP/6-311++G(d,p) level of theory. The neutron-derived molecular geometries were used for calculating these wave-functions, via Gaussian09.[30] In order to establish relationships between the cation···anion interactions and the charge-density distributions of the chromophores, theoretical models containing cation-only and cation-plus-anion pairs of ions were investigated. Given the fact that simulated diffraction intensities and phases are known for these theoretical structure factors, the phase-constrained multipolar refinement, available in XD2006,[27] was employed to construct corresponding theoretical MMs.

5.2.5 X-ray wave-function refinement

C.M. Ashcroft undertook all X-ray wave-function refinements, with the HAR of **DAST** undertaken by L.A. Malaspina, University of Brenen, Germany. C.M. Ashcroft used the XWR results for analysis.

The XWR method[32] was employed via the program TONTO[33] as outlined in §2.9 on **DAST** and **BP3** using the same data resolution as that employed for the respective multipolar modeling (**DAST**: $\sin\theta/\lambda = 0.77$ Å^{-1}; **BP3**: $\sin\theta/\lambda = 1.04$ Å^{-1}). All refinements were undertaken at the HF/def2-SVPD level of theory. Initial attempts to refine the ADPs of the hydrogen atoms for **DAST** using HAR lead to some hydrogen ADPs being highly oblate or indefinable due to non-positive definite (NDP); possibly due to data resolution issues. Consequently, all hydrogen atoms in **DAST** were refined isotropically. A self-consistent field of point charges and dipoles up to 8 Å around the central molecule were applied to account for crystal environment effects.

Convergence of the XWR was assured by testing the refinement test statistic, χ^2, against a range of λ_L values. The XWR was allowed to run in λ_L steps of 0.1 increments until convergence was achieved. Full convergence was achieved at $\lambda_L = 1.4$ (**DAST**) and 0.5 (**BP3**). The following figures-of-merit were obtained: R = 0.0299 (**DAST**), 0.0348 (**BP3**); R_w= 0.0372 (**DAST**), 0.0383 (**BP3**); GOF ($\sqrt{\chi^2}$) = 1.72 (**DAST**), 3.52 (**BP3**); χ^2 of 2.95 (**DAST**), 12.37 (**BP3**). The residual electron density was analyzed and revealed maximum residuals of 0.16 $Å^{-3}$ for H(24) (**DAST**) and 0.11 $Å^{-3}$ for O(3) (**BP3**). The residual density maps were either essentially featureless (**40**) or at the very least revealed a random distribution of residuals that could not be attributed to specific bonding features; they were thus deemed adequate for the given quality of data (*cf.* Appendix C, §C.4). The respective fitted wave functions were subsequently used to undertake a topological analysis of **DAST** and **BP3** via the program Multiiwfn[34] as per §2.9.3.

5.3. Results and Discussion

A range of structural models of **DAST** and **BP3** were built up ion-by-ion, initially using DFT to calculate various types of ionic clusters. These provided important checks to verify previous work on calculations involving cation···anion, cation···cation, and anion···anion interactions. The results, detailed in the Appendix D, §D.1, corroborate previous findings that anion···anion interactions in **DAST** and **BP3** have negligible effect on their NLO response[10] while cation···cation interactions in **DAST** and **BP3** promote ICT, providing an overall positive contribution to the ensuing NLO activity of the chromophores[5]. The nature of cation···anion interactions presents a much more complex situation. For example, a previous structural study[2] on crystalline **DAST** and **BP3** suggested that cation···anion interactions could be responsible for either an enhancement or reduction of β upon crystallization, depending on their exact nature. Such interactions are thus the focus of the electronic structure models described in the next two sections.

5.3.1 Cation···anion interactions: The effect of Columbic contributions

Cation···anion interactions in **DAST** and **BP3** were first modeled via a negative point charge approach that is similar to that reported by Kim *et al.*[4], with one important exception being that this work used the neutron-derived molecular structures as a geometrical basis, and considered the positions of the five (**DAST**) and nine (**BP3**) closest anions to the respective cation. Similar to the results observed by Kim and co-workers,[4] the overall electrostatic perturbation effects were found to average out and the molecular hyperpolarizabilities remained almost unchanged (Fig. 5.2). This result can be rationalized in terms of the crystal packing arrangement of these compounds. In **DAST** for example, the molecular plane of the stilbazolium cation adopts a nearly perpendicular arrangement relative to the pTS$^-$ anion, and each layer of cations is sandwiched between two parallel layers of anions. Consequently, it is likely that electrostatic perturbations, originating from the anions, that are located at the top or bottom-layer or, donor or acceptor-side, eventually cancel each other out as they propagate between these alternative layers of the crystal lattice.

BP3 similarly experiences little change in its molecular hyperpolarizabilities for its closest anions, indicating that electrostatic perturbation effects average out like in **DAST**. However, it is worth noting that the arrangement of **BP3** is slightly different to that of **DAST**, with the stilbazolium cation of **BP3** relative to its pTS$^-$ anion being less perpendicular than in **DAST**. Furthermore, their different space groups, Cc (**DAST**) and $P2_1$ (**BP3**), render **BP3** with half the number of neighboring ions to that of **DAST**, with cation-anion pairs arranging themselves in layers. The formation of these cation-anion pairs will nevertheless cause the electrostatic perturbations which impact on the NLO response in **DAST** and **BP3**.

One may therefore conclude that Coulombic interactions are not the primary concern; rather, the dominating factor responsible for the crystal-induced reduction of the NLO response in **DAST** and **BP3** can be attributed to the hydrogen bonds and short van der Waals contacts between cations and anions, which is consistent by the previous report by Cole *et al.*[2] for a range of DAST-derivatives.

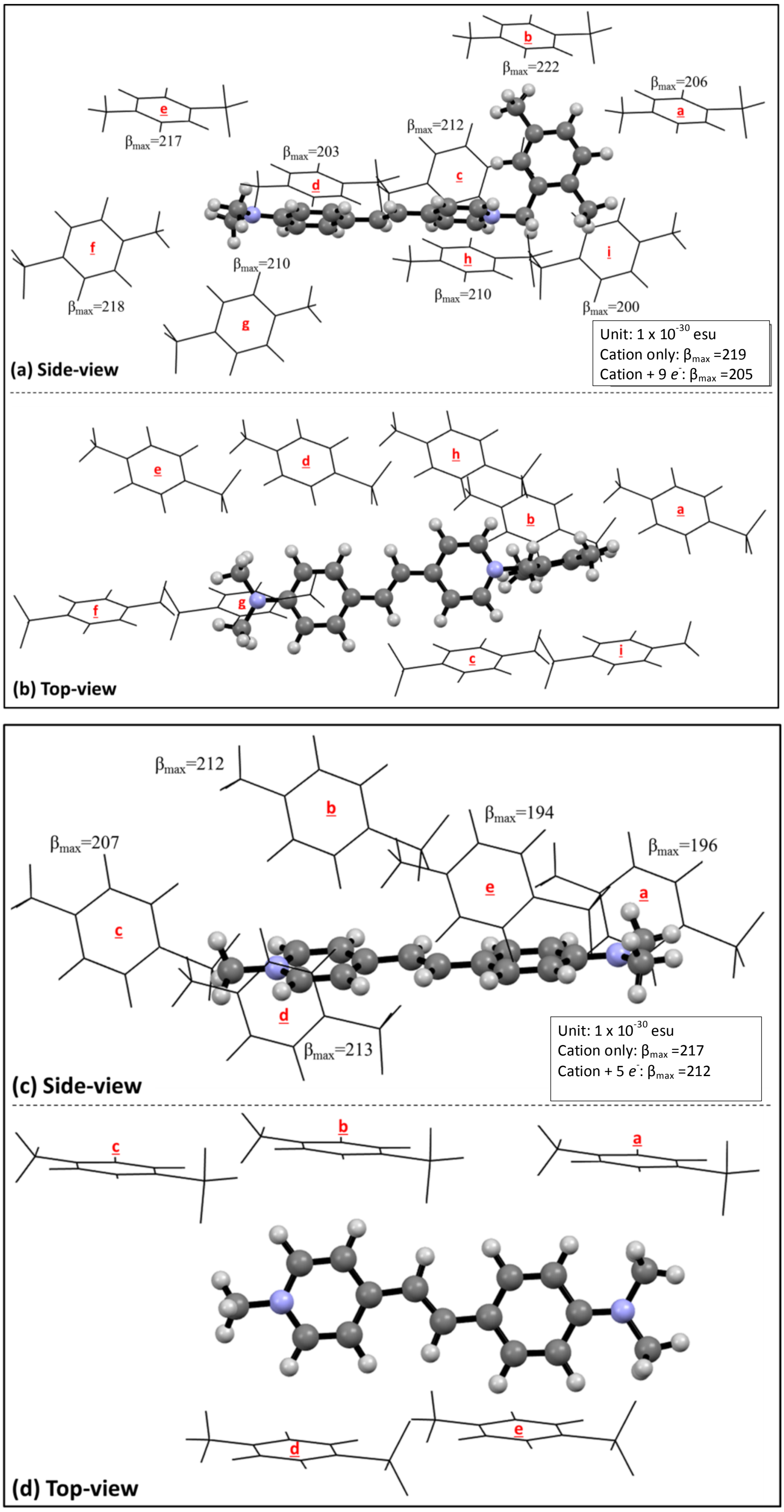

Figure 5.2. Anion/point-charge positional effect on the molecular hyperpolarizability, β_{max}, of (a)-(b) **BP3** and (c)-(d) **DAST** cations.

5.3.2 Cation···anion interactions: Effects of the crystalline environment

5.3.2.1 Model descriptions

The crystalline environment of **DAST** and **BP3** was built up piecewise via three distinct steps that employed the models and data described in Figure 5.3; all models used structure factors, F, which had been generated by different methods to determine the effects of the crystalline environment on ICT and thus the NLO response. The first step engaged DFT to build up a supercell of cations and this was compared with a cognate supercell of cations surrounded by their nearest-neighbour anion (Fig. 5.3a); this model essentially permits an assessment of the impact of these specific cation···anion interactions on the ICT of the respective cations in **DAST** and **BP3**. The second step used DFT to build up an isolated cation and anion pair using a self-consistent field (SCF) model from which theoretical structure factors (F*) were generated; in turn, these were refined against experimentally-derived structure factors (F) from the X-ray diffraction data of **DAST** and **BP3**. This tempering of F* to F data via a refinement process means that the influence of the crystalline environment of each organic salt is implicitly incorporated into the model of the isolated cation and anion pair; thus, the impact of crystal forces on ICT can be distinguished (Fig. 5.3b). The third step presented the model of **DAST** or **BP3** in their full crystal lattice environment that used experimental X-ray diffraction data. This permitted an evaluation of the full exposure of **DAST** and **BP3** ions to crystal field effects as well as more directed forces such as interionic interactions (Fig. 5.3c). A validation of these models was undertaken and this is presented in the Appendix D.

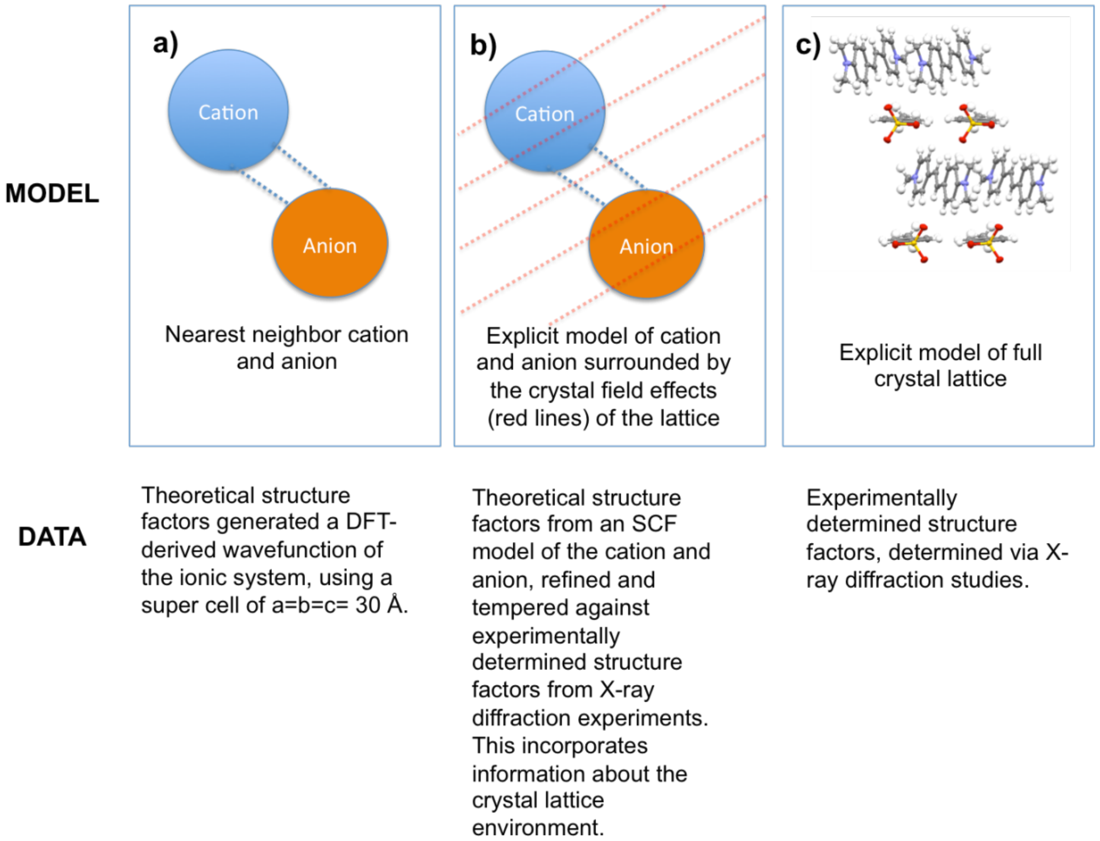

Theoretical structure factors generated a DFT-derived wavefunction of the ionic system, using a super cell of $a=b=c= 30$ Å.

Theoretical structure factors from an SCF model of the cation and anion, refined and tempered against experimentally determined structure factors from X-ray diffraction experiments. This incorporates information about the crystal lattice environment.

Experimentally determined structure factors, determined via X-ray diffraction studies.

Figure 5.3. An illustration of the three-step process by which structural models of **DAST** and **BP3** are built up in order to determine how the ions are influenced by their crystal environment.

5.3.2.2 Overarching structural features of cations of DAST and BP3

A cross-comparison of bond lengths for the cations of both **DAST** and **BP3** across all structural models (a)-(c) is provided in Fig. 5.4(a-c) respectively. There are certain overarching similarities between **DAST** and **BP3** as anticipated. For example, the pyridinium ion in ring 2 of both chromophores acts as the electron acceptor, while the ethylamino group adjacent to ring 1 is the electron donor. Rings 1 and 2 exhibit distinct quinoidal character; *cf*. the two shorter bond lengths for C(13)-C(14), C(11)-C(10) of ring 1 and C(5)-C(6), C(3)-C(2) of ring 2. The intervening bridge consists of an alternating 'single-double-single' bonding chain, as indicated by the bond lengths across all structural models.

While the D-π-A motifs are the same for **BP3** and **DAST**, **BP3** naturally differs from **DAST** in that its cation contains an additional 2,5-dimethylbenzyl moiety. The primary contribution of this moiety is to impart a steric influence on the crystal packing of the **BP3** chromophore in the solid state, rather than present any significant electronic ICT contribution. Indeed, this moiety aligns perpendicular to the D-π-A backbone of **BP3**; as such, its 2,5-dimethylbenzyl group (dihedral angle: ~93.7 ^{O} [C(6)-N(1)-

C(1)-C(24)]) will preclude any effective ICT via the C(1)-C(24) bonds, as confirmed by its respective bond lengths across all structural models.

All of these findings corroborate those of Cole *et al.*[2] and thus benchmarks these new data as having good accuracy.

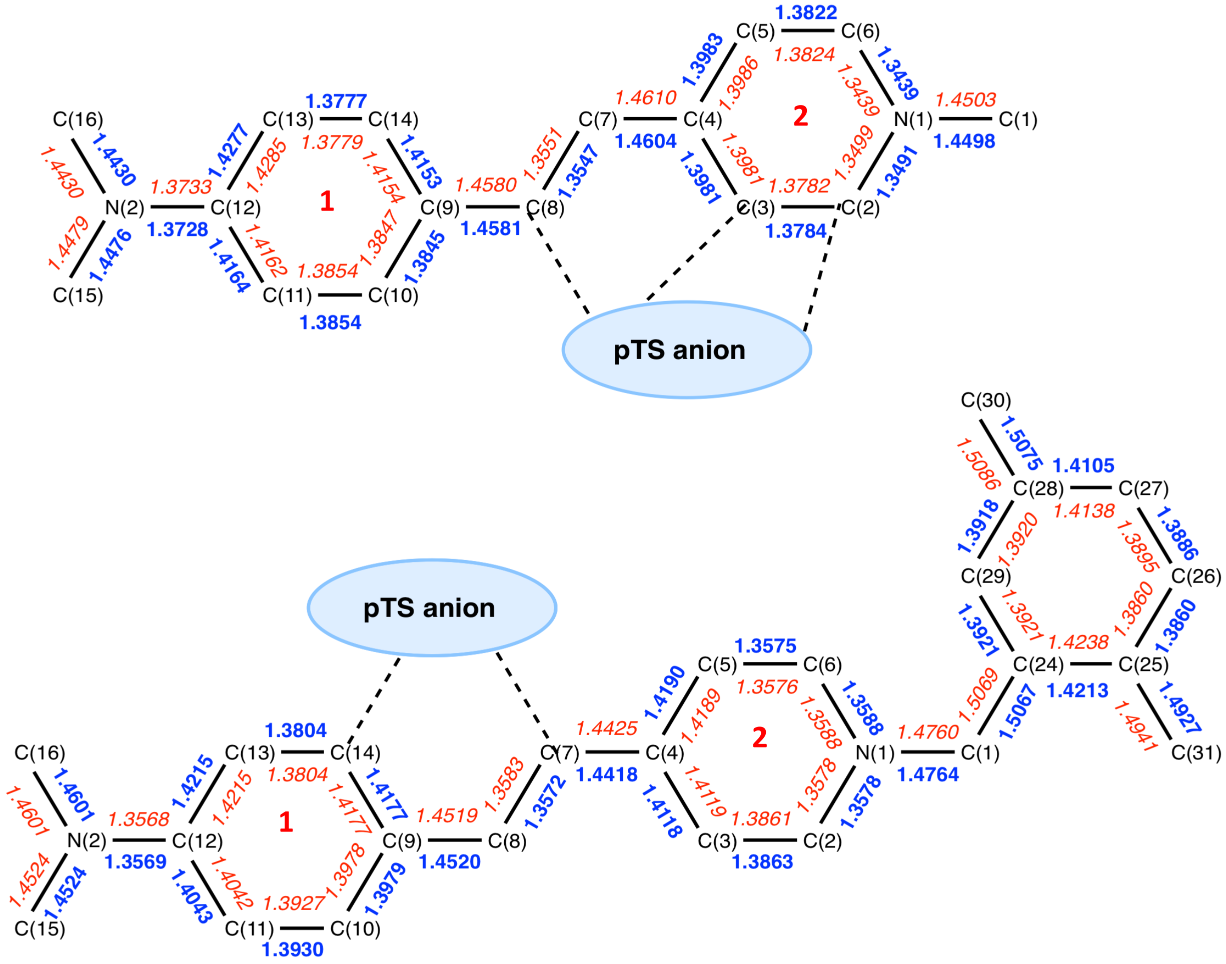

Figure 5.4(a). Bond lengths for the cationic chromophore in **DAST** (top) and **BP3** (bottom) for model a). The different colours indicate models with (blue), and without (red) the closest anion

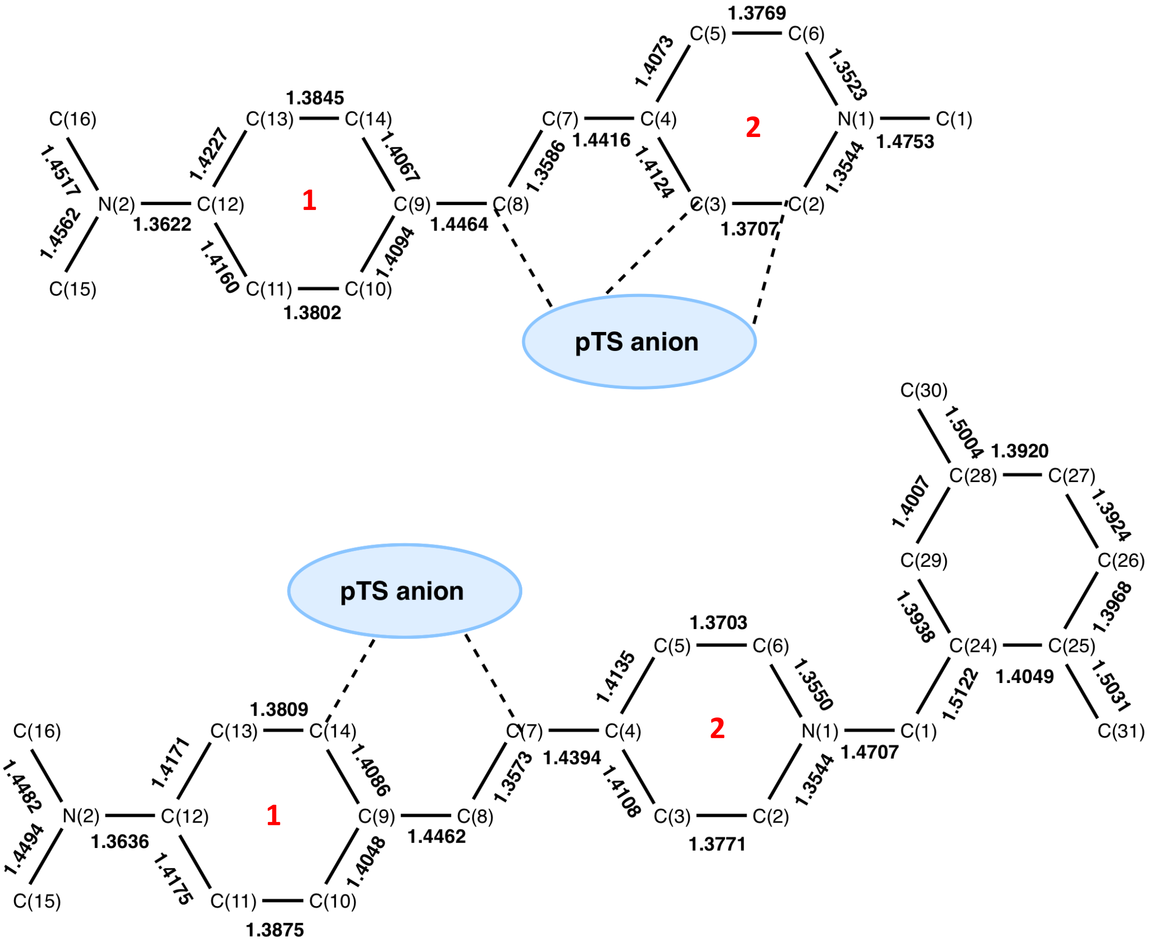

Figure 5.4(b). Bond lengths for the cationic chromophore in **DAST** (top) and **BP3** (bottom) for model b).

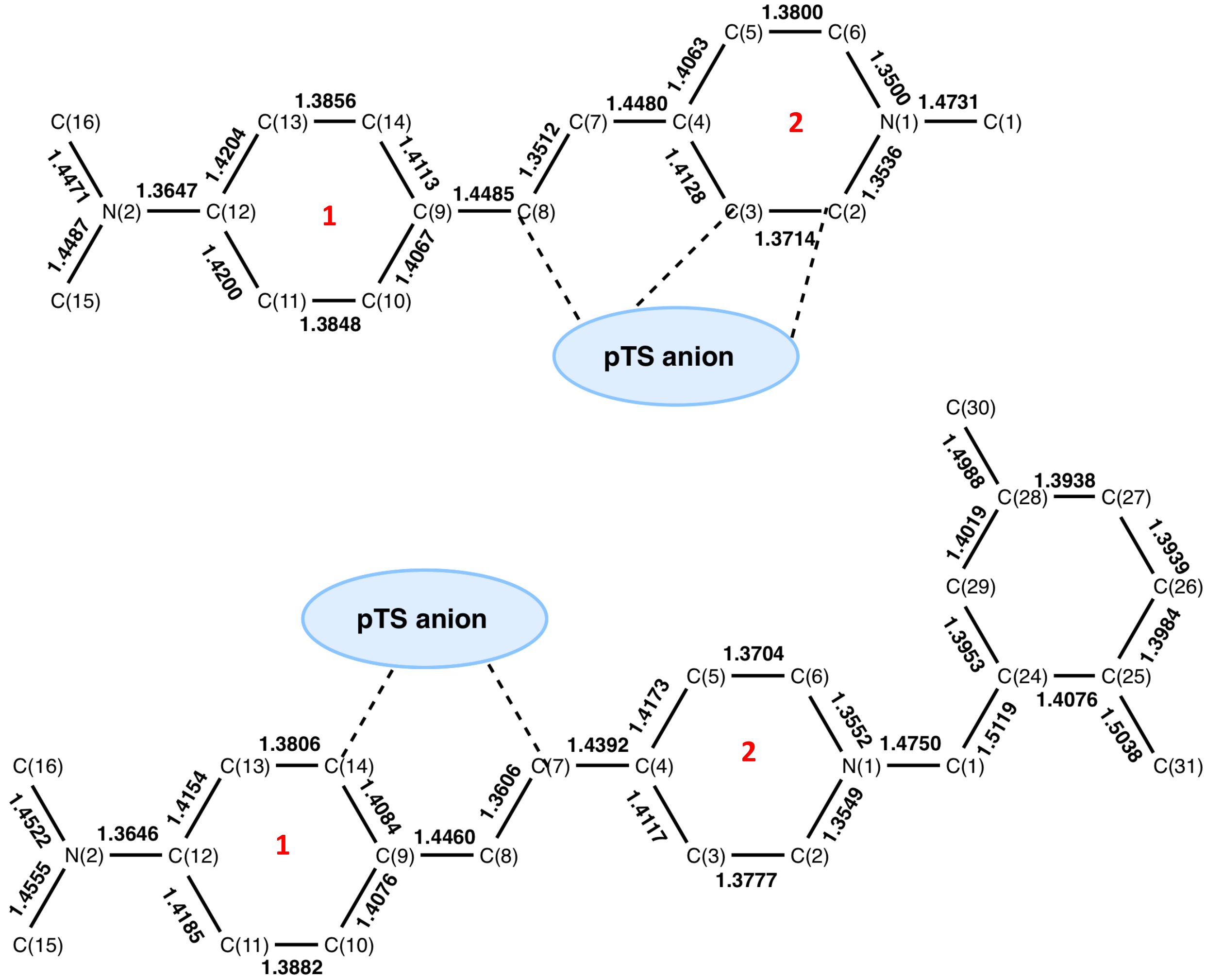

Figure 5.4(c). Bond lengths for the cationic chromophore in **DAST** (top) and **BP3** (bottom) for model c). The different colours indicate models with (blue), and without (red) the closest anion

5.3.2.3 Bond-length metrics for data analysis of ICT and thus NLO response

The 'strength-length' relationship in chemical bonding can be correlated to the extent of ICT and thus the NLO response.[19] To this end, two bond-length descriptors are herein employed to evaluate the bond-length averages and bond-length alternation (BLA) in three distinct carbon-based π-conjugated structural fragments of **DAST** and **BP3** that are common to their cations: the quinoidal ring (ring 1), the non-heteroatomic part of ring 2, and the bridge that connects them (as labelled on Figure 5.1). Bond-length averages are simply the statistical mean of the bond lengths in a given structural fragment. BLA can be described in several different ways. It is described here in its simplistic form, i.e. the statistical mean of all bond-length differences between vicinal carbon-carbon bonds within a specified molecular fragment. In cases where a bond connects to multiple bonds, the smallest bond-length difference of all options available is employed; e.g. the bond-length difference involving a bond that projects from an aromatic ring, there being two bonds from the ring that connect to this bond; the overall BLA calculation contains such cases. This BLA formalism may be considered as the classical method of assessing the extent of delocalization ensuing within a π-conjugated fragment of a molecular chromophore. This has been used extensively to analyse D-π-A structural motifs in organic NLO materials to deduce the level of ICT and thus their inherent prospects for NLO function[19,20].

5.3.2.4 Intra-ionic charge-transfer and π-conjugation trends in cationic moieties of DAST and BP3

The intra-ionic charge transfer across cations of **DAST** and **BP3** can be quantified in fine detail, by breaking down their contributions into those of ring 1, the non-heteroatomic part of ring 2, and the bridge. The average bond-lengths for each moiety, as well as their BLA values, were calculated for each structural model, as were their overall BLA values of the cations (see Tables 5.3 and 5.4). Clear trends across the structural models are highlighted with arrow annotations.

Table 5.3. A table of bond length average in the cationic segments of **DAST** and **BP3.** The arrows show clear monotonic trends within expected errors

Metric →	Bond length averages in cation moiety (Å)					
Model ↓	DAST ring 1	BP3 ring 1	DAST bridge	BP3 bridge	DAST 4C-ring2	BP3 4C-ring2
(a) red	1.4014	1.4024	1.4247	1.4176	1.3893	1.3936
(a) blue	1.4012	1.4025	1.4244	1.4170	1.3892	1.3937
(b)	1.4033	1.4027	1.4155	1.4143	1.3918	1.3929
(c)	1.4048	1.4031	1.4159	1.4153	1.3926	1.3943

Table 5.4. A table of bond length alternation (BLA) values and, overall BLA for the cationic segments of **DAST** and **BP3**. The arrows show clear monotonic trends within expected errors

Metric →	Bond length alternation (BLA) in cation moiety (Å)						Overall BLA (Å)	
Model ↓	DAST ring 1	BP3 ring 1	DAST bridge	BP3 bridge	DAST 4C-ring 2	BP3 4C-ring 2	D-π-A of DAST	D-π-A of BP3
(a) red	0.0271	0.0220	0.1044	0.0889	0.0122 ↑	0.0313	0.0491	0.0428
(a) blue	0.0269	0.0219	0.1046	0.0897	0.0120	0.0314	0.0490	0.0429
(b)	0.0225 ↓	0.0192 ↓	0.0854	0.0855 ↓	0.0257	0.0265 ↓	0.0417	0.0407 ↓
(c)	0.0204	0.0194	0.0971	0.0820	0.0247	0.0288	0.0446	0.0400

All of the BLA values for the **BP3** cation decrease monotonically, revealing that the structural behaviour of the three moieties is uniform and is representative of the entire D-π-A motif in each cation. These results also evidence a high level of internal consistency, thus corroborating the robustness of the four multi-phase structural models detailed in Table 5.2. This reduction in BLA from gas to solid-state is particularly marked between models (a) and (b), whereupon crystal forces start to influence the cation; the BLA continues to diminish until model (c) when the cation is contained within its full crystal lattice environment. BLA changes in ring 1 of **BP3** are modest, and their absolute

BLA values are the lowest of the entire **BP3** cation irrespective of the model; ring 1 thus appears to present a highly delocalized nature. In stark contrast, the bridge exhibits the highest absolute BLA values irrespective of the model; indeed, the bond lengths of the bridge display a distinct tendency towards a 'single-double-single' canonical form of bonding across all models. Nonetheless, its BLA values drop markedly with the onset, and thence progressive build-up, of crystal forces, in common with ring 1. The carbon-based component of ring 2 in **BP3** shows a similar trend in reduction, but with much smaller absolute BLA values to the extent that they represent a ring with a high level of delocalization.

The overall BLA value for **BP3** cations in the crystal lattice environment (model (c)) is striking, by virtue of it being a 'perfect' BLA value for organic NLO applications, according to the indications of the Valence Effective Hamiltonian (VEH) models for which β is maximized for molecules whose |BLA| modulus is 0.04.[35] Table 5.2 shows that the overall BLA value for **BP3** cations tends to this 'perfect' value, as models progressively accommodate more intra-ionic interactions and proceed from gas phase to solid-state. In other words, the progressive build-up of intra-ionic interactions in the D-π-A portion of **BP3** cations optimizes its β value, until its crystalline form manifests 'perfect' NLO prospects from a purely electronic perspective.

This BLA calculation does not consider any steric influences on β that **BP3** cations might issue beyond the D-π-A moiety. This 'perfect' BLA value of the **BP3** cation is unlikely to be deterred by any internal BLA contribution from the tosylate anion as this is deemed to contribute negligibly to β (*cf*. Appendix D, §D.1). However, cation···anion *interactions* can readily affect the overall β, as has been shown by Cole *et al.*[2] Such interactions are considered implicitly for the D-π-A portion of the **BP3** cation in this demonstrated optimization of β, via the bond length changes caused by such interactions. However, electronic effects in the **BP3** cation beyond the D-π-A pathway are not considered by the BLA diagnostics. Moreover, steric effects are neglected in BLA analysis.

The effect of the two N heteroatoms and their substituents, and the associated positive charge on N(1) in **BP3**, that lie beyond its D-π-A motif, are thus considered separately. The bond lengths of the ethylamino group (D) display conventional structural configurations across all models, as expected. However, the acceptor group, A, manifests in a more complicated fashion. Its positive charge on N(1) is stabilized by its adjoining 2,5-dimethylbenzyl group whose ring is essentially aromatic in nature. The extent of this aromaticity can in fact be calculated by a distinct BLA value that is computed specifically for this ring. This shows that its aromatic nature is enhanced as the **BP3** cation transitions from its gas to solid-state structural phase, manifesting a distinct drop in an already small BLA value (model a, red: 0.0199; blue: 0.0180) between the gas phase, and models (b) and (c) that incorporate crystal field effects and whose BLA values (model (b): 0.0066; model (c): 0.0068) are so small that they approach the cyanine limit.[35] This high extent of ring delocalization is thus propelled by crystal field effects. Its ring current is nonetheless isolated by its bridge to N(1), increasingly so as the model progresses from the gas-phase to the solid-state, *vis a vis* the progressively more single-bonded character of the C(1)-C(24) bond, whose length increases monotonically from 1.5069-1.5119 Å from model (a, red) to model (c); see Fig. 5.4. Meanwhile, the N(1)-C(1) bond maintains a characteristically σ-bonded character across all models.[43] Indeed, this ring is out-of-plane with the D-π-A moiety of the **BP3** cation, as previously noted. These models thus show that this aromatic ring tends towards perfect delocalization and thus greater electronic isolation from the rest of the cation, as **BP3** tends towards crystallization. Fig. 5.5 also illustrates that this 2,5-dimethylbenzyl group is involved in three C-H···O interactions; one of these will impact on the BLA of its ring; the other two will not as they connect to the bridge between the rings; they could nonetheless still affect β.

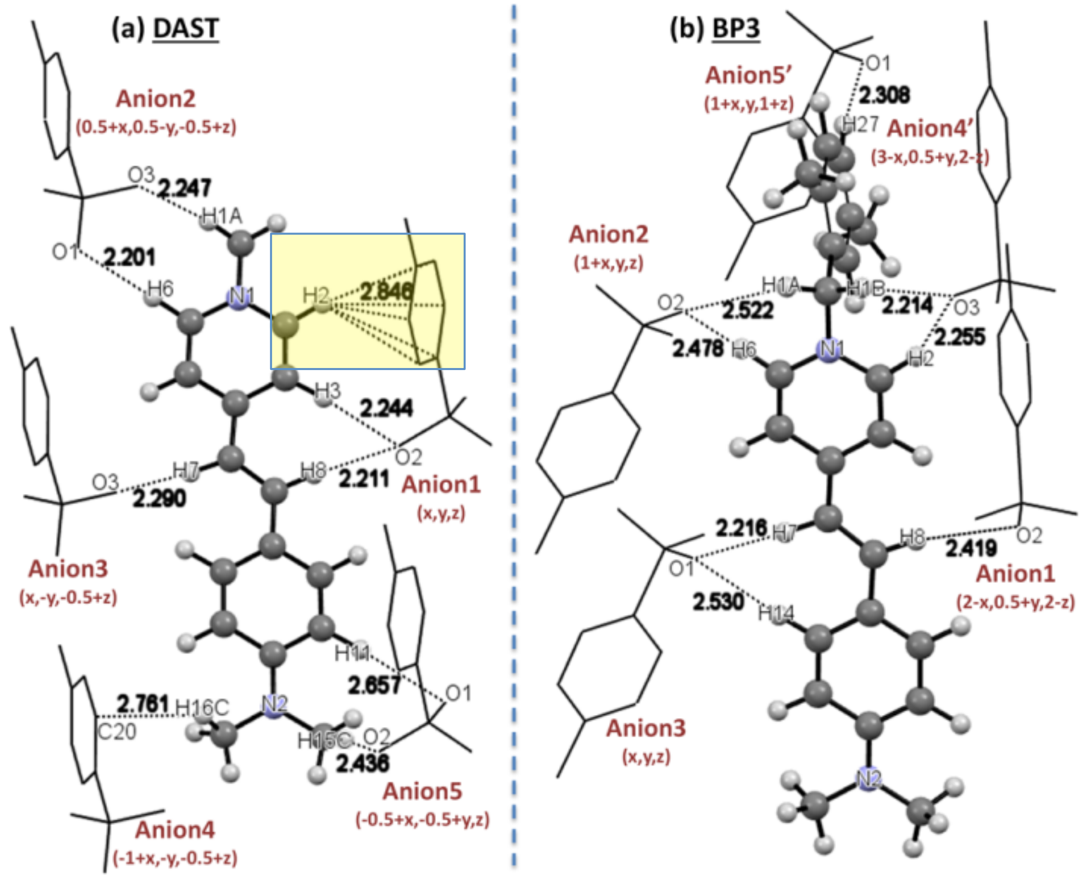

Figure 5.5. Cation···anion interactions in **DAST** (a) and **BP3** (b). Reprint and adapted from Cole *et al.*[2]. C-H···C(π) interactions in **DAST** are highlighted yellow. Note, the anion has a $-SO_3$ unit as per Fig 5.1. However, only O atoms partaking in an interaction are here labelled.

The cation of **DAST** exhibits more variable bond-length characteristics than that of **BP3**. Its ring 1 exhibits average bond lengths and BLA trends that are akin to those of the **BP3** cation. In contrast, the average bond lengths associated with its bridge are markedly longer (weaker) than those of **BP3** for models (a, red) and (a, blue), i.e. when cations of **DAST** are not subjected to crystal forces; their BLA values are correspondingly higher than those of the **BP3** cation for these two models. However, these average bond lengths and BLA values drop markedly between model (a) and (b), to the extent that both of these bond length metrics become essentially the same as the cognate values for model (b) of the **BP3** cation. Model (c) shows a curious feature whereby the BLA value for the bridge in the cation of **DAST** returns to nearly the BLA values of the models in (a); its average bond length also increases, albeit slightly. This suggests that while crystal forces modeled outside of a crystal lattice augment the ICT for **DAST**, the explicit incorporation of highly directed forms of crystal forces such as hydrogen-bonding, held within a crystal lattice as per model (c), deters ICT. The trend observed for ring 2 in the cation of **DAST** is particularly striking, when set against that of **BP3**. The average bond lengths of the carbon-component of ring 2 for the cation of **DAST** are shorter (stronger) than those of **BP3** for model (a), which is entirely counterpoint to the situation observed for the bridging unit that is common to these cations. The BLA values for the carbon-component of ring 2 are significantly lower for cations of **DAST** than **BP3** for model (a), thus corroborating the validity of this trend. Moreover, these BLA values display entirely opposite trends with those for the cation of **DAST** diminishing with the removal of crystal forces, while those of **BP3** diminish as crystal forces are introduced. The diminution of these BLA values for cations of **DAST** upon removing crystal forces is such that those of model (a) come close to the cyanine limit. Given that ring 2 contains a positive charge on N(1), this striking difference between **BP3** and **DAST** is likely to result, at least in part, from the much greater charge stabilization on N(1) by the electron donating benzyl rather than methyl substituents in **BP3** and **DAST**, respectively. Another rationale for this striking difference could be the C-H···C(π) interaction that is present in **DAST** but absent in **BP3** (see Fig. 5.5, yellow box). Indeed, Cole *et al.* highlighted this distinction in inter-ionic interactions between **DAST** and **BP3** as the key reasons for their different NLO prospects.

The overall BLA values for the cation of **DAST** naturally reflect the lack of clear monotonic trend between models (a) to (c) for the bridging unit given its high BLA value will dominate the overall BLA metric. The BLA values themselves indicate a decent level of ICT, and thus good NLO prospects, judging from their proximity to the ideal BLA = 0.04 Å value posed by VEH calculations.[35] Indeed, the results indicate that the cation of **DAST** becomes near ideal (BLA = 0.0417 Å) when crystal forces are introduced in model (b); however, this BLA is compromised once cations of **DAST** are incorporated into the crystal lattice environment of model (c). This suggests that while crystal forces from essentially non-directional electrostatic interionic interactions appear to augment ICT in the D-π-A cationic moiety of **DAST**, directed interionic interactions such as hydrogen bonds deter ICT and thus the NLO response in **DAST**. This surmise corroborates previous notions proposed by Cole *et al.*[5] In contrast to **BP3**, the D-π-A moiety of **DAST** is synonymous to its entire cation except for its methyl extremities. Therefore, the ICT from the cation of **DAST** is likely to represent its full β contribution save for any possible effect of the few C-H$\cdots$O hydrogen-bonds that involve the methyl groups (see Fig. 5.5); the cation of **DAST** has no large substituents beyond its D-π-A moiety to cause steric effects, in contrast to **BP3**.

5.3.3 NLO activity: Comparison of the molecular hyperpolarizability determined by five independent methods

The NLO responses of **DAST** and **BP3** in the gas, liquid, and solid state are shown in Table 5.3. Since their molecular hyperpolarizabilities in crystal form have so far only been estimated via a derivation based upon respective reports of powder SHG efficiencies, the electrostatic moments derived from the experimental charge densities (two models: **MM_exp** for **BP3**; **TAAM_exp** for **DAST**) were also used herein to determined its crystalline-state molecular hyperpolarizability using the empirical method derived by Higginbotham *et al.*[15] (*cf,* §1.2.2.4).

Table 5.3: Summary of the molecular optical nonlinearity of **DAST** and **BP3** characterized using different methods.

	DAST	BP3
β_0^{DFT} **(gas)**	159	194
β_0^{XWR} **(gas + crystal field)**	116	194
β_0^{HRS} **(solution)**[#]	120 ± 15[^]	180 ± 20[&]
β_{zzz}^{Powder} **(crystal)**	37 ± 10	110 ± 10
β_0^{MM} **(crystal)**	17 (unrefined TAAM) 43 (monopole refined)	109

[#] The errors in β_{HRS} were predicated by the 20% statistical error on the evaluation of β for the Crystal Violet HRS reference sample, since this error propagates through to the uncertainty in β.
[^] HRS value previously reported by Teshome *et al.*[21]
[&] HRS value previously reported by Cole *et al.*[5]

The calculated β_0^{MM} values for **BP3** and **DAST** are listed in Table 5.3 along with the β_{zzz}^{Powder}, β_0^{HRS}, β_0^{XWR}, and β_0^{DFT} values. Concerning the charge-density derivations of the molecular hyperpolarizability in the crystalline state generated from this work, the β_0^{MM} value for **BP3** is in excellent agreement with the β_{zzz}^{Powder} value obtained from the measured powder SHG efficiency, while β_0^{MM} and β_{zzz}^{Powder} are in general agreement for **DAST**. Table 5.3 permits a cross-comparison of the β values of **DAST** and **BP3**, derived using the five independent methods, from which it is clear that the effects of crystal lattice packing impede both **DAST** and **BP3** from achieving their maximum potential as NLO-active chromophores. This is particularly true for **DAST,** where a reduction of ~73% is observed between the gas phase (DFT) and the solid state, compared to a much lower reduction of 44% for **BP3** under analogous circumstances; indeed, β for **BP3** barely drops until it is incorporated into its crystal lattice environment. This is to be anticipated when considered together with the assessments of §5.3.2.4, where the presence of short interionic interactions between the respective cations and anions in **DAST** cause a significant reduction in ICT once cations of **DAST** were incorporated into a crystal lattice environment. In comparison, the D-π-A motif of **BP3** presents a perfect BLA value in its crystal lattice environment. It can nonetheless be affected by steric effects and cation···anion interactions that lie beyond this D-π-A motif in the **BP3** cation, which form on crystallization as noted in §5.3.2.4; thus a significant drop in β for **BP3** is only observed upon forming its crystalline state. This diminution is much less in **BP3** than in **DAST** owing to the lack of C-H···C(π) interionic interactions in **BP3**, in contrast to **DAST**; thereby, the concerted presence of C-H···C(π) and C-H···O cation···anion interactions in **DAST** derivatives has been found to deter their NLO prospects considerably**.**[5] Furthermore, the C-H···O cation···anion interactions that are present in **BP3** that lie beyond its D-π-A motif include its shortest such interaction (see Fig. 5.5); its perfect BLA value in the crystal lattice environment is thus somewhat protected from cation···anion interactions.

Table 5.3 reveals that the molecular hyperpolarizability for **DAST** also drops considerably between the gas and solution phase; in stark contrast to **BP3**, which remains the same within error. This reduction of β for **DAST** is likely to be a consequence of the possibility of forming deleterious C-H···C(π) and C-H···O cation···anion contacts once **DAST** is surrounded by a medium (crystal forces for the XWR model, or a solution for the experimental results). The β value for the XWR, model (b), in **DAST** is thus the same as β determined by experiment in solution within experimental error. The directional nature of crystal forces will be minimal in this XWR model formalism; so it captures interionic interactions in a similarly subtle and non-direction specific fashion to solution-based results. The full directional nature of the cation···anion interionic interactions will only be felt in model (c) which explicitly incorporates the influence of the crystal lattice environment; thus, β for **DAST** drops heavily again between the solution and solid-state phase results.

On a technical point, there are two β_0^{MM}(crystal) values given for **DAST**. β_0^{MM} for **DAST**, as derived from the **TAAM_exp** model, is perhaps a little underestimated, being just at the mark of 2σ error, *cf.* (17 x 10^{-30} esu) compared to (37 ± 10) x 10^{-30} esu for β_{zzz}^{Powder}. This is unsurprising given the limited accuracy of a TAAM model, especially that which pertains to the multipolar population of its atoms. Indeed, the value of β_0^{MM} is deduced using the equation of Higginbotham *et al.*, which requires the determination of quadrupolar and octupolar atomic moments using Stockholder spatial partitioning; so incorrect multipolar populations will have a significant impact on the accurate determination of

β_0^{MM}. As a consequence of the unusual β_0^{MM} result for **DAST** determined by the **TAAM_exp** model, and given the importance of correctly assigned multipolar populations, an attempt was made to refine all monopole populations against the X-ray data of **DAST**, while all the other higher-order multipolar terms were kept unrefined; the limiting resolution of the X-ray data mandated this restriction to a monopolar model for charge-density analysis. The β_0^{MM} value (43 x 10^{-30} esu) derived from this modified **TAAM_exp** model of **DAST** is a bit more in line with the β_{zzz}^{Powder} value, confirming the importance of the accurate assignment of multipolar populations in the undertaking of a Stockholder spatial partitioning of the molecular charge density of a molecule.

5.4. Conclusions

The intra-ionic and inter-ionic interactions in **DAST** and its derivative, **BP3**, have been related to their NLO function at the molecular scale, and across multiple phases via four structural models. BLA analysis reveals distinct intra-ionic trends in terms of the ICT and thus NLO capabilities of the D-π-A motifs in **DAST** and **BP3** across the gas, {gas + crystal forces}, solution, and crystalline states of matter. The D-π-A motif for **BP3** tends to a perfect BLA value upon crystallization. Better stabilization of its positively charged nitrogen by its N-substituted benzyl group, relative to the corresponding methyl group on **DAST**, helps towards achieving this perfect BLA value for **BP3**. The β value of **BP3** is essentially constant in all phases except for the crystalline state, where it appears to be deterred via C-H$\cdots$O cation$\cdots$anion interactions that are not associated with the D-π-A constituent of the **BP3** cation. In stark contrast, the β value for **DAST** is progressively deterred from the gas phase to its crystalline form. This multi-phase deleterious effect in **DAST** appears to be primarily a consequence of its manifestation of *both* C-H$\cdots$C(π) and C-H$\cdots$O cation$\cdots$anion interactions which have been shown previously to deter **DAST** derivatives.[5] The lower ability of **DAST** to stabilize positive charge on the nitrogen of its pyridinium constituent, as opposed to **BP3** whose positive charge is stabilized by a large benzyl side group, may also be a factor in this difference between **DAST** and **BP3**; indeed, their opposite BLA trends observed in ring 2 were found to deter the overall BLA value of the D-π-A motif for **DAST**. The molecular hyperpolarizability, β, which provides the molecular measure of the second-order NLO effect, has been derived via the {gas+crystal forces} and solid-state structural models and compared to reported experimental values of β measured in solution or in a powder, as well as gas-phase *ab initio* DFT calculations. The β values follow the same structural trends as those observed for the competition between intra-ionic and inter-ionic interactions in **BP3** and **DAST**, thus rationalizing their respective NLO origins at the molecular scale. This is exciting both scientifically and technically; technically because this study presents a rare application of multi-phase determinations of β, with the especially scarce evaluations of β in the crystalline state derived *solely* from X-ray diffraction data,[14] and in the gas state with the influence of crystal forces incorporated using XWR;[32,36] with all results comparing very nicely. Scientifically, these results not only corroborate our previous findings that certain cation$\cdots$anion interactions dictate the NLO function of **DAST** and its derivatives; they also afford newfound structure-property relationships and an associated knowledge base whose fine detail and multi-phase information about **DAST**-based compounds is primed for the molecular engineering of new **DAST** derivatives with better tailored NLO properties.

5.5. References

(1) Teshome, A.; Bhuiyan, M. D. H.; Gainsford, G. J.; Ashraf, M.; Asselberghs, I.; Williams, G. V. M.; Kay, A. J.; Clays, K. Synthesis, Linear and Quadratic Nonlinear Optical Properties of Ionic Indoline and N,N-Dimethylaniline Based Chromophores. *Opt. Mater.* **2011**, *33* (3), 336–345.

(2) Cole, J. M.; Lin, T.-C.; Edwards, A. J.; Piltz, R. O.; Depotter, G.; Clays, K.; Lee, S.-C.; Kwon, O.-P. Concerted Mitigation of O···H and C(π)···H Interactions Prospects Sixfold Gain in Optical Nonlinearity of Ionic Stilbazolium Derivatives. *ACS Appl. Mater. Interfaces* **2015**, *7* (8), 4693–4698.

(3) Oudar, J. L.; Zyss, J. Structural Dependence of Nonlinear-Optical Properties of Methyl-(2,4-Dinitrophenyl)-Aminopropanoate Crystals. *Phys. Rev. A* **1982**, *26* (4), 2016–2027.

(4) Kim, J.; Kwon, O.-P.; Jazbinsek, M.; Park, Y. C.; Seo, J.-I.; Lee, Y. S. Quantum Chemical Evaluation of Ionic Nonlinear Optical Chromophores and Crystals Considering the Counteranion Effects. *J. Phys. Chem. C* **2011**, *115* (47), 23535–23542.

(5) Follonier, S.; Fierz, M.; Biaggio, I.; Meier, U.; Bosshard, C.; Günter, P. Structural, Optical, and Electrical Properties of the Organic Molecular Crystal 4-N,N- Dimethylamino-4′ -N′ -Methyl Stilbazolium Tosylate. *JOSA B* **2002**, *19* (9), 1990–1998.

(6) Duan, X.-M.; Konami, H.; Okada, S.; Oikawa, H.; Matsuda, H.; Nakanishi, H. Influence of Counter Anion on Geometries, Electronic Structures and Nonlinear Optical Properties of Dimethylaminostilbazolium Cation: An Investigation by Semiempirical Calculation. *J. Mol. Struct. THEOCHEM* **2000**, *531* (1), 65–77.

(7) Nunzi, F.; Fantacci, S.; De Angelis, F.; Sgamellotti, A.; Cariati, E.; Ugo, R.; Macchi, P. Theoretical Investigations of the Effects of J-Aggregation on the Linear and Nonlinear Optical Properties of E-4-(4-Dimethylaminostyryl)-1-Methylpyridinium [DAMS+]. *J. Phys. Chem. C* **2008**, *112* (4), 1213–1226.

(8) Sainudeen Zuhail; Ray Paresh Chandra. Nonlinear Optical Properties of Ionic NLO Chromophores: An Attempt to Bridge the Gap between Computation and Experiment. *Int. J. Quantum Chem.* **2005**, *105* (4), 348–358.

(9) Duan, X.-M.; Okada, S.; Oikawa, H.; Matsuda, H.; Nakanishi, H. Comparatively Large Second-Order Hyperpolarizability of Aromatic Sulfonate Anion with Short Cutoff Wavelength. *Jpn. J. Appl. Phys.* **1994**, *33* (11A), L1559.

(10) Cole, J. M.; Goeta, A. E.; Howard, J. A. K.; McIntyre, G. J. X-Ray and Neutron Diffraction Studies of the Non-Linear Optical Compounds MBANP and MBADNP at 20 K: Charge-Density and Hydrogen-Bonding Analyses. *Acta Crystallogr. B* **2002**, *58* (4), 690–700.

(11) Cole, J. M.; Lin, T.-C.; Ashcroft, C. M.; Perez-Moreno, J.; Tan, Y.; Venkatesan, P.; Higginbotham, A. P.; Pattison, P.; Edwards, A. J.; Piltz, R. O.; et al. Relating the Structure of Geminal Amido Esters to Their Molecular Hyperpolarizability. *J. Phys. Chem. C* **2016**, *120* (51), 29439–29448.

(12) Cole, J. M.; Copley, R. C. B.; McIntyre, G. J.; Howard, J. A. K.; Szablewski, M.; Cross, G. H. Charge-Density Study of the Nonlinear Optical Precursor DED-TCNQ at 20 K. *Phys. Rev. B* **2002**, *65* (12), 125107.

(13) Lin, T.-C.; Cole, J. M.; Higginbotham, A. P.; Edwards, A. J.; Piltz, R. O.; Pérez-Moreno, J.; Seo, J.-Y.; Lee, S.-C.; Clays, K.; Kwon, O.-P. Molecular Origins of the High-Performance Nonlinear Optical Susceptibility in a Phenolic Polyene Chromophore: Electron Density Distributions, Hydrogen Bonding, and Ab Initio Calculations. *J. Phys. Chem. C* **2013**, *117* (18), 9416–9430.

(14) Higginbotham, A. P.; Cole, J. M.; Blood-Forsythe, M. A.; Hickstein, D. D. Identifying and Evaluating Organic Nonlinear Optical Materials via Molecular Moments. *J. Appl. Phys.* **2012**, *111* (3), 033512.

(15) Robinson, F. N. H. Nonlinear Optical Coefficients. *Bell Syst. Tech. J.* **1967**, *46* (5), 913–956.

(16) Jazbinsek, M.; Mutter, L.; Gunter, P. Photonic Applications With the Organic Nonlinear Optical Crystal DAST. *IEEE J. Sel. Top. Quantum Electron.* **2008**, *14* (5), 1298–1311.

(17) *Characterization Techniques and Tabulations for Organic Nonlinear Optical Materials*; Kuzyk, M. G., Dirk, C. W., Eds.; Optical engineering; Marcel Dekker: New York, 1998.

(18) Clays, K.; Persoons, A. Hyper-Rayleigh Scattering in Solution. *Phys. Rev. Lett.* **1991**, *66* (23), 2980–2983.

(19) Cole, J. M. Organic Materials for Second-Harmonic Generation: Advances in Relating Structure to Function. *Philos. Trans. R. Soc. Lond. Ser. Math. Phys. Eng. Sci.* **2003**, *361* (1813), 2751–2770.

(20) Marder, S. R.; Gorman, C. B.; Tiemann, B. G.; Perry, J. W.; Bourhill, G.; Mansour, K. Relation Between Bond-Length Alternation and Second Electronic Hyperpolarizability of Conjugated Organic Molecules. *Science* **1993**, *261* (5118), 186–189. https://doi.org/10.1126/science.261.5118.186.

(21) Sheldrick, G. M. A Short History of *SHELX*. *Acta Crystallogr. A* **2008**, *64* (1), 112–122.

(22) Madsen, A. Ø. *SHADE* Web Server for Estimation of Hydrogen Anisotropic Displacement Parameters. *J. Appl. Crystallogr.* **2006**, *39* (5), 757–758.

(23) Blessing, R. H. On the Differences between X-Ray and Neutron Thermal Vibration Parameters. *Acta Crystallogr. B* **1995**, *51* (5), 816–823.

(24) Volkov, A.; Messerschmidt, M.; Coppens, P. Improving the Scattering-Factor Formalism in Protein Refinement: Application of the University at Buffalo Aspherical-Atom Databank to Polypeptide Structures. *Acta Crystallogr. D Biol. Crystallogr.* **2007**, *63* (2), 160–170.

(25) Dominiak, P. M.; Volkov, A.; Li, X.; Messerschmidt, M.; Coppens, P. A Theoretical Databank of Transferable Aspherical Atoms and Its Application to Electrostatic Interaction Energy Calculations of Macromolecules. *J. Chem. Theory Comput.* **2007**, *3* (1), 232–247.

(26) Volkov, A.; Li, X.; Koritsanszky, T.; Coppens, P. Ab Initio Quality Electrostatic Atomic and Molecular Properties Including Intermolecular Energies from a Transferable Theoretical Pseudoatom Databank. *J. Phys. Chem. A* **2004**, *108* (19), 4283–4300.

(27) Volkov, A; Macchi, P; Farrugia, L. J; Gatti, C; Mallinson, C; Richter, T; Koritsanszky, T. *XD2006 - a Computer Program for Multipole Refinement, Topological Analysis of Charge Densities and Evaluation of Intermolecular Energies from Experimental or Theoretical Structure Factors.*; 2006.

(28) Kohn, W.; Sham, L. J. Self-Consistent Equations Including Exchange and Correlation Effects. *Phys. Rev.* **1965**, *140* (4A), A1133–A1138.

(29) Hohenberg, P.; Kohn, W. Inhomogeneous Electron Gas. *Phys. Rev.* **1964**, *136* (3B), B864–B871.

(30) Frisch, M. J; Trucks, G. W; Schlegel, H. B.; Scuseria, G. E; Robb, M. A; Cheeseman, J. R; Scalmani, G; Barone, V; Mennucci, B; Petersson, G. A; et al. *Gaussian09*; Gaussian, Inc.: Wallingford CT, 2009.

(31) Volkov, A.; Koritsanszky, T.; Chodkiewicz, M.; King, H. F. On the Basis-Set Dependence of Local and Integrated Electron Density Properties: Application of a New Computer Program for Quantum-Chemical Density Analysis. *J. Comput. Chem.* **2009**, *30* (9), 1379–1391.

(32) Woińska, M.; Jayatilaka, D.; Dittrich, B.; Flaig, R.; Luger, P.; Woźniak, K.; Dominiak, P. M.; Grabowsky, S. Validation of X-Ray Wavefunction Refinement. *ChemPhysChem* **2017**, *18* (23), 3334–3351.

(33) Jayatilaka, D.; Grimwood, D. J. Tonto: A Fortran Based Object-Oriented System for Quantum Chemistry and Crystallography. In *Computational Science — ICCS 2003*; Sloot, P. M. A., Abramson, D., Bogdanov, A. V., Gorbachev, Y. E., Dongarra, J. J., Zomaya, A. Y., Eds.; Lecture Notes in Computer Science; Springer Berlin Heidelberg, 2003; pp 142–151.

(34) Lu, T.; Chen, F. Multiwfn: A Multifunctional Wavefunction Analyzer. *J. Comput. Chem.* **2012**, *33* (5), 580–592.

(35) Dähne, S.; Radeglia, R. Revision Der Lewis-Calvin-Regel Zur Charakterisierung Vinyloger. Polyen- Und Polymethinähnlicher Verbindungen. *Tetrahedron* **1971**, *27* (15), 3673–3693.

(36) Hickstein, D. D.; Cole, J. M.; Turner, M. J.; Jayatilaka, D. Modeling Electron Density Distributions from X-Ray Diffraction to Derive Optical Properties: Constrained Wavefunction versus Multipole Refinement. *J. Chem. Phys.* **2013**, *139* (6), 064108.

Chapter 6

Molecular origins of octupolar nonlinear optical activity in dichlorobis(3-pyridinecarboxaldehyde-*κ-N*)Zn(II) deduced by high-resolution X-ray diffraction analysis and *ab initio* calculations

6.1 Introduction

The studies presented in Chapters 3-5 focused on a range of organic NLO active chromophores, and attempted to relate their structure to their function, augmenting the already well-established canon of structure-property relationships[1]. On the other hand however, similar studies of organometallic complexes for NLO applications have emerged less frequently; unsurprising, considering the more complicated structure-function relationships associated with organometallic complexes. Indeed, concerted efforts to establish well-defined structure-function relationships for the NLO activity of organometallic complexes, from which their SHG activity can be assessed and rationalized, have not yet matured. This contrasts starkly to the situation in the field of SHG-active organic materials where structure-function relationships are now very well advanced[1]. This contrast likely results as a consequence of the more complicated electronic charge characteristics associated with organometallic chemistry e.g. crystal field theory and ligand field theory, the nature of will determine metal-to-ligand charge transfer (MLCT), ligand-to-metal charge transfer (LMCT), or even intra-ligand charge transfer (ILCT); electrochemical redox reactions and levels of coordinative (un)saturation that will determine metal oxidation states and metal site reactivity, and whether charge-transfer proceeds to or from the metal species. Such charge-transfer characteristics in organometallic complexes are too complicated for simple structural data analysis tools such as bond-length-alternation (BLA)[1,2] to determine the nature of intramolecular charge transfer (ICT) and thence likely extent of NLO function in a given material.[3,4]

There are also practical difficulties associated with unraveling structure-function relationships in SHG-active materials. On the one hand, structural information is dependent on the ability to collect high-quality, high-resolution X-ray diffraction data; while NLO function cannot be determined optically at the molecular level in the solid state. In terms of the former, With this in hand, and given the recent improvements in the collection techniques of high-resolution X-ray data at synchrotron facilities[5,6], studies into the NLO activity of organometallic complexes, and their rationalized design for bespoke applications, should begin to rapidly mature into a mainstream research area.

At the same time, scholarly interest in octupolar materials and the three-dimensional nature of their NLO response has increased over the last decade or so, and has led to a modest increase in the number of studies of the NLO activity of octupolar, organic compounds[7–11], and organometallic complexes[12–16]. Nevertheless, investigation of octupolar materials and their NLO properties are still in their infancy, especially octupolar organometallics, despite their postulation decades ago by Zyss[17,18] and Ledoux[19]. It is therefore surprising that such compounds have not received more attention to date.

In their seminal works, Zyss and co-workers have demonstrated that compounds with octupolar symmetries can be subdivided into two classes: (i) compounds with dipolar and octupolar contributions, and (ii) compounds that contain octupolar contributions exclusively. An advantage of the latter is that they do not suffer from the dipole-induced propensity to dimerize. This characteristic feature of pure octupolar molecules arises from their molecular symmetry and thus, imposes restrictions on the allowed point groups of octupolar materials, i.e., D_{3h}, D_3, T_d or D_{2d}.. Herein, we present an evaluation of the molecular origins of the NLO properties of an octupolar organometallic complex with pseudo-D_{2d} point group symmetry: dichlorobis(3-pyridinecarboxaldehyde-*κ*-*N*)Zn(II) (**45**) *cf.* Fig 6.1(a). Its crystal structure was reported by Y. Li, Z. Liu, and H. Deng[20]. This complex was first identified as a potentially promising NLO-active octupolar organometallic complex, through a data-mining study (Cole *et al.;* unpublished). Since then, solution-state NLO responses of a series of Zn-based complexes, that were designed based on **45** has been found (Cole *et al.;* unpublished). This paper further augments these previous reports, and provides a through evaluation of the molecular origins of the NLO responses of **45**.

The structure-function relationships of **45**, and its ensuing NLO response are examined in terms of its intramolecular charge-transfer (ICT) characteristics, crystal field effects, and molecular hyperpolarizability (β), through a concerted use of X-ray diffraction studies and *ab initio* calculations. Given the typically large errors (10-30%)[21] associated with the determination of β coefficients, four independent methods were used to determine β: i) multipolar modeling of electron densities using high-resolution X-ray diffraction data, ii) X-ray wave-function refinement[22] iii) optical measurements using hyper-Rayleigh scattering (HRS)[23] and iv) density functional theory (DFT)[24] calculations in the gas phase. In i), β was determined empirically from the multipolar modeling (MM)[25] of the molecular electron densities obtained from high-resolution X-ray diffraction data. This employs an empirical relation between the quadrupolar and octupolar moments of a specific atom and β, which is based on the theory of Robinson[26]. As well as providing solid-state measures of β, multipolar refinements permit a full topological analysis of the bonding and ICT throughout the molecule, which enables a qualitative and quantitative examination of the molecular bonding and, a determination of the electronic ICT characteristics that underline the molecular origins of its NLO responses. So far, this empirical method has remained relatively unexplored, most likely due to the circumstance that a sufficiently accurate correlation model between atomic multipolar moments and β has only been developed recently.[27] Higginbotham *et. al.* have successfully applied this model to three distinct types of NLO materials: two organic chromophores that exist in zwitterionic[28] or neutral forms[29] and a organometallic compound.[30] Since then, other studies have used this method to successfully determine the molecular hyperpolarizability of a range of organic NLO chromophores[31,32,]. Nevertheless, more case studies are needed to further probe the limitations of this empirical approach. In ii) the initial experimental atomic coordinates and ADPs from the multipolar refinement along with SHADE2.1[33] generated H corrections were used to calculate a wave-function of **45** in the gas-phase, fitted to the experimental X-ray diffraction data. Theoretical X-ray structure factors were then generated from this wave-function and subsequently refined against the experimental structure factors obtained from the charge-density study.

We begin by assessing the molecular structure of **45** by conventional single-crystal X-ray diffraction, whereby a particular focus will be placed on identifying the π-conjugated ICT pathways. Subsequently, the linear and non-linear optical properties is assessed using a variety of materials characterization techniques such as UV-vis spectroscopy, charge-density analysis, X-ray wave-function refinement, DFT calculations, and hyper-Rayleigh scattering measurements. The enumeration of β via methods (i-iv) is undertaken, and reveals the NLO response of **45** in multiple phase states i.e. solid state, liquid, and gas phase, from which the impact of crystal field effects and intermolecular interactions on the NLO processes of **45** are determined. Furthermore, discussions that assess the level of consistency of β determined by these independent methods are also presented, providing assurance against the well-known accuracy issues associated with β evaluations. With this assurance in hand, the study concludes with an assessment of the potential of **45**, with a view to bespoke NLO device applications.

6.2 Experimental and Computational Methods

6.2.1 Synthesis and crystallization of 45

Compound **45** was obtained via the previously reported synthetic route outlined in Scheme 6.1

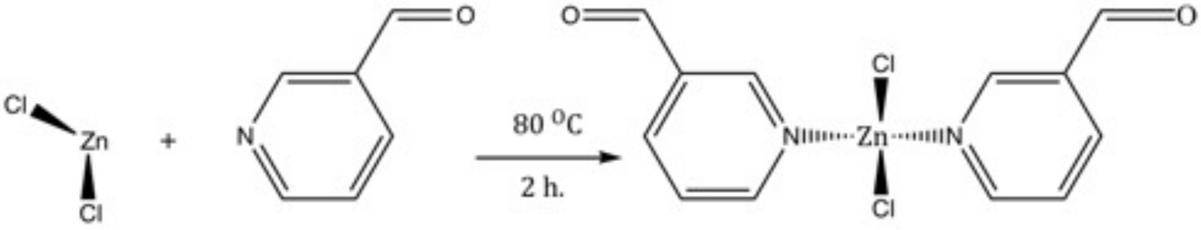

Scheme 6.1. Synthesis of **45**.

High-quality single crystals of **45** were obtained by slow evaporation of the solvent from ethanolic solutions of **45**.

6.2.2 High-resolution single-crystal synchrotron X-ray diffraction data

A crystal of **45** with dimension of 0.10 x 0.07 x 0.01 mm was mounted on a 5 µm diameter fiber tip with paratone oil and cooled down to 100 K with an Oxford Cryojet. A single crystal X-ray diffraction experiments were conducted at ChemMatCARS (sector 15) of the Advanced Photon Source (APS), Argonne National Laboratory (ANL). The beam energy was 30 keV (0.41328 Å) [standard wavelength] and the beam size at the sample was 0.1 x 0.1 mm^2. Data were collected using a Bruker D8 fixed-chi diffractometer equipped with an APEX II CCD detector used to capture a series of data frames over multiple φ scans of crystal orientations, which were collected in increments of 0.3° and an exposure time of 0.6 s, ω offset: 20°, and κ offset: 45°, sample-to-detector distance: 130 mm. Data collection and integration were performed with APEX II suite software. The reduction of data was conducted with SAINT v.8.32B program included in the APEX suite. SORTAV[34,35] was used for the implementation of empirical absorption corrections, data sorting, and merging as per §2.2.2 and §2.2.3. A data resolution of up to $\sin\theta/\lambda = 1.04$ Å^{-1} was achieved.

6.2.3 Independent atom model structural refinement

A conventional IAM crystal structure refinement was undertaken using SHELX[36] (*cf* §2.2.5) and confirmed the space Pnma [a = 5.7509 Å; b = 12.1999 Å; c = 19.0906 Å; α=β=γ=90.00 °; Z=4].This afforded R1 (I >2s(I)) and wR2 values of 0.0281 and 0.0712 for all observed reflections.

6.2.4 Multipolar structural refinement

Initial atomic coordinates and ADPs for all non-hydrogen atoms were obtained from the IAM refinement of the X-ray data and used as a starting point for the multipolar refinement. Initial atomic coordinates for hydrogen atoms were set according to reference neutron-determined X-H bond lengths,[37] while their ADPs were determined using SHADE2.1,[33] and these remained constant in all refinements. The multipolar refinement was carried out using the XD2006 program suite.[38] Residual electron-density maps of the final charge-density model of **45** (*cf.* Appendix A; A.3) were essentially featureless at the 0.1 eÅ^{-3} level, with the exception of the areas around the Zn and, two Cl atoms. Here, raw electron density of up to 0.443 eÅ^{-3} was observed around the Cl atoms, while a peak of 0.628 eÅ^{-3} was observed around the Zn ion; Zn ions are notorious for their problematic modeling in charge density analyses.[6,39] Indeed, charge-density modeling of transition metals still presents a major challenge for charge-density studies. Zn is particularly challenging due to its $3d^{10}4s^{2}$ electron configuration, with the *4s* orbital inducing a highly spherical, diffuse valence electron density. Consequently, effective partitioning of electrons into multipolar terms can be challenging, and the inability to achieve featureless residual electron density around Zn atoms is well documented. The NLO compound, zinc tris(thiourea)sulfate (ZTS), for example, shows similar values of residual electron density around the Zn atom (0.5 eÅ^{-3})[30]. Owing to the highly diffuse nature of the *4s* orbital of the Zn atom, methods have been devised that attempt to circumvent this obstacle; e.g. the Su-Coppens-Macchi (SCM)[40,41]. The SCM databank treats the *4s* shell as part of the core electron density and thus, the valence electrons are taken from the aspherical *3d* shell instead of the spherical *4s* shell. To minimize possible artifacts present around the Zn atom, the multipolar refinement was carried out especially carefully. The final model was also assessed via the Hirshfeld rigid bond test,[42] which calculates the difference of the mean-square displacement amplitudes (DMSDAs) in the directions of the bonds. The maximum DMSDA for **45** (0.0008 Å^{2} for C(1)-C(6)) is sufficiently low to assume appropriate deconvolution of all bonding and thermal motion effects. Some shashlik-type residual density was observed around the Zn and the two Cl atoms, indicative of potential anharmonic libration[43,44]. However, the refinement of the Gram-Charlier anharmonic thermal parameters was not included in the final model, given that they yielded unrealistic values, and that Kuhs' criterion[45] was not satisfied.

The least-squares refinement statistics on F for the final multipolar model yielded R = 0.0203, Rw = 0.0249 ($w = 1/\sigma^{2}$), GOF = 1.35, and a data-to-parameter ratio of 21.7.

6.2.5 X-ray wave-function refinement

The XWR method[22] was employed via the program TONTO[46] as outlined in §2.9 on **45**. Initially, a Hirshfeld atom refinement (HAR)[47,48] was performed at the HF-6-31G(d,p) level of theory, by applying a self-consistent field (SCF) calculation to a non-interacting molecule, using as input the atomic coordinates and ADPs from the multipolar refinement. The data used for the XWR were cutoff at the same resolution as those used for the multipolar model for consistency and comparison ($\sin\theta/\lambda \leq$

1.04 Å^{-1}). An assessment of the residual electron density maps for this initial HAR showed that the presence of shashlik density around the Zn and Cl atoms was sufficiently marked that the input to the HAR needed to include the 3rd-order Gram-Charlier (3GC) anharmonic thermal parameters. A discussion on the validity of including 3GC in the model parameters for the HAR is provided in Appendix C. §C.5. The refined atomic coordinates, ADPs, and 3GC parameters of the HAR were subsequently used as a starting point for the construction of a theoretical molecular wave-function at the HF/def2-TZVP level of theory.

Convergence was assured by testing the refinement test statistic, χ^2, using a range of λ_L values. The XWR was allowed to run until convergence was achieved. The point at which to terminate an XWR fitting is still very much up for debate and no routine method is yet decided upon within the field. However, running XWR until convergence fails is one of the accepted XWR termination approaches used.[49] Convergence up to λ_L = 1.2 afforded agreement values of R = 0.0188, R_w = 0.0234, GOF = 1.28, and χ^2 = 1.61. The residual electron density was analyzed, which revealed a maximum residual of 0.08 Å^{-3} for C(6). The resulting wave-function was used to carry out a topological analysis of **1** using the Multiwfn program,[50], to assess its validity against the multipolar model and is deposited as Supplementary Material. Optical properties of the molecule, including its (hyper)polarizability, were determined.[51]

6.2.6 *Ab Initio* density functional theory calculations

Electrostatic moments and (hyper)polarizability values of **45** were calculated by DFT using Gaussian09[52] as per §2.10. X-ray structures of **45** were used for the initial geometry. Initially, IAM-derived atomic position parameters were used to undertake a ground-state geometry optimization that comprised finding the minimum on the potential energy surface of the ground state. All default settings for Gaussian09 were maintained. DFT calculations were carried out at the Cam-B3YLP/6-31+G(d,p) level of theory. Subsequently, the components of the (hyper)polarizability tensor of the structure were calculated at the same level of theory.

6.3 Results and Discussion

6.3.1 Molecular architecture of 45

The molecular structure of **45** in the crystalline-form, determined by conventional single-crystal X-ray diffraction analysis, is shown in Fig. 6.1, and reveals clear implications regarding its potential as an NLO chromophore. The complex formally exhibits C_m point-group symmetry but has very high octupolar characteristics owing to its pseudo-octupolar point group, D_{2d}, configuration. Formal D_{2d} symmetry is barred because of the *meta*-positioning of the carboxaldehyde that precludes 2-fold rotational symmetry; *para*-positioning would afford pure octupolar symmetry, which would mean all dipolar NLO contributions would cancel to zero. However, β is a sum of dipolar and octupolar contributions, and dipolar contributions tend to be stronger than octupolar NLO effects; so the pseudo-octupolar geometric nature of **45** actually stands to provide a greater overall SHG output than its purely octupolar counterpart, since it gains significantly in dipolar contribution at the modest expense of octupolar contributions.

The Zn ion coordinates to four ligands in a tetrahedral configuration coordinating to two chlorides and an electron withdrawing carboxaldehyde group. Identical ligands are *cis* to each other, thus rendering a mirror plane that bisects the same ligands from each other (Fig 6.1(c)). The monodentate nature of the ligands will help to sustain a regular tetrahedral geometry (Cl-Zn-N angles range from 104.8^o - 112.1^o), despite the large size differences of each type of ligand and disparate coordination lengths, Zn-X (X = Cl or N). The more regular the tetrahedral zinc configuration, the greater the molecule is aligned towards pure octupolar symmetry. The linear and non-linear optical properties of **45** are now presented in order to assess the extent of its dipolar and octupolar contributions, whereupon the results will need to be set against intra-molecular and inter-molecular charge transfer considerations.

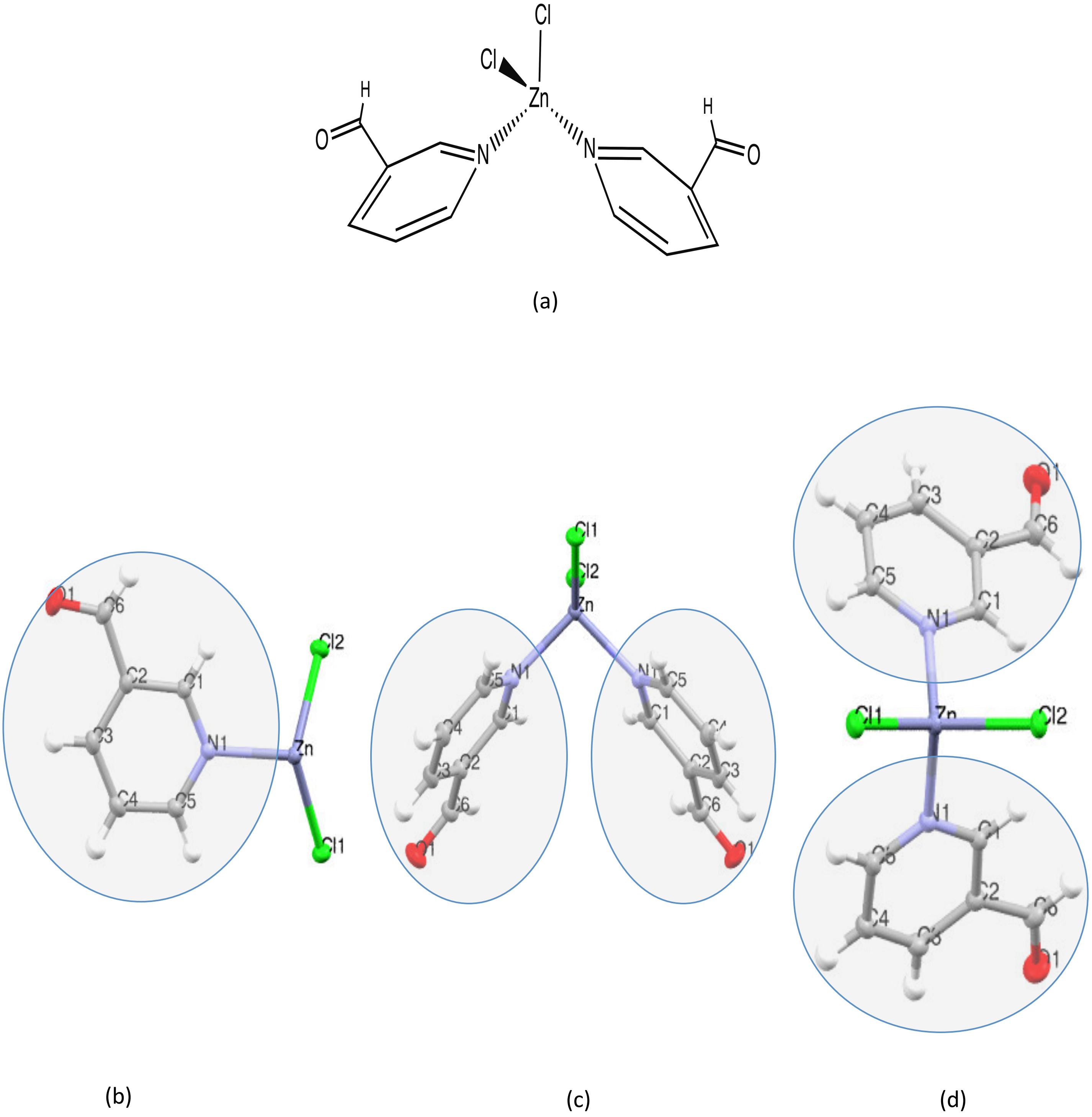

Figure. 6.1. Chemical structure of dichlorobis(3-pyridinecarboxaldehydeκN)Zn(II) (a). 50% atomic displacement parameter (ADP) plots (T = 100K) and D-π-A motif of **45** as viewed along the crystallographic z (asymmetric unit) (b), y (c) and x (d) axes. Shaded regions enclose co-planar atoms.

6.3.2 Optical properties

6.3.2.1 Linear optical properties

The solution-based UV/vis absorption spectrum for **45** was recorded and its maximum peak absorption wavelength, λ_{max}^{peak} determined. Compound **45** shows two peaks, both of which are outside of the visible range of the spectrum indicating that the complex has good nonlinearity-transparency trade off within this region akin to other octupolar structures[53] and in particular tetrahedral zinc-based organometallic NLO chromophores[14]. The two peaks are centered at λ_{max}^{peak} = 232 nm and 267 nm; these values are approximate given that the peaks are not clearly defined.

Complementary DFT calculations at the Cam-B3LYP/6-31G+(d,p) level of theory enabled the associated optical transitions in **45** to be related to perturbations in its electronic structure. Molecular orbitals (MOs) were generated via the program GaussView[54], and are defined by the frontier orbitals, namely the highest occupied and lowest unoccupied molecular orbitals (HOMO and LUMO) and, other noteworthy MOs where relevant, such as the LUMO+1 (Fig 6.2). Through analysis of the HOMO, LUMO and LUMO+1 the extent, and direction of shifts in the molecular electron density of a compound, upon excitation, can be inferred, thereby providing a rudimentary assessment of a complex's possible ICT-induced polarization, and NLO abilities.

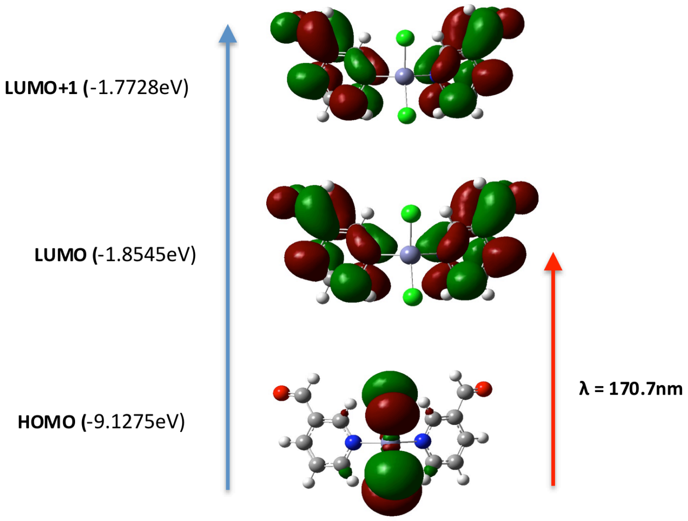

Figure. 6.2. HOMO, LUMO, and LUMO+1 of **1**, calculated at the Cam-B3LYP/6-31G+(d, p) level of theory.

A comparison of the HOMO and LUMO of **45** reveals optical absorptions in the molecule are accompanied by a significant shift in the electron density from the zinc dichloride moiety to the *3*-pyridinecarboxaldehyde ligands. Notwithstanding a change in sign, moving up in energy to the LUMO+1 sees no further shift in the electron density, thus suggesting that the adoption of a two-level model for **45,** from which its (hyper)polarizability can be determined, is sufficient in this case study. Such features in the DFT-generated molecular orbitals of **45** demonstrate that the ICT facilitates an optically active ‘push-pull’ interaction within the complex, with the electron-withdrawing carboxaldehyde group providing a ‘pull’ effect of electronic charge from the complementary ‘push’ effects of the electron-donating zinc dichloride moiety via the delocalized pyridyl ring. Furthermore, these ICT effects demonstrate the formation of multi-directional polarization across the complex into the two functionalized pyridyl moieties, which is indicative of its octupolar character.

6.3.2.2 Non-linear optical properties

The non-linear optical (NLO) properties of **45** were assessed by an examination of its hyperpolarizability (β), which acts as a molecular measure of the second-harmonic generation (SHG) properties of a material. Four independent methods were used for the determination of β, and the results are summarized in Table 6.1. The β values of **45** were determined in the gas phase (via DFT calculations), gas phase + crystal-field forces (XWR methods), solution state (via HRS measurements), and crystalline phase (using charge-density analysis). The evaluation and comparison of these independently obtained β values is sensible, given the large errors (~10-30%) that are typically associated with the enumerations of β coefficients. Additionally, the determination of β across multiple states of matter allows an assessment of the NLO responses of **45** in different phases; in particular, this will help to reveal salient crystal-field effects, which may become important for future device applications which are typically in the crystalline form.

Table 6.1. Molecular hyperpolarizability (β) values for the gas phase, gas state but subjected to crystal field forces, solution state, and single-crystal form of **45**, obtained from DFT calculations, hyper-Rayleigh scattering measurements, X-ray wave-function refinement methods, and charge-density analysis (using two different atomic partitioning methods: Stockholder[55] and QTAIM[56].

Method	β / 10^{-30} esu
DFT Cam-B3LYP/6-31+G(d,p)	3.029
XWR def2-TZVP	2.490
HRS*	5.500± 0.500
Charge density (XD)/Stockholder	11.490
Charge density (XD)/QTAIM	11.439

*The error in β HRS was predicated by the 20% statistical error on the evaluation of β for the Crystal Violet HRS reference sample.

Gas-phase calculations of β and solution-phase HRS experimental determinations of β are well established; see for example[8,57–61]for more comprehensive reviews. However, the rarity by which solid-state β values are derived from X-ray diffraction data renders it worth detailing herein. For the determination of β of **45** in its single-crystal form, the multipolar moments of each atom in the charge-density distribution are used, together with the empirical calculation for β (*cf.* Eq. 1.10):[35] See §1.2.2.4 for more on the partition methods and the empirical calculation of β.

6.3.2.2.1 Comparison of β values determined from the four independent methods

Table 6.1 reveals that the hyperpolarizability of **45** increases gradually as the level of intermolecular interaction between the molecules increases i.e. gas phase < liquid phase < solid state. The gas and {gas+crystal field forces} values derived from DFT and XWR, respectively, are in good agreement, whereby the small differences in β are most likely attributable to the use of different functionals and basis sets (XWR: HF/def-TZVP *vs.* DFT: Cam-B3LYP/6-31+G(d,p)). An analysis of the isolated molecule, which is nonetheless influenced by crystal field forces, provides an invaluable benchmark to compare the contributions to β from an individual molecule against those of supramolecular effects that will be contained within β values obtained from solution and solid-state methods.

The solution-phase value of β appears to be approximately double that of the gas-phase values, which suggests that the deionized water, i.e., the solvent used in the HRS measurements, has a small but significant polarization effect on the molecules of **45**. A marked effect on the HRS values can occur if the solvent used is especially polar. Indeed, original HRS measurements on the industry standard NLO material *p*NA revealed the influence of polar solvents on HRS measurements[23]. It can therefore be assumed that molecular aggregation are most likely absent for molecules of **45** within deionized water. The lack of molecular aggregation in **45** is of practical importance given that the aggregation of chromophores is well-known to cause detrimental effects on the NLO performance of the material.[62–64] In instances where molecular aggregation produces deleterious effects, NLO device processing problems are commonly encountered.[65]

Direction-specific supramolecular interactions are only accounted for in the solid-state charge-density values, which derive β from a model that incorporates the crystal lattice environment. The β value derived from the single-crystal form of **45** are more than four times greater than that of the XWR value of β, wherein only non-direction-specific crystal field forces are considered. This comparison demonstrates that minimal crystal field forces of a non-directional electrostatic nature act on this complex; rather, significant directional supramolecular effects such as hydrogen bonds or other specific intermolecular interactions must be the primary cause of the multi-phase differences in the molecular hyperpolarizability of **45**.

On a technical note, it is particularly encouraging that the two solid-state values obtained using different partition methods are in excellent agreement, demonstrating the internal consistency of the multipolar model and the equal suitability of these two atomic partitioning methods for the evaluation of β from charge-density data.

Fig. 6.3 shows high levels of agreement across all components of the hyperpolarizability tensor for these two methods and also highlights the substantial 3D (octupolar) character of the second-order response of **45**; i.e. β_{ijk} coefficients with significant intensity beyond β_{iii} (where i=x,y or z). The tensorial components of β outlined in Fig. 6.3 exposes the dominance of the hyperpolarisability in the first principal orthogonal component (*xxx*), with the next significant components propagating from non-cyclically related cross-terms (*xyy, xzz, xxy*), illustrating a deviation from Kleinman symmetry in terms of the NLO behavior of **45**. Failure of Kleinmann symmetry (also known as overall perturbation symmetry) in relation to the non-resonant NLO properties of chromophores has previously been reported[66].

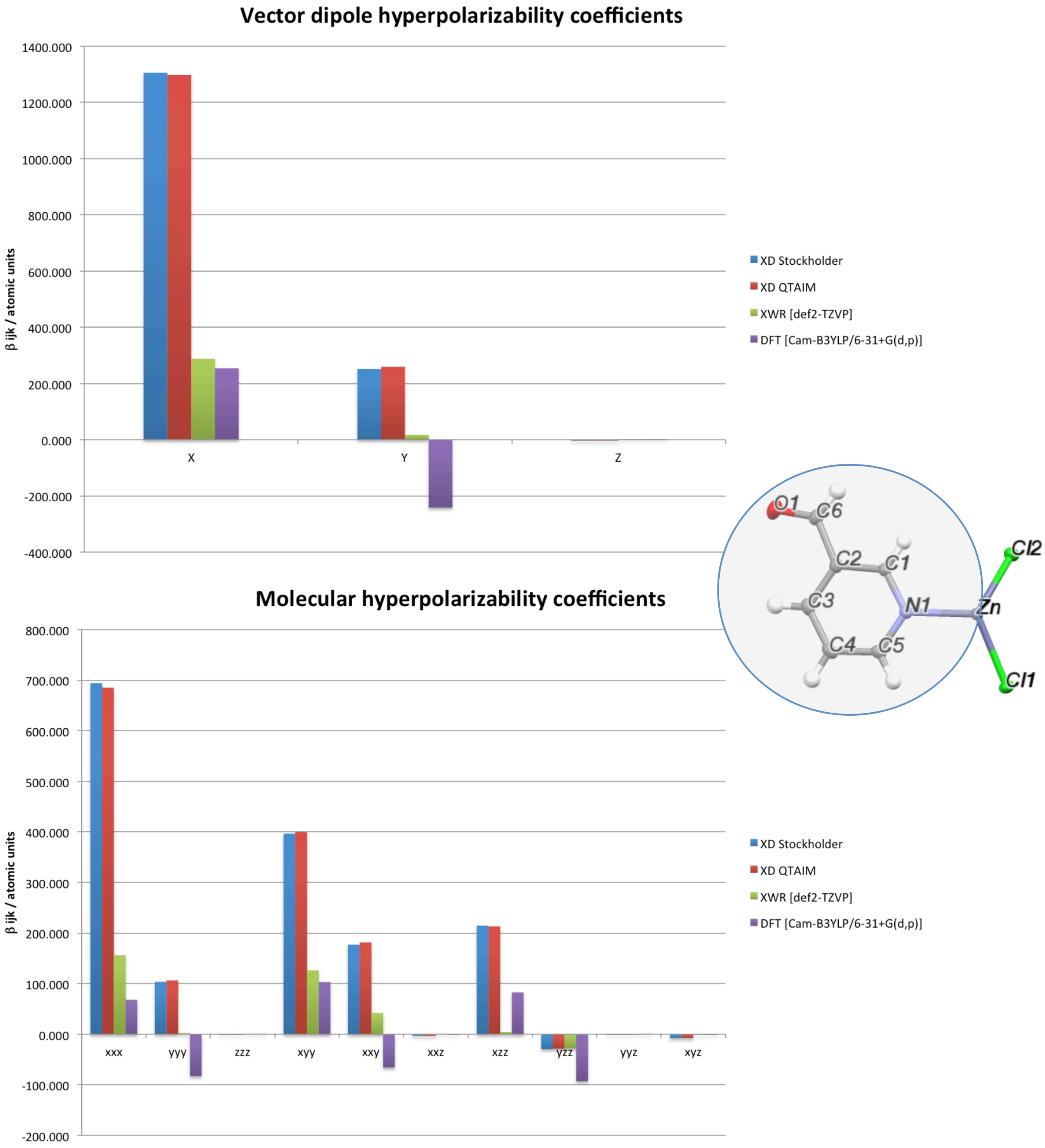

Figure 6.3. Molecular hyperpolarizability (top) and molecular vector dipole hyperpolarizability (bottom) coefficients for **45**. The complex, as viewed down the z-axis, is presented (right)

The vector dipole hyperpolarisability values further demonstrate the multi-dimensional NLO behavior of **45**, with both the *x* and *y* components being significant, and the *z* component, being small but non-zero, exemplifying the three-dimensional nature of the NLO activity in **45,** which must correspond to the nature of charge transfer phenomena which is observed in the complex. To this end, the nature of ICT that is responsible for these dipolar and 3-D octupolar contributions of **45**, as well as the presence of direction-specific intermolecular bonds that are expected to affect the NLO response of **45** at the supramolecular level are considered.

6.3.3 Structural interpretation of NLO effects from intra-molecular and inter-molecular charge-transfer considerations

6.3.3.1 Establishing structure-function relationships from intra-molecular charge transfer

The propensity for ICT to occur in the xy plane as shown in Fig. 6.3 is understandable given that the *3*-pyridinecarboxaldehyde ligands also sit within this plane. To this end, the presence of π-bonding density between the ionic Zn center and the N atoms of the pyridyl ligands, facilitates the formation of a charge transfer pathway into the pyridyl ring via metal-to-ligand charge-transfer (MLCT) wherein the electronic charge experiences a 'pull' across to the electron-withdrawing aldehyde substituent of the pyridyl ring. Inspection of Fig. 6.3 also reveals the presence of a *yzz* component to the hyperpolarizability that likely corresponds to movement of charge between the out-of-plane chloride ligands and the Zn ion center. However, this component is relatively small which tends to suggest that it would be helpful to assess the nature by which chloride ligands coordinate to Zn.

6.3.3.2 Characterizing the nature of Zn-Cl bonding

The character of the Zn-Cl bonding in **45** was assessed through the use of electron deformation density (Fig 6.4, (a-b)) and Laplacian maps (Fig 6.4, (c-d)) as well as, the kinetic energy density per electron, $G(r)/\rho(r)$, and total energy density, $H(r)$ descriptors (Table 6.2), which, can be used to classify different types of bonding, as shown by Bader[61] *cf.* Table 2.3 in §2.6.2.2. Electron-deformation density maps depict the difference between the multipolar and the independent (spherical) atom model, and consequently, reveal both the bonding and charge polarization characteristics of **45** across the molecule. Meanwhile, Laplacian maps display the second derivative of the electron density ($\nabla^2\rho$), where $\nabla\rho(r) = 0$. In the context of a charge-density study then, the Laplacian map represents the degree of local electronic-charge depletion or concentration around an atom.

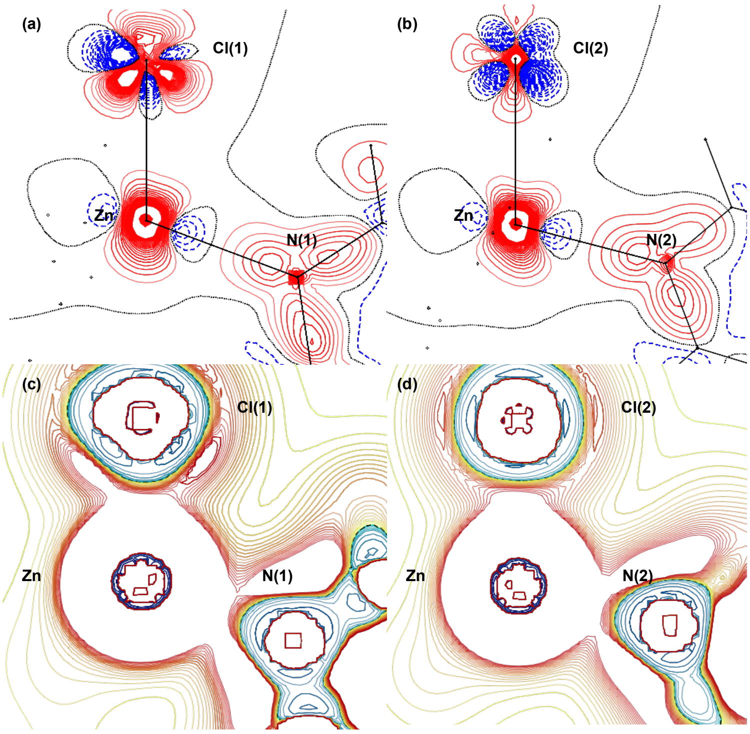

Figure. 6.4. Multipolar-model-generated deformation electron density (a,b) and Laplacian (c,d) maps of the Cl(1)-Zn-N(1) (a,c) and Cl(2)-Zn-N(2) (b,d) region. Red lines represent areas with positive signum, while blue lines represent areas with negative signum, and black lines areas of zero. The color scale in the Laplacian maps refers to local concentrations (blue) and depletions (red) of electronic charge. Contour levels are shown at 0.1 eÅ^{-3} linear scaling (deformation densities) and 0.1 eÅ^{-5} gradient scaling (Laplacians).

Inspection of both the electron deformation density (Fig 6.4, (a-b)) and Laplacian maps (Fig 6.4, (c-d)) for the Zn-Cl bonds reveal a distinct polarized bonding between the chlorides and the Zn ion centre. The Laplacian maps are particularly telling in this respect, as the presence of electron density concentrations between the Zn ion and chlorides precludes the potential for a more classically ionic bond type. This visual assessment of the Zn-Cl bonds was qualified through the kinetic energy density per electron, *G(r)/ρ(r)*, and total energy density, *H(r)* descriptors (Table 6.2), which are also suggestive of a distinct polar shared bond persisting between both Zn ion and chlorides, indicated by their $G(r)/\rho(r) \geq 1$ and $H(r) < 0$ values.

Table 6.2. Summary of the energy density descriptors for the Zn-Cl(X) bonds. ρ(r) is the electron density, $\nabla^2\rho$(r) the Laplacian (second-derivate) of the electron density. The energy descriptors G(r)/ρ(r) and H(r) are the kinetic energy density per electron and total energy respectively.

Bond	ρ(r)	$\nabla^2\rho$(r)	R_{ij}	d_1	d_2	G(r)/ρ(r)	H(r)	Bond type *cf.* Table 2.3
Zn-Cl(1)	0.491	6.48	2.2287	1.0300	1.1987	1.116	-0.014	Polar shared
Zn-Cl(2)	0.525	6.63	2.1907	1.0230	1.1677	1.113	-0.018	Polar shared

It should be noted however that the small ρ(r) values and large $\nabla^2\rho$(r) values indicate that these polar shared bonds are potentially approaching classical ionic bonding, presumably as the bonds are in fact highly dative. Given the non-zero *yzz* component of the hyperpolarizability of **45**, the polar shared bond is thought to facilitate ICT between the chlorides and Zn ion, which acts to augment the NLO effects of the complex. Now that we appreciate the character of the Zn-Cl bonding, it's helpful to take a more detailed look at the Zn-N bonding, including the pyridinecarboxaldehyde topologies as a whole.

6.3.3.3 Characterizing the nature of Zn-N bonding

The Zn-N bonding, extending into the aromatic rings, is investigated visually via Fig 6.4 and Fig 6.5, and reveals once again a strong polarized type bond between the Zn-N bonds. It is worth noting that due to symmetry constraints both the Zn-N(1) and Zn-N(2) bond are modeled identically in the multipolar model and thus their maps and respective energy descriptors will be the same.

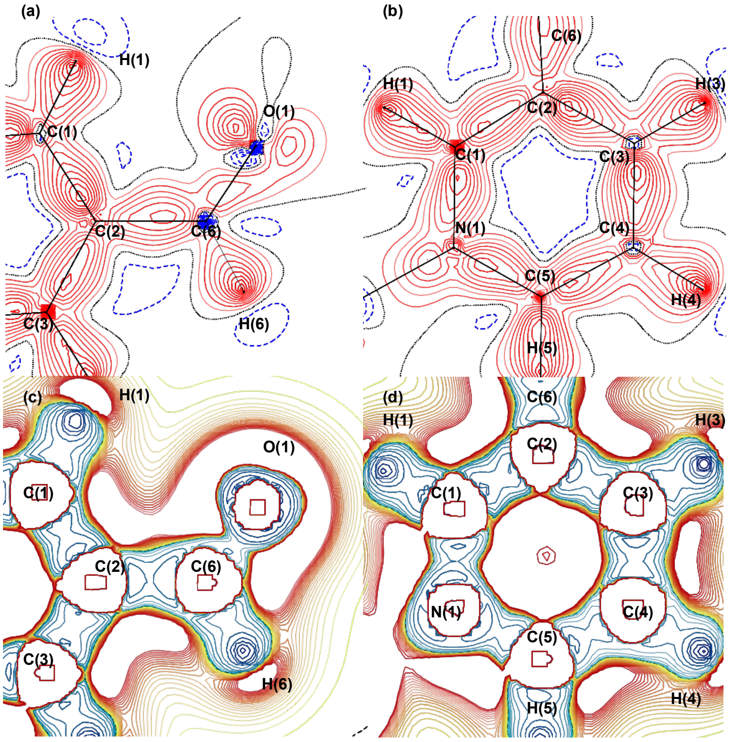

Figure. 6.5. Multipolar-model-generated deformation electron density (a,b) and Laplacian (c,d) maps of the 3-pyridinecarboxaldehyde ligand. Red lines represent areas with positive signum, while blue lines represent areas with negative signum, and black lines areas of zero. The color scale in the Laplacian maps refers to local concentrations (blue) and depletions (red) of electronic charge. Contour levels are shown at 0.1 $eÅ^{-3}$ linear scaling (deformation densities) and 0.1 $eÅ^{-5}$ gradient scaling (Laplacians).

As with Fig. 6.4, Fig. 6.5 reveals a distinct polarization of electron deformation density in the Zn-N bonds toward the Zn ion centre, while their energy descriptors; *G(r)/ρ(r)* of 1.159, and, *H(r)* of -0.017 confirm their polar shared character similar to the Zn-Cl bonds discussed in the previous section. This stands to reason given that both the Zn-Cl and Zn-N bonds will be dative, as a consequence of the Cl and N Lewis bases donating electron pairs to the Lewis acidic Zn ion.

Turning to the pyridinecarboxaldehyde ligands as a whole, the pyridyl rings between the Zn ion and the functionalized aldehyde groups presents as being highly delocalized (π-conjugated) (Figure 6b,d) with the bonds appearing polarized throughout the ring either toward the N atom e.g. C(4)-C(5), C(1)-C(2), C(5)-N(1) or, toward the aldehyde group e.g. C(2)-C(3), C(3)-C(4), N(1)-C(1), suggesting a competing ‘push-pull’ of electron density ensues across the pyridyl ring. The functionalized aldehyde group also appears to show π-conjugated character, however to confirm this the electron density, $\rho(r)$, Laplacian function, $\nabla^2\rho$(r) and bond ellipticity values of all the bonds in the pyridinecarboxaldehyde unit were determined to assess their level of conjugation. See §2.6.2.1 for information on bond ellipticity.

Through evaluation of these parameters for each bond (Table 6.3) one is able to assess the level of π-conjugation within the molecule. The use of the bond ellipticity as a measure of π-conjugation, as an alternative to the more traditional BLA methods[1,2] has been proposed before[28] and has received new-found attention recently[67].

Table 6.3 Parameters of non-hydrogen (3, −1) bond critical points. ρ (eÅ^{-3}) is the electron density; $\nabla^2\rho$ is the Laplacian; ε is the ellipticity of the bond.[56]

Bond	ρ(r) [eÅ^{-3}]	∇^2ρ(r) [eÅ^{-5}]	ε
O(1)-C(6)	2.582	-13.157	0.10
N(1)-C(1)	2.527	-22.230	0.15
N(1)-C(5)	2.455	-26.124	0.24
C(1)-C(2)	2.182	-20.149	0.24
C(2)-C(3)	2.109	-18.639	0.26
C(2)-C(6)	1.891	-15.106	0.11
C(3)-C(4)	2.237	-18.418	0.14
C(5)-C(4)	2.090	-17.338	0.13

From Table 6.3 it can be seen that all the bonds associated with the pyridinecarboxaldehyde ligand possess large ε values (> 0.1) indicative of π-bonding, while their respective ρ(r) and ∇^2ρ(r) values confirm that all bonds in the pyridinecarboxaldehyde ligand are covalent, as expected.

Having confirmed that π-conjugation ensues in the pyridinecarboxaldehyde ligands, we return to the maps to assess polarization and ICT across the unit. Most striking is the electronic polarization of electron deformation density along the C(6)-O(1) double bond (Fig 6.5) which, likely arises on account of the deactivating, i.e. electron-withdrawing, character of the aldehyde substituent. Thus its presence on the pyridyl ring is expected to result in a depletion (electron 'pull') of electron density from the π-conjugated system, creating an overall net polarization toward the aldehyde group, forming two dipolar D-π-A type architecture across the Zn-N-(pyridyl)-aldehyde units. Consequently this will cause ICT to ensue between the Zn ion centre and the aldehyde group, facilitated via the π-conjugated media (MLCT).

6.3.3.4 Overarching structural classification of the intra-molecular charge transfer in 45

Following from the assessments of the previous section we summarize the ICT in **45**, and herein link it to its resulting NLO properties. Characterization of the bonds in **45** has helped to identify the presence of ICT across the molecule, and in which direction it travels. The complex under study comprises of two D-A interactions between the chlorides and the Zn ion and two dipolar D-π-A frameworks that combined facilitate 3-D MLCT effects, as corroborated by the 3-D nature of the hyperpolarizability tensor of **45**. Collectively, these individual dipolar D-π-A components of the complex combine in a pseudo-octupolar formation of D_{2d} symmetry to yield an octupolar 3-D NLO response. This octupolar response is augmented by the presence of dipolar contributions to the molecular hyperpolarizability of **45**, which persists as a consequence of the pyridyl ligands being functionalized at the *meta*- position in a *cis*- configuration. Were the aldehyde groups to be at the *para*- position, the opposing organic ligands would counteract each other, cancelling out the dipolar contributions of the complex. Next we assess the supramolecular effects in **45** in an attempt to rationalize the major increases in the hyperpolarizability of **45** as one moves to the solid-state.

6.3.4 Establishing structure-function relationships from inter-molecular charge transfer

An analysis of the intra- and intermolecular short contacts, including hydrogen bonding, of **45** was undertaken using PLATON[68]. This revealed the absence of classic intermolecular hydrogen bonds. However, the presence of two intermolecular hydrogen interactions were determined (Fig 6.6(a)) with bond lengths and angles of 2.582(8) Å and 123.0(5) ^{O} [C(3)-H(3)¨O’(1)] and, 2.456(8) Å and 145.0(5) ^{O} [C(4)-H(4)¨O’(1)] respectively which will contribute to the centrosymmetric nature by which **45** crystallizes in the solid-state phase (space group of **45**: Pnam). Fig 6.6(b) further reveals the presence of two intermolecular interactions between Cl(2) and H’(6) with lengths of 3.317(2) Å. This interaction should help minimise any potential for large amounts of anharmonic libration in the terminal Cl(2) atom.

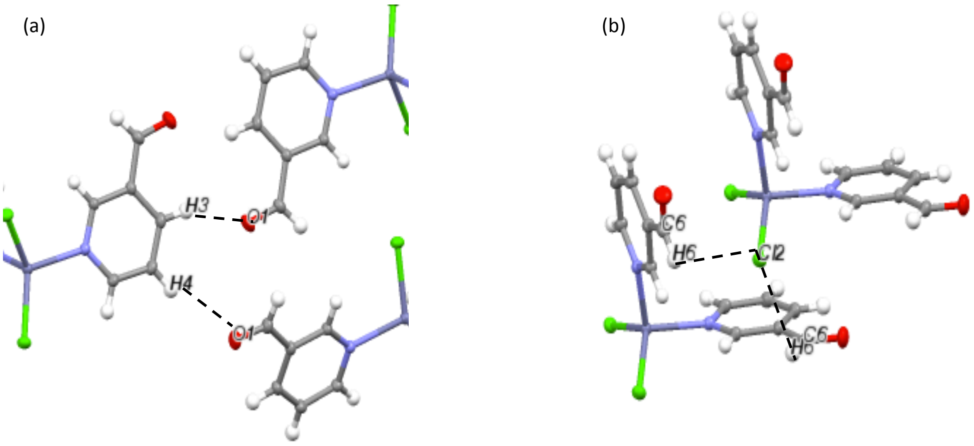

Figure. 6.6. Molecular structure of **45** highlighting the intermolecular H¨O (a) and C¨Cl (b) interactions.

Topological analysis emanating from the multipolar model of **45** was used to further characterize these hydrogen intermolecular interactions using the BCPs of these interactions. Specifically the λ_3 eigenvalue of the Hessian matrix is determined and assessed with respect to the interaction distances, d(H ¨ O), which have been correlated and studied extensively by Espinosa *et al.*[69,70]. The topological parameters of these three hydrogen interactions are listed in Table 6.4.

Table 6.4. Parameters of intermolecular hydrogen interactions. ρ (e$Å^{-3}$) is the electron density; $\nabla^2\rho$ is the Laplacian; λ_3 is the third component of the Hessian matrix; R_{ij} is the length (Å) of the bond path between the atoms.

Bond	ρ [e$Å^{-3}$]	$\nabla^2\rho$ [e$Å^{-5}$]	R_{ij} [Å]	λ_3
O(1)···H'(3)	0.036	0.853	2.4377	1.12
O(1)···H'(4)	0.026	0.751	2.5022	0.94
Cl(2)···H'(6)	0.057	0.631	2.9913	0.97

In agreement with the classification of hydrogen interactions by Espinosa *et al.* all three hydrogen interactions exhibit positive λ_3 indicative of the presence of real hydrogen interactions. The strongest of these interactions is the O(1)···H'(3) interaction; this is unsurprising given its shorter bond path length (R_{ij}) with respect to the other two hydrogen interactions. These intermolecular hydrogen interactions, which are responsible for the crystallization arrangements of **45**, facilitate an augmentation in the NLO response of the complex in the solid-state phase in two main ways: (i) the stronger O···H hydrogen interactions cause layers of **45** to stack upon one another either side of the unit cell, while (ii) the weaker Cl···H hydrogen interactions causes complex to stack on top/bottom layers in the crystal lattice. As a consequence of this sheet-like stacking arrangement, hyperpolarizability components should be augmented in the *X* and *Y* (and to a smaller extent the *Z*) directions as a consequence of the O···H induced stacking, while the Cl···H induced stacking will see an augmentation in the *X* direction; in Fig. 6.3 significant contributions are seen in the xxy and xyy components in agreement with this assessment. Furthermore, it is worth highlighting that the result of these three interactions together is to form regularly alternating sheets of the complex.

6.4 Conclusion

The NLO activity of dichlorobis(3-pyridinecarboxaldehydeκN)Zn(II) has been reported through characterization of its structural and optical properties via a range of charge density analysis, hyper-Rayleigh scattering, and *ab initio* techniques. To this end, the molecular architectures and intramolecular charge transfer aspects of the electronic structure of **45** were identified and related to its optical properties, especially the molecular hyperpolarizability, Given the notorious difficulties in obtaining reliable values of the molecular hyperpolarizability, evaluation using four independent methods (in one of three states of matter): density functional theory (gas phase) & XWR (gas phase + crystal field effects), hyper-Rayleigh scattering (solution-phase), and charge-density analysis (solid-state) was undertaken. In the case of the charge-density model, two different β values are presented. These two β values arise due to existence of several types of atomic partitioning methods available to determine the multipolar moments, which are needed for the empirical calculation of β. Herein, β values were enumerated from multipolar moments derived from stockholder and QTAIM partitioning methods. A comparison of the results revealed that these two atomic partitioning methods produced equally reliable β values, emphasizing the internal consistency of the multipolar model. Topological analysis of the molecular charge density of **45** via multipolar modeling provided a detailed description of the chemical bonding across the molecule in the solid-state phase. This in turn, enabled the determination of the origins and nature of the ICT in **45,** with the marked NLO phenomena of the complex being identified as a consequence of its tetrahedral octupolar design. Furthermore, these findings indicated that **45** has promise as a new organometallic NLO chromophore, when suitably poled in a media that circumvents its macroscopic centrosymmetry. This however is eminently achievable, given the rapid and continuing rise in thin-film technology and the emerging embodiment of NLO phenomena in nanotechnology[71,72].

6.5 References

(1) Cole, J. M. Organic Materials for Second-Harmonic Generation: Advances in Relating Structure to Function. *Philos. Trans. R. Soc. Lond. Ser. Math. Phys. Eng. Sci.* **2003**, *361* (1813), 2751–2770.

(2) Marder, S. R.; Gorman, C. B.; Tiemann, B. G.; Perry, J. W.; Bourhill, G.; Mansour, K. Relation Between Bond-Length Alternation and Second Electronic Hyperpolarizability of Conjugated Organic Molecules. *Science* **1993**, *261* (5118), 186–189.

(3) Cheng, L. T.; Tam, W.; Stevenson, S. H.; Meredith, G. R.; Rikken, G.; Marder, S. R. Experimental Investigations of Organic Molecular Nonlinear Optical Polarizabilities. 1. Methods and Results on Benzene and Stilbene Derivatives. *J. Phys. Chem.* **1991**, *95* (26), 10631–10643.

(4) Cheng, L. T.; Tam, W.; Marder, S. R.; Stiegman, A. E.; Rikken, G.; Spangler, C. W. Experimental Investigations of Organic Molecular Nonlinear Optical Polarizabilities. 2. A Study of Conjugation Dependences. *J. Phys. Chem.* **1991**, *95* (26), 10643–10652.

(5) Coppens, P. Charge-Density Analysis at the Turn of the Century. *Acta Crystallogr. A* **1998**, *54* (6), 779–788.

(6) Coppens, P.; Iversen, B.; Larsen, F. K. The Use of Synchrotron Radiation in X-Ray Charge Density Analysis of Coordination Complexes. *Coord. Chem. Rev.* **2005**, *249* (1–2), 179–195.

(7) Ledoux, I.; Zyss, J.; Siegel, J. S.; Brienne, J.; Lehn, J.-M. Second-Harmonic Generation from Non-Dipolar Non-Centrosymmetric Aromatic Charge-Transfer Molecules. *Chem. Phys. Lett.* **1990**, *172* (6), 440–444.

(8) Verbiest, T.; Clays, K.; Samyn, C.; Wolff, J.; Reinhoudt, D.; Persoons, A. Investigations of the Hyperpolarizability in Organic Molecules from Dipolar to Octopolar Systems. *J. Am. Chem. Soc.* **1994**, *116* (20), 9320–9323.

(9) Stadler, S.; Feiner, F.; Bräuchle, Ch.; Brandl, S.; Gompper, R. Determination of the First Hyperpolarizability of Four Octupolar Molecules and Their Dipolar Subunits via Hyper-Rayleigh Scattering in Solution. *Chem. Phys. Lett.* **1995**, *245* (2–3), 292–296.

(10) Cho, B. R.; Lee, S. J.; Lee, S. H.; Son, K. H.; Kim, Y. H.; Doo, J.-Y.; Lee, G. J.; Kang, T. I.; Lee, Y. K.; Cho, M.; et al. Octupolar Crystals for Nonlinear Optics: 1,3,5-Trinitro-2,4,6-Tris(Styryl)Benzene Derivatives. *Chem. Mater.* **2001**, *13* (5), 1438–1440.

(11) Cho, B. R.; Chajara, K.; Oh, H. J.; Son, K. H.; Jeon, S.-J. Synthesis and Nonlinear Optical Properties of 1,3,5-Methoxy-2,4,6-Tris(Styryl)Benzene Derivatives. *Org. Lett.* **2002**, *4* (10), 1703–1706.

(12) Zyss, J.; Dhenaut, C.; Chauvan, T.; Ledoux, I. Quadratic Nonlinear Susceptibility of Octupolar Chiral Ions. *Chem. Phys. Lett.* **1993**, *206* (1–4), 409–414.

(13) Sénéchal, K.; Maury, O.; Le Bozec, H.; Ledoux, I.; Zyss, J. Zinc(II) as a Versatile Template for the Design of Dipolar and Octupolar NLO-Phores. *J. Am. Chem. Soc.* **2002**, *124* (17), 4560–4561.

(14) Maury, O.; Le Bozec, H. Molecular Engineering of Octupolar NLO Molecules and Materials Based on Bipyridyl Metal Complexes. *Acc. Chem. Res.* **2005**, *38* (9), 691–704.

(15) Renouard, T.; Bozec, H. L.; Brasselet, S.; Ledoux, I.; Zyss, J. Tetrahedral Bipyridyl Copper(I) Complexes: A New Class of Non-Dipolar Chromophore for Nonlinear Optics. *Chem. Commun.* **1999**, *0* (10), 871–872.

(16) Lequan, M.; Branger, C.; Simon, J.; Thami, T.; Chauchard, E.; Persoons, A. First Hyperpolarizability of Organotin Compounds with Td Symmetry. *Adv. Mater.* **1994**, *6* (11), 851–853.

(17) Zyss, J. Molecular Engineering Implications of Rotational Invariance in Quadratic Nonlinear Optics: From Dipolar to Octupolar Molecules and Materials. *J. Chem. Phys.* **1993**, *98* (9), 6583–6599.

(18) Zyss, J.; Brasselet, S.; Thalladi, V. R.; Desiraju, G. R. Octupolar versus Dipolar Crystalline Structures for Nonlinear Optics: A Dual Crystal and Propagative Engineering Approach. *J. Chem. Phys.* **1998**, *109* (2), 658–669.

(19) Zyss, J.; Ledoux, I. Nonlinear Optics in Multipolar Media: Theory and Experiments. *Chem. Rev.* **1994**, *94* (1), 77–105.

(20) Li, Y.; Liu, Z.; Deng, H. Dichloridobis(Pyridine-3-Carbaldehyde-KN)Zinc(II). *Acta Crystallogr. Sect. E Struct. Rep. Online* **2007**, *63* (12), m3065–m3065.

(21) *Characterization Techniques and Tabulations for Organic Nonlinear Optical Materials*; Kuzyk, M. G., Dirk, C. W., Eds.; Optical engineering; Marcel Dekker: New York, 1998.

(22) Woińska, M.; Jayatilaka, D.; Dittrich, B.; Flaig, R.; Luger, P.; Woźniak, K.; Dominiak, P. M.; Grabowsky, S. Validation of X-Ray Wavefunction Refinement. *ChemPhysChem* **2017**, *18* (23), 3334–3351.

(23) Clays, K.; Persoons, A. Hyper-Rayleigh Scattering in Solution. *Phys. Rev. Lett.* **1991**, *66* (23), 2980–2983.

(24) Kohn, W.; Sham, L. J. Self-Consistent Equations Including Exchange and Correlation Effects. *Phys. Rev.* **1965**, *140* (4A), A1133–A1138.

(25) Coppens, P. *X-Ray Charge Densities and Chemical Bonding*; Oxford University Press: Chester, England : Oxford ; New York, 1997.

(26) Robinson, F. N. H. Nonlinear Optical Coefficients. *Bell Syst. Tech. J.* **1967**, *46* (5), 913–956.

(27) Higginbotham, A. P.; Cole, J. M.; Blood-Forsythe, M. A.; Hickstein, D. D. Identifying and Evaluating Organic Nonlinear Optical Materials via Molecular Moments. *J. Appl. Phys.* **2012**, *111* (3), 033512.

(28) Cole, J. M.; Copley, R. C. B.; McIntyre, G. J.; Howard, J. A. K.; Szablewski, M.; Cross, G. H. Charge-Density Study of the Nonlinear Optical Precursor DED-TCNQ at 20 K. *Phys. Rev. B* **2002**, *65* (12), 125107.

(29) Cole, J. M.; Goeta, A. E.; Howard, J. A. K.; McIntyre, G. J. X-Ray and Neutron Diffraction Studies of the Non-Linear Optical Compounds MBANP and MBADNP at 20 K: Charge-Density and Hydrogen-Bonding Analyses. *Acta Crystallogr. B* **2002**, *58* (4), 690–700.

(30) Cole, J. M.; D. D Hickstein. Molecular Origins of Nonlinear Optical Activity in Zinc Tris(Thiourea)Sulfate Revealed by High-Resolution x-Ray Diffraction Data and Ab Initio Calculations. *Phys. Rev. B* **2013**, *88* (18), 184105.

(31) Lin, T.-C.; Cole, J. M.; Higginbotham, A. P.; Edwards, A. J.; Piltz, R. O.; Pérez-Moreno, J.; Seo, J.-Y.; Lee, S.-C.; Clays, K.; Kwon, O.-P. Molecular Origins of the High-Performance Nonlinear Optical Susceptibility in a Phenolic Polyene Chromophore: Electron Density Distributions, Hydrogen Bonding, and Ab Initio Calculations. *J. Phys. Chem. C* **2013**, *117* (18), 9416–9430.

(32) Cole, J. M.; Lin, T.-C.; Ashcroft, C. M.; Perez-Moreno, J.; Tan, Y.; Venkatesan, P.; Higginbotham, A. P.; Pattison, P.; Edwards, A. J.; Piltz, R. O.; et al. Relating the Structure of Geminal Amido Esters to Their Molecular Hyperpolarizability. *J. Phys. Chem. C* **2016**, *120* (51), 29439–29448.

(33) Madsen, A. Ø. *SHADE* Web Server for Estimation of Hydrogen Anisotropic Displacement Parameters. *J. Appl. Crystallogr.* **2006**, *39* (5), 757–758.

(34) Blessing, R. H. An Empirical Correction for Absorption Anisotropy. *Acta Crystallogr. A* **1995**, *51* (1), 33–38.

(35) Blessing, R. H. Outlier Treatment in Data Merging. *J. Appl. Crystallogr.* **1997**, *30* (4), 421–426.

(36) Sheldrick, G. M. A Short History of *SHELX*. *Acta Crystallogr. A* **2008**, *64* (1), 112–122.

(37) Allen, F. H.; Kennard, O.; Watson, D. C.; Brammer, L.; Orpen, A. G.; Taylor, R. Tables of Bond Lengths Determined by X-Ray and Neutron Diffraction. Part 1. Bond Lengths in Organic Compounds. *J. Chem. Soc. Perkin Trans. 2* **1987**, No. 12, S1–S19.

(38) Volkov, A; Macchi, P; Farrugia, L. J; Gatti, C; Mallinson, C; Richter, T; Koritsanszky, T. *XD2006 - a Computer Program for Multipole Refinement, Topological Analysis of Charge Densities and Evaluation of Intermolecular Energies from Experimental or Theoretical Structure Factors.*; 2006.

(39) Koritsanszky, T. S.; Coppens, P. Chemical Applications of X-Ray Charge-Density Analysis. *Chem. Rev.* **2001**, *101* (6), 1583–1628.

(40) Su, Z.; Coppens, P. Nonlinear Least-Squares Fitting of Numerical Relativistic Atomic Wave Functions by a Linear Combination of Slater-Type Functions for Atoms with Z = 1–36. *Acta Crystallogr. A* **1998**, *54* (5), 646–652.

(41) Macchi, P.; Coppens, P. Relativistic Analytical Wave Functions and Scattering Factors for Neutral Atoms beyond Kr and for All Chemically Important Ions up to I−. *Acta Crystallogr. A* **2001**, *57* (6), 656–662.

(42) Hirshfeld, F. L. Can X-Ray Data Distinguish Bonding Effects from Vibrational Smearing? *Acta Crystallogr. Sect. A* **1976**, *32* (2), 239–244. https://doi.org/10.1107/S0567739476000533.

(43) Herbst-Irmer, R.; Henn, J.; Holstein, J. J.; Hübschle, C. B.; Dittrich, B.; Stern, D.; Kratzert, D.; Stalke, D. Anharmonic Motion in Experimental Charge Density Investigations. *J. Phys. Chem. A* **2013**, *117* (3), 633–641.

(44) Meindl, K.; Herbst-Irmer, R.; Henn, J. On the Effect of Neglecting Anharmonic Nuclear Motion in Charge Density Studies. *Acta Crystallogr. A* **2010**, *66* (3), 362–371.

(45) Kuhs, W. F. Generalized Atomic Displacements in Crystallographic Structure Analysis. *Acta Crystallogr. A* **1992**, *48* (2), 80–98.

(46) Jayatilaka, D.; Grimwood, D. J. Tonto: A Fortran Based Object-Oriented System for Quantum Chemistry and Crystallography. In *Computational Science — ICCS 2003*; Sloot, P. M. A., Abramson, D., Bogdanov, A. V., Gorbachev, Y. E., Dongarra, J. J., Zomaya, A. Y., Eds.; Lecture Notes in Computer Science; Springer Berlin Heidelberg, 2003; pp 142–151.

(47) Capelli, S. C.; Bürgi, H.-B.; Dittrich, B.; Grabowsky, S.; Jayatilaka, D. Hirshfeld Atom Refinement. *IUCrJ* **2014**, *1* (5), 361–379.

(48) Jayatilaka, D. Wave Function for Beryllium from X-Ray Diffraction Data. *Phys. Rev. Lett.* **1998**, *80* (4), 798–801.

(49) Gatti, C.; Macchi, P. *Modern Charge-Density Analysis*; Springer Science & Business Media, 2012.

(50) Lu, T.; Chen, F. Multiwfn: A Multifunctional Wavefunction Analyzer. *J. Comput. Chem.* **2012**, *33* (5), 580–592.

(51) Hickstein, D. D.; Cole, J. M.; Turner, M. J.; Jayatilaka, D. Modeling Electron Density Distributions from X-Ray Diffraction to Derive Optical Properties: Constrained Wavefunction versus Multipole Refinement. *J. Chem. Phys.* **2013**, *139* (6), 064108.

(52) Frisch, M. J; Trucks, G. W; Schlegel, H. B.; Scuseria, G. E; Robb, M. A; Cheeseman, J. R; Scalmani, G; Barone, V; Mennucci, B; Petersson, G. A; et al. *Gaussian09*; Gaussian, Inc.: Wallingford CT, 2009.

(53) Alcaraz, G.; Euzenat, L.; Mongin, O.; Katan, C.; Ledoux, I.; Zyss, J.; Blanchard-Desce, M.; Vaultier, M. Improved Transparency–Nonlinearity Trade-off with Boroxine-Based Octupolar Molecules. *Chem. Commun.* **2003**, *0* (22), 2766–2767.

(54) Dennington, R; Todd, K; Millam, J. *GaussView*; Semichem Inc: Shawnee Mission, KS, 2009.

(55) Hirshfeld, F. L. Bonded-Atom Fragments for Describing Molecular Charge Densities. *Theor. Chim. Acta* **1977**, *44* (2), 129–138.

(56) Bader, R. F. W. Atoms in Molecules. *Acc. Chem. Res.* **1985**, *18* (1), 9–15.

(57) Kaatz, P.; Shelton, D. P. Polarized Hyper-Rayleigh Light Scattering Measurements of Nonlinear Optical Chromophores. *J. Chem. Phys.* **1996**, *105* (10), 3918–3929.

(58) Bredas, J. L.; Meyers, F.; Pierce, B. M.; Zyss, J. On the Second-Order Polarizability of Conjugated .Pi.-Electron Molecules with Octupolar Symmetry: The Case of Triaminotrinitrobenzene. *J. Am. Chem. Soc.* **1992**, *114* (12), 4928–4929.

(59) Long, N. J. Organometallic Compounds for Nonlinear Optics—The Search for En-Light-Enment! *Angew. Chem. Int. Ed. Engl.* **1995**, *34* (1), 21–38. https://doi.org/10.1002/anie.199500211.

(60) Nalwa, H. S. Organometallic Materials for Nonlinear Optics. *Appl. Organomet. Chem.* **1991**, *5* (5), 349–377.

(61) Kim, H. M.; Cho, B. R. Second-Order Nonlinear Optical Properties of Octupolar Molecules Structure–Property Relationship. *J. Mater. Chem.* **2009**, *19* (40), 7402–7409.

(62) Tekin, S.; Yaglioglu, H. G.; Elmali, A.; Kürüm, U.; Yanık, H.; Tekdaş, D. A.; Durmuş, M.; Ahsen, V. The Effect of Aggregation on the Nonlinear Optical Absorption Performance of Indium and Gallium Phthalocyanines in a Solution and Co-Polymer Host. *Mater. Chem. Phys.* **2013**, *138* (1), 270–276.

(63) Würthner, F.; Yao, S.; Debaerdemaeker, T.; Wortmann, R. Dimerization of Merocyanine Dyes. Structural and Energetic Characterization of Dipolar Dye Aggregates and Implications for Nonlinear Optical Materials. *J. Am. Chem. Soc.* **2002**, *124* (32), 9431–9447.

(64) Cole, J. M.; Lin, T.-C.; Edwards, A. J.; Piltz, R. O.; Depotter, G.; Clays, K.; Lee, S.-C.; Kwon, O.-P. Concerted Mitigation of O···H and C(π)···H Interactions Prospects Sixfold Gain in Optical Nonlinearity of Ionic Stilbazolium Derivatives. *ACS Appl. Mater. Interfaces* **2015**, *7* (8), 4693–4698.

(65) Hales, J. M.; Kim, H.; Barlow, S.; Getmanenko, Y.; Zhang, Y.; Giesking, R.; Risko, C.; Shahin, S.; Kieu, K.; Norwood, R. A.; et al. Polymethines with Macroscopic Optical Nonlinearities Suitable for All-Optical Signal Processing; OSA, 2014; p STu3H.4.

(66) Dailey, C. A.; Burke, B. J.; Simpson, G. J. The General Failure of Kleinman Symmetry in Practical Nonlinear Optical Applications. *Chem. Phys. Lett.* **2004**, *390* (1), 8–13.

(67) Lopes, T. O.; Machado, D. F. S.; Risko, C.; Brédas, J.-L.; de Oliveira, H. C. B. Bond Ellipticity Alternation: An Accurate Descriptor of the Nonlinear Optical Properties of π-Conjugated Chromophores. *J. Phys. Chem. Lett.* **2018**, *9* (6), 1377–1383.

(68) Spek, A. L. Single-Crystal Structure Validation with the Program *PLATON*. *J. Appl. Crystallogr.* **2003**, *36* (1), 7–13.

(69) Espinosa, E.; Souhassou, M.; Lachekar, H.; Lecomte, C. Topological Analysis of the Electron Density in Hydrogen Bonds. *Acta Crystallogr. B* **1999**, *55* (4), 563–572.

(70) Espinosa, E.; Molins, E.; Lecomte, C. Hydrogen Bond Strengths Revealed by Topological Analyses of Experimentally Observed Electron Densities. *Chem. Phys. Lett.* **1998**, *285* (3), 170–173.

(71) Deng, H.-D.; Li, G.-C.; Dai, Q.-F.; Ouyang, M.; Lan, S.; Trofimov, V. A.; Lysak, T. M. Size Dependent Competition between Second Harmonic Generation and Two-Photon Luminescence Observed in Gold Nanoparticles. *Nanotechnology* **2013**, *24* (7), 075201.

(72) Ronchi, M.; Pizzotti, M.; Orbelli Biroli, A.; Righetto, S.; Ugo, R.; Mussini, P.; Cavazzini, M.; Lucenti, E.; Salsa, M.; Fantucci, P. Second-Order Nonlinear Optical (NLO) Properties of a Multichromophoric System Based on an Ensemble of Four Organic NLO Chromophores Nanoorganized on a Cyclotetrasiloxane Architecture. *J. Phys. Chem. C* **2009**, *113* (7), 2745–2760.

Chapter 7

The molecular origins of the nonlinear optical activity of octupolar dihalidebis(3-chloropyridine-κ-*N*)Zn(II) complexes revealed via the concerted use of high-resolution X-ray diffraction and *ab initio* calculations

7.1 Introduction

Having presented a rare study on the NLO activity of the complex dichlorobis(3-pyridinecarboxaldehyde-*κ*-*N*)Zn(II) in Chapter 6, we now finally turn to the final results Chapter of this thesis. Herein we continue the theme of presenting a study of organometallic complexes, and present a study on the NLO activity of two new organometallic complexes, This study is particularly unique and rare in that it presents a charge density study of organometallic complex containing the heavy element bromine, thus making it an especially challenging study

In parallel to the development of synchrotron facilities across the globe, the field of charge density analysis has begun to explore regions of chemical space over the last few decades that had previously been inaccessible[1,2], mostly due to the inability to collect high-quality, high-resolution X-ray diffraction data. One area of the chemical space to benefit from this development is organometallic complexes, especially those that contain heavy atoms[1,2]. As a consequence of these developments, the nonlinear optical (NLO) activity of organometallic complexes, and their associated structure-property relationships are beginning to be explored[3]. Conversely, structure-property relationships regarding NLO activity have been studied extensively for organic NLO compounds[4]. With this knowledge base in hand, the concerted and rationalized design of new organic compounds for bespoke NLO applications grows commensurately[5–7] and shows no sign of abating as the demand for ever greater optical transmission speeds continues to increase.

At the same time, the majority of research into the NLO activity of organometallics to date has concentrated on dipolar complexes, which consist of a central D-π-A backbone architecture, through which intramolecular charge transfer (ICT) proceeds to produce an NLO response. This response can then be further modulated by additional ligands in an effort to fine-tune the overall NLO response of the complex. More intricate organometallic complexes however, such as those classified as octupolar, have in general been less often the subject of studies[8–11], while organic octupolar materials have fared slightly better in this regard[12–14] Octupolar compounds have been postulated by Zyss and Ledoux in the 1990s, and their huge potential as NLO-active materials was subsequently demonstrated[15,16]. Compounds with octupolar symmetry can be subdivided into two classes: (i) compounds with dipolar and octupolar contributions, and (ii) compounds that contain exclusively octupolar contributions. One advantage of the latter is that these compounds do not suffer from the dipole-induced propensity to dimerize. This characteristic feature of pure octupolar molecules arises from their molecular symmetry and thus, imposes restrictions on the allowed point groups of octupolar materials, i.e., D_{3h}, D_3, T_d or D_{2d}.

Herein, we present a study into the molecular origins of the NLO properties of the two octupolar organometallic complexes (3-chloropyridine-κ-*N*)$_2$ZnX$_2$ (**46**: X = Cl; **47**: X = Br) that possess pseudo-D_2

point-group symmetry (Fig 7.1). The structure-property relationships of **46** and **47**, and their ensuing NLO responses were examined in terms of their ICT characteristics, crystal field effects, and molecular hyperpolarizability (β), via a concerted use of X-ray diffraction and *ab initio* calculations. Given three independent methods for the determination of β coefficients were used in this study due to the typically large errors (10-30%)[17] associated with β enummerations: i) multipolar modeling of electron densities around each atom using high-resolution X-ray diffraction data, ii) optical measurements using hyper-Rayleigh scattering (HRS), and iii) density functional theory (DFT) calculations in the gas phase; HRS and DFT methods for the determination of β are now standard practice and well documented. Enumeration of β via method i) was determined empirically from the multipolar modeling (MM) of the molecular electron densities obtained from high-resolution X-ray diffraction data. This employs an empirical relation between the quadrupolar and octupolar multipolar moments of a specific atom and β, which is based on the theory of Robinson[18].

As well as providing solid-state measures of β, multipolar refinements permit a full topological analysis of the bonding and ICT throughout the molecule, which enables a qualitative and quantitative examination of the molecular bonding as well as a determination of the electronic ICT characteristics that underline the molecular origins of its NLO responses. So far, this empirical method has remained relatively unexplored, most likely due to the circumstance that a sufficiently accurate correlation model between atomic multipolar moments and β has only been developed recently[19]. Higginbotham *et. al.* have successfully applied this model to three distinct types of NLO materials: two organic chromophores that exist in zwitterionic[20] or neutral forms[21] and a organometallic compound[3]. Since then, other studies have used this method to successfully determine the molecular hyperpolarizability of a range of organic NLO[6,7] and organometallic (*cf.* Chapter 6) materials. Nevertheless, more case studies are needed to continue to probe the limitations of this new empirical approach.

This chapter begins by assessing the molecular structure of **46** and **47** by conventional single-crystal X-ray diffraction, with a particular focus placed on identifying the π-conjugated ICT pathways. Subsequently, the linear and non-linear optical properties of **46** and **47** are assessed using a variety of materials characterization techniques such as UV-vis spectroscopy, charge-density analyses, DFT calculations, and hyper-Rayleigh scattering measurements. The enumeration of β via methods i-iii) is undertaken, and reveals the NLO responses of **46** and **47** in multiple phase states i.e. solid state, liquid, and gas phase, from which the impact of crystal field effects and intermolecular interactions on the NLO processes of **46** and **47** are determined. Furthermore, discussions that assess the level of consistency of β determined by these independent methods are also presented, providing assurance against the well-known accuracy issues associated with β evaluations. With this assurance in hand, the study concludes with an assessment of the potential of **46** and **47**, with a view to bespoke NLO device applications.

7.2 Experimental and Computational Methods

7.2.1 Synthesis and crystallization of 46 and 47

Compound **46** and **47** was obtained via the previously reported synthetic route outlined in Scheme 7.1

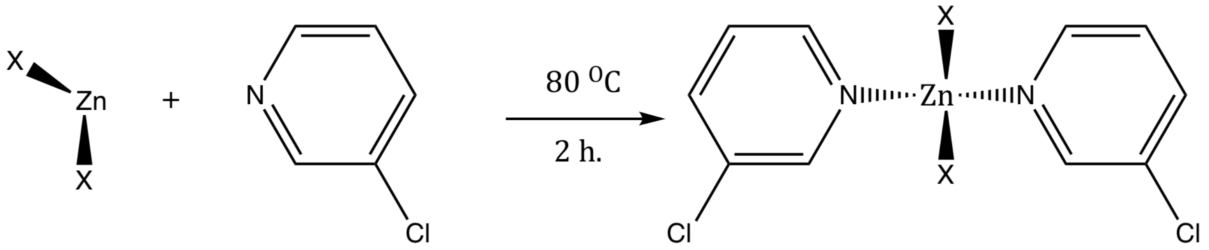

1: X = Cl
2: X = Br

Scheme 7.1. Synthesis of **46** and **47**.

High-quality single crystals of **46** and **47** were obtained by slow evaporation of the solvent from ethanolic solutions of **46** and **47**.

7.2.2 High-resolution single-crystal synchrotron X-ray diffraction data

A crystal with dimension of (0.01 x 0.04 x 0.04 mm) **46**, (0.01 x 0.04 x 0.04 mm) **47** was mounted on a 5 µm diameter fiber tip with paratone oil and cooled down to 100 K with an Oxford Cryojet. A single crystal X-ray diffraction experiments were conducted at ChemMatCARS (sector 15) of the Advanced Photon Source (APS), Argonne National Laboratory (ANL). The beam energy was 30 keV (0.41328 Å) [standard wavelength] and the beam size at the sample was 0.1 x 0.1 mm^2. Data were collected using a Bruker D8 fixed-chi diffractometer equipped with an APEX II CCD detector used to capture a series of data frames over multiple φ scans of crystal orientations, which were collected in increments of 0.3° and an exposure time of 0.6 s, ω offset: 20°, and κ offset: 45°, sample-to-detector distance: 130 mm. Data collection and integration were performed with APEX II suite software. The reduction of data was conducted with SAINT v.8.32B program included in the APEX suite. SORTAV[22,23] was used for the implementation of empirical absorption corrections, data sorting, and merging as per §2.2.2 and §2.2.3. A data resolution of up to sinθ/λ = 1.00 Å^{-1} was achieved for both complexes.

7.2.3 Independent atom model structural refinement

A conventional IAM crystal structure refinement was undertaken by full matrix least square on F^2 using SHELXL[24] (*cf* §2.2.5) and confirmed the space P$\bar{1}$ [a= 7.2756 Å; b= 7.8089 Å; c= 13.1119 Å; α= 94.97^{o}; β= 90.65^{o}; γ= 117.72^{o}; Z= 2] (**46**) and, P$\bar{1}$ [a= 7.3816 Å; b= 7.9864 Å; c= 13.4129 Å; α= 83.41^{o}; β= 89.03^{o}; γ= 63.51^{o}; Z=2] (**47**).This afforded R1 (I >2s(I)) and wR2 values of 0.0281 and 0.0712 (**46**) and, 0.0281 and 0.0712 (**47**) for all observed reflections.

7.2.4 Multipolar structural refinement

Initial atomic coordinates and ADPs for all non-hydrogen atoms were obtained from the IAM refinement of the X-ray data (*cf.* §II, B) and used as the starting point for the multipolar refinement. Initial atomic coordinates for hydrogen atoms were set according to neutron-determined reference X-H bond lengths[25], while their ADPs were determined using SHADE2.1[26] and remained fixed during all subsequent refinements. The multipolar refinement was carried out using the XD2006 program suite[27]. Residual electron-density maps of the final charge-density model of **46-47** (*cf.* SI) were essentially featureless at the 0.1 $eÅ^{-3}$ level, with the exception of the areas around the ZnX_2 moieties in **46** (X = Cl) and **47** (X = Br). Here, raw electron density of up to 0.371 $eÅ^{-3}$, 0.838-1.152 $eÅ^{-3}$, and 0.673 $eÅ^{-3}$ were measured around the Cl (**46**), Br (**47**), and Zn atoms, respectively. The unresolved residual electron density around the Zn atom in **46-47** is hardly surprising, given the well-documented problems associated with modeling the charge density of Zn. Indeed, charge-density modeling of transition metals still presents a major challenge for charge-density studies[1,2]. Zn is particularly challenging due to its $3d^{10}4s^2$ electron configuration, wherein the *4s* orbital induces a highly spherical, diffuse valence-electron density. Consequently, effective partitioning of electrons into multipolar terms can be challenging, and the inability to achieve featureless residual electron density around Zn atoms is well documented. For example, the zinc tris(thiourea)sulfate (ZTS) compound studied by Hickstein & Cole shows similar values of residual electron density around the Zn atom (0.5 $eÅ^{-3}$)[3].

Owing to the highly diffuse nature of the *4s* orbital of the Zn atom, methods such as the Su-Coppens-Macchi databank (SCM) have been devised in an attempt to circumvent this obstacle.[28,29] The SCM databank treats the *4s* shell as part of the core electron density and thus, the valence electrons are taken from the aspherical *3d* shell instead of the spherical *4s* shell. To minimize possible erroneous artifacts around the Zn atom, the multipolar refinement of the Zn atom was carried out especially carefully. The final model was also assessed via the Hirshfeld rigid bond test[30], which calculates the difference of the mean-square displacement amplitudes (DMSDAs) in the directions of the bonds. Maximum DMSDA values of 0.0007 $Å^2$ [C(3)-C(4)] for **46** and -0.0053 $Å^2$ [Zn-N(1)] for **47** were observed.

Shashlik-type residual density was observed around the Zn atom (**46-47**) and the two Br atoms (**47**), which is indicative of potential anharmonic libration. Consequently, the refinement of Gram-Charlier anharmonic thermal parameters up to the 4th order for the Zn and Br atoms was undertaken for **47**. Gram-Charlier refinement of the Zn atom in **46** was not undertaken as Kuhs' criterion[31] was not satisfied in this case.

Least-squares refinement statistics on F for the final multipolar model yielded R = 0.0217 (**46**) and 0.0227 (**47**), R_w = 0.0251 (**46**) and 0.0217 (**47**) ($w = 1/\sigma^2$), GOF = 1.34 (**46**) and 4.35 (**47**), as well as a data-to-parameter ratio of 27.7 (**46**) and 19.9 (**47**).

7.2.5 *Ab Initio* density functional theory calculations

Electrostatic moments and (hyper)polarizability values of **46** and **47** were calculated by DFT using Gaussian09[32] as per §2.10. X-ray structures of **46** and **47** were used for the initial geometry. Initially, IAM-derived atomic position parameters were used to perform a ground-state geometry optimization that comprised finding the minimum on the potential energy surface of the ground state. All default settings for Gaussian09 were maintained. DFT calculations were carried out at the B3YLP/6-31+G(2d,p) (**46**) and B3YLP/6-311+G(2d,p) (**47**) level of theory as informed by the literature[33]. Subsequently, the components of the (hyper)polarizability tensor of the structure were calculated at the same level of theory.

7.3 Results and Discussion

7.3.1 Molecular architecture of 46 and 47

The molecular architectures of heteroleptic complexes **46** and **47** were determined via conventional X-ray diffraction data. The complexes formally exhibits C_m point-group symmetry but has very high octupolar characteristics owing to its pseudo-octupolar point group, D_{2d}, configuration. Formal D_{2d} symmetry is prevented due to *meta*-positioning of the chlorines, which precludes 2-fold rotational symmetry (Fig 7.1); *para*-positioning would afford pure octupolar symmetry, which would mean all dipolar NLO contributions would cancel to zero. However, is a sum of dipolar and octupolar contributions, and dipolar contributions tend to be stronger than octupolar NLO effects; so the pseudo-octupolar geometric nature of **46** and **47** actually stands to provide a greater overall SHG output than its purely octupolar counterpart, since it gains significantly in dipolar contribution at the modest expense of octupolar contributions.

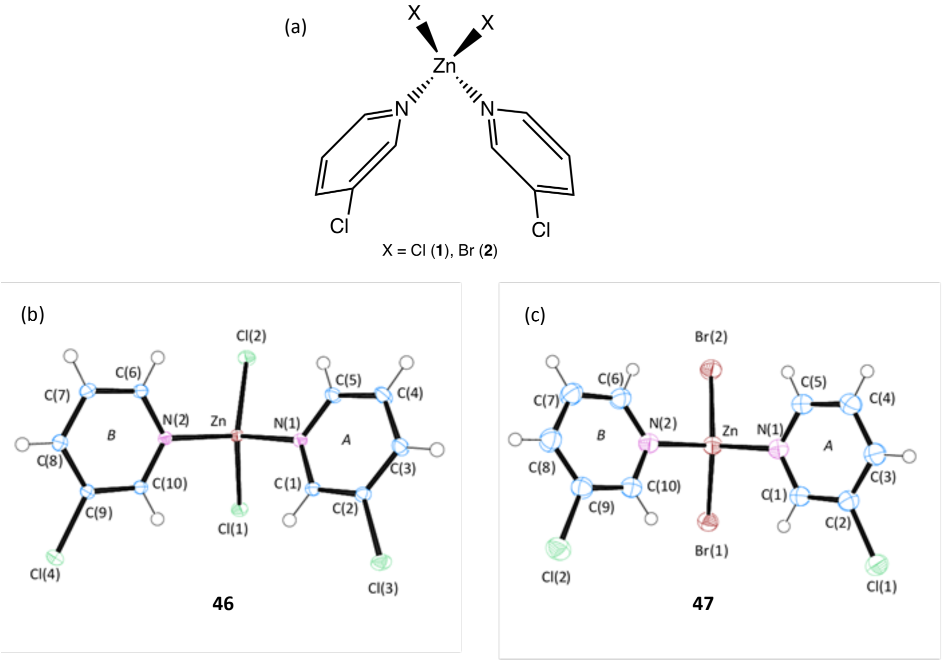

Figure 7.1. Chemical structures for **46** and **47** and schematic illustration of their octupolar pseudo-D_{2d} symmetry (a). Molecular structures of **46** (b) and **47** (c) with ADP ellipsoids set to 50% probability.

Both complexes consist of a central Zn^{2+} Lewis acid, bound to two Cl^- (**46**), Br^- (**47**) Lewis bases, which participate in donor-acceptor interaction to form a ZnX_2-type unit. This unit is in turn coordinated to two 3-chloropyridine ligands, to form a tetrahedral geometry, with identical ligands persisting in a *cis-* configuration (Fig. 7.1). Bond lengths of the Zn-X and Zn-N bonds, along with the dihedral angles between the functionalized pyridine ligands and the ZnX_2 moieties are provided in Table 7.1 and Table 7.2 respectively, and confirm the tetrahedral nature of these two coordination complexes which, lends well to their octupolar nature. It is interesting to note that in both **46** and **47**, the two oppositely positioned pyridyl rings do not possess the same dihedral angles relative to the ZnX_2 moieties and thus as such, the structure of these two complexes is distorted.

Table 7.1. Bond lengths (Å) between the Zn-X and Zn-N bonds of **46** (X = Cl) and **47** (X = Br).

Compound	Bond	Bond length (Å)
1	Zn-Cl(1) / Zn-Cl(2)	**2.2151(1) / 2.2168(1)**
	Zn-N(1) / Zn-N(2)	**2.0787(1) / 2.0487(1)**
2	Zn-Br(1) / Zn-Br(2)	2.3685(1) / 2.3542(1)
	Zn-N(1) / Zn-N(2)	2.0666(1) / 2.0948(1)

Table 7.2. Dihedral angles (°) between the functionalized pyridyl ligands and the ZnX_2 moiety in **1** (X = Cl) and **2** (X = Br).

Compound	Pyridyl ring (*cf*. Fig 1)	Bond	Dihedral angle (^{O})
1	*A*	C(1) – N(1) – Zn – Cl(1)	38.43(1)
		C(5) – N(1) – Zn – Cl(2)	4.25(1)
	B	C(6) – N(2) – Zn – Cl(2)	22.04(1)
		C(10) – N(2) – Zn – Cl(1)	20.01(1)
2	*A*	C(1) – N(1) – Zn – Br(1)	19.09(1)
		C(5) – N(1) – Zn – Br(2)	25.13(1)
	B	C(6) – N(2) – Zn – Br(2)	6.64(1)
		C(10) – N(2) – Zn – Br(1)	38.13(1)

The linear and non-linear optical properties of **46** and **47** are now presented in order to assess the extent of their dipolar and octupolar contributions, whereupon the results will need to be set against intra-molecular and inter-molecular charge transfer considerations.

7.3.2 Optical properties

7.3.2.1 Linear optical properties

The solution-based UV/vis absorption spectra for **46** and **47** were recorded. Complexes **46** and **47** exhibit peaks outside the visible range of the spectrum, which indicates a good nonlinearity-transparency tradeoff for both complexes in this region. A common λ^{peak} was found to occur at 267 nm; it is assumed this peak arises from the 3-chloropyridne ligands, given that it is present in both complexes. Peaks pertaining to the ZnX_2 do not occur on the spectrum. They are believed to occur below the cutoff wavelength of the spectrometer used (200 nm).

Complementary DFT calculations at B3LYP/6-31+G(2d,p) (**46**) and B3LYP/6-311+G(2d,p) (**47**) level of theory enabled the associated optical transitions in **46** and **47** to be related to perturbations in its electronic structure. Molecular orbitals (MOs) were generated via the program GaussView[40] and are defined by the frontier orbitals, i.e., the highest occupied (HOMO) and lowest unoccupied molecular orbitals (LUMO). Other important MOs, such as the LUMO+1, were also generated (Fig. 7.2). An analysis of the HOMO, LUMO and LUMO+1 allows gauging the degree and direction of shifts in the molecular electron density of a compound upon excitation, which provides a rudimentary assessment of the ICT-induced polarization and NLO abilities of a given complex.

A comparison of frontier orbitals of **46** and **47** reveal a number of characteristics that imply that they will both preform well as NLO chromophores (Fig. 7.2). Firstly, both complexes exhibit a stark shift in their electron density away from the Zn(dihalide) moiety, into the two 3-chloropyridine ligands, via the Zn atom that connects the electron donors with the electron acceptors via a π-conjugated network of bonds. In both **46** and **47**, a noticeable shift is observed in the electron density upon transition from the LUMO to the LUMO+1, indicating that a two-level model is sufficient for the determination of the NLO response of both complexes. Most strikingly, however, are the lower energies of the HOMO, LUMO and LUMO+1 of **46** compared to those of **47**, while the energy gap between the HOMO and LUMO transition in **47** is also smaller than in **46** (ΔE = 0.515 eV). This indicates that stimulated optical transitions in **47** not only occur at a lower energy threshold, but the input energy required to facilitate this optical transition is also smaller. Consequently, it is assumed that the activation of NLO activity in **47** will require a lower input energy than that in **46.** Furthermore, small quantities of electron density on the chlorine in the *meta*- position of the pyridine group in the LUMO and LUMO+1 of **47** implies that the -*I* effect of these chlorines may be stronger than in **46**, thus indicating that the extent of ICT from the Zn(dibromide) unit to the 3-chloropyridine ligands is slightly greater than the analogous ICT from the Zn(dichloride) unit in **46**.

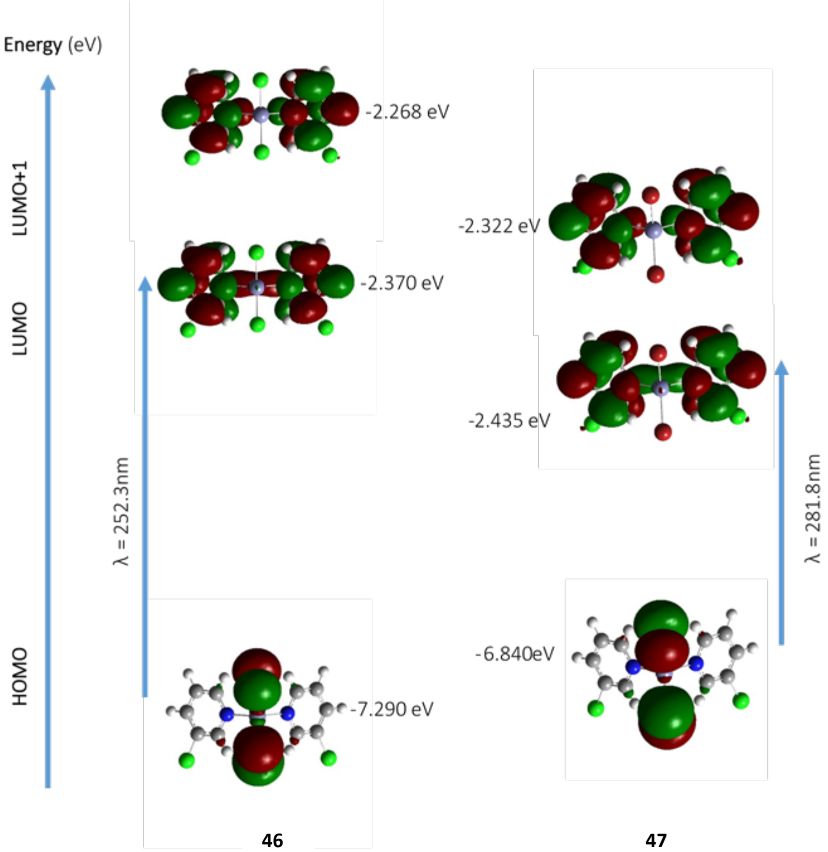

Figure. 7.2. *Ab-initio*-derived frontier orbitals (HOMO, LUMO, and LUMO+1) of **46** and **47**.

In terms the intramolecular charge transfer (ICT) pathway of **46** and **47,** it is envisaged, given that the metal center of these two structures is both co-ordinatively saturated, and is in a low oxidation state that, the ICT pathway of both **46** and **47**, consists of a ZnX_2 electron donating moiety, and two 3-chloropyridine electron acceptors, mediated via π-conjugated bonds forming a D-π-A architecture from which NLO activity may ensue. Given the difference in dihedral angle between the two pyridyl units with respect to ZnX_2 unit in **46** and **47**, an analysis of intra- and intermolecular interactions was undertaken to assess the presence of potential interactions which may account for the differences in angle between these two pyridyl ligands.

7.3.2.2 Non-linear optical properties

The NLO properties of **46** and **47** were assessed by determination of their first molecular hyperpolarizability (β) in three different phases, i.e., in the gas phase, as well as in the liquid and solid state, which acts as a molecular measure of the second-harmonic generation (SHG) properties of a given material (Table 7.3). The evaluation and comparison of these independently obtained β values is prudent, given the large errors (~10-30 %) that are typically associated with the enumerations of β coefficients[17]. Additionally, the use of several different methods allows the assessment of the NLO responses of **46** and **47** in different phases, helping to reveal salient crystal-field effects, which may become important for future device applications.

Table 7.3. Molecular hyperpolarizability (β) values for the solid state, solution, and gas phase obtained from a charge-density analysis, hyper-Rayleigh scattering measurements, and DFT calculations.

Method	β / 10^{-30} esu	
	46	**47**
Charge density/Stockholder	7.071	N/A
Charge density/QTAIM	7.217	11.722
HRS*	2.000 ± 0.500	3.500 ± 1.000
DFT#	3.148	3.325

*The error in β derived from HRS were predicated based on the 20% statistical error on the evaluation of β for the HRS reference sample (Crystal Violet).

#*Ab initio* DFT calculations were carried out at the B3LYP/6-31+G(2d,p) (**46**) and B3LYP/6-311+G(2d,p) (**47**) level of theory.

Gas-phase calculations of β and solution-phase HRS experimental determinations of β are well established; see for example[3,14,34–37] for more comprehensive reviews. However, the rarity by which solid-state β values are derived from X-ray diffraction data renders it worth detailing herein. The determination of β for **46** and **47** in its single-crystal form, the multipolar moments of each atom in the charge-density distribution are used, together with the empirical calculation for β (*cf.* Eq. 1.10):[19] For this study, two distinct solid-state β values were determined for **46**, while in the case of **47** only one determination was possible due to software limitations. See §1.2.2.4 for more on the partition methods and the empirical calculation of β.

7.3.2.2.1 Comparison of β values determined from the four independent methods

Table 7.3 presents the hyperpolarizability values of **46** and **47**, which allows gauging the impact of the intermolecular interactions and crystal-field effects on the NLO responses of these two complexes. Firstly, the similarity of the two β enumerations for **46** in the solid-state, using the two distinct partitioning methods, Stockholder and QTAIM, is reassuring. It suggests desirable levels of internal consistency for the multipolar models, and equal suitability of these two atomic partitioning methods for the evaluation of β from charge-density data. Alas, the same assessment for internal consistency cannot be achieved for **47**, as the Stockholder partitioning method is not available in XD2006 for compounds with Br atoms.

A cross-comparison of the β values for **46** and **47** in the three different phase states reveals that a stark change in the NLO activity of the two complexes occurs in the solid state, while their NLO responses are similar in the liquid and gas phase; albeit that the **46** > **47** trend holds in all phases. This suggests that the crystal-field effects of the two complexes, which will be felt predominantly in the solid state, are prominent and have a tangible, beneficial impact on the NLO responses of the two compounds. These crystal-field effects are by definition not present in the liquid or gas phase, and thus the respective β values decrease. Noticeably, the percentage decrease in β between the liquid phase (HRS value) and the solid state (QTAIM) for both complexes is similar (**46**: ~ 72 % decrease; **47**: ~ 70 % decrease). This implies that the interactions and crystal-field effects for **46** and **47** should most likely be comparable.

Strikingly, the β values for the liquid (HRS) and gas phase (DFT) for both **46** and **47** are comparable, indicating that the interactions that occur in the solid state, and which augment the hyperpolarizability of the complexes, are absent in the liquid and gas phase. Although this is anticipated for the gas phase, the close agreement between the HRS and DFT enumerations further infers that interactions are minimal in the liquid phase, too, which implies no molecular aggregation effects occur in solution. The reluctance of molecules of **46** and **47** to aggregate in solution arises probably from the tetrahedral coordination geometry of the central Zn ion, which hampers stacking via e.g. π-π stacking interactions. Yet, such stacking and aggregation effects are critical for the evaluation of a compound's potential for real-world device applications. A regularly observed feature in NLO chromophores, aggregation can facilitate dimerization or clustering of the molecules in solution, commonly induced by the presence of high molecular dipole moments in the molecules, which arise from an electronic 'push-pull' effect. These aggregation effects can in turn affect the electronic structure of the chromophore, and thus its molecular polarization, which is integral to its NLO responses. Accordingly, aggregation phenomena can be advantageous[7,21,38–43] or deleterious to the NLO capabilities of the material[44–46]. In instances where molecular aggregation produces deleterious effects, NLO device processing problems are commonly encountered[47] e.g., centrosymmetry issues that can arise during thin-film processing, which can deter NLO effects.

Comparing **46** and **47** reveals a consistently enhanced β value for **47** compared to **46** across all three phases. Changing from $ZnCl_2$ to $ZnBr_2$, i.e., from Cl^- to the less electronegative Br^- most likely results in an improved electron donation as a result of the resonance donation of the Br atom being greater than that of the Cl. As a consequence, the Br atoms provide more electron density to participate in ICT phenomena across the complex. This in turn increases the polarization across the D-π-A framework of the complex, and thus increases its NLO response. Studies of the impact of differing halogen substitution in dipolar organometallic NLO-active materials have been reported previously, and similarly reveal the improved hyperpolarizability that ensues as Cl is switched for Br[48].

A deeper evaluation of the hyperpolarizabilities of **46** and **47** via the individual coefficients of the hyperpolarizability 3 x 3 rank tensor enables an analysis of the NLO responses of the complexes in terms of their specific molecular structures. The coefficients for both complexes were determined in the solid-state and gas phases and are shown in Fig. 7.2.

From the graph of the hyperpolarizability coefficients of **46** and **47** in Fig. 7.2 significant components can be seen to persist in the direction of all three principle axes, *xxx*, *yyy*, and *zzz*. Furthermore, this trend is evident both for solid-state and gas-phase structures. The origins of this 3D nature of the hyperpolarizability tensor of **46** and **47** becomes clear when assessed in conjunction with information regarding the arrangement and position of the complexes in their unit cells. Fig. 7.3 shows the molecular structures of **46** and **47** along their *y*-axis in their unit cells, and highlights the need for a 3D ICT effect to occur given the specific positioning and molecular geometry of these complexes, as previously discussed in §7.3.1.

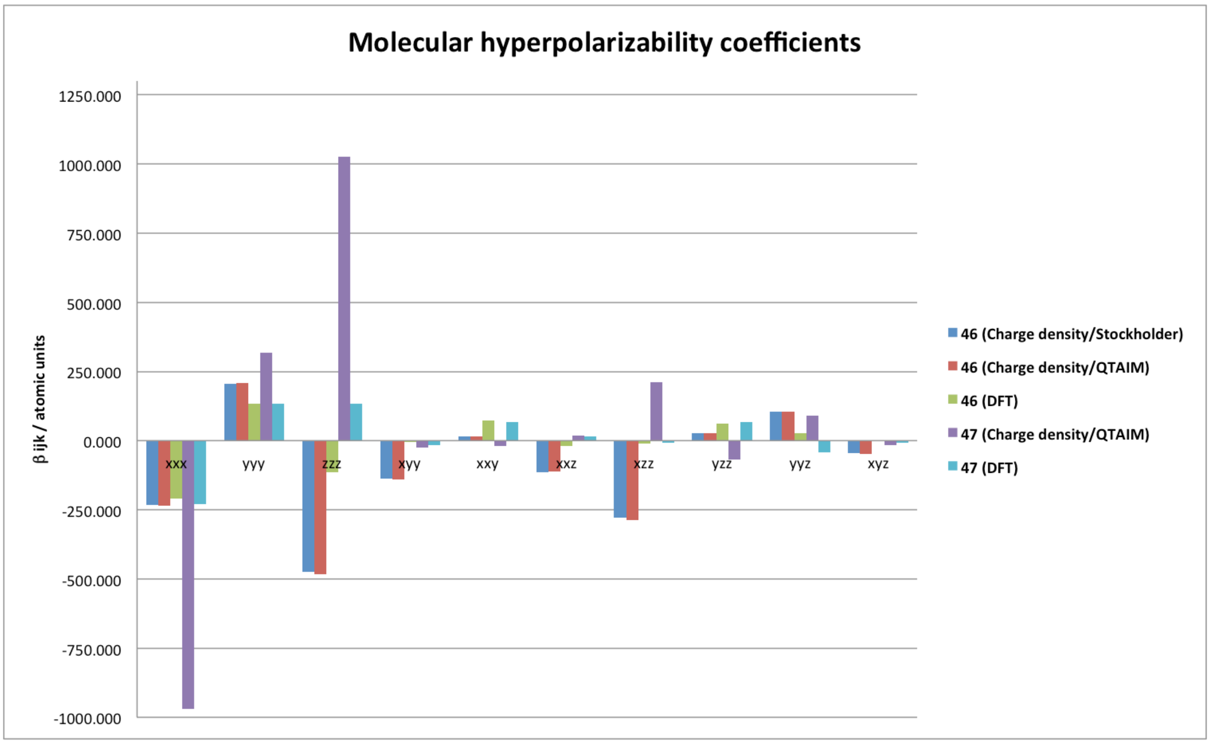

Figure 7.2. Molecular hyperpolarizability coefficients for **1** and **2** in the solid state, solution, and the gas phase.

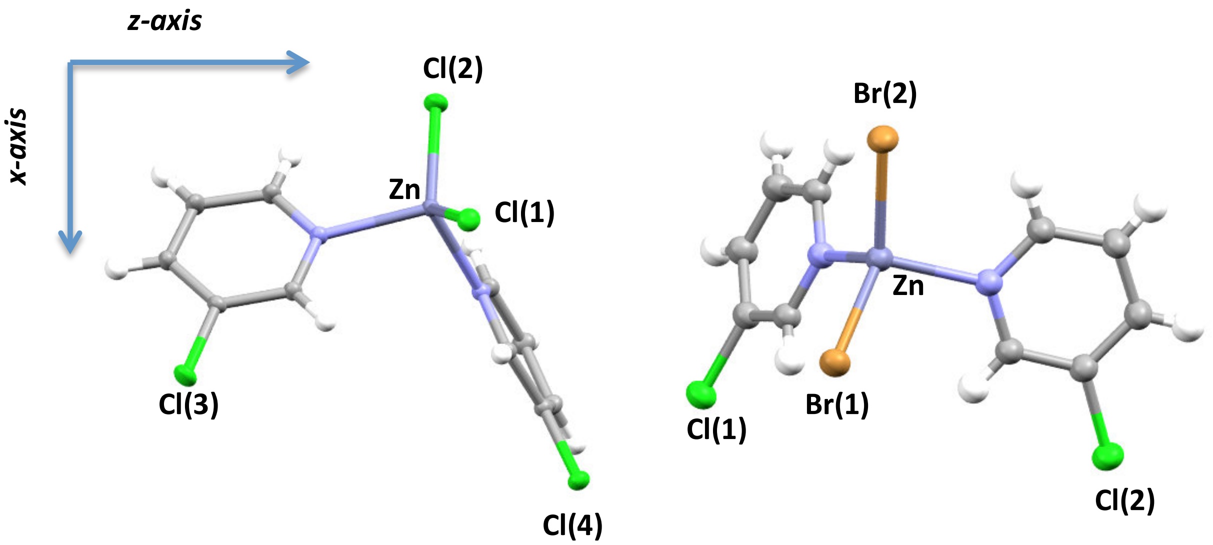

Figure 7.3. Complexes **46** (left) and **47** (right) viewed along the y-axis in their unit cell. Only selected atoms have been labelled.

It is clear from a comparison of Fig. 7.3 with the components shown in Fig 7.2 that the hyperpolarizability of complexes **46** and **47** exhibit a 3-D nature given that an ICT of electronic charge density from the Zn(dihalide) electron donor to the *meta*-positioned electron withdrawing chlorides on the functionalized pyridyl rings requires movements of charge density along the three principle crystallographic axes. ICT of charge density from the Cl^- (**46**) and Br^- (**47**) to the Zn ion center precipitates along the x- and y-axes. The 'pull' effect exerted by the *meta*-positioned chlorides on both **46** and **47** then draw electron density towards them resulting in a transfer of electronic charge through the z- and x-axes, with the pyridyl rings of **46** and **47** siting predominately in the xy- or xz-plane. Meanwhile, twists in the Zn-N bonds in both complexes, that likely arise due to crystal packing effects, mean that one of the pyridyl rings in each complex does not lie perfectly in the xy- and xz-planes but, also encroaches upon the yz-plane (*cf.* §7.3.1; **46**: Ring *A*, **47**: Ring *B*). The 3D origins of the NLO activity of the two complexes are thus apparent.

7.3.3 Structural interpretation of NLO effects from intra-molecular and inter-molecular charge-transfer considerations

7.3.3.1 Establishing structure-property relationships from intra-molecular charge transfer

Given that the 3-chloropyridines ligands of **46** and **47** lie mainly in either the xz or xy planes (*cf.* Fig 7.3) it is understandable that the majority of the ICT within these two complexes persists in these two planes as seen in Fig 7.2 by the predominant x and z-based hyperpolarizability components. These ligands, which are bonded to the Zn ion through the N atom of the pyridyl ring, provide pi-media, through which a metal-to-ligand charge transfer (MLCT) interaction can occur, setting up a charge transfer pathway from the donating ZnX_2 moiety into the 3-chloropyridine ligand. The ICT is further facilitated by a 'pull' effect exerted by the *meta*-substituted chlorine atoms, which act to withdraw electron density into the pyridyl rings from the ZnX_2 moiety. Fig 7.2 also reveals that there are small, but non-zero, hyperpolarizability components in the associated with the y directions, with the dominant being yyy, and xyy. These, given the orientation of the complexes (Fig 7.3), likely arises due to charge transfer between the out-of-plane halide ligands and the Zn ion center. We now use multipolar models to assess the nature of the four Zn ion-to-ligand bonds to further determine the main ICT pathways within the two complexes.

To further elucidate the nature of the ICT in these two complexes the character of the Zn-X and Zn-N bonding in **46** and **47** were assessed through the use of electron deformation density (Fig 7.4 and 7.5, (a-b)) and Laplacian maps (Fig 7.4 and 7.5, (c-d)). Electron-deformation maps depict the difference between the multipolar and the independent (spherical) atom model, and consequently, reveal both the bonding and charge polarization characteristics of **46** across the molecule. Meanwhile, Laplacian maps display the second derivative of the electron density ($\nabla^2\rho$), where $\nabla\rho(r) = 0$. In the context of a charge-density study then, the Laplacian map represents the degree of local electronic-charge depletion or concentration around an atom

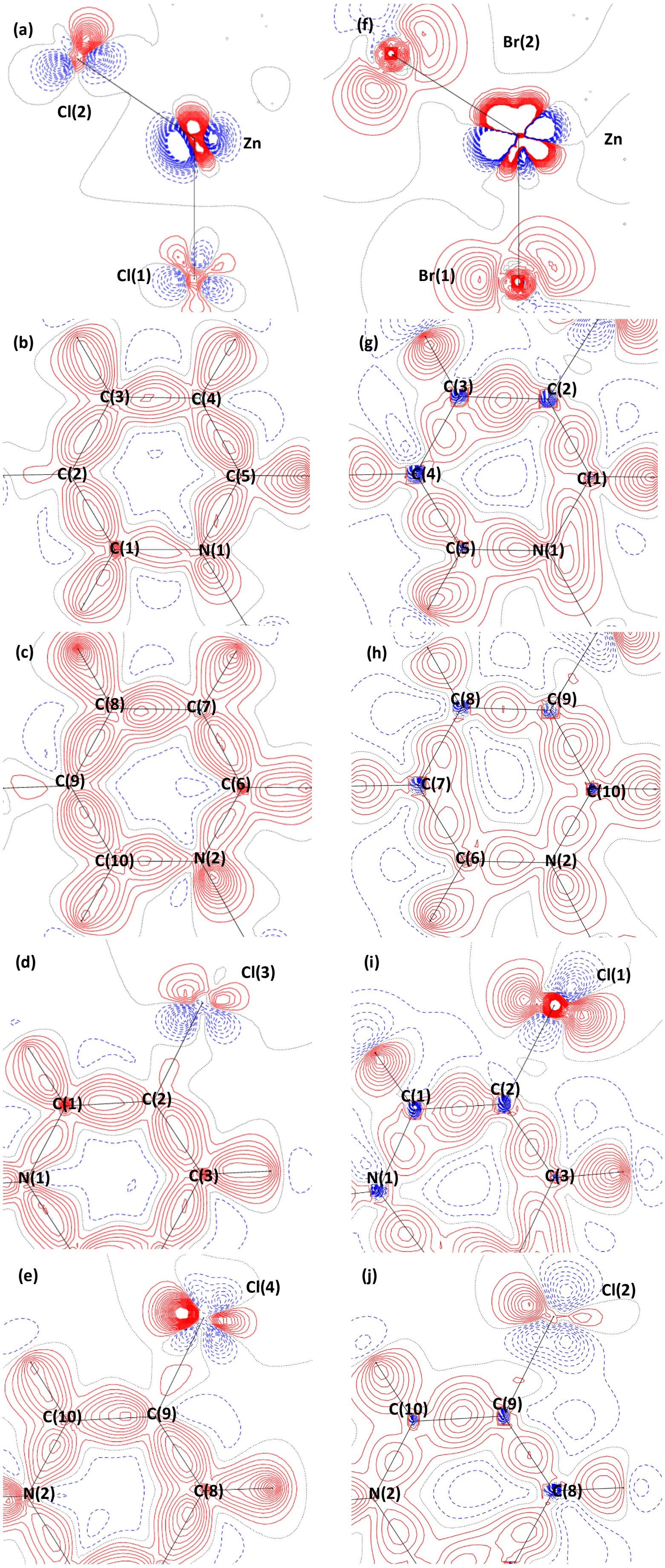

Figure 7.4. Multipolar-model-generated deformation-electron-density maps of **46** (a-e) and **47** (f-j), split into individual molecular segments. Red lines represent areas with positive signum, while blue lines represent areas with negative signum, and black lines areas of zero. Contour levels are shown at 0.1 eÅ^{-3} linear scaling

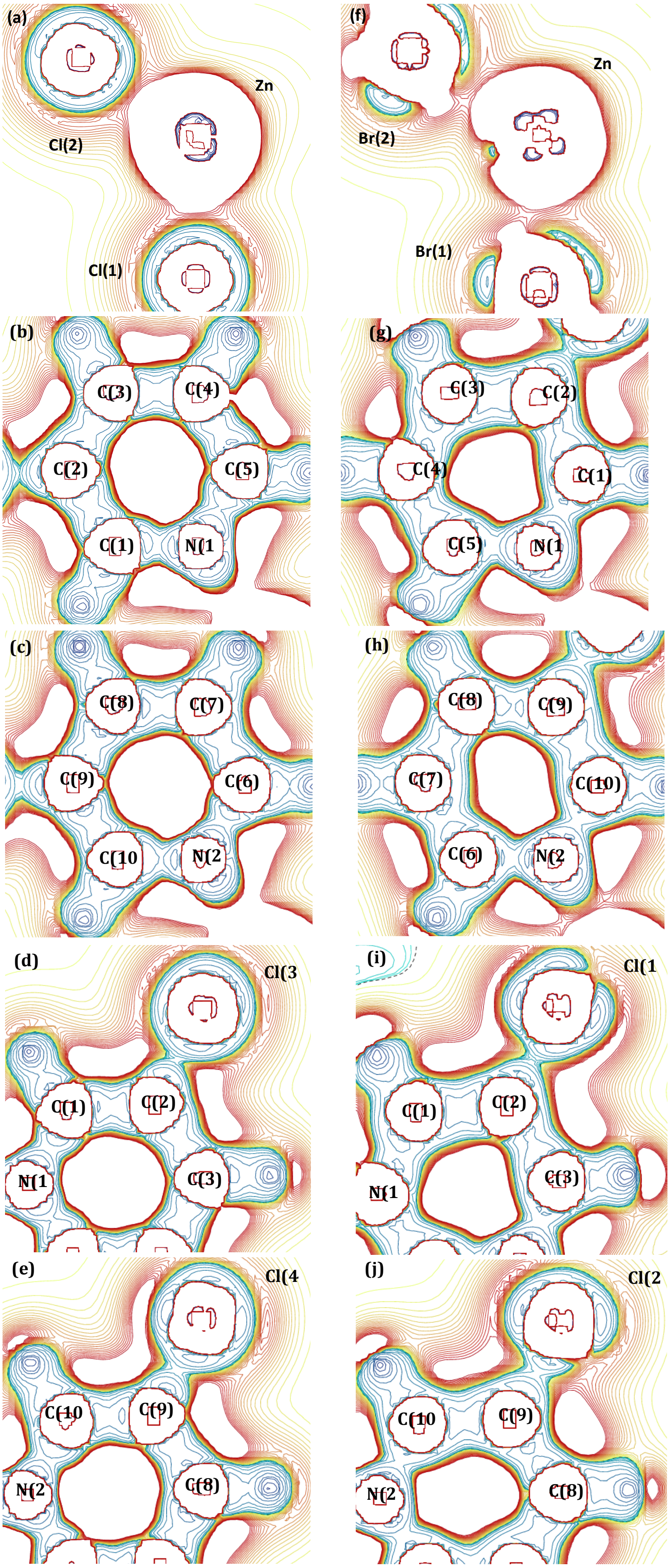

Figure 7.5. Multipolar-model-generated Laplacian maps for **46** (a-e) and **47** (f-j), split into individual molecular segments. The color scale in the Laplacian maps refers to local concentrations (blue) and depletions (red) of electronic charge. Contour levels are shown at 0.1 e$Å^{-5}$ gradient scaling.

7.3.3.2 Characterizing the nature of Zn-halide bonding

Turning first the Zn-halide bonding in **46** and **47** the distinct absence of electron density along the bond pathways between the halides and the Zn ion (Fig 7.4, a-b), coupled with the electron density concentrations between the atoms observed in the Laplacian maps (Fig 7.5, a-b) are indicative of a highly dative bonding between the atoms, as expected. It is also expected that these bonds will be highly polarized, and thus a topological analysis was undertaken to provide a quantitative characterization of the bonds in accordance with the classification scheme of Bader (*cf.* Table 2.3 in §2.6.2.2.)[49].

Calculated energy descriptors of the Zn-halide bonds using Bader's Quantum Theory of Atoms In Molecules (QTAIM) are provided in Table 7.4 and reveal that all the Zn-halide bonds are ostensibly polar shared; the Zn-Br(2) bond is very close to meeting the polar shared criteria. It is also instructive at this stage to compare the Zn-halide bonds of **46** against those of **47.** Upon first inspection the Zn-Cl and Zn-Br bonds of **46** and **47** they present as somewhat similar, with similar values of ρ(r) and $\nabla^2\rho$(r). However, comparing the bond path between the Cl and Br atoms, and the bond critical point (BCP) of their respective bond with the Zn ion is revealing. While in **46**, the polarization of the Zn-Cl polar shared bonds appear directed toward the Zn ion ($d_1 < d_2$), in the case of **47** this is reversed with the bond polarized toward the Br atoms ($d_1 > d_2$). This makes sense given the greater polarizability of Br compared to Cl.

Table 7.4. Summary of the bond-type classifications of bonds according to energy density descriptors. ρ(r) is the electron density, $\nabla^2\rho$(r) the Laplacian (second-derivate) of the electron density. The energy descriptors G(r)/ρ(r) and H(r) are the kinetic energy density per electron and total energy respectively. R_{ij} is the length (Å) of the bond path between the atoms; d_1 and d_2 represent the distance (Å) between the first and second atoms specified in the bond column and the critical point, respectively

Bond	ρ [eÅ^{-3}]	$\nabla^2\rho$ [eÅ^{-5}]	R_{ij} [Å]	d_1 [Å]	d_2 [Å]	G(r)/ρ(r) [a.u.]	H(r) [a.u.]	Bond type *cf.* Table IV
				46				
Zn-Cl(1)	0.478	6.004	2.2150	1.0219	1.1930	1.078	-0.014	Polar shared
Zn-Cl(2)	0.472	5.858	2.2169	1.0243	1.1926	1.067	-0.014	Polar shared
Zn-N(1)	0.485	6.789	2.0800	1.0076	1.0724	1.150	-0.012	Polar shared
Zn-N(2)	0.565	8.389	2.0504	0.9803	1.0702	1.242	-0.017	Polar shared
Cl(3)-C(2)	1.297	-0.980	1.7198	0.9462	0.7736	0.921	-0.203	Covalent
Cl(4)-C(9)	1.334	-2.977	1.7223	0.9546	0.7677	0.870	-0.164	Covalent
				47				
Zn-Br(1)	0.428	5.367	2.3713	1.2948	1.0765	1.042	-0.010	Polar shared
Zn-Br(2)	0.445	4.949	2.3460	1.2909	1.0511	1.078	-0.014	Polar shared
Zn-N(1)	0.564	6.760	2.0771	1.0011	1.0759	1.108	-0.022	Polar shared
Zn-N(2)	0.596	6.644	2.0902	0.9942	1.0960	1.090	-0.027	Polar shared
Cl(1)-C(2)	1.191	-1.222	1.7276	0.9553	0.7723	0.856	-0.164	Covalent
Cl(2)-C(9)	1.255	-2.690	1.7387	0.9237	0.8149	0.835	-0.183	Covalent

7.3.3.3 Characterizing the nature of Zn-N bonding

Next we look at the Zn-N bonds of **46** and **47** and, by extension, the 3-chloropyridine ligands in both complexes. Visual inspection of the maps of these bonds (Fig 7.4 and 7.5, b-c, g-h) reveal that the Zn-N bonds in both complexes are once again, highly dative, and polarized. As with the Zn-halide bonds, QTAIM energy descriptors were derived to verify the classification of these bonds as polar shared, and are given in Table V; here all energy descriptors are consistent with polar shared bonding.

In terms of the 3-chloropyridine ligands in **46** and **47** as a whole, the electron deformation density maps are suggestive of the formation of a highly delocalized, pi-conjugated network of bonds, through which ICT could ensue, with all four pyridyl rings experiencing polarization of its electron density toward either the Zn ion or *meta*-positioned chlorine atoms. Noticeably, the small amount of electron deformation density (red contours) between the pyridyl rings and the chlorines suggests a polarized covalent bond persists between them and the pyridyl rings. The extent of this polarization was assessed via the energy descriptors method as in previous sections (Table 7.5) and confirms their covalent polar-shared nature. At the same time, the bond ellipticity values of all the bonds in the 3-chloropyridine unit were determined to assess the pi-conjugation of the pyridyl rings. The bond ellipticity, ε is a direct measure of the level of asphericity in a bond cross at its bond critical point (BCP), and thus can be used to identify σ- and π-bond character. Where $\varepsilon = 0$, σ bonding ensues, while double bonds, which will present significant levels of asphericity in the bond cross section, will have large ε values signifying π-bonding. Through evaluation of these parameters for each bond (Table 7.5) π-bonding throughout the pyridyl rings and

Table 7.5. Parameters of all non-hydrogen (3, −1) bond critical points of the pyridyl ring; ρ (eÅ^{-3}): electron density; $\nabla^2\rho$: Laplacian; ε: bond ellipticity.

Bond	ρ [eÅ^{-3}]	∇²ρ [eÅ^{-5}]	ε
	46		
C2-Cl(3)	1.297	-0.980	0.10
C9-Cl(4)	1.334	-2.977	0.09
N(1)-C(1)	2.183	-19.507	0.22
C(1)-C(2)	2.163	-19.546	0.23
C(2)-C(3)	2.179	-19.791	0.17
C(3)-C(4)	2.111	-19.982	0.26
C(4)-C(5)	2.167	-20.035	0.34
C(5)-N(1)	2.378	-23.470	0.12
N(2)-C(6)	2.225	-19.254	0.16
C(6)-C(7)	2.209	-19.600	0.09
C(7)-C(8)	2.174	-20.624	0.20
C(8)-C(9)	2.252	-21.339	0.24
C(9)-C(10)	2.223	-20.859	0.18
C(10)-N(2)	2.377	-19.326	0.11
	47		
C2-Cl(3) / Cl(1)	1.191	-1.222	0.13
C9-Cl(4) / Cl(2)	1.255	-2.690	0.13
N(1)-C(1)	2.172	-18.759	0.09
C(1)-C(2)	1.975	-17.171	0.29
C(2)-C(3)	2.232	-21.550	0.13
C(3)-C(4)	1.848	-15.838	0.23
C(4)-C(5)	2.020	-18.244	0.24
C(5)-N(1)	2.213	-16.935	0.11
N(2)-C(6)	2.198	-17.577	0.09
C(6)-C(7)	1.959	-14.614	0.13
C(7)-C(8)	1.940	-19.117	0.22
C(8)-C(9)	1.900	-15.631	0.53
C(9)-C(10)	2.133	-19.314	0.10
C(10)-N(2)	2.190	-16.508	0.10

between the pyridyl and the chlorines was confirmed, with the BCPs directed toward the XXX atoms. Given the -I/+M nature of the chlorine substituents, in conjunction with the polarized nature of the $C_{pyridyyl}$-Cl covalent bonds, the chlorine substitution is expected to exert an electron density withdrawing effect, 'pulling' electron density into the pyridyl rings from the ZnX_2 moieties of **46** and **47**.

7.3.3.4 Overarching structural classification of the intra-molecular charge transfer in 46 and 47

From the two previous sections (7.3.3.2 and 7.3.3.3) the similarities and differences between the overarching ICT pathways of **46** and **47** become apparent. Both **46** and **47** exhibit metal-to-ligand charge transfer (MLCT) from the ZnX_2 moiety to the 3-chloropyridine ligands, whose chlorine substituents appear to provide an electron 'pull' effect, resulting in ICT into the pyridyl rings. Consequently, two D-pi-A frameworks are set up either side of the ZnX_2 moiety from which the NLO activity of these two complexes likely emanates. However, **46** and **47** will experience differing NLO responses, due to the change of the halide bonded to the Zn ion center from Cl (**46**) to Br (**47**). As the halide on the ZnX_2 moiety is changed from Cl to the more polarizable Br atom the ICT from the halide is expected to increase, resulting in an overall increase in the complex's NLO response; this is confirmed by the increase in the x-based and y-based components of the molecular hyperpolarizability of **47**, which corresponds to the planes within which the Br atoms reside.

6.3.4 Establishing structure-property relationships from inter-molecular charge transfer

An analysis of the intra- and intermolecular short contacts in **46** and **47** was undertaken PLATON[50] and Mercury[51] revealed the absence of classic intramolecular hydrogen bonds. However, intermolecular hydrogen interactions were observed in **46** and **47** between the Zn-bound halides and some H atoms of the pyridyl rings of the closest neighboring molecule in the unit cell (Fig. 7.6(a)). In **46** bond lengths and angles of 2.937(1) Å [Cl(1) --- H(6)] , 163(5) °,[Zn-Cl(1) --- H(6)] , 2.916(12) Å [Cl(4) --- H(8)] , 104.0(5) ° [Zn-Cl(4) --- H(8)], 2.932(2) Å [Cl(3) --- H(4)], 152(5) °,[Zn-Cl(3) --- H(4)], and 2.910(4) Å [Cl(3) --- H(5)], 121.0(5) ° [Zn-Cl(3) --- H(5)]. Meanwhile in **47**, two similar intermolecular hydrogen interactions persist (Fig. 7.6(b)), with lengths and angles of 3.036(10) Å [Br(2) --- H(1)], 149(1) ° [Zn-Br(2) --- H(1)] and 3.029(10) Å [Br(1) --- H(4)], 137(1) ° [Zn-Br(1) --- H(4)]. Given the greater electronegativity of Cl compared to Br, it is expected that the Cl interactions of **46** will have a greater impact than the Br interactions in **47,** as witnessed by the greater difference in the dihedral angles between the pyridyl rings and the ZnX_2 of **46**. These halide interactions likely contribute toward the crystal packing of **46** and **47** in the solid-state.

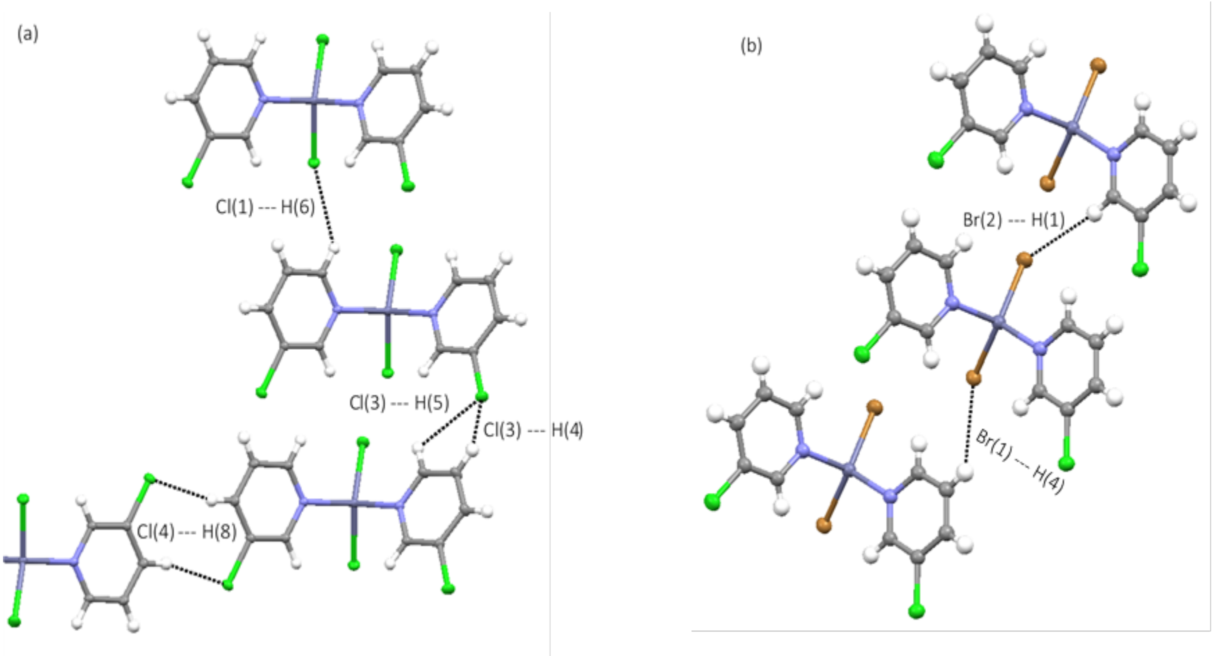

46 **47**

Figure 7.6. Crystal packing structure of **46** (a) and **47** (b) with intermolecular Cl···H (a) and Br···H (b) interactions.

Topological analyses of the intermolecular hydrogen interactions in **46** and **47** was undertaken, including the determination of the λ_3 eigenvalue of the Hessian matrix, which have been identified by Espinosa *et al.*[52,53] as a marker for the presence of true hydrogen interactions. The topological parameters of these three hydrogen interactions are listed in Table 7.6.

Table 7.6. Parameters of intermolecular hydrogen interactions. ρ (eÅ^{-3}) is the electron density; $\nabla^2\rho$ is the Laplacian; λ_3 is the third component of the Hessian matrix; R_{ij} is the length (Å) of the bond path between the atoms.

Bond	ρ [eÅ^{-3}]	$\nabla^2\rho$ [eÅ^{-5}]	R_{ij} [Å]	λ_3
		46		
Cl(1) ··· H’(6)	0.048	0.638	2.8717	0.90
Cl(3) ··· H’(4)	0.052	0.640	2.9040	0.92
Cl(3) ··· H’(5)	0.045	0.620	2.9239	0.87
Cl(4) ··· H’(4)	0.055	0.757	2.7686	1.08
		47		
Br(1) ··· H’(4)	0.027	0.288	3.0011	0.43
Br(2) ··· H’(1)	0.043	0.297	2.9985	0.61

The multipolar model-derived intermolecular hydrogen interactions (Table 7.6) all exhibit positive λ_3 indicative of the presence of real hydrogen interactions, with the strongest (shortest) interactions being present in **46**. These intermolecular hydrogen interactions, which are responsible for the crystallization arrangements of both **46** and **47**, result in the formation of a sheet-like stacking arrangement in the solid-state phase, which will amplify their NLO responses in this phase state.

7.4 Conclusion

The NLO activity of two cognate octupolar organometallic complexes, bis(3-chloropyridine-κ-*N*)ZnX_2 (**46**: X = Cl; **47**: X = Br), have been reported through characterization of their structural and optical properties via a range of charge density analyses, hyper-Rayleigh scattering, and *ab initio* calculations. The molecular architectures and intramolecular charge transfer aspects of the electronic structure of **46** and **47** were identified and related to its optical properties, especially their molecular hyperpolarizability. Given the notorious difficulties in obtaining reliable values for the molecular hyperpolarizability, evaluation using four independent methods, in one of three states of matter was undertaken using density functional theory (gas-phase), hyper-Rayleigh scattering (solution-phase), and charge-density analyses (solid-state) respectively. In the case of the charge-density analyses, two different β values are presented were their extraction is possible. These β values arise because there are several types of atomic partitioning methods that are available to determine the multipolar moments, which are needed for the empirical calculation of β. Herein, β values were enumerated from multipolar moments derived from Stockholder (**46** only) and QTAIM (**46** and **47**) partitioning methods. A comparison of the results revealed that these two atomic partitioning methods produced equally reliable β values in the case of **46**, emphasizing the internal consistency of the multipolar model. Topological analyses of the molecular charge densities of **46** and **47** via multipolar modeling provided a detailed description of the chemical bonding across the complexes in the solid-state. This in turn, enabled the determination of the origins and nature of the ICT in **46** and **47,** with the marked NLO phenomena of the complex being identified as a consequence of its tetrahedral octupolar design. The results of this chapter expose the real-world potential of **46** and **47** as new organometallic NLO-active materials that could be incorporated into new NLO applications and devices. Furthermore, although by no means exhaustive, this study also suggests that the investigation of other similar organometallic complexes based upon **46** and **47** are likely worth investigating further. Simple changes such as the alteration of the dihalide to a diiodide moiety could see an even greater NLO response, while the re-configuration of the functionalized pyridyl ligands of these complexes into a *trans*-configuration will likewise impact their overall NLO activity.

7.5 References

(1) Coppens, P. Charge-Density Analysis at the Turn of the Century. *Acta Crystallogr. A* **1998**, *54* (6), 779–788.

(2) Coppens, P.; Iversen, B.; Larsen, F. K. The Use of Synchrotron Radiation in X-Ray Charge Density Analysis of Coordination Complexes. *Coord. Chem. Rev.* **2005**, *249* (1–2), 179–195.

(3) Cole, J. M.; D. D Hickstein. Molecular Origins of Nonlinear Optical Activity in Zinc Tris(Thiourea)Sulfate Revealed by High-Resolution x-Ray Diffraction Data and Ab Initio Calculations. *Phys. Rev. B* **2013**, *88* (18), 184105.

(4) Cole, J. M. Organic Materials for Second-Harmonic Generation: Advances in Relating Structure to Function. *Philos. Trans. R. Soc. Lond. Ser. Math. Phys. Eng. Sci.* **2003**, *361* (1813), 2751–2770.

(5) Cole, J. M.; Waddell, P. G.; Wilson, C. C.; Howard, J. A. K. Molecular and Supramolecular Origins of Optical Nonlinearity in N-Methylurea. *J. Phys. Chem. C* **2013**, *117* (48), 25669–25676.

(6) Cole, J. M.; Lin, T.-C.; Ashcroft, C. M.; Perez-Moreno, J.; Tan, Y.; Venkatesan, P.; Higginbotham, A. P.; Pattison, P.; Edwards, A. J.; Piltz, R. O.; et al. Relating the Structure of Geminal Amido Esters to Their Molecular Hyperpolarizability. *J. Phys. Chem. C* **2016**, *120* (51), 29439–29448..

(7) Lin, T.-C.; Cole, J. M.; Higginbotham, A. P.; Edwards, A. J.; Piltz, R. O.; Pérez-Moreno, J.; Seo, J.-Y.; Lee, S.-C.; Clays, K.; Kwon, O.-P. Molecular Origins of the High-Performance Nonlinear Optical Susceptibility in a Phenolic Polyene Chromophore: Electron Density Distributions, Hydrogen Bonding, and Ab Initio Calculations. *J. Phys. Chem. C* **2013**, *117* (18), 9416–9430.

(8) Sénéchal, K.; Toupet, L.; Ledoux, I.; Zyss, J.; Bozec, H. L.; Maury, O. First Lanthanide Dipolar Complexes for Second-Order Nonlinear Optics. *Chem. Commun.* **2004**, *0* (19), 2180–2181.

(9) Zyss, J.; Dhenaut, C.; Chauvan, T.; Ledoux, I. Quadratic Nonlinear Susceptibility of Octupolar Chiral Ions. *Chem. Phys. Lett.* **1993**, *206* (1–4), 409–414.

(10) Maury, O.; Le Bozec, H. Molecular Engineering of Octupolar NLO Molecules and Materials Based on Bipyridyl Metal Complexes. *Acc. Chem. Res.* **2005**, *38* (9), 691–704.

(11) Lequan, M.; Branger, C.; Simon, J.; Thami, T.; Chauchard, E.; Persoons, A. First Hyperpolarizability of Organotin Compounds with Td Symmetry. *Adv. Mater.* **1994**, *6* (11), 851–853.

(12) Stadler, S.; Feiner, F.; Bräuchle, Ch.; Brandl, S.; Gompper, R. Determination of the First Hyperpolarizability of Four Octupolar Molecules and Their Dipolar Subunits via Hyper-Rayleigh Scattering in Solution. *Chem. Phys. Lett.* **1995**, *245* (2–3), 292–296.

(13) Zyss, J.; Van, T. C.; Dhenaut, C.; Ledoux, I. Harmonic Rayleigh Scattering from Nonlinear Octupolar Molecular Media: The Case of Crystal Violet. *Chem. Phys.* **1993**, *177* (1), 281–296.

(14) Kim, H. M.; Cho, B. R. Second-Order Nonlinear Optical Properties of Octupolar Molecules Structure–Property Relationship. *J. Mater. Chem.* **2009**, *19* (40), 7402–7409.

(15) Zyss, J.; Ledoux, I. Nonlinear Optics in Multipolar Media: Theory and Experiments. *Chem. Rev.* **1994**, *94* (1), 77–105.

(16) Zyss, J. Molecular Engineering Implications of Rotational Invariance in Quadratic Nonlinear Optics: From Dipolar to Octupolar Molecules and Materials. *J. Chem. Phys.* **1993**, *98* (9), 6583–6599.

(17) *Characterization Techniques and Tabulations for Organic Nonlinear Optical Materials*; Kuzyk, M. G., Dirk, C. W., Eds.; Optical engineering; Marcel Dekker: New York, 1998.

(18) Robinson, F. N. H. Nonlinear Optical Coefficients. *Bell Syst. Tech. J.* **1967**, *46* (5), 913–956.

(19) Higginbotham, A. P.; Cole, J. M.; Blood-Forsythe, M. A.; Hickstein, D. D. Identifying and Evaluating Organic Nonlinear Optical Materials via Molecular Moments. *J. Appl. Phys.* **2012**, *111* (3), 033512.

(20) Cole, J. M.; Copley, R. C. B.; McIntyre, G. J.; Howard, J. A. K.; Szablewski, M.; Cross, G. H. Charge-Density Study of the Nonlinear Optical Precursor DED-TCNQ at 20 K. *Phys. Rev. B* **2002**, *65* (12), 125107.

(21) Cole, J. M.; Goeta, A. E.; Howard, J. A. K.; McIntyre, G. J. X-Ray and Neutron Diffraction Studies of the Non-Linear Optical Compounds MBANP and MBADNP at 20 K: Charge-Density and Hydrogen-Bonding Analyses. *Acta Crystallogr. B* **2002**, *58* (4), 690–700.

(22) Blessing, R. H. An Empirical Correction for Absorption Anisotropy. *Acta Crystallogr. A* **1995**, *51* (1), 33–38.

(23) Blessing, R. H. Outlier Treatment in Data Merging. *J. Appl. Crystallogr.* **1997**, *30* (4), 421–426.

(24) Sheldrick, G. M. A Short History of *SHELX*. *Acta Crystallogr. A* **2008**, *64* (1), 112–122.

(25) Allen, F. H.; Kennard, O.; Watson, D. C.; Brammer, L.; Orpen, A. G.; Taylor, R. Tables of Bond Lengths Determined by X-Ray and Neutron Diffraction. Part 1. Bond Lengths in Organic Compounds. *J. Chem. Soc. Perkin Trans. 2* **1987**, No. 12, S1–S19.

(26) Madsen, A. Ø. *SHADE* Web Server for Estimation of Hydrogen Anisotropic Displacement Parameters. *J. Appl. Crystallogr.* **2006**, *39* (5), 757–758.

(27) Volkov, A; Macchi, P; Farrugia, L. J; Gatti, C; Mallinson, C; Richter, T; Koritsanszky, T. *XD2006 - a Computer Program for Multipole Refinement, Topological Analysis of Charge Densities and Evaluation of Intermolecular Energies from Experimental or Theoretical Structure Factors.*; 2006.

(28) Macchi, P.; Coppens, P. Relativistic Analytical Wave Functions and Scattering Factors for Neutral Atoms beyond Kr and for All Chemically Important Ions up to I−. *Acta Crystallogr. A* **2001**, *57* (6), 656–662.

(29) Su, Z.; Coppens, P. Nonlinear Least-Squares Fitting of Numerical Relativistic Atomic Wave Functions by a Linear Combination of Slater-Type Functions for Atoms with Z = 1–36. *Acta Crystallogr. A* **1998**, *54* (5), 646–652.

(30) Hirshfeld, F. L. Can X-Ray Data Distinguish Bonding Effects from Vibrational Smearing? *Acta Crystallogr. Sect. A* **1976**, *32* (2), 239–244.

(31) Kuhs, W. F. Generalized Atomic Displacements in Crystallographic Structure Analysis. *Acta Crystallogr. A* **1992**, *48* (2), 80–98.

(32) Frisch, M. J; Trucks, G. W; Schlegel, H. B.; Scuseria, G. E; Robb, M. A; Cheeseman, J. R; Scalmani, G; Barone, V; Mennucci, B; Petersson, G. A; et al. *Gaussian09*; Gaussian, Inc.: Wallingford CT, 2009.

(33) Ivanova, B.; Spiteller, M. AgI and ZnII Complexes with Possible Application as NLO Materials – Crystal Structures and Properties. *Polyhedron* **2011**, *30* (2), 241–245.

(34) Verbiest, T.; Clays, K.; Samyn, C.; Wolff, J.; Reinhoudt, D.; Persoons, A. Investigations of the Hyperpolarizability in Organic Molecules from Dipolar to Octopolar Systems. *J. Am. Chem. Soc.* **1994**, *116* (20), 9320–9323.

(35) Bredas, J. L.; Meyers, F.; Pierce, B. M.; Zyss, J. On the Second-Order Polarizability of Conjugated .Pi.-Electron Molecules with Octupolar Symmetry: The Case of Triaminotrinitrobenzene. *J. Am. Chem. Soc.* **1992**, *114* (12), 4928–4929.

(36) Long, N. J. Organometallic Compounds for Nonlinear Optics—The Search for En-Light-Enment! *Angew. Chem. Int. Ed. Engl.* **1995**, *34* (1), 21–38. https://doi.org/10.1002/anie.199500211.

(37) Nalwa, H. S. Organometallic Materials for Nonlinear Optics. *Appl. Organomet. Chem.* **1991**, *5* (5), 349–377.

(38) Coradin, T.; Clément, R.; Lacroix, P. G.; Nakatani, K. From Intercalation to Aggregation: Nonlinear Optical Properties of Stilbazolium Chromophores−MPS3 Layered Hybrid Materials. *Chem. Mater.* **1996**, *8* (8), 2153–2158.

(39) Datta, A.; Pati, S. K. Dipole Orientation Effects on Nonlinear Optical Properties of Organic Molecular Aggregates. *J. Chem. Phys.* **2003**, *118* (18), 8420–8427.

(40) Duan, Y.; Ju, C.; Yang, G.; Fron, E.; Coutino-Gonzalez, E.; Semin, S.; Fan, C.; Balok, R. S.; Cremers, J.; Tinnemans, P.; et al. Aggregation Induced Enhancement of Linear and Nonlinear Optical Emission from a Hexaphenylene Derivative. *Adv. Funct. Mater.* **2016**.

(41) Kwon, O.-P.; Kwon, S.-J.; Jazbinsek, M.; Seo, J.-Y.; Kim, J.-T.; Seo, J.-I.; Lee, Y. S.; Yun, H.; Günter, P. Phenolic Polyene Crystals with Tailored Physical Properties and Very Large Nonlinear Optical Response. *Chem. Mater.* **2011**, *23* (2), 239–246.

(42) Cole, J. M.; Howard, J. A. K.; McIntyre, G. J. Influence of Hydrogen Bonding on the Second Harmonic Generation Effect: Neutron Diffraction Study of 4-Nitro-4′-Methylbenzylidene Aniline. *Acta Crystallogr. B* **2001**, *57* (3), 410–414.

(43) Thalladi, V. R.; Boese, R.; Brasselet, S.; Ledoux, I.; Zyss, J.; Jetti, R. K. R.; Desiraju, G. R. Steering Non-Centrosymmetry into the Third Dimension: Crystal Engineering of an Octupolar Nonlinear Optical Crystal. *Chem. Commun.* **1999**, No. 17, 1639–1640.

(44) Tekin, S.; Yaglioglu, H. G.; Elmali, A.; Kürüm, U.; Yanık, H.; Tekdaş, D. A.; Durmuş, M.; Ahsen, V. The Effect of Aggregation on the Nonlinear Optical Absorption Performance of Indium and Gallium Phthalocyanines in a Solution and Co-Polymer Host. *Mater. Chem. Phys.* **2013**, *138* (1), 270–276.

(45) Würthner, F.; Yao, S.; Debaerdemaeker, T.; Wortmann, R. Dimerization of Merocyanine Dyes. Structural and Energetic Characterization of Dipolar Dye Aggregates and Implications for Nonlinear Optical Materials. *J. Am. Chem. Soc.* **2002**, *124* (32), 9431–9447.

(46) Cole, J. M.; Lin, T.-C.; Edwards, A. J.; Piltz, R. O.; Depotter, G.; Clays, K.; Lee, S.-C.; Kwon, O.-P. Concerted Mitigation of O···H and C(π)···H Interactions Prospects Sixfold Gain in Optical Nonlinearity of Ionic Stilbazolium Derivatives. *ACS Appl. Mater. Interfaces* **2015**, *7* (8), 4693–4698.

(47) Hales, J. M.; Kim, H.; Barlow, S.; Getmanenko, Y.; Zhang, Y.; Giesking, R.; Risko, C.; Shahin, S.; Kieu, K.; Norwood, R. A.; et al. Polymethines with Macroscopic Optical Nonlinearities Suitable for All-Optical Signal Processing; OSA, 2014; p STu3H.4.

(48) De, S.; Mitra, R.; Samuelson, A. G.; Das, P. K. First Hyperpolarizability of Ru-Half-Sandwich Complexes: The Effect of Halogen Atom Substitution on the Ancillary Ligand. *J. Organomet. Chem.* **2015**, *785* (Supplement C), 72–76. https://doi.org/10.1016/j.jorganchem.2015.01.013.

(49) Bader, R. F. W. Atoms in Molecules. *Acc. Chem. Res.* **1985**, *18* (1), 9–15.

(50) Spek, A. L. Single-Crystal Structure Validation with the Program *PLATON*. *J. Appl. Crystallogr.* **2003**, *36* (1), 7–13.

(51) Macrae, C. F.; Edgington, P. R.; McCabe, P.; Pidcock, E.; Shields, G. P.; Taylor, R.; Towler, M.; van de Streek, J. *Mercury* : Visualization and Analysis of Crystal Structures. *J. Appl. Crystallogr.* **2006**, *39* (3), 453–457.

(52) Espinosa, E.; Molins, E.; Lecomte, C. Hydrogen Bond Strengths Revealed by Topological Analyses of Experimentally Observed Electron Densities. *Chem. Phys. Lett.* **1998**, *285* (3), 170–173.

(53) Espinosa, E.; Souhassou, M.; Lachekar, H.; Lecomte, C. Topological Analysis of the Electron Density in Hydrogen Bonds. *Acta Crystallogr. B* **1999**, *55* (4), 563–572.

Chapter 8

Conclusions and Outlook

8.1 Conclusions

This thesis began by providing a review of the state-of-the-art in NLO chromophores to-date and assesses the relative merits and pitfalls of the different types of NLO-active materials that are typically investigated for optoelectronic applications, from the typical organic dipolar D-π-A chromophore, through to octupolar organometallics; the latter being a subsection of NLO materials science that still experiences a dearth in knowledge and understanding. This is especially seen by the distinct lack of a framework of well-defined structure-function relationships from which the NLO activity of octupolar and organometallics can be rationalised. Indeed, during the compilation of the review, the distinct absence of a framework of structure-function relationships for orgnometallic NLO materials was starkly apparent and lead to the classification scheme of Cole & Ashcroft[1]. It is hoped that with this classification in hand, the multidisciplinary field of NLO-active materials development and discovery will be better equipped to cultivate a well-defined panoply of structure-function relationships for dipolar organometallic complexes, helping to bring them into line with dipolar organic chromophores, whose advance has benefited from a structured and rationalised approach. Further work however needs to be undertaken to extend this classification scheme incorporate octupolar materials.

With this review in hand, the results of this thesis presented studies on a range of NLO-active materials spanning both the dipolar and octupolar regimes. Both organic and organometallic materials are presented, with the organic studies including examples of both neutral and ionic chromophores. Each of these studies provided an extensive assessment of each material's first molecular hyperpolarizability, β using a multi-phase approach, allowing an assessment of their NLO responses in the gas- solution and solid-state phase, and consequently, an opportunity to assess the impact of intermolecular and crystal-field interactions on NLO activity in each molecular species.

The main results of this thesis began in Chapters 3 and 4, and presented two cognate series of organic chromophores. In Chapter 3 a multi-phase enumeration of β for five EPAM chromophores revealed crystal-field effects and intermolecular interactions have minimal impact on their NLO responses, while the chemical composition of an arene substitution and its position can provide an easy, but effective method for the tweaking of NLO responses in materials. This study also provided further confirmation of the relative strength and robustness of the multipolar modelling method for undertaking charge density analysis, and their use in the evaluation of β, even in the absence of 'ideal' data-quality. Meanwhile, Chapter 4, which presented three benzylamino-based chromophores, gauged the applicability of the relatively new X-ray wave-function refinement (XWR) method as a complementary tool in charge density studies. Importantly, the success of this study, which was able to yield good topological analyses of these three chromophores, revealing the unique charge density 'leakage' effect crucial to the rationalization of their ICT phenomena, was despite the absence of high-resolution X-ray data. This is thus testament to the strength of this new method, and suggests that the XWR method is well placed to become a significant computational tool in the field of charge density analysis in the years to come in its own right. Of course, this was only one small study on small organic systems; thus more work would need to be undertaken to validate the XWR method's application to low-resolution data sets in general. This result however is nonetheless promising, and could prove invaluable to the study of materials where the collection of high-quality, high-resolution X-ray data sets is non-trivial.

In Chapter 5 a concerted use of experimental and computational techniques elucidated the effects of intermolecular cation---anion interactions in two ionic organic chromophores, wherein the XWR method was once again employed using both low- and high-resolution data sets providing further confirmation of its applicability in low-resolution data regimes. The results of this chapter, that uses panoply of experimental and theoretical methods, reveal the important effect that interionic interactions have on the NLO activity of **DAST-**derivatives, **DAST** being a commercially important material. Furthermore, given the unique nature of the XWR method, in that it ostensibly provides a gas-phase assessment of a system, tempered by information pertaining to crystal lattice effects, the potential of the XWR method to be used as an intermediary between the gas-phase, and the solid-state is demonstrated.

Work then turns toward the less well-known study of octupolar organometallic complexes in Chapters 6 and 7. In Chapter 6, experimental validation is provided for a new series of small Zn-based complexes with pseudo-T_d octupolar symmetry that were previously identified through a data mining study of the Cambridge Structural Database. The work herein on this complex confirmed both its octupolar nature, via the measurement of its depolarization ratio, and also provides a thorough analysis of its NLO activity and origins via gas-phase DFT, XWR, HRS measurements and charge density analysis. This four-fold assessment of the NLO of the complex dichlorobis(3-pyridinecarboxaldehydeκN)Zn(II), is a rare example of an extensive cross-phase beta enumeration of an octupolar organometallic complex; which are particularly challenging even for state-of-the-art experimental and computational materials characterisation methods. Furthermore, the use of the XWR method to provide complementary topological analysis of the complex is very rare in the literature, given that the XWR method has not been extensively used in the study of transition metal complexes to date. Indeed, the use of the anharmonic Gram-Charlier (GC) correction code on a metal complex is the first of its kind, and, although unable to remove libration effects completely, is promising. The use of GC corrections via XWR require further study, however, given the XWR methods ability to yield good results even in the absence of high-resolution data sets, the potential to use the XWR method to yield GC correction values that could be incorporated into experimental charge density studies, similar to the computationally-derived corrections regularly used for hydrogen atoms, could be realized in the future.

Finally, Chapter 7 presents a first of its kind charge density analysis of two transition metal octupolar complexes that descend the halogen series; as such one of the complexes investigated, contains two heavy elements, namely Zn and Br. Once again a multi-phase enumeration of β was achieved, and highlighted the efficiency of these small organometallic complexes, especially when placed into the context of other T_d and pseudo-T_d octupolar organometallic complexes. When compared with the complex investigated in Chapter 6, these three organometallic complexes reveal the tuneability of their NLO responses via differing ligation. Given these three complexes were designed and developed based on a results of data-mining studies, this work further endorses the concerted use of theory and experiment, in the identification of new NLO materials.

8.2 Outlook

8.2.1 Materials Design and Discovery

The future of the NLO field, especially in the area of bespoke design of NLO-active materials for specific optoelectronic and telecoms applications looks promising. The already well-established rationalized approach to the design of new organic chromophores for NLO applications, via the structure-function relationship approach, continues apace. Meanwhile, the organometallic equivalents, although require work, have the potential to achieve just as much success as their organic counterparts if a rationalized approach to their investigation is developed in order to facilitate the identification of similar structure-function relationships. Understandably, given their more complex chemistry, this has not been forthcoming over the last few decades, and may be a consequence of the multi-disciplinary nature of the NLO field, which sees many non-chemists. However, reviews to date have demonstrate the huge potential of organometallics for NLO applications, and thus further neglect in pursing this area of NLO materials discovery in a more structured and rationalized way would be a considerable oversight; especially given the versatility of organometallics, that have huge potential to form the bulk of the bespoke design for specific NLO applications market. Turing to octupolar materials, the current dearth of knowledge on these materials, and their underrepresentation in the literature seems counterintuitive given their superior NLO activity, compared to dipolar materials. As such, much more work on octupolar materials, especially organometallic octupolar materials, should be championed. As more studies are undertaken, these materials too, could benefit from a rationalized structure-function relationship approach.

To this end, the concerted use of theory and experiment, especially where certain types experimental data may not be easily available will prove invaluable e.g. charge density data of organometallics. While experimental approaches, such as charge density analysis and HRS are now well established, the emergence of new computational techniques e.g. XWR, begin to make the study of materials were sufficient data aren't available, a real possibility. Coupled with the greater accessibility of high-performance computing (HPC) and the growing importance of 'big data', a move toward larger scale data-driven NLO materials prediction seems pertinent at this time, and has already had some success[1]. Furthermore, combined experimental and computational approaches in materials discovery have even received government attention of late and, is one of the core principles of the Materials Genome Initiative[2], i.e. concerted use of theory and computation in materials discovery efforts is imperative if one is to achieve the transformative reduction in 'molecule-to-market' innovation timescales that is considered necessary to remain globally competitive.

8.2.2 High-throughput β determinations

Given the increased availability of HPC as discussed in §8.2.1, the possibility for high-throughput calculations to determine the molecular hyperpolarizability of materials has potential to become a reality e.g. MD-cluster calculations could predict β values comparable to HRS determinations, while XWR methods could provide detailed topological analysis. This method of property determinations of NLO-active materials could see the development of databases of topological and property information for NLO-active materials similar to the already well established Cambridge Structural Database (CSD)[3]. Furthermore, the formation of such databases containing a plethora of topological analysis seems to be increasingly possible given the development of the XWR method, which we have shown is able to yield good results even with good-quality low-resolution X-ray data. Given these initial results, and pending further exploration, large-scale XWR calculations could be undertaken via direct extraction of CIF and data files from the CSD, at least for small organic chromophores to begin. Moreover, given that the XWR code is in continual development, its capabilities are envisaged to increase over time.

Obviously, given the size of the CSD (953,375 unique crystal structures as of September 2018), the materials selected for input into any such high-throughput XWR calculation would need to be screened and selected based on metrics that determine the materials' promise as an NLO material. Luckily, the rational manner by which organic and organometallic molecules can be built up from their donor, acceptor and π-media to create SHG function, in accordance with structure-property relationships, provides the tools to predict the propensity of a material to yield good second order NLO responses. With this in mind, the development of data-mining strategies and programs that encode these relationships into algorithmic logic in an attempt to systematically predict new SHG-active chromophores has been demonstrated[1], and could be used in conjunction with the XWR, to facilitate the creation of an NLO-active materials database, which could be used to elucidate new potential structure-function relationships, and identify materials for further exploration.

8.2.3 NLO of Nanomaterials: The Move Toward Nanoparticles

As the trends of the incorporation of optical circuitry and optical devices into ever-smaller regimes i.e. nano size, increases apace, the need to research, design and develop new NLO materials for nanotechnology applications becomes ever more important. The NLO of nanomaterials of course presents its own challenges, given that the need forever increasing NLO response sizes increases in tandem with the need to scale the material down to the nano regime. This potentially places a new NLO response-material size trade off that has to be considered, and approached with care.

One direction of study that has yielded interesting results to date is the study of NLO properties of nanoparticles, with the most prevalent examples comprising nanoparticles of gold, silver and copper. For a detailed review the reader is directed to the review of Zhang & Wang[4]. The use of nanoparticles as SHG-active materials is growing. However, as one enters the world of nano, quantum effects become more important. For example the shape and size of nanoparticles can have a significant impact on their SHG response, owing to quantum confinement effects. Recent work by Nappa *et al.*[5] further confirms the importance of size considerations and the effect of particle size on the SHG activity of the materials. Here they revealed that the level sphericity of the nanoparticle used for the generation of SHG is important, and impacts the nature of the SHG-origins. Namely, for nanoparticles that are not smooth and highly spherical the SHG effect arises from dipolar contributions, similar to dipolar organic materials. However, as the particle diameter is increased such that it is larger than the input wavelength of light, then retardation effects cannot be ignored. This in turn causes the origin of it particles SHG response to switch from pure dipolar to possessing a much more quadrupolar contribution *cf* Kelly *et al*.[6]

Indeed, nanomaterials have their own unique set of light properties as a consequence of surface plasmon resonances (SPRs); ostensibly, oscillations of the conduction electrons at the surface of a nanoparticle. As a consequence of these SPRs however, SHG responses in nanoparticles have in fact been shown to exhibit massive enhancements, whereby the SPRs generate very large local electromagnetic fields.[7]

8.3 References

(1) Cole, J. M.; Weng, Z. F. Discovery of High-Performance Organic Non-Linear Optical Molecules by Systematic 'Smart Material' Design Strategies. In *Multi-Functional Materials and Structures III*; Advanced Materials Research; Trans Tech Publications, 2010; Vol. 123, pp 959–962.

(2) *"Materials Genome Initiative for Global Competitiveness", U.S. Government White Paper; National Science and Technology Council, Executive Office of the President of the United States (2011)*.

(3) Allen, F. H. The Cambridge Structural Database: A Quarter of a Million Crystal Structures and Rising. *Acta Crystallogr. B* **2002**, *58* (3), 380–388.

(4) Zhang, Y.; Wang, Y. Nonlinear Optical Properties of Metal Nanoparticles: A Review. *RSC Adv.* **2017**, *7* (71), 45129–45144.

(5) Nappa, J.; Russier-Antoine, I.; Benichou, E.; Jonin, C.; Brevet, P. F. Second Harmonic Generation from Small Gold Metallic Particles: From the Dipolar to the Quadrupolar Response. *J. Chem. Phys.* **2006**, *125* (18), 184712.

(6) Kelly, K. L.; Coronado, E.; Zhao, L. L.; Schatz, G. C. The Optical Properties of Metal Nanoparticles: The Influence of Size, Shape, and Dielectric Environment. *J. Phys. Chem. B* **2003**, *107* (3), 668–677.

(7) Barnes, W. L.; Dereux, A.; Ebbesen, T. W. Surface Plasmon Subwavelength Optics. *Nature* **2003**, *424*, 824.

Appendix A

Residual Electron Density Maps for Experimental Charge Density Studies

A.1 Residual Electron Density Maps for Compounds 35-39 (Chapter 3)

An ideal residual density plot would be flat, areas that contain residual electron density correspond to regions that are not being completely modelled. In the case of **38,** the largest residual density is near the chlorine atoms, which is to be expected since these are the heaviest atoms within the structures. The maximum residual density in these plots is 0.40eÅ around Cl(1).

The refinement of the structure of **39** presented problems leading to residual maps that still show some large features in the region connecting the two aryl rings. In this region, electron density up to 0.45 eÅ^{-3} was observed close to C(7). The maximum residual density in these plots is 0.45eÅ^{-3} around Cl(1).

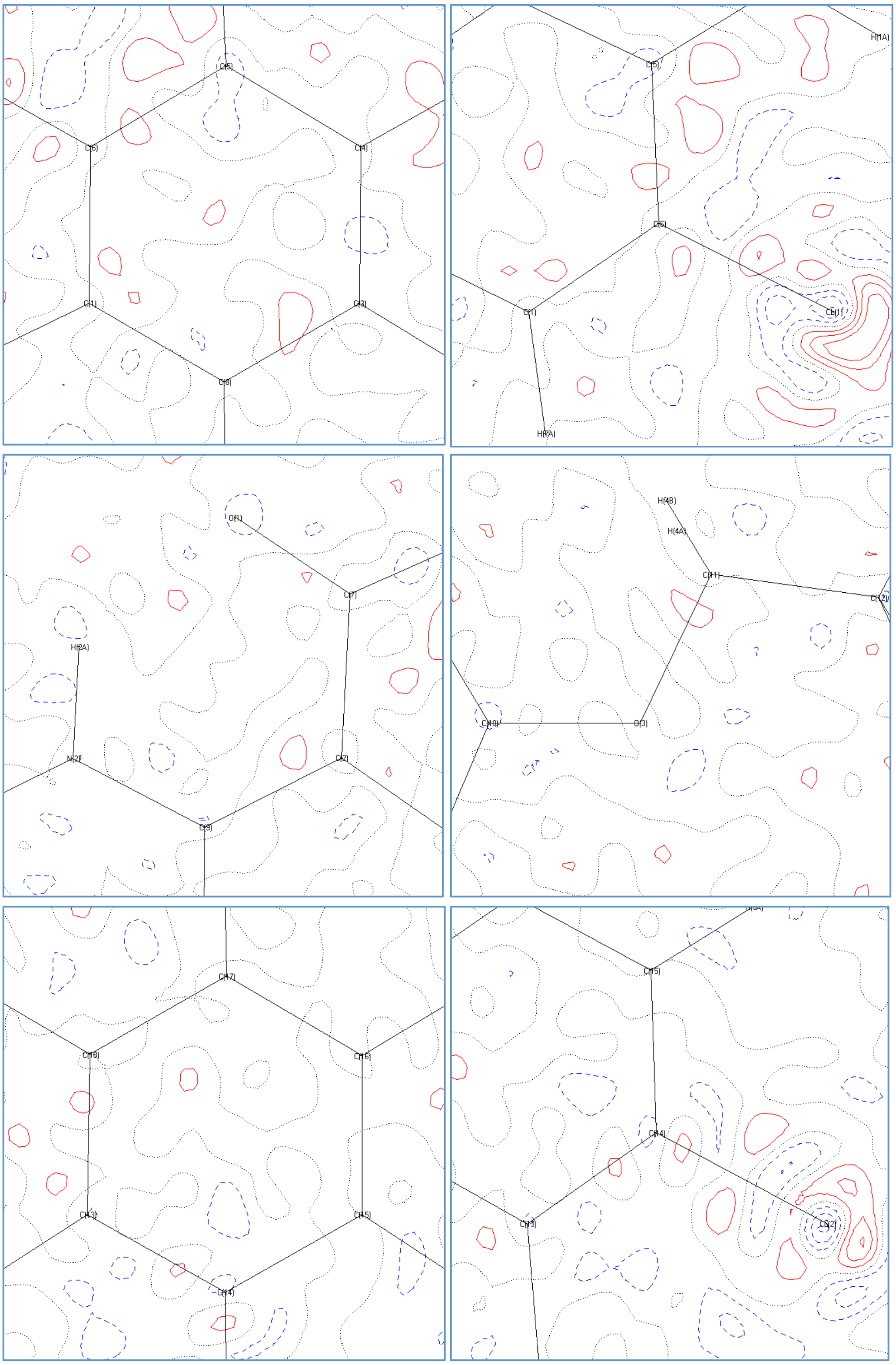

Figure A1 Residual density maps of compound **38** at contour level of 0.1 eÅ^{-3}. Red lines are positive (actual electron density), blue lines are negative, black lines are zero.

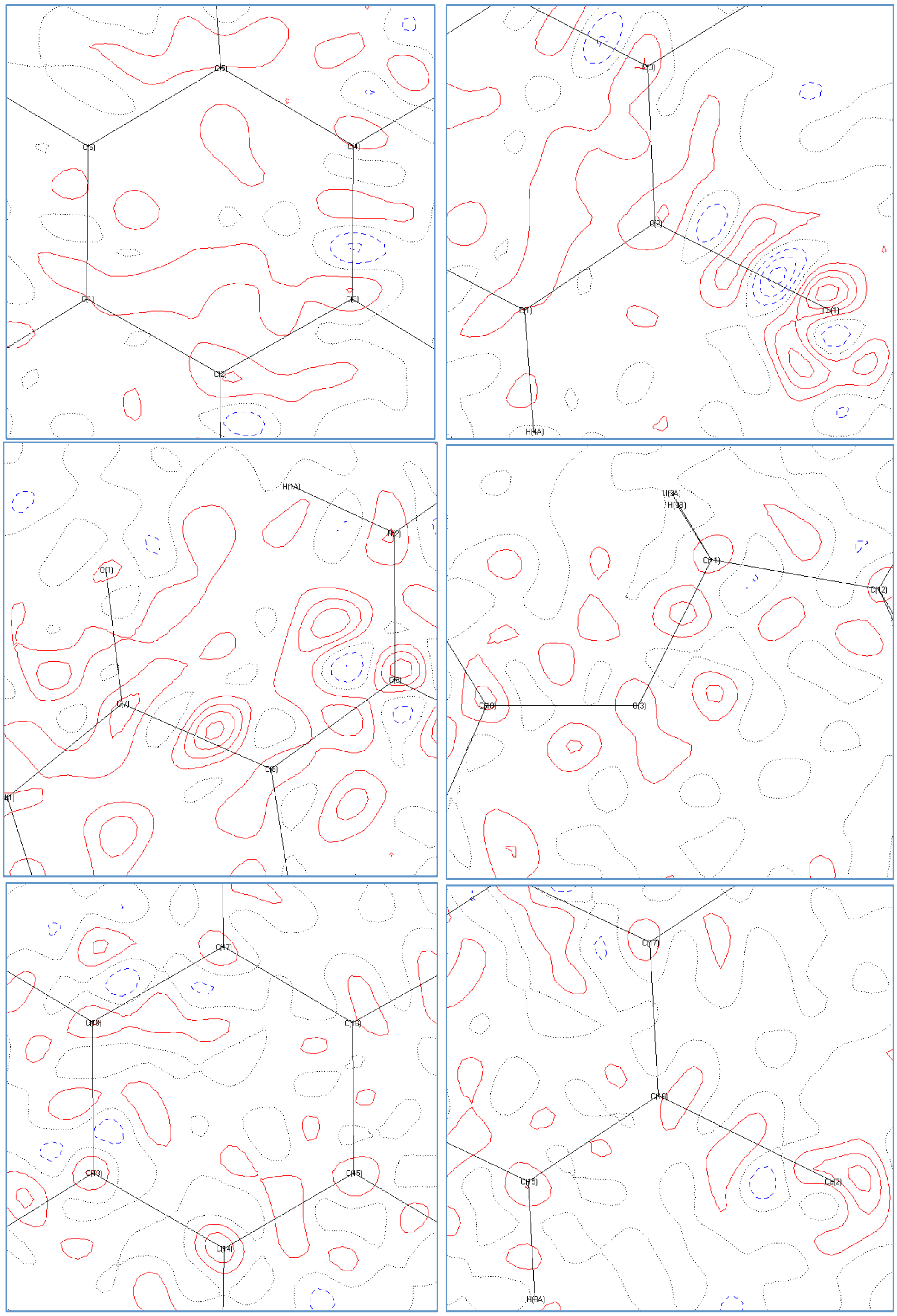

Figure A2 Residual density maps of compound **39** at contour level of 0.1 eÅ^{-3}. Red lines are positive (actual electron density), blue lines are negative, black lines are zero.

A.2 Residual Electron Density Maps for DAST & BP3 (Chapter 5)

An ideal residual density plot would be flat, areas that contain residual electron density correspond to regions that are not being completely modelled, as is the case for **DAST** and **BP3**.

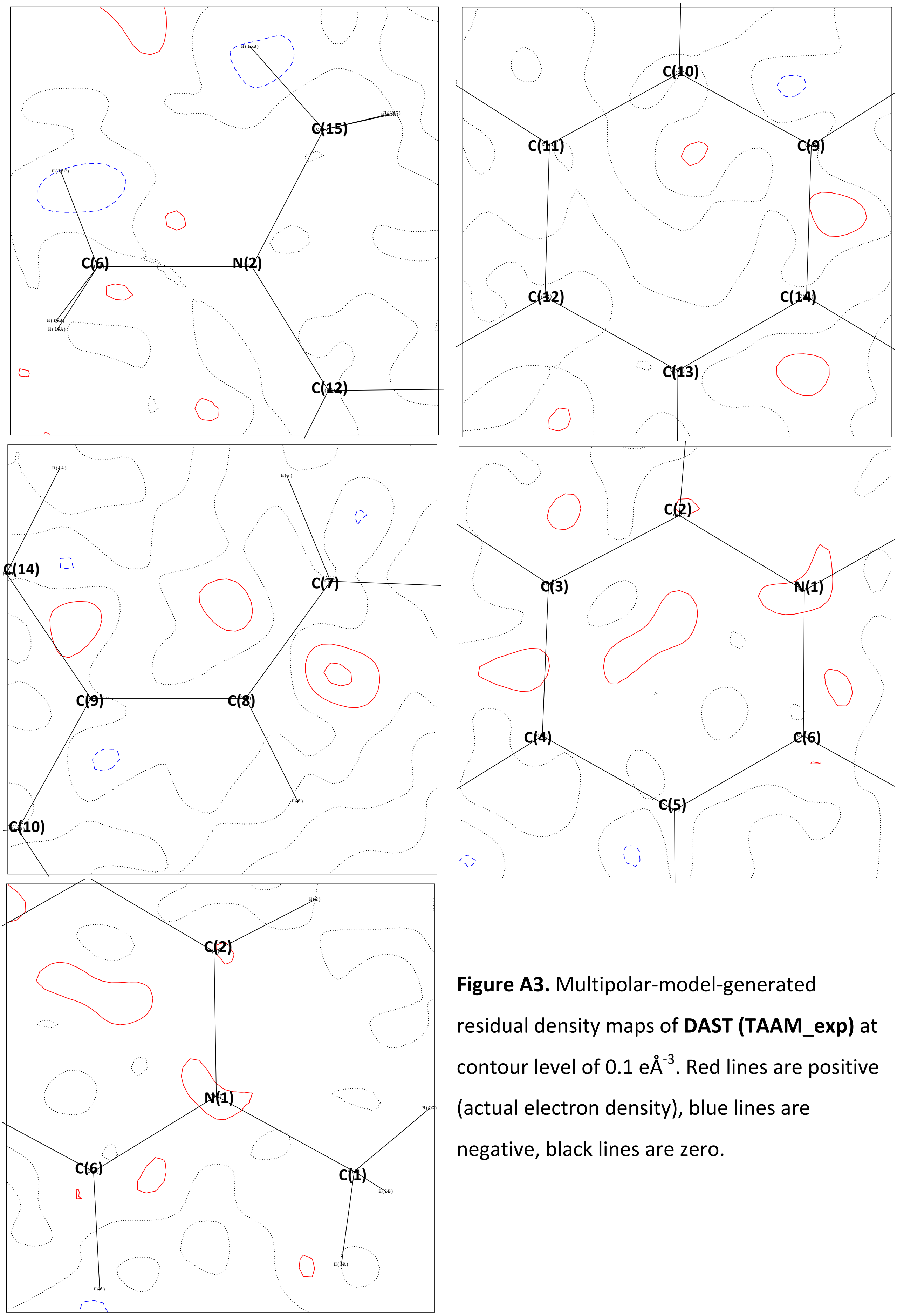

Figure A3. Multipolar-model-generated residual density maps of **DAST (TAAM_exp)** at contour level of 0.1 eÅ^{-3}. Red lines are positive (actual electron density), blue lines are negative, black lines are zero.

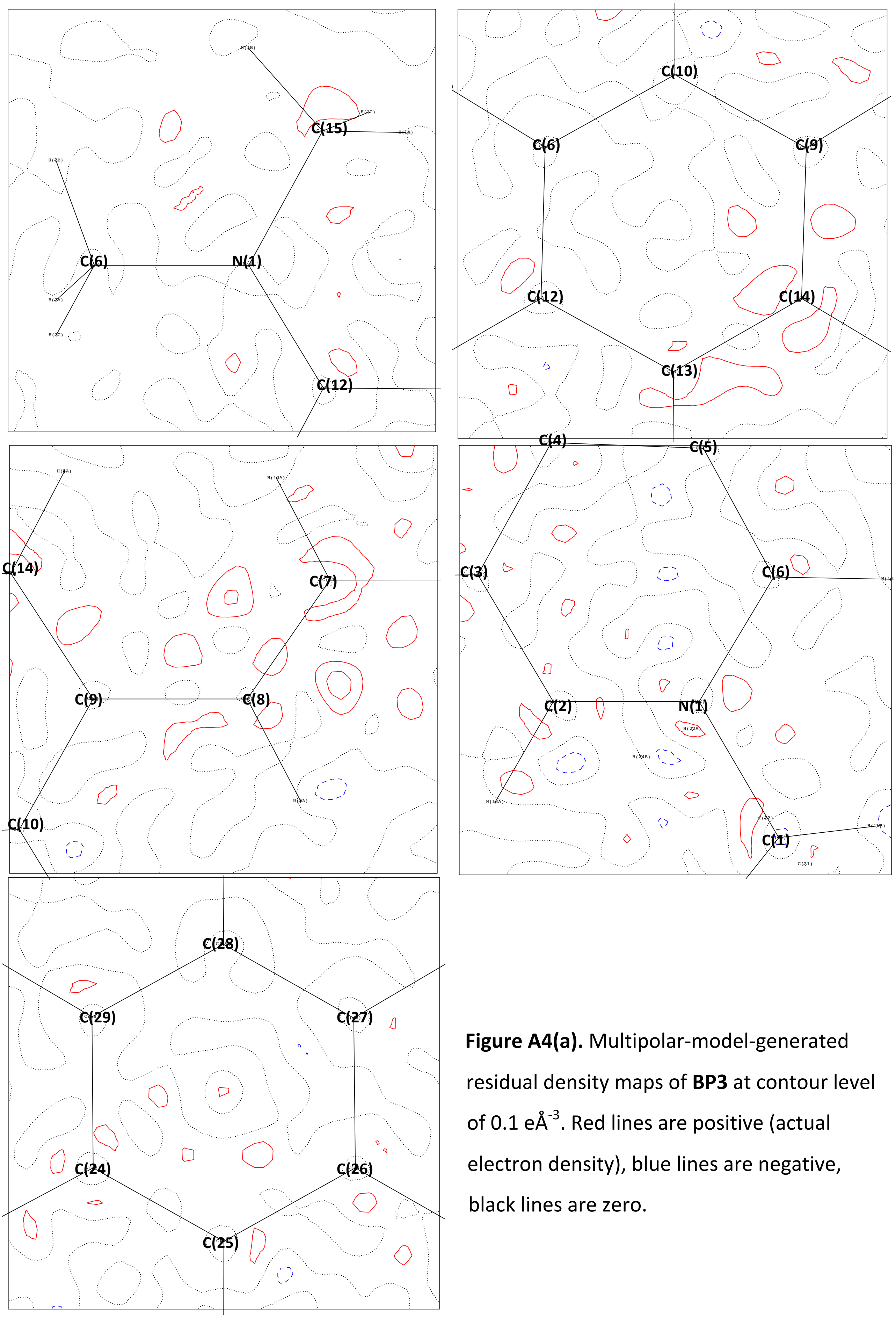

Figure A4(a). Multipolar-model-generated residual density maps of **BP3** at contour level of 0.1 eÅ^{-3}. Red lines are positive (actual electron density), blue lines are negative, black lines are zero.

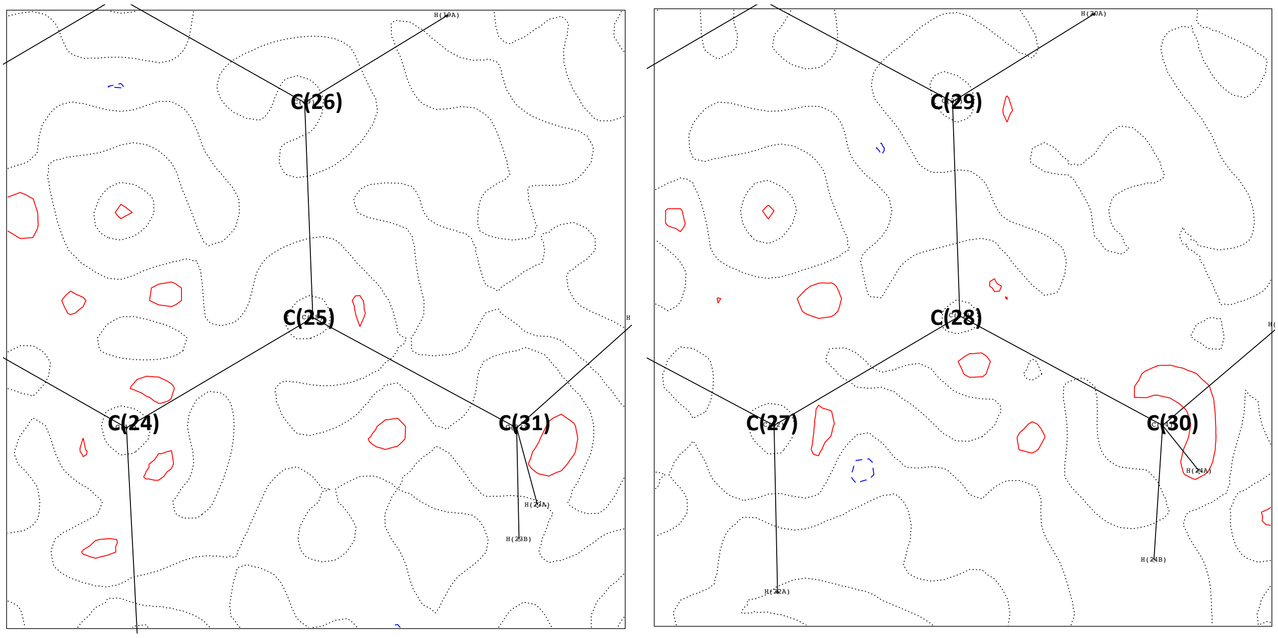

Figure A4(b). Multipolar-model-generated residual density maps of **BP3** at contour level of 0.1 eÅ^{-3}. Red lines are positive (actual electron density), blue lines are negative, black lines are zero.

A.3 Residual Electron Density Maps for 45 (Chapter 6)

An ideal residual density plot would be flat, i.e., areas that contain residual electron density correspond to regions that are not completely modelled. The maximum residual density in these plots is 0.443 eÅ^{-3} around the Cl atoms, while 0.628 eÅ^{-3} surrounds Zn.

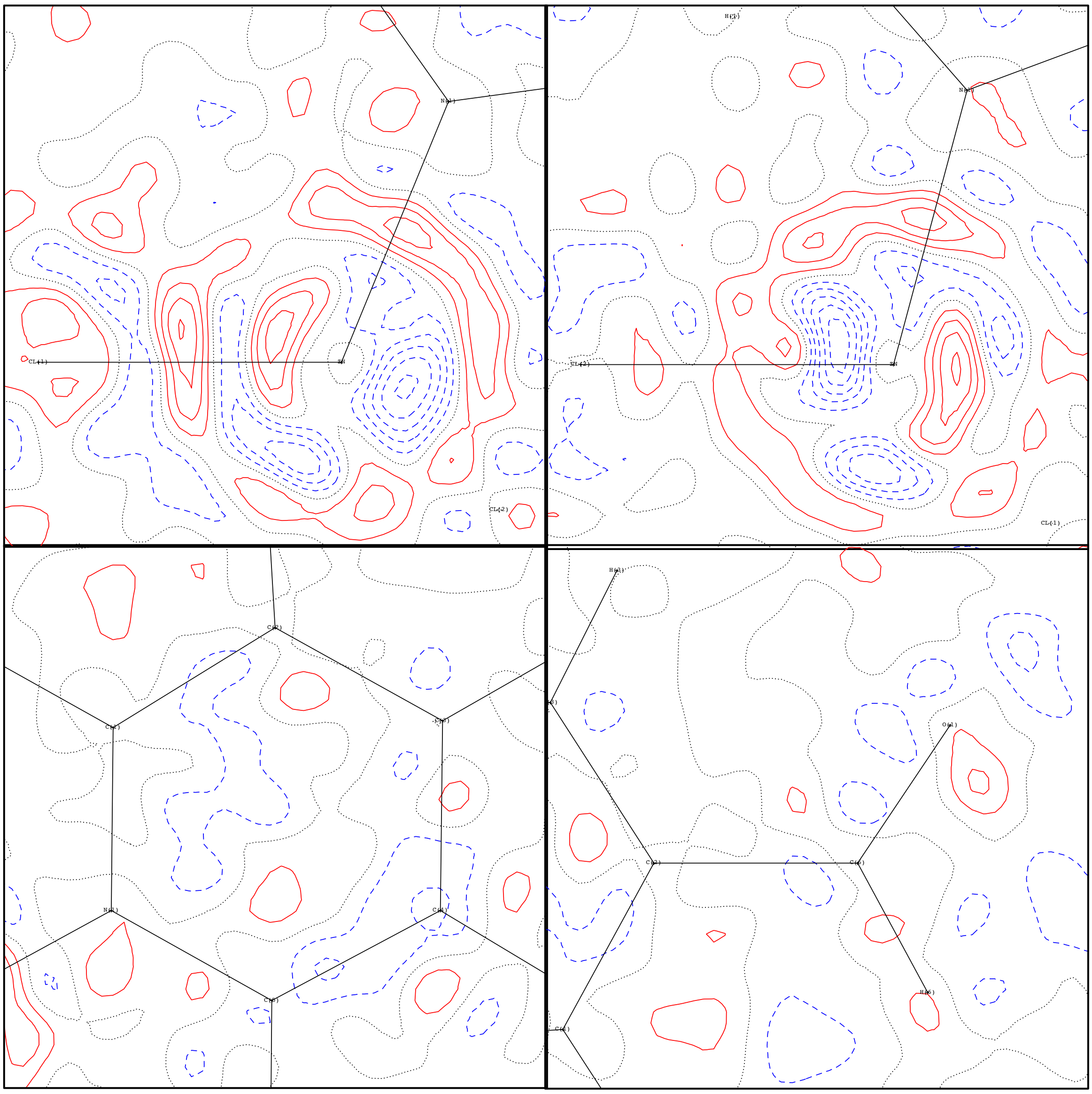

Figure A5 Multipolar-model-generated residual electron density maps of **45** at contour level of 0.1 eÅ^{-3}. Red lines are positive (actual electron density), blue lines are negative, black lines are zero.

A.4 Residual Electron Density Maps for 46 and 47 (Chapter 7)

An ideal residual density plot would be flat, i.e., areas that contain residual electron density correspond to regions that are not completely modelled. The maximum residual density in these plots is 0.371 eÅ^{-3} around the Cl atoms, while 0.673 eÅ^{-3} surrounds Zn (**1**) and, 1.152 eÅ^{-3} and 0.838 eÅ^{-3} around the two Br atoms (**2**).

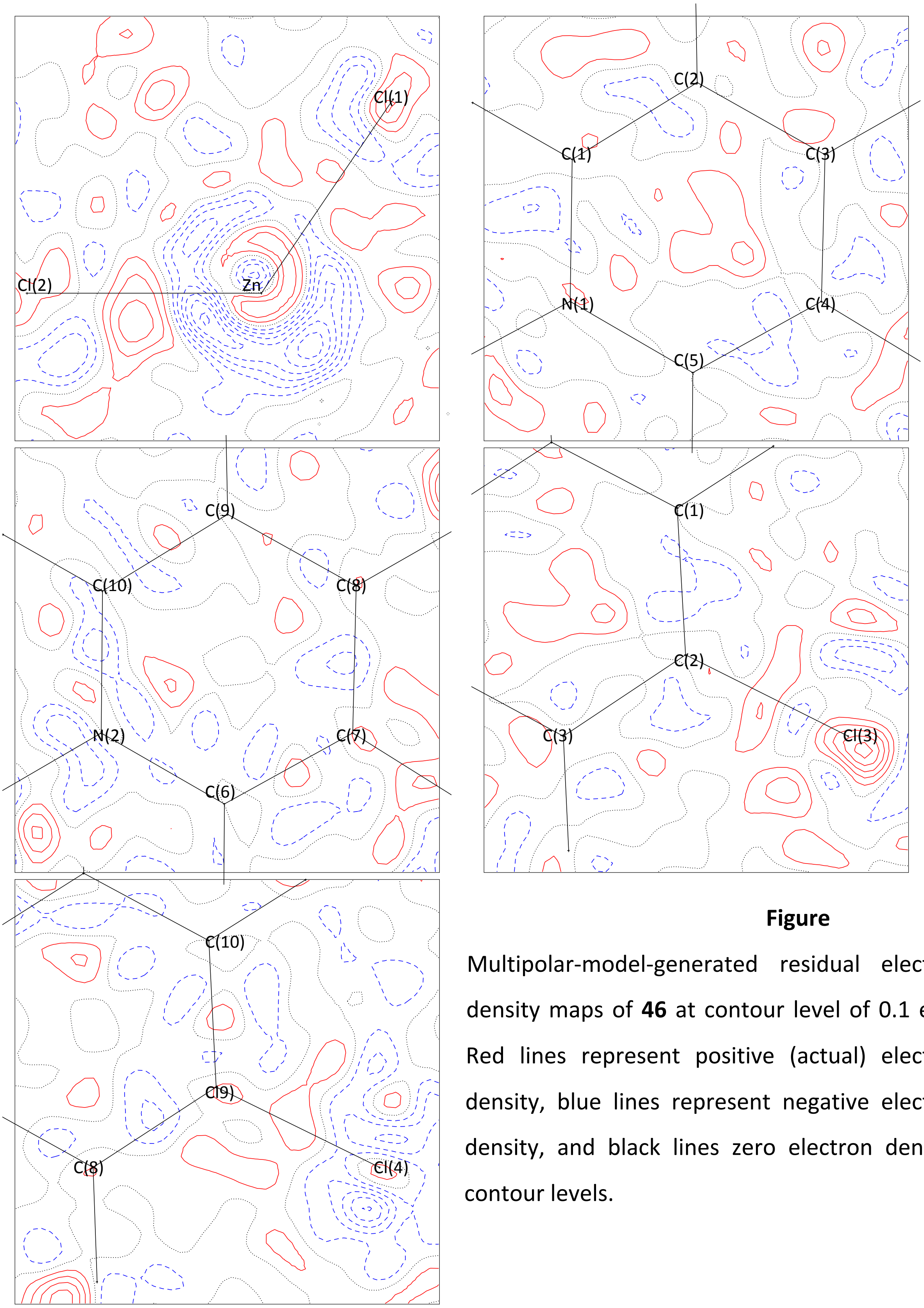

Figure A6 Multipolar-model-generated residual electron density maps of **46** at contour level of 0.1 eÅ^{-3}. Red lines represent positive (actual) electron density, blue lines represent negative electron density, and black lines zero electron density; contour levels.

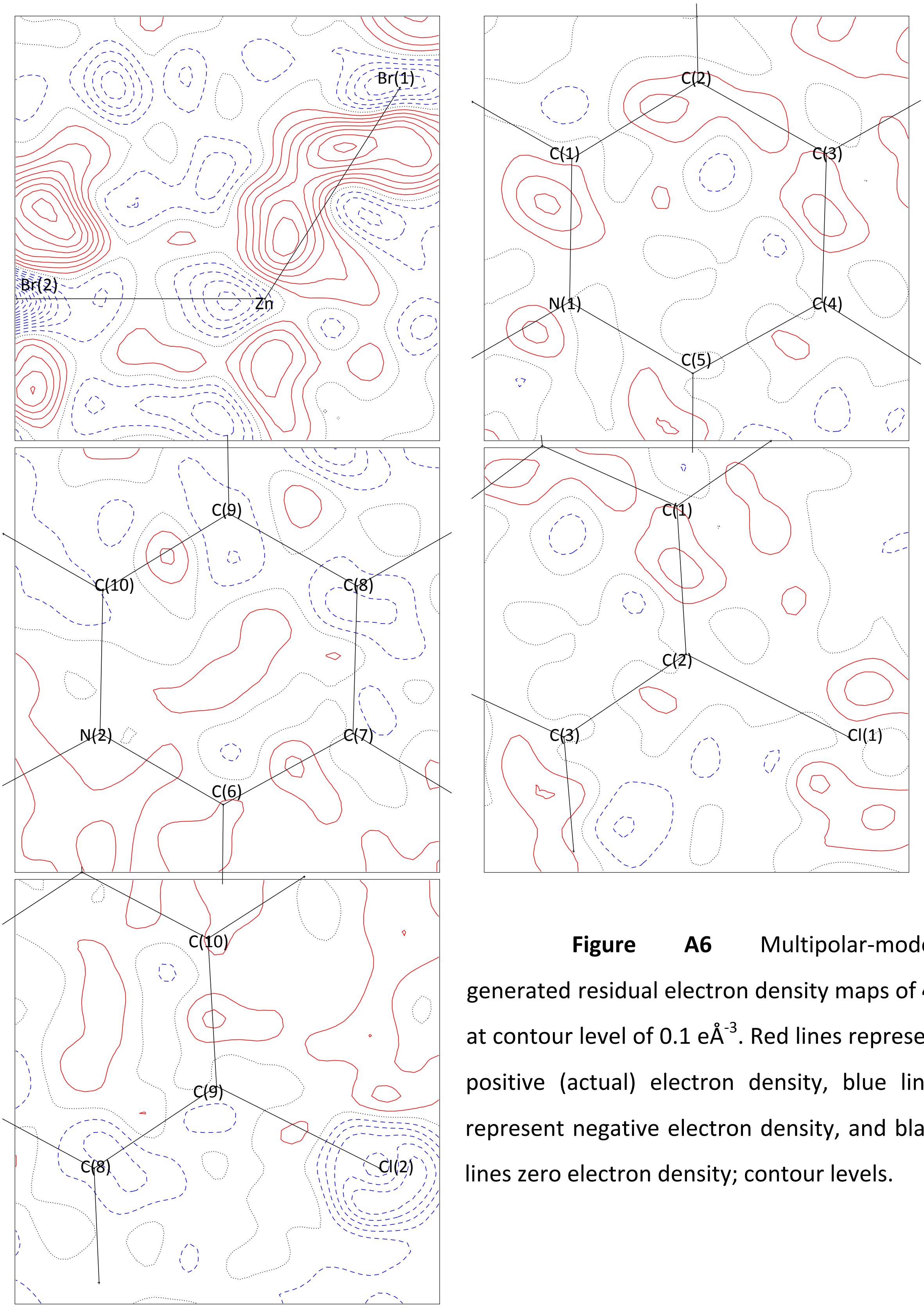

Figure A6 Multipolar-model-generated residual electron density maps of **47** at contour level of 0.1 eÅ^{-3}. Red lines represent positive (actual) electron density, blue lines represent negative electron density, and black lines zero electron density; contour levels.

Appendix B

Supplementary Information pertaining to Experimental Charge Density Studies

B.1 Critical Point Searches of C-Cl Bonds in Compounds 38 & 39

Table B.1 A summary of the critical point analysis on the Cl-C bonds in compound **38**.

Bond	$\rho(r)$ [eÅ^{-3}]	$\nabla^2\rho(r)$ [eÅ^{-5}]	R_{ij} [Å]	d_1 [Å]	d_2 [Å]	Hessian Eigenvalues			ε
Cl(1)-C(6)	1.303	-1.222	1.7360	0.9253	0.8107	-7.14	-5.90	11.82	0.21
Cl(2)-C(14)	1.280	-1.261	1.7415	0.9663	0.7752	-7.38	-6.65	12.77	0.11

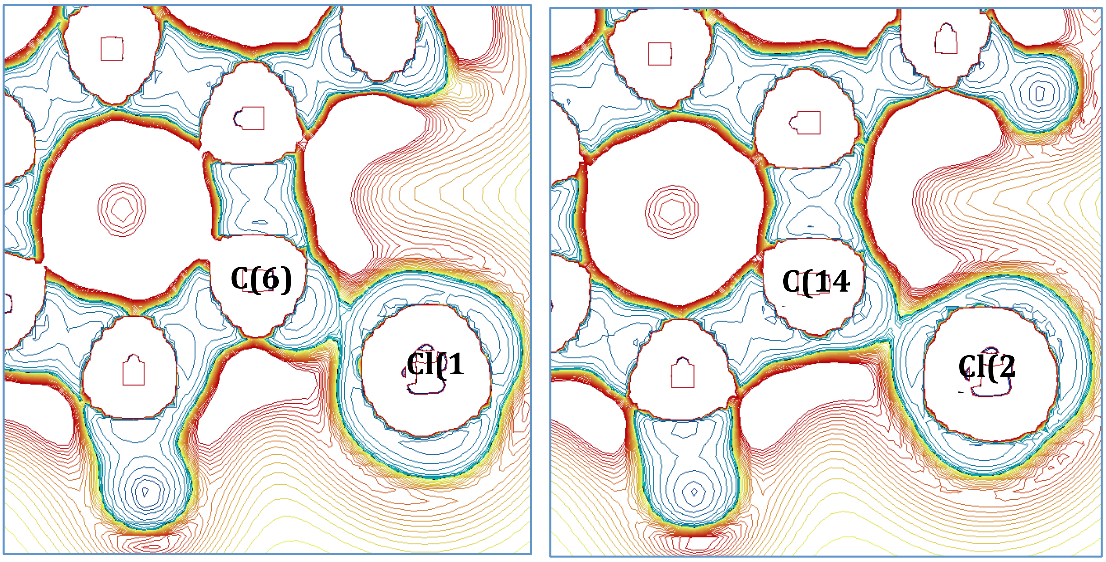

Figure B1 Laplacian maps in the plane of the C(6)-Cl(1) and C(14)-Cl(2) *covalent bonds* in compound **38**.

Table B.1 A summary of the critical point analysis on the Cl-C bonds in compound **39**.

Bond	$\rho(r)$ [eÅ^{-3}]	$\nabla^2\rho(r)$ [eÅ^{-5}]	R_{ij} [Å]	d_1 [Å]	d_2 [Å]	Hessian Eigenvalues			ε
Cl(1)-C(2)	1.219	1.229	1.7413	0.9273	0.8140	-7.89	-7.02	16.14	0.12
Cl(2)-C(16)	1.159	1.867	1.7381	0.9557	0.7824	-7.17	-6.31	15.34	0.14

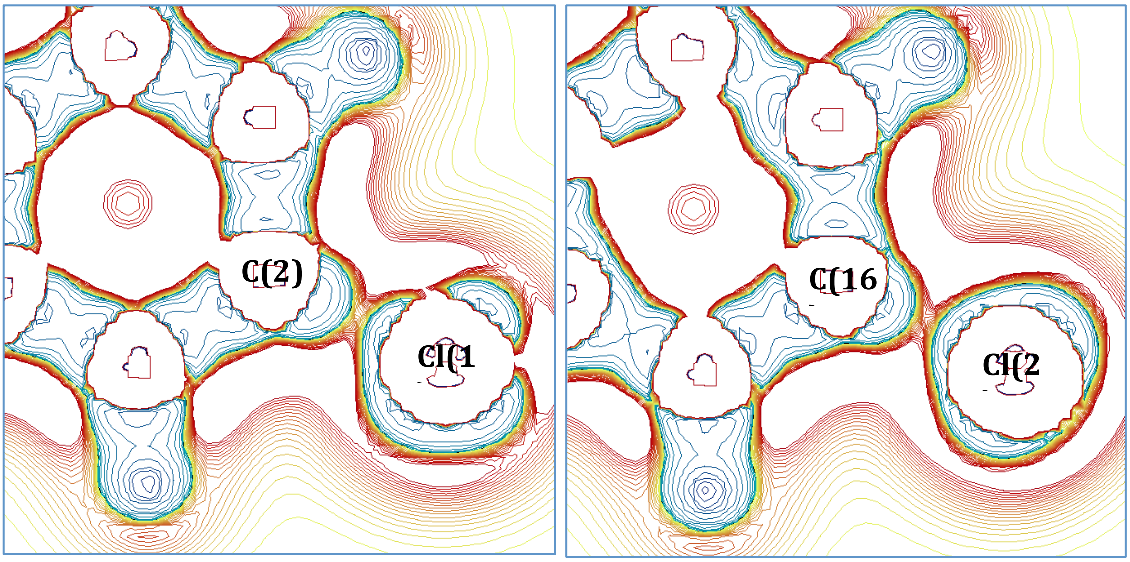

Figure B2 Laplacian maps in the plane of the C(2)-Cl(1) and C(16)-Cl(2) *ionic bonds* in **39**.

Appendix C

Supplementary Information pertaining to X-ray Wavefunction Refinements

C.1 XWR-derived Residual Electron Density Maps of Compounds 40-42 (Chapter 4)

The residual electron density map of **40** is flat and featureless except for a few small residual density features that appear to be randomly distributed and which cannot be attributed to any specific segments or atoms within the molecule.

The residual electron density maps for **41** and **42** appear somewhat more featured than that of **40**. That said, most of those features are randomly distributed and cannot be attributed to unmodeled bonding or lone-pair phenomena, except for the terminal Cl atoms. In the case of the Cl atoms, residual density is observed in the residual electron density maps of **41** and **42** either within the bonding region or, at the position of the Cl atom itself. Nevertheless, the residual electron density residing on the Cl atom of **41** is small (0.13 eÅ^{-3}). In the case of **42**, the unmodeled residual density of the two Cl atoms is higher (0.24 eÅ^{-3}) which is nevertheless still modest; and, it appears to have a shashlik character, which can be a sign of anharmonic libration of the atom. The presence of such anharmonic libration is not surprising given the terminal position of the Cl atoms. Owing to the absence of high resolution data, a Gram-Charlier (GC) anharmonic refinement of **42** could not be undertaken.[1] As a consequence of this unmodeled 0.24 eÅ^{-3} residual electron density, care was taken when assessing the viability of the model of **42** and its associated determined properties. The fitting statistics for **42** are nevertheless acceptable (*cf.* §4.2.3) and the bonding parameters associated with the Cl atoms are reasonable (*cf.* §4.3.2.2; Table 4.4) as were their respective electron deformation density (*cf.* §C.2 and Laplacian maps (*cf.* §3.2.2).

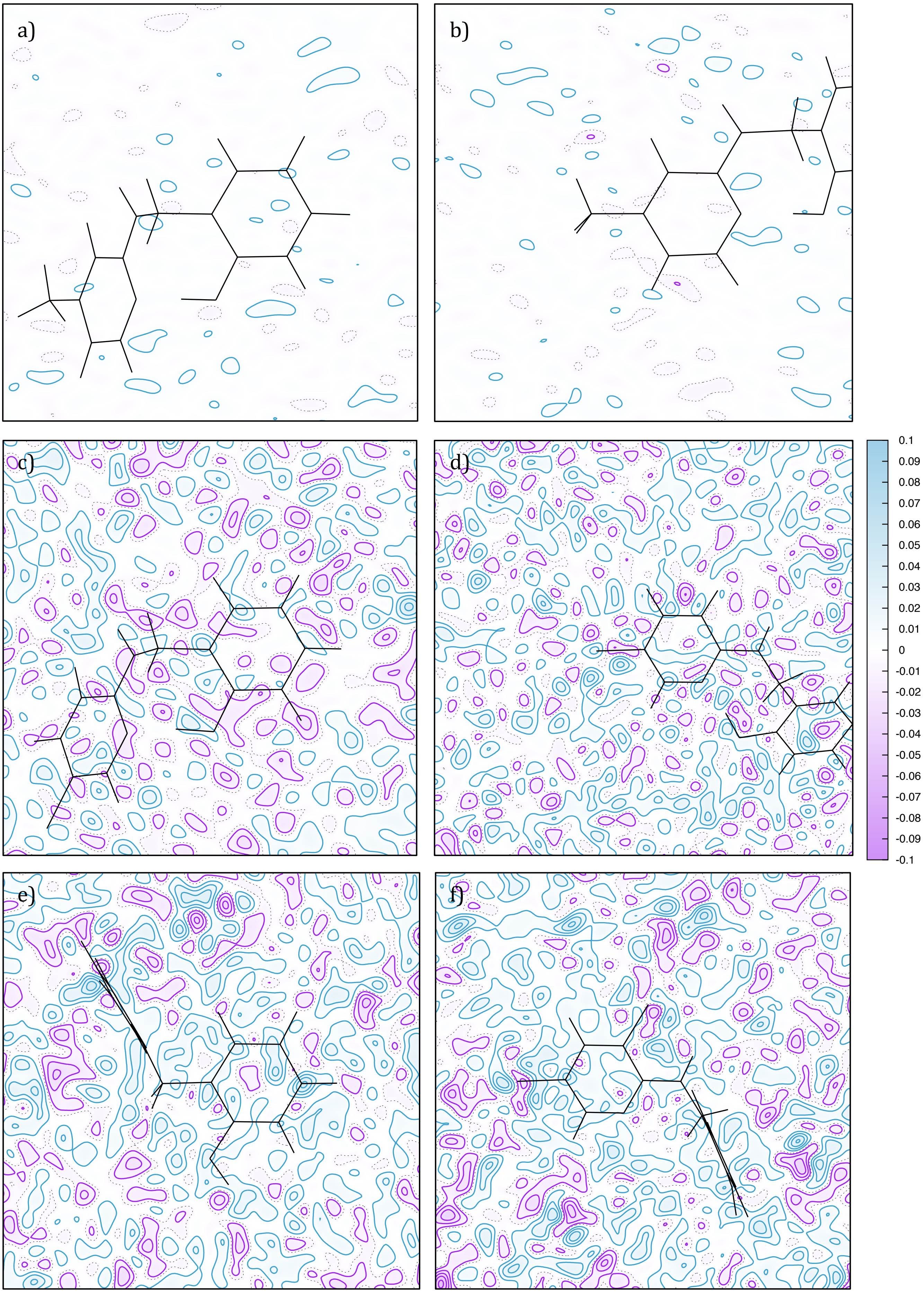

Figure C1 Residual electron density maps for **40** (a-b), **41** (c-d), and **42** (e-f) (contour level: 0.1 eÅ^{-3}).

C.2 XWR-derived Topological Results of Compounds 41-42 (Chapter 4)

Table C1. Parameters of the (3, -1) BCPs and HB BCP of **41**. ρ(r) [eÅ^{-3}] is the electron density (ED); $\nabla^2\rho$(r) [eÅ^{-5}] is the Laplacian of the ED; ε is the ellipticity of the bond; G(r)/ρ(r) [a.u.] is the kinetic energy density per electron; H(r) [a.u.] is the energy density.

Bond	*ρ(r)* [eÅ^{-3}]	*$\nabla^2\rho$(r)* [eÅ^{-5}]	ε	G(r)/ρ(r) [a.u]	H(r) [a.u]	Bond type *cf.* Table 2.
C1-C2	2.121	-21.422	0.32	0.305	-0.318	Covalent (π)
C2-C3	2.158	-24.732	0.07	0.223	-0.328	Covalent (σ/π)
C3-C4	2.198	-14.586	0.10	1.234	-0.553	Polar shared (π)
C4-C5	2.197	-24.325	0.19	0.267	-0.339	Covalent (π)
C5-C6	2.153	-26.009	0.08	0.221	-0.340	Covalent (π)
C6-C1	2.184	-26.721	0.03	0.194	-0.340	Covalent (σ)
C6-O	2.061	-14.540	0.09	1.135	-0.498	Polar shared (π)
C1-C7	1.774	-17.652	0.01	0.188	-0.232	Covalent (σ)
C7-N1	1.722	-11.960	0.07	1.027	-0.386	Polar shared (σ/π)
N1-C8	2.187	-21.922	0.01	0.985	-0.547	Covalent (σ)
C8-N2	2.358	-25.603	0.09	0.975	-0.606	Covalent (π)
N2-C9	2.198	-14.586	0.10	1.234	-0.553	Polar shared (π)
C9-C10	2.257	-24.820	0.28	0.287	-0.354	Covalent (π)
C10-C11	2.119	-21.581	0.26	0.289	-0.315	Covalent (π)
C11-C12	2.220	-23.691	0.23	0.301	-0.345	Covalent (π)
C12-C8	2.108	-22.805	0.19	0.270	-0.321	Covalent (π)
C10-Cl1	1.397	-9.947	0.05	0.327	-0.171	Covalent (σ)
H Bond (N2---H1)	0.479	2.378	0.05	0.723	-0.027	Mixed

Table C2. Parameters of the (3, -1) BCPs and HB BCP of **42.** ρ(r) [eÅ^{-3}] is the electron density (ED); $\nabla^2\rho$(r) [eÅ^{-5}] is the Laplacian of the ED; ε is the ellipticity of the bond; G(r)/ρ(r) [a.u.] is the kinetic energy density per electron; H(r) [a.u.] is the energy density.

Bond	$\rho(r)$ [eÅ^{-3}]	$\nabla^2\rho(r)$ [eÅ^{-5}]	ε	G(r)/ρ(r) [a.u]	H(r) [a.u]	Bond type *cf.* Table 2.
C1-C2	2.124	-20.521	0.23	0.328	-0.316	Covalent (π)
C2-C3	2.081	-20.107	0.14	0.284	-0.296	Covalent (π)
C3-C4	2.173	-22.202	0.27	0.334	-0.338	Covalent (π)
C4-C5	2.164	-22.443	0.14	0.283	-0.324	Covalent (π)
C5-C6	2.172	-23.271	0.23	0.319	-0.344	Covalent (π)
C6-C1	2.156	-21.654	0.28	0.301	-0.321	Covalent (σ)
C6-O	1.942	-3.512	0.25	1.462	-0.457	Polar shared (π)
C1-C7	1.683	-14.757	0.06	0.212	-0.206	Covalent (σ)
C7-N1	1.793	-15.123	0.06	0.936	-0.406	Covalent (σ)
N1-C8	2.373	-33.849	0.09	0.608	-0.565	Covalent (σ/π)
C8-N2	2.369	-33.417	0.01	0.576	-0.549	Covalent (σ)
N2-C9	2.233	-15.679	0.08	1.208	-0.562	Polar shared (σ)
C9-C10	2.279	-26.777	0.07	0.250	-0.362	Covalent (σ)
C10-C11	2.124	-22.341	0.10	0.250	-0.310	Covalent (π)
C11-C12	2.232	-23.474	0.28	0.311	-0.346	Covalent (π)
C12-C8	2.136	-24.201	0.09	0.220	-0.321	Covalent (σ)
C10-Cl1	1.419	-9.815	0.06	0.314	-0.168	Covalent (σ)
C12-Cl2	1.431	-10.187	0.06	0.297	-0.169	Covalent (σ)

C.3 XWR-derived Electron Deformation Density Maps of Compounds 40-42 (Chapter 4)

Electron deformation density (EED) maps, derived from the XWR wavefunctions, for **40-42**, as referred to in Chapter 4, are presented in Fig C2. Green lines represent areas with positive signum, while purple lines represent areas with negative signum, and dotted lines areas of zero (EDD). Contour levels are shown at 0.1 eÅ^{3} linear scaling.

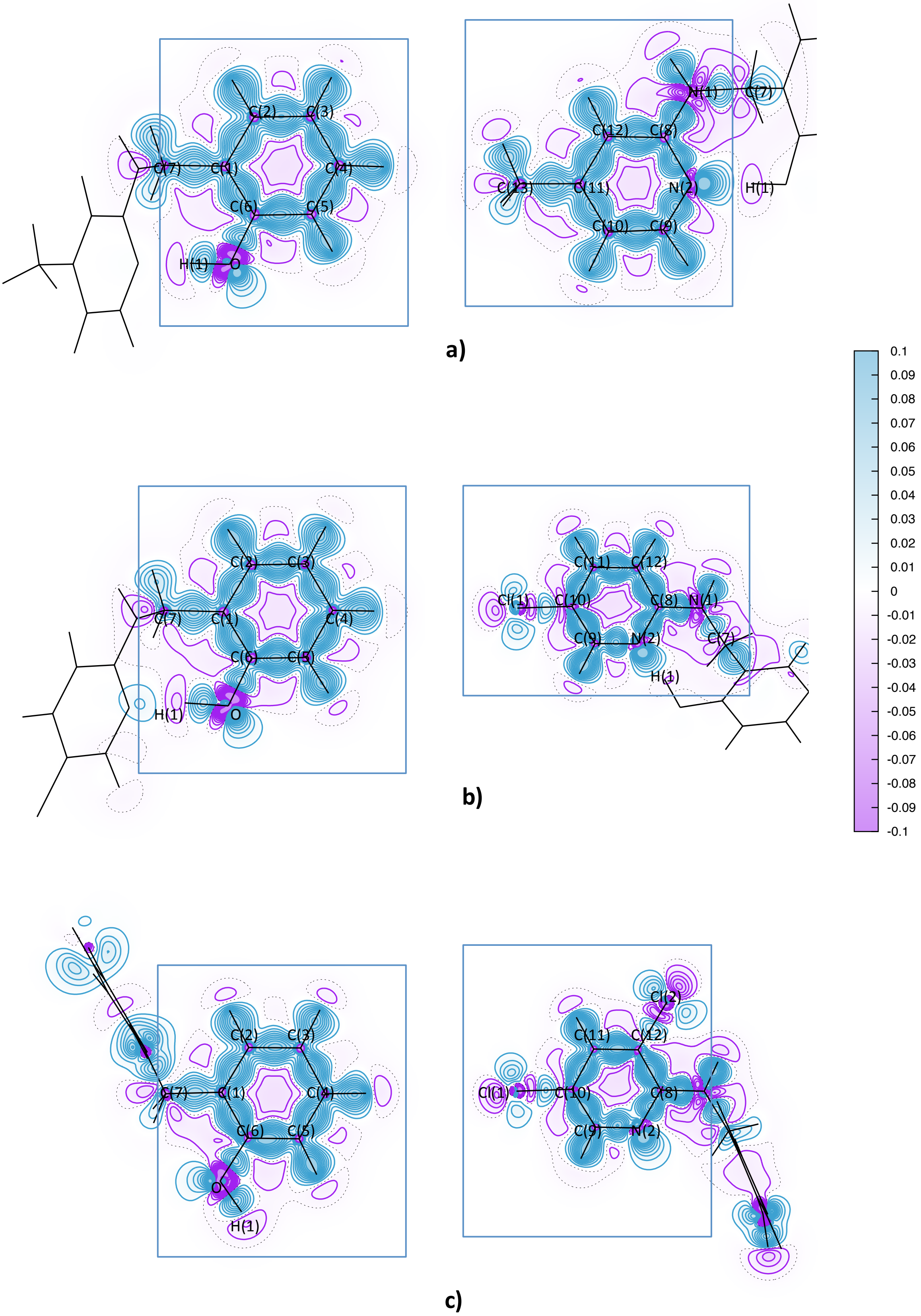

Figure C2. Electron deformation density (EDD) maps of **40** (a), **41** (b) and **42** (c). Boxed segments are in the plane of the page. Green lines represent areas with positive signum, while purple lines represent areas with negative signum, and dotted lines areas of zero (EDD). Contour levels are shown at 0.1 eÅ^{-3} linear scaling

C.4 XWR-derived Residual Electron Density Maps of Compounds DAST & BP3 (Chapter 5)

Residual electron density maps for **DAST** and **BP3** are presented in Fig S8-S10; purple lines represent positive electron density, while blue lines represent negative electron density, and black lines represent zero electron density (contour levels = 0.1 eÅ^{-3}). An ideal residual electron density plot would be flat; while areas that contain residual electron density correspond to regions that are not completely modeled.

The residual electron density maps for **DAST** and **BP3** present with some residual electron density features. However, most of those features are randomly distributed and cannot be attributed to unmodeled bonding or lone-pair phenomena. The one exception in both cases is the increased density around the *p*-toluenesulfonate anion, especially the sulfonate moiety, where a residual electron density of 0.11 eÅ^{-3} and -0.10 eÅ^{-3} are observed around the O(2) and O(1) atoms respectively. Nevertheless, residual electron density in the region of 0.1 eÅ^{-3} is modest and thus is deemed acceptable in these cases; especially given that the charge density of the *p*-toluenesulfonate anion does not form an integral part of this XWR analysis.

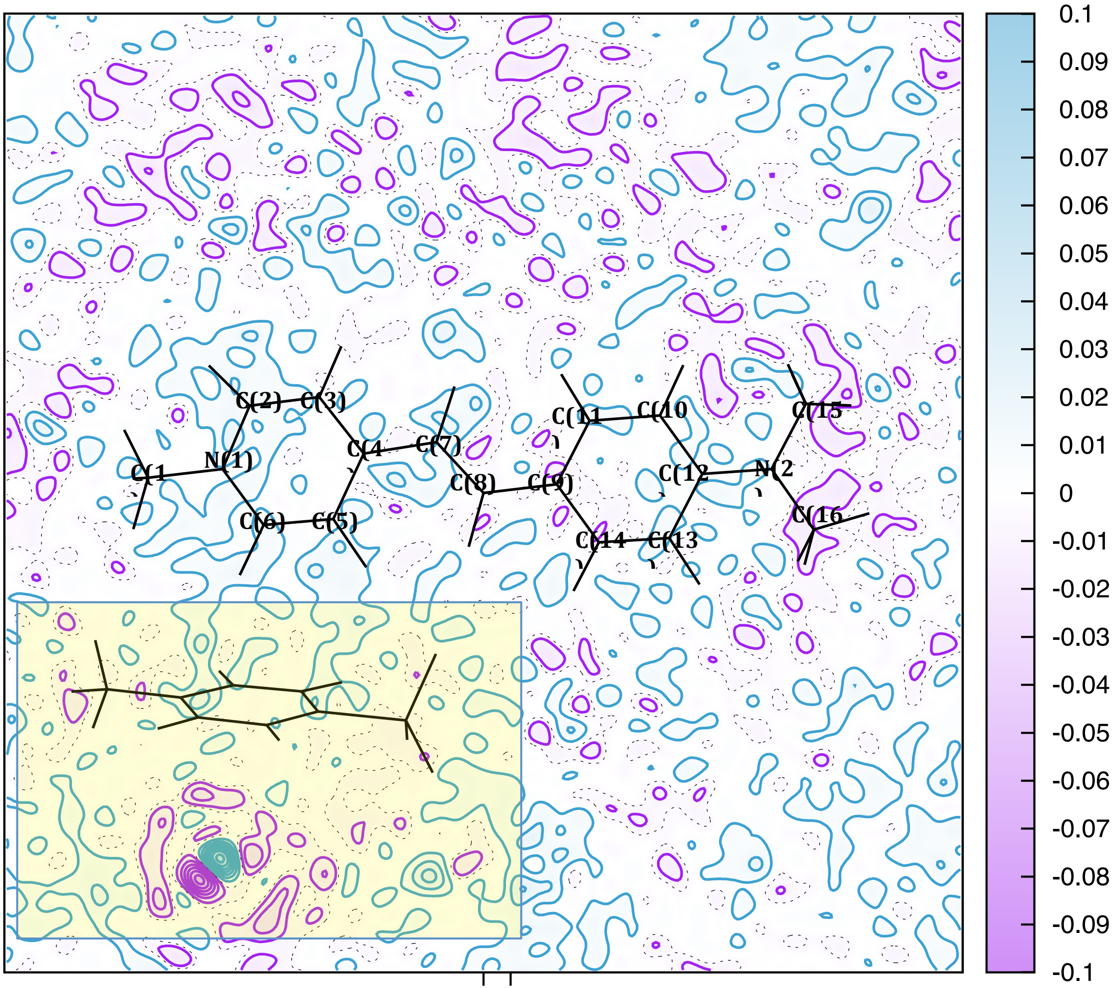

Figure C3. Residual electron density map for **DAST.** Boxed yellow region contains the anion and its respective residual electron density (contour level: 0.1 eÅ^{-3}).

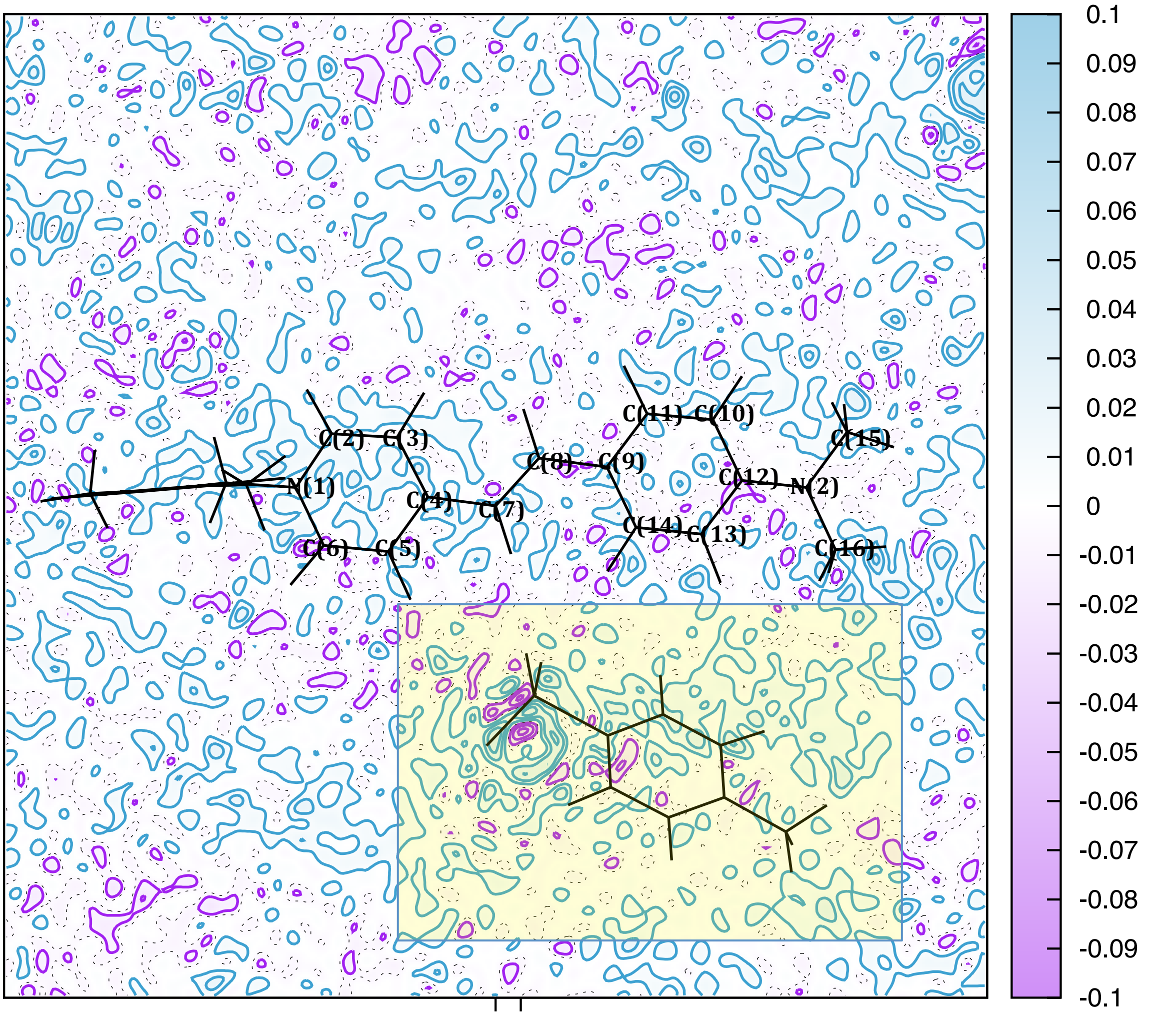

Figure C4. Residual electron density map for **BP3** viewed along the N(1) to N(2) pathway**.** Boxed yellow region contains the anion and its respective residual electron density (contour level: 0.1 eÅ^{-3}).

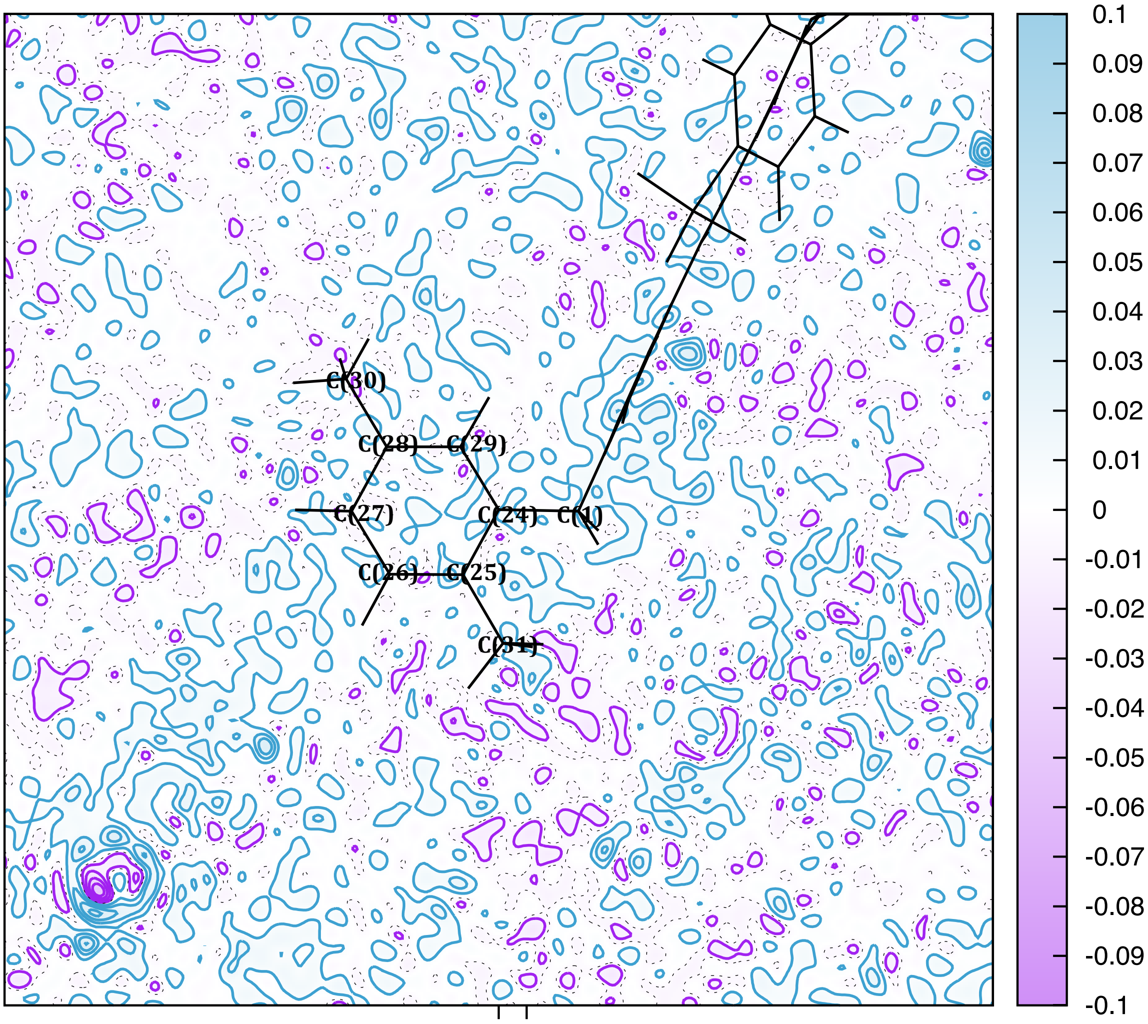

Figure C5. Residual electron density map for **BP3** viewed from the 2,5-dimethylbenzyl moeity (contour level: 0.1 eÅ^{-3}).

C.5 XWR of Compound 45: The application of Gram-Charlier Refinements (Chapter 6)

Residual electron density maps are presented in Fig. C6. Subsequently, a topological analysis of the model was carried out through the use of electron-deformation density and Laplacian maps, similar to the multipolar model (Figs. C7 and C8). A comparison between the multipolar model maps (Figs. 6.4 and 6.5) and those generated by XWR demonstrates the efficacy of the XWR method in modeling the electron density of simple transition metal complexes and, corroborates the results of the multipolar model of **45**. Furthermore, the ability of the XWR method to provide a satisfactory refinement when 3rd order Gram-Charlier (3GC) parameters are included is highly promising, considering that these could not be incorporated into the analogous multipolar model due to insufficient data resolution. The improvement of the deformation density of the Zn atom after the inclusion of the 3GC parameters is particularly noteworthy (Fig C8) and highlights the importance of considering anharmonicity in refinements when present. Moreover, these particular results suggest that the data resolution restrictions for the Gram-Charlier refinement formulated by Kuhs[1] may in fact be excessive in the context of XWR. This supports previous reports that, at least for heavy atoms, the Kuhs' Criteria may be too strict[2]. The ability of the XWR method to yield results in agreement with experimentally derived multipolar models and, in this case, yield reasonable Gram-Charlier refinement, despite not possessing data of sufficient resolution, is promising. Accordingly, the XWR method represents a highly powerful new tool in the area of charge density analysis.

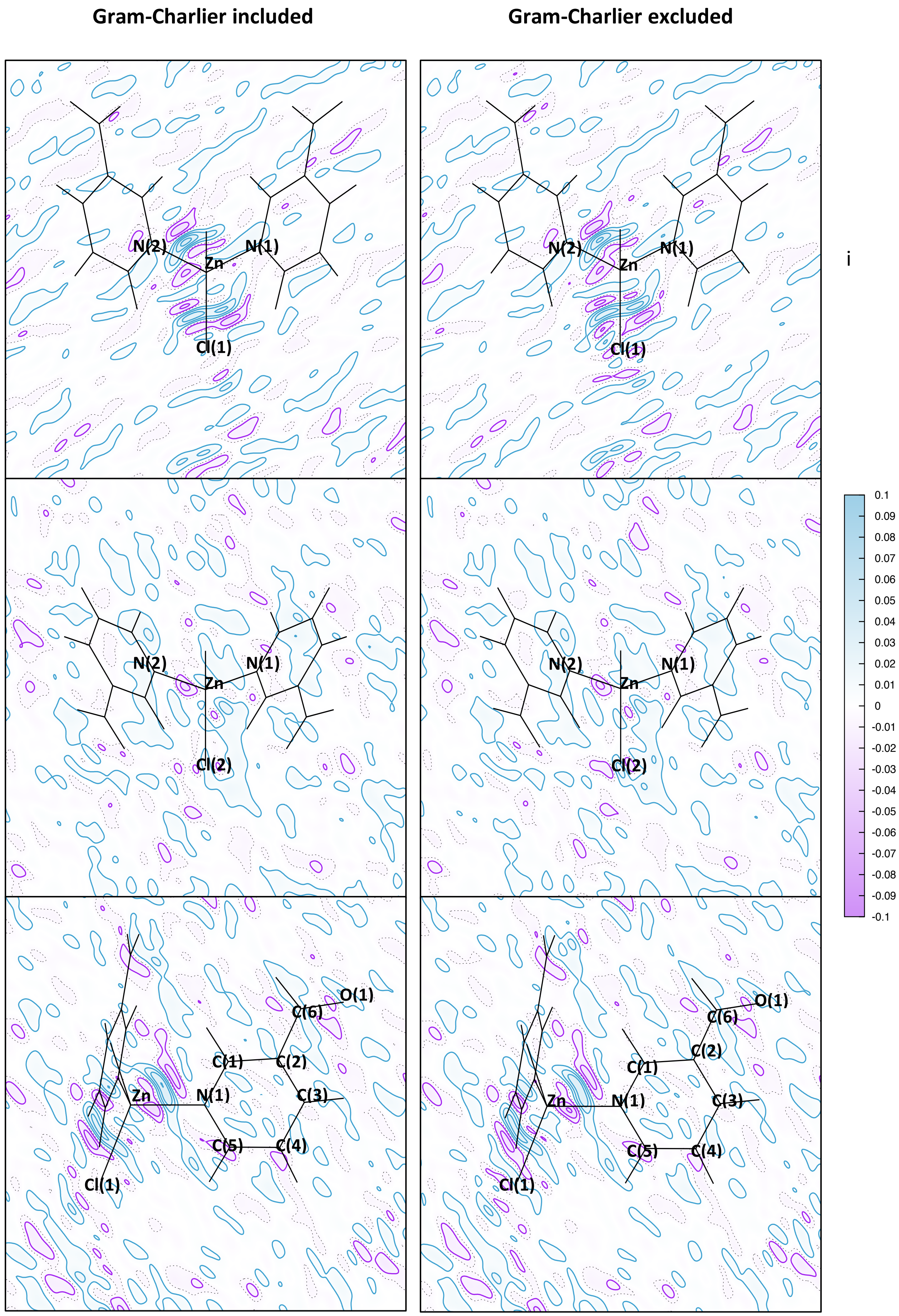

Figure C6. XWR-generated residual electron density maps of **45** at a contour level of 0.1 eÅ^{-3} for the Gram-Charlier-included and the Gram-Charlier-excluded refinements.

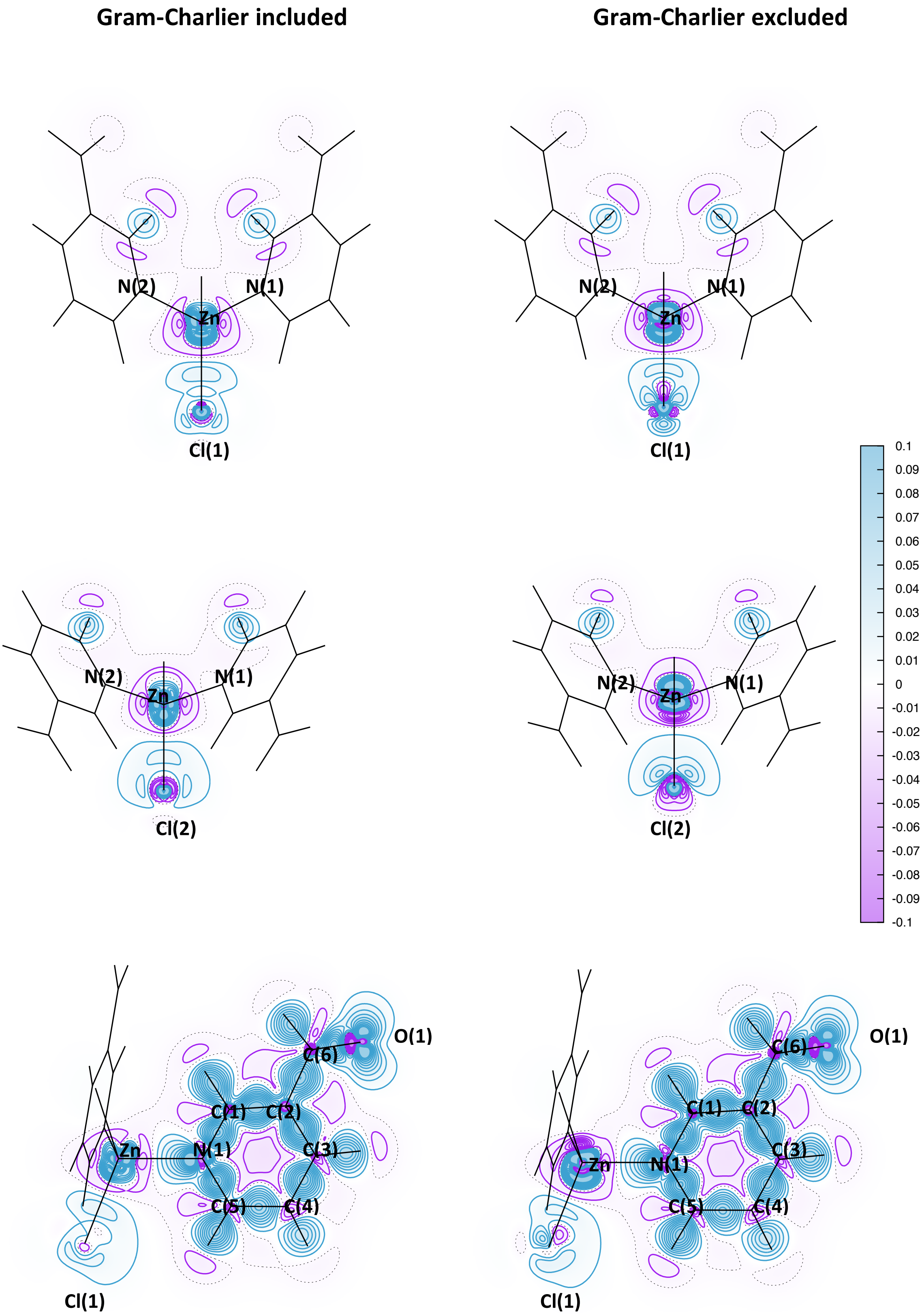

Figure C7. XWR-generated electron deformation density maps of **45** at a contour level of 0.1 eÅ^{-3} for the Gram-Charlier-included and the Gram-Charlier-excluded refinements.

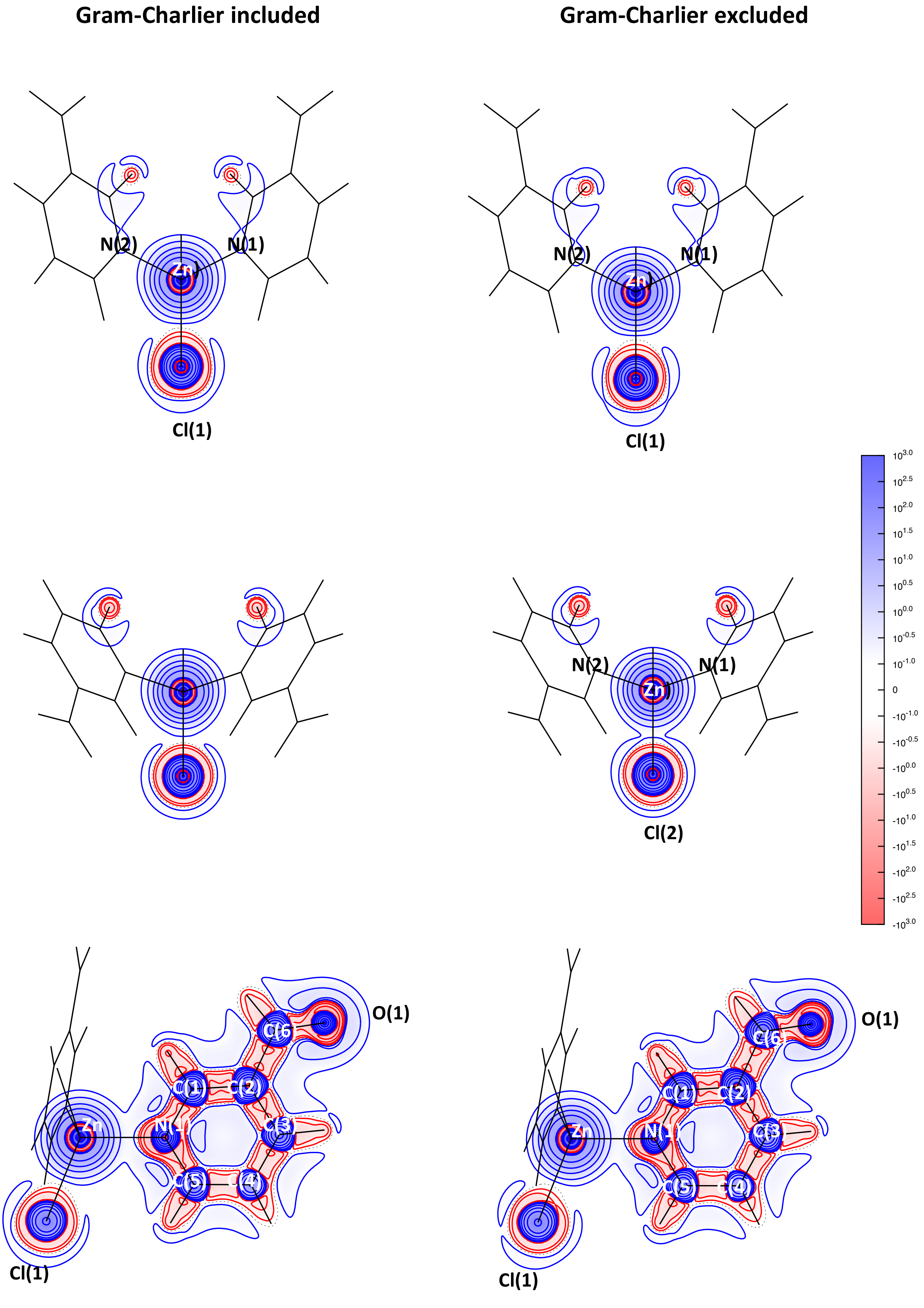

Figure C8. XWR-generated Laplacian maps of **45** at a contour level of 0.1 eÅ^{-5} (gradient scaling) for the Gram-Charlier-included and the Gram-Charlier-excluded refinements.

Initial attempts to carry out a Hirshfeld atom refinement (HAR)[3], as implemented in the program TONTO[4], using the initial multipolar model coordinates and ADPs of **45** as the starting point revealed the presence of shashlik residual density around the Zn ion and Cl atoms, indicative of thermal libration of these atoms. Upon convergence, the HAR-refined coordinates and ADPs were used as the starting point of an X-ray wave-function refinement in accordance with the regime of Jayatilaka and Grimwood.[5] However, the residual density maps of the converged XWR revealed that shashlik residuals persisted around the Zn ion and Cl atoms. Consequently, a refinement of the Gram-Charlier (GC) anharmonic thermal parameters was attempted in the initial HAR for Zn, Cl(1), and Cl(2). Reasonable values for the GC tensor were achieved up to the 3rd order (Table C3). Their probability density function (PDF) plots were also assessed and deemed reasonable (Fig C8). 4th order GC values resulted in an increase in the test statistic, χ^2, and were thus not included. This resulted in an amelioration of the shashlik residuals, albeit to a lower degree around Cl(1), and a significant improvement in the deformation density of the Zn atom, once a full XWR was undertaken.

Table C3. The 3rd order Gram-Charlier coefficients (x 10^2) for the Zn ion and Cl atoms in **45**.

Atom	C_{xxx}	C_{yyy}	C_{zzz}	C_{xxy}	C_{xxz}	C_{xyy}	C_{yyz}	C_{xzz}	C_{yzz}	C_{xyz}
Zn	-0.022(5)	-0.0103(5)	0.0	-0.0097(14)	0.0	-0.0033(6)	0.0	-0.0005(3)	-0.00045(12)	0.0
Cl(1)	-0.030(12)	-0.0037(12)	0.0	-0.017(3)	0.0	-0.0021(14)	0.0	0.0087(7)	0.0007(3)	0.0
Cl(2)	0.047(13)	-0.0112(11)	0.0	-0.017(3)	0.0	-0.0007(13)	0.0	-0.0030(7)	-0.0045(3)	0.0

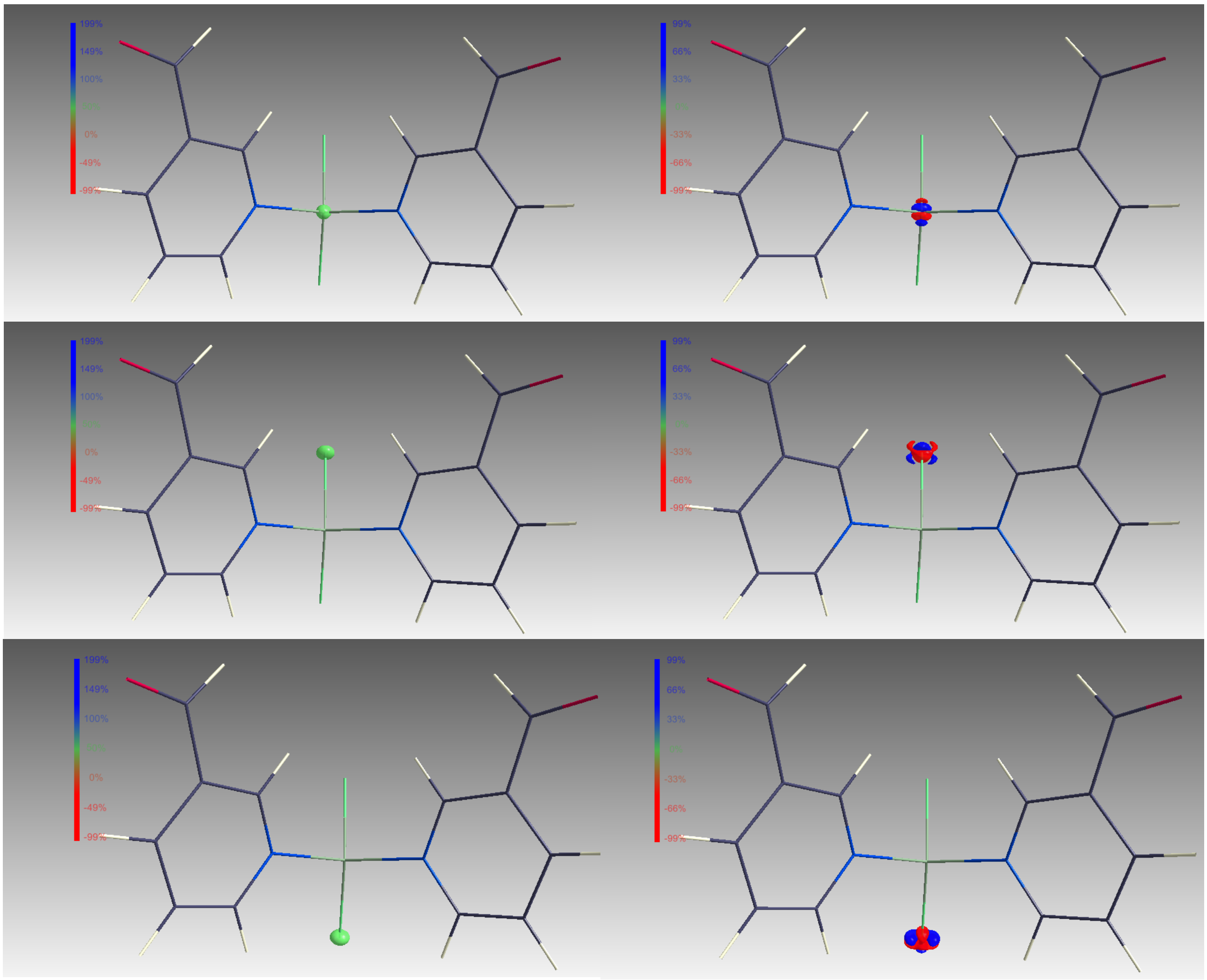

Figure C9. Probability density functions of the Gram-Charlier refined atoms [Zn, Cl(1), Cl(2)] (left: 2nd and 3rd order; right: 3rd order only); PDFs were generated using MoleCoolQT.[6]

A comparison of the results from the GC-included XWR and the GC-excluded refinements is shown in Table C4.

Table C4. A comparison of the refinement statistics for the Gram-Charlier-excluded and Gram-Charlier-included XWR refinements.

Parameter	Gram-Charlier-included refinement	Gram-Charlier-excluded refinement
λ	1.20	1.20
χ^2	1.61	1.69
R(F)	0.0189	0.0192
R_w(F)	0.0234	0.0240
Goodness of Fit (GOF)	1.27	1.69
N° of reflections (N_r)	5704	5704
N° of parameters (N_p)	154	136
Min / max residuals [eÅ^{-3}]	0.087 / -0.043	0.089 / -0.047

C.5 References

(1) Kuhs, W. F. Generalized Atomic Displacements in Crystallographic Structure Analysis. *Acta Crystallogr. A* **1992**, *48* (2), 80–98.

(2) Herbst-Irmer, R.; Henn, J.; Holstein, J. J.; Hübschle, C. B.; Dittrich, B.; Stern, D.; Kratzert, D.; Stalke, D. Anharmonic Motion in Experimental Charge Density Investigations. *J. Phys. Chem. A* **2013**, *117* (3), 633–641.

(3) Capelli, S. C.; Bürgi, H.-B.; Dittrich, B.; Grabowsky, S.; Jayatilaka, D. Hirshfeld Atom Refinement. *IUCrJ* **2014**, *1* (5), 361–379.

(4) Jayatilaka, D.; Grimwood, D. J. Tonto: A Fortran Based Object-Oriented System for Quantum Chemistry and Crystallography. In *Computational Science — ICCS 2003*; Sloot, P. M. A., Abramson, D., Bogdanov, A. V., Gorbachev, Y. E., Dongarra, J. J., Zomaya, A. Y., Eds.; Lecture Notes in Computer Science; Springer Berlin Heidelberg, 2003; pp 142–151.

(5) Jayatilaka, D.; Grimwood, D. J. Wavefunctions Derived from Experiment. I. Motivation and Theory. *Acta Crystallogr. A* **2001**, *57* (1), 76–86.

(6) Hübschle, C. B.; Dittrich, B. MoleCoolQt – a Molecule Viewer for Charge-Density Research. *J. Appl. Crystallogr.* **2011**, *44* (1), 238–240.

Appendix D

Supplementary Information pertaining to *ab initio* DFT Calculations

D.1 Additional DFT Calculations of DAST and BP3

Table D1. *Ab-initio*-derived hyperpolarizability values for the NLO-active cations of **DAST** and **BP3** in the presence of one, two, or three cations.

Number of cations	**DAST**		**BP3**	
	β_0	**Difference in β_0 from 1 cation (% increase)**	β_0	**Difference in β_0 from 1 cation (% increase)**
1	218.78	0.00	219.85	0.00
2	569.57	350.79 (160 %)	459.29	239.44 (109 %)
	468.79	250.01 (114 %)	459.29	239.44 (109 %)
3	705.46	486.68 (222 %)	N/A	---
	669.35	450.57 (206 %)	N/A	---
	899.27	680.49 (311 %)	N/A	---

Calculations undertaken by T.-C. Lin.

These DFT calculations reveal that cation···cation interactions in **DAST** and **BP3** promote the first hyperpolarizability, β_0. This is a consequence of the promotion of ICT, providing an overall positive contribution to the ensuing NLO activity of the chromophores.

Regarding anion···anion interactions, it is highly unlikely that these interactions will cause degradation of the effective molecular hyperpolarizability, β_0 in **DAST** and **BP3**. It has been shown that the pTS$^-$ anions, such as those contained in **DAST** and **BP3**, are very inefficient NLO chromophores, when compared to the stilbazolium cations[1]. They thus stand to contribute a negligible or minimal effect on the overall macroscopic NLO activity of **DAST** and **BP3**.

D.2 References

(1) Duan, X.-M.; Okada, S.; Oikawa, H.; Matsuda, H.; Nakanishi, H. Comparatively Large Second-Order Hyperpolarizability of Aromatic Sulfonate Anion with Short Cutoff Wavelength. *Jpn. J. Appl. Phys.* **1994**, *33* (11A), L1559.